

University of Windsor

Scholarship at UWindor

Electronic Theses and Dissertations

Theses, Dissertations, and Major Papers

2016

Increasing Efficiency of Ti-6Al-4V Machining by Cryogenic Cooling and using Nanolubricants

Girish Krishnamurthy
University of Windsor

Follow this and additional works at: <https://scholar.uwindsor.ca/etd>

Recommended Citation

Krishnamurthy, Girish, "Increasing Efficiency of Ti-6Al-4V Machining by Cryogenic Cooling and using Nanolubricants" (2016). *Electronic Theses and Dissertations*. 5835.
<https://scholar.uwindsor.ca/etd/5835>

This online database contains the full-text of PhD dissertations and Masters' theses of University of Windsor students from 1954 forward. These documents are made available for personal study and research purposes only, in accordance with the Canadian Copyright Act and the Creative Commons license—CC BY-NC-ND (Attribution, Non-Commercial, No Derivative Works). Under this license, works must always be attributed to the copyright holder (original author), cannot be used for any commercial purposes, and may not be altered. Any other use would require the permission of the copyright holder. Students may inquire about withdrawing their dissertation and/or thesis from this database. For additional inquiries, please contact the repository administrator via email (scholarship@uwindsor.ca) or by telephone at 519-253-3000ext. 3208.

Increasing Efficiency of Ti-6Al-4V Machining by Cryogenic Cooling and using Nanolubricants

By

Girish Krishnamurthy

A Thesis

**Submitted to the Faculty of Graduate Studies
through the Department of Mechanical, Automotive
and Materials Engineering
in Partial Fulfillment of the Requirements for
the Degree of Master of Applied Science at the
University of Windsor**

Windsor, Ontario, Canada

2016

© 2016 Girish Krishnamurthy

Increasing Efficiency of Ti-6Al-4V Machining by Cryogenic Cooling and using Nanolubricants

By

Girish Krishnamurthy

APPROVED BY:

**D. Green, Outside Program Reader
Department of Mechanical, Automotive & Materials Engineering**

**V. Stoilov, Program Reader
Department of Mechanical, Automotive & Materials Engineering**

**A.T. Alpas, Advisor
Department of Mechanical, Automotive & Materials Engineering**

21 July, 2016

DECLARATION OF ORIGINALITY

I hereby certify that I am the sole author of this thesis and that no part of this thesis has been published or submitted for publication.

I certify that, to the best of my knowledge, my thesis does not infringe upon anyone's copyright nor violate any proprietary rights and that any ideas, techniques, quotations, or any other material from the work of other people included in my thesis, published or otherwise, are fully acknowledged in accordance with the standard referencing practices. Furthermore, to the extent that I have included copyrighted material that surpasses the bounds of fair dealing within the meaning of the Canada Copyright Act.

I declare that this is a true copy of my thesis, including any final revisions, as approved by my thesis committee and the Graduate Studies office, and that this thesis has not been submitted for a higher degree to any other University or Institution.

ABSTRACT

Generation of high localized cutting zone temperatures leading to dissolution wear hinders machinability of Ti alloys using uncoated carbide tools and polycrystalline diamond (PCD) tools. In addition, the thermo-plastic instability exhibited by titanium alloys promotes serrated chip formation that causes fluctuations in the cutting forces leading to chatter and severe flank wear. This work considers two methods to mitigate these problems during cutting of Ti-6Al-4V, namely, cryogenic machining to influence chip segmentation, and the use of WS₂ blended metal removal fluids (MRF) to influence interface coefficient of friction (COF). Cryogenic machining of Ti-6Al-4V at 45 m/min and 0.15 mm/rev led to easier fracture of chip segments due to decrease in toughness of the material. Analyses of fracture surfaces of the chips showed that the decrease in toughness was due to increased presence of shear ridges at low temperatures. The role of COF was determined using pin-on-disk experiments. Iterative tests of Ti-6Al-4V pins sliding against uncoated WC-Co disk showed that the addition of WS₂ nanoparticles to MRF are capable of decreasing the interface COF lower than that under MRF lubricated conditions alone. Orthogonal machining of Ti-6Al-4V at a cutting speed of 29.5 m/min, feed rate of 0.4 mm/rev under dry conditions generated an average cutting force of 400 N. Under MRF + WS₂ lubricated conditions, the average cutting force reduced to 190 N, which was 52% lower than dry conditions. The low COF values due to the MRF + WS₂ lubricant reduces the interface temperature and thus aids in machining.

DEDICATION

To my beloved brother,

Mr. Hari Krishnan

Who always made me run the extra mile,



To my parents,

Mr. Krishnamurthy and

Mrs. Chellamal

*For their constant love, endless support and
encouragement*

ACKNOWLEDGEMENT

I would like to express my sincere gratitude to my advisor, Dr. A.T. Alpas for his constant encouragement, support and patience during my graduate studies. Working under his expert guidance has been a great learning experience.

I would also like to thank my committee members: Dr. D. Green and Dr. V. Stoilov for their invaluable discussions, suggestions and time. Sincere thanks to Mr. A. Jenner and Mr. P. Seguin for their invaluable help with the designing, construction and calibration of the force measurement system. I would also like to thank Mr. T. Bolger, Mr. S. Budinsky, and Mr. M. St. Pierre from the Technical Support Centre for providing assistance with the orthogonal machining experiments.

Special thanks to Dr. Sukanta Bhowmick for his constant encouragement and support throughout my graduate study. I would also like to extend my appreciation to fellow researchers: Mr. M.Z.U. Khan, Mr. A. Banerji, Mr. M. Tas, Mr. Z. Cui, Dr. G. Sun, Mr. M. Lou and Mr. Z. Yang for their constant support and friendship.

Financial assistantship provided by Natural Sciences and Engineering Research Council of Canada (NSERC) through a Strategic Network (CANRIMT) is gratefully acknowledged.

Table of Contents

DECLARATION OF ORIGINALITY	iii
ABSTRACT	iv
DEDICATION	v
ACKNOWLEDGEMENT	vi
LIST OF FIGURES	x
LIST OF SYMBOLS	xix
Chapter 1	1
1. INTRODUCTION	1
1.1 Research Outline	1
1.2 Research Objectives	3
Chapter 2	4
2. LITERATURE SURVEY	4
2.1 Theory of Metal Cutting	4
2.1.1 Mechanisms and Mechanics of Metal Cutting	6
2.1.2 Types of Metal Cutting Process	7
2.1.2.1 Orthogonal Cutting Process	7
2.1.2.2 Oblique Cutting Process	7
2.1.3 Chip Formation	8
2.1.4 Forces and Stresses Generated during Orthogonal Cutting	11
2.1.5 Microstructural Deformation due to Orthogonal Cutting	12
2.1.6 Estimation of Shear Angle	14
2.1.7 Estimation of Flow Stress	15
2.1.8 Estimation of Flow Strain	16
2.2 Titanium Alloys – An Overview	17
2.2.1 Crystal Structure	17
2.3 Introduction to Ti-6Al-4V	19
2.3.1 Mechanical Properties of Ti-6Al-4V	19
2.4 Machining of Ti-6Al-4V	24
2.4.1 Machinability of Ti-6Al-4V	25
2.5 Chip Formation Mechanisms	26
2.5.1 Adiabatic Shear Mechanism	26
2.5.2 Periodic Crack Development Mechanism	28
2.6 Cryogenic Machining	30

2.6.1 Heat Generation during Machining	31
2.7 Effects of Cryogenic Cooling in Machining Processes	32
2.7.1 Effect on Material Properties	32
2.7.2 Effect on Cutting Temperature	33
2.7.3 Effect on Tool Wear and Tool Life	36
2.7.4 Effect on Surface Roughness and Dimensional Deviation	39
2.7.5 Effect on Cutting Forces	42
2.8 Introduction to Nano-fluids	43
2.9 Effect of Nanofluids on machining	45
2.9.1 Effect on Cutting Forces and Surface Roughness	46
2.9.2 Effect on COF and Wear Rate	52
2.9.3 Effect on Cutting Zone Temperature	58
2.9.4 Mechanism of Friction behaviour of Nanoparticles	59
2.10 Summary of Literature Survey	63
Chapter 3	64
3. EXPERIMENTAL PROCEDURE	64
3.1 Workpiece and Tool Materials	64
3.2 Conventional Orthogonal Machining	65
3.2.1 Measurement of Force Components	66
3.2.2 Components of Force Measurement System	67
3.2.3 Calibration of Force Sensor	69
3.3 Cryogenic Machining Approach	71
3.4 Nanolubricant Machining Approach	71
3.4.1 Measurement of Coefficient of Friction	71
3.4.2.1 Measurement of Cutting Zone Temperature:	73
3.5 Surface Roughness Measurements	75
3.6 Metallography	76
3.7 In-situ Machining Experiments	76
3.8 Differences in Cutting Geometries between In-situ and Conventional Machining	78
Chapter 4	80
4. EXPERIMENTAL RESULTS	80
4.1 Conventional Orthogonal Machining of Ti-6Al-4V – Ambient and Cryogenic Conditions	80
4.1.1 Measurement of Forces during Orthogonal Machining	81
4.1.2 Quantitative Analyses of Chip Morphology	83

4.1.2.1 Chip Thickness	83
4.1.2.2 Shear Displacement	84
4.1.2.3 Shear Angle.....	89
4.1.2.4 Width of chip segment	89
4.1.2.5 Lateral Displacement of Chip Segments	89
4.1.3 Fracture Surface Morphology	91
4.1.4 Microstructural Interpretation of Serrated Chip Formation	92
4.1.5 Effect of temperature on fracture behaviour of Ti-6Al-4V	98
4.2 Nanolubricant Machining	95
4.2.1 Effect of WS ₂ Nanoparticles on the COF of WC-Co vs. 319Al	95
4.2.2 Effect of WS ₂ Nanoparticles on Cutting Forces Generated with Uncoated WC-Co vs. 319Al	99
4.2.3 Effect of WS ₂ Nanoparticles on the Surface Roughness of Machined Part	101
4.2.4 Effect of WS ₂ Nanoparticles on Tool Wear and Adhesion	103
4.2.5 Effect of WS ₂ Nanoparticles on the COF of WC-Co vs. Ti-6Al-4V	105
4.2.7 Effect of WS ₂ Nanoparticles on Surface Roughness of Machined Part	111
4.2.8 Effect of WS ₂ Nanoparticles on Tool Wear and Adhesion	113
4.2.9 Raman Spectroscopy on Cutting Edge:	115
Chapter 5	118
5. DISCUSSION	118
5.1 Serrated Chip Formation Mechanism	118
5.2 Correlation between Chips from In-situ and Conventional Machining	121
5.3 Tool Wear, Diffusion and Adhesion	122
5.4 Analysis of Fracture Surfaces	124
5.5 Schematic Representation of Tearing Topographical Surface	128
5.6 Influence of nanoparticles on COF	129
5.7 Mechanism of Friction Reduction	132
Chapter 6	135
CONCLUSIONS	135
6.1 Conclusions.....	135
6.2 Future Work.....	137
REFERENCES.....	139
LIST OF CONFERENCES.....	149
LIST OF PUBLICATIONS	150
VITA AUCTORIS	151

LIST OF FIGURES

CHAPTER 2

- Figure 2.1:** Deformation zones in a workpiece during orthogonal machining process [10] 6
- Figure 2.2:** Mechanism of metal cutting in an orthogonal machining process showing a cutting tool with rake angle ' α ' forming a chip with a shear angle ' ϕ ' [10]..... 7
- Figure 2.3:** Schematic of metal cutting showing (a) orthogonal cutting process where the cutting tool is perpendicular to the direction of machining, and (b) oblique cutting process where the cutting tool is at an angle ' λ ' to the direction of machining [11] 8
- Figure 2.4:** Two broad categories of chip segments formed during orthogonal machining of Ti 140A at different experimental conditions, namely, (a) continuous chips of Ti 140A formed at a cutting speed of 30 m/min, feed rate of 0.13 mm/rev, (b) cyclic chips of Ti 140A formed at a cutting speed of 45 m/min and feed rate of 0.26 mm/rev [12] 10
- Figure 2.5:** Types of cyclic chip segments (a) wavy chips formed during machining AISI 1015 at a cutting speed of 30 m/min and feed rate of 0.13 mm/rev, (b) segmented chips formed during machining of AISI 1015 at a cutting speed of 50 m/min and feed rate of 0.20 mm/rev, (c) catastrophic shear chips formed during machining of Ti-6Al-4V at a cutting speed of 5 m/s and feed rate of 0.12 mm/rev, (d) discontinuous chips formed during machining of 319Al at a cutting speed of 35 m/min and feed rate 0.25 mm/rev [14, 15] 10
- Figure 2.6:** Merchant circle diagram showing the different forces generated during an orthogonal cutting process where F_C and F_T or F_f are the cutting and feed forces, F_s and F are the shear forces on the shear plane and rake face, F_N and N are the normal forces on the shear plane and rake face respectively, ϕ and α are the shear and rake angles respectively, A_c and A_0 are the cut and uncut chip thickness respectively. [16] .. 11
- Figure 2.7:** Cross sectional optical micrograph of Cu just ahead of the tool tip after orthogonal machining [18]..... 13
- Figure 2.8:** A computer generated image of the cross-section of the machined workpiece with the chip still attached. The image was obtained by determining the location of each point on the deformation lines and these were plot ted to actual scale shown on the diagram [19]..... 13

Figure 2.9: Schematic diagram showing the measurement of shear angles ‘ ϕ ’ from the slopes of the deformation lines at an angle of ‘ θ ’ [19].....	14
Figure 2.10: (a) Phase diagram of Ti-6Al-4V showing the different types of titanium alloys based on the alloying composition, (b) Unit cell of hexagonal close packed structure and body centred cubic structure of the α and β phase in a Ti-6Al-4V alloy [28]	18
Figure 2.11: TEM bright-field images of: (a) fine ($3\ \mu\text{m}$); and (b) coarse ($11\ \mu\text{m}$) grained Ti-6Al-4V deformed at 600°C with a strain rate of 10^{-3}s^{-1} ($\epsilon=0.3$) [30]	20
Figure 2.12: True stress-strain curves for Ti-6Al-4V at various temperatures and strain rates [31]	21
Figure 2.13: Variation of ultimate tensile strength and yield stress of Ti-6Al-4V with temperature [32, 33, 34].....	21
Figure 2.14: Variations of strain rate sensitivity as a function of temperature for deformation at a true strain of 0.05 under different strain rate ranges [31]	22
Figure 2.15: Variation of hardness of Ti-6Al-4V with temperature measured on a Rockwell C-scale [35].....	23
Figure 2.16: Temperature dependence of yield stress of Ti-6Al-4V at low and high strain rates compared to α -Ti [36].....	24
Figure 2.17: Sequential steps leading to serrated chip formation in Ti-6Al-4V. (a) Thermal softening and strain hardening results in instability, which leads to strain localization along a shear surface (band). This shear surface originates from the tool tip and gradually curves upwards until it meets the free surface, (b) Tool’s gradual advancement applies an increased amount of force, at which point a crack initiates at the tool tip and gradual flattening increases the contact between the tool and the material ahead, (c) Propagation of the crack along the path of strain localization, (d) The chip being formed pushes the previously formed chip by bulging and gradually flattening, thus shifting its contact towards the tool face. As the upsetting progresses, more and more stress is generated, which causes intense shear between the segment being formed and the one before it. [2]	28
Figure 2.18: Formation of a serrated chip through periodic crack development process. (a) Material at point C moves upward along CD, which has the same applied load direction. (b) A shear crack initiates at point D, which runs from the surface in a downward direction toward the tool tip along the path DO, (c) As the tool advances, the chip glides outward along the cracked surface until the next crack forms at D’ [37].....	29

Figure 2.19: Measured and predicted cutting tool temperatures under different machining environments [54]	35
Figure 2.20: Comparison of (a) flank wear, (b) cutting zone temperature under wet and cryogenic machining of Ti-6Al-4V with increasing cutting velocity [61]	37
Figure 2.21: (a, b) Average wear of the primary flank during dry cutting and using cryogenic coolant, (c, d) Average wear of the nose during dry cutting and using cryogenic coolant [62].....	39
Figure 2.22: Variation of (a) surface roughness, and (b) dimensional accuracy with machining time under different cutting environments [52]	41
Figure 2.23: Variation of surface roughness with cutting velocity under wet and cryogenic machining of Ti-6Al-4V [61].....	42
Figure 2.24: Comparison of (a) cutting, and (b) feed forces under wet and cryogenic machining of Ti-6Al-4V with increasing cutting velocity [61]	43
Figure 2.25: Variation in cutting forces while machining with base oil and nanoparticle suspended base oil [79]	46
Figure 2.26: Cutting force generated during milling of Al-2017 with (a) normal lubricating oil, and (b) 1.5 wt.% nanoparticle blended lubricating oil. A 22% decrease in cutting force was achieved using the 1.5 wt.% nanoparticle blended lubricant compared to the base lubricant [80]	47
Figure 2.27: Surface profile of machined surface under (a) normal lubricating conditions, (b) 0.5 wt.% carbon-onion enriched lubricating conditions, (c) 1 wt.% carbon onion enriched lubricating conditions, (d) 1.5 wt.% carbon onion enriched lubricating conditions. The average surface roughness of the machined surface decreased from 0.380 μm under normal lubricating oil conditions to 0.204 μm under 1.5 wt.% carbon-onion blended lubricating oil conditions [80]	48
Figure 2.28: Variation in surface roughness of the machined Al6061 sample with increasing nanoparticle concentration. The least average surface roughness was recorded using the 0.5 wt.% nanoparticle concentration in lubricating oil [81].....	49
Figure 2.29: SEI micrographs of the surface of Al6061 subjected to milling with (a) normal lubricating oil, (b) 0.2 wt.% SiO ₂ blended lubricating oil [82]	50

Figure 2.30: Cutting forces during milling of Al6061 with increasing nanoparticle concentration. The least cutting force was recorded with 0.2 wt.% SiO ₂ concentration in lubricant oil [82].....	50
Figure 2.31: Average torque generated during micro-drilling of Al6061 with different coolants [83].....	51
Figure 2.32: SEM Micrographs of the drilled holes under (a) compressed air (CA) lubrication, (b) vegetable oil with 2 wt.% nanodiamond (ND) particles [83]	51
Figure 2.33: Friction coefficient of the SF oil with and without nanoparticles [84]	52
Figure 2.34: The time-dependence of friction force for oil and oil + IF blend at load of 260 N. The friction force under IF nanoparticle blended oil was found to be lower than the plain lubricating oil throughout the sliding experiment [85]	53
Figure 2.35: The effect of load on the wear rate of pin lubricated with oil and oil + IF lubricants [85]	54
Figure 2.36: Schematic of third body model under friction with nanoparticles [85].....	54
Figure 2.37: Mean friction coefficients for base oil and nanofluids [86].....	55
Figure 2.38: Magnitude of (a,b) COF, (c,d) specific energy obtained during grinding of EN24 steel using different lubricants [87].....	57
Figure 2.39: Variation of grinding zone temperatures during sliding of grey cast iron disks under different cooling environments [88]	58
Figure 2.40: Demonstration of rolling friction mechanism where an IF nanoparticle completes one complete rotation is shown from images (a) through (f). The rotation can be tracked with the help of arrow marks shown in the nanoparticle [93].....	60
Figure 2.41: Demonstration of sliding behaviour of an IF nanoparticle. The white dot represents the initial point of sliding [93]	61
Figure 2.42: Demonstration of exfoliation mechanism for an IF nanoparticle. (a,b) The microscope probe is positioned closer to the nanoparticle, (c,d) Uniaxial compression of the nanoparticle by the microscopic probe, (e,f) When the microscopic probe begins to slide after making contact, the nanoparticle begins to exfoliate and this forms a film over the surface of the workpiece [93]	62

Figure 2.43: Schematic representation of the three dominant friction reduction mechanisms for a nanoparticle [93].....	63
---	----

CHAPTER 3

Figure 3.1: Optical microstructure of Ti-6Al-4V after etching with Kroll’s reagent for 10 s showing the presence of α and β phases	64
--	----

Figure 3.2: Cutting tools used for (a) in-situ experiments – uncoated tungsten carbide tool, (b) conventional machining – PCD tool.....	65
--	----

Figure 3.3: Experimental setup for orthogonal machining showing the position of cutting tool and the strain sensor assembly for obtaining cutting force data.....	67
--	----

Figure 3.4: Data acquisition system of the force sensor where the electrical signal obtained during machining is transferred wirelessly to the base station and then via USB to the PC	68
---	----

Figure 3.5: Calibration curves of the force sensor in (a) cutting force direction, (b) thrust force direction.....	70
---	----

Figure 3.6: (a) An isometric view of the modifications made in the cutting tool for housing the thermocouple during continuous cutting of Ti-6Al-4V, (b) A top view of the cutting tool showing the depth of the hole for the thermocouple, and its proximity to the cutting edge.....	74
---	----

Figure 3.7: Calibration curve for the thermocouple used during continuous turning of Ti-6Al-4V	75
---	----

Figure 3.8: (a) Overview of the experimental setup for in-situ machining of Ti-6Al-4V, (b, c) Close up view of the setup showing the cutting tool, feed direction, and the microscope in the sample plane of view as the workpiece.....	77
--	----

Figure 3.9: 3D models to illustrate the difference between (a) conventional machining, and (b) in-situ machining	79
---	----

CHAPTER 4

Figure 4.1: Variation of cutting, feed, resultant and shear forces during orthogonal machining of Ti-6Al-4V under (a) ambient, and (b) cryogenic machining environments	82
--	----

Figure 4.2: (a) Optical microstructure of chips obtained during dry machining of Ti-6Al-4V showing the closely spaced chip segments, (b) Optical microstructure of chips obtained during cryogenic machining of Ti-6Al-4V showing broader chip segments with cracks between successive chip segments. The method adopted to measure the various chip parameters are also indicated..... 84

Figure 4.3: (a) SEM of chip segments obtained during dry machining of Ti-6Al-4V indicating the steps involved in a chip formation in SEI mode, (b) Microstructure of the chip after etching with Kroll's reagent showing the shear localization in SEI mode, (c) Higher magnification of the zone marked by a white box in (b) showing the adiabatic shear band and β particles in SEI mode, (d) Schematic representation of a chip obtained from dry machining condition illustrating the formation of adiabatic shear bands (ASB) due to intersegment shearing..... 87

Figure 4.4: SEM of chips obtained from cryogenic machining of Ti-6Al-4V showing a typical chip formed under low temperatures in SEI mode, (b) Schematic representation of a chip obtained from cryogenic machining condition showing easier fracture between chip segments compared to the chips obtained from dry machining condition..... 88

Figure 4.5: SEM of chip segments obtained during (a) dry, (b) cryogenic machining of Ti-6Al-4V alloy. The chips obtained under cryogenic machining conditions show a lateral displacement as against the chips from dry conditions that are seized together..... 90

Figure 4.6: Low magnification SEM of fracture surface of chip segments obtained from cryogenic machining of Ti-6Al-4V indicating all the regions of interest, (b) High magnification SEM of fracture surface showing elongated shear dimples. The white box indicates the location where the high magnification SEM image was taken..... 92

Figure 4.7: Microstructural observation during orthogonal cutting of Ti-6Al-4V under ambient conditions (a) showing crack initiation during chip formation, (b) showing serrated chip formation without gaps between chip segments, (c) High magnification SEM (SEI mode) of typical chips obtained from dry machining showing the attached chip segments..... 95

Figure 4.8: Sequential microstructural observation of continuous chip formation during in-situ machining of AA6061 where (a) Shows the initiation of a plastic zone just ahead of the tool tip, (b, c) shows increase in plastic zone size due to advancement in tool, (d) Formation of a chip segment separating from the deformed zone and the formation of a new plastic zone for the next chip segment..... 96

Figure 4.9: (a) Microstructural observation during orthogonal machining of Ti-6Al-4V under cryogenic conditions, (b) High magnification SEM image (SEI mode) showing

typical chips obtained from cryogenic machining showing separations between chip segments..... 97

Figure 4.10: Variation of impact toughness of Ti-6Al-4V with temperature. A linear relationship was observed between toughness and temperature for Ti-6Al-4V 99

Figure 4.11: Variation of impact toughness of 4140 steel with temperature. The inset images show the fracture surfaces of the impact test samples tested at cryogenic and ambient temperatures..... 100

Figure 4.12: Low magnification optical macrographs of Ti-6Al-4V impact samples tested at (a) $-196\text{ }^{\circ}\text{C}$, (b) $-95\text{ }^{\circ}\text{C}$, (c) $0\text{ }^{\circ}\text{C}$, (d) $25\text{ }^{\circ}\text{C}$, showing the decrease in shear lip area with decrease in temperature..... 95

Figure 4.13: Variation of COF with the number of revolutions when uncoated WC-Co was tested against 319Al counterface in (a) dry (unlubricated) and with MRF lubricated conditions, (b) MRF, MRF + WS_2 lubricated conditions with varying concentrations. (c) Variation of running-in and steady state COF for MRF, MRF + WS_2 lubricated sliding conditions. Each point represents the average value of the three iterative tests performed in all test conditions. The error bars denote the standard deviation about the mean COF value from the three iterative tests..... 98

Figure 4.14: Variation of cutting forces generated during orthogonal cutting of 319Al at a cutting speed of 29.7 m/min , feed rate of 0.4 mm/rev and a 1 mm depth of cut under (a) dry machining condition, (b) MRF, MRF + WS_2 lubricated conditions. The average cutting force was calculated from the more stable response as shown in (a) and (b), (c) Bar chart showing a comparison of the average cutting forces during the orthogonal machining tests under different machining conditions. The error bar denotes the standard deviation about the mean cutting force from the two iterative tests 101

Figure 4.15: Surface profiles of machined surface in (a) dry, (b) MRF, (c) MRF + 1% WS_2 machining conditions. (d) Comparison of average and root mean square roughness for all machining conditions. The error bars represent the standard deviation about the mean surface roughness value from the two iterative tests. The inset image shows the spots on the machined surface where the roughness data were taken from..... 103

Figure 4.16: SEM (SEI mode) of the rake and flank faces of the uncoated WC-CO cutting tool after subjecting to orthogonal cutting of 319Al under (a), (b) dry; (c), (d) MRF; (e), (f) MRF + 1% WS_2 machining conditions 104

Figure 4.17: Variation of COF with the number of revolutions when uncoated WC-Co was tested against Ti-6Al-4V counterface in (a) dry (unlubricated) and with MRF lubricated conditions, (b) MRF, MRF + WS_2 lubricated conditions with varying concentrations. (c) Variation of running-in and steady state COF for MRF, MRF + WS_2

lubricated sliding conditions. Each point represents the average value of the three iterative tests performed in all test conditions. The error bars denote the standard deviation about the mean COF value from the three iterative tests 108

Figure 4.18: *Variation of cutting forces generated during orthogonal cutting of Ti-6Al-4V at a cutting speed of 29.5 m/min, feed rate of 0.4 mm/rev and a 1 mm depth of cut under (a) dry machining condition, (b) MRF, MRF + WS₂ lubricated conditions, (c) Plot of comparison of the average cutting forces during the orthogonal machining tests under different machining conditions, (d) Plot of comparison of average cutting zone temperature generated during each machining condition..... 111*

Figure 4.19: *Surface profiles generated during orthogonal machining of Ti-6Al-4V at a cutting speed of 95 m/min, feed rate of 0.12 mm/rev and a 1 mm depth of cut under (a) dry, (b) MRF, (c) MRF + 1% WS₂ machining environments..... 112*

Figure 4.20: *SEM (SEI mode) of the rake and flank faces of the uncoated WC-CO cutting tool after subjected to orthogonal cutting of Ti-6Al-4V under (a), (b) dry; (c), (d) MRF; (e), (f) MRF + 1% WS₂ machining conditions..... 115*

Figure 4.21: *Micro-Raman spectra of (a) WS₂ nanoparticles, (b) the cutting edge that was subjected to machining of Ti-6Al-4V at a cutting speed of 29.7 m/min, 0.4 mm/rev, 1 mm depth of cut under MRF + 1% WS₂ conditions..... 117*

CHAPTER 5

Figure 5.1: *Sequential steps describing serrated chip formation under ambient machining conditions. (a) Thermal softening and strain hardening results in instability, which leads to strain localization along a shear surface (band). This shear surface originates from the tool tip and gradually curves upwards until it meets the free surface, (b) Tool's gradual advancement applies an increased amount of force, at which point a crack initiates at the tool tip and gradual flattening increases the contact between the tool and the material ahead, (c) Propagation of the crack along the path of strain localization, (d) The chip being formed pushes the previously formed chip by bulging and gradually flattening, thus shifting its contact towards the tool face. As the upsetting progresses, more and more stress is generated, which causes intense shear between the segment being formed and the one before it. The cycle repeats with the strain localization for the next chip segment 120*

Figure 5.2: *Serrated chip formation under (a) dry machining condition showing no separations between chip segments, and (b) cryogenic machining condition showing prominent gaps between successive chip segments 121*

Figure 5.3: Low magnification SEM of fracture surfaces of Ti-6Al-4V at (a) cryogenic temperature, (b) room temperature	126
Figure 5.4: High magnification SEM of fracture surfaces of Ti-6Al-4V at (a) cryogenic temperature, (b) room temperature	127
Figure 5.5: Slip line field for sharp crack in plane strain conditions [111].....	129
Figure 5.6: Schematic of the sequence of events during fracture by formation of shear ridges [108]	129
Figure 5.7: Variation of COF for uncoated WC-Co sliding against (a) 319Al, (b) Ti-6Al-4V pin, under different environments.....	132

LIST OF SYMBOLS

α	Rake angle of cutting tool
ϕ	Shear angle
F_c	Cutting force
F_f	Feed/ Thrust force
F_R	Resultant force
F_S	Shear force on the shear plane
F_N	Normal force on the shear plane
w	Width of cut
γ	Shear strain during orthogonal machining
θ	Deformation angle
H	Vicker's hardness number
σ	Flow stress
F_{System}	Total force on the force measurement system
M	Total mass of the slotted weight
g	Acceleration due to gravity
C	Specific heat capacity

ρ	Density
m	Strain rate sensitivity
$\dot{\epsilon}$	Strain rate
T	Temperature
\dot{c}	Rate of dissolution
c	Concentration of the dissolved material at the interface
D	Diffusivity of the dissolved material
N_0	Number of available substitutional sites for solid 'A' in solid 'B' per unit volume
k	Boltzmann constant
ΔG	Activation energy for dissolution
β	Number of atoms leaving and joining the solution
μ_R	Running-in coefficient of friction
μ_S	Steady state coefficient of friction

Chapter 1

INTRODUCTION

1.1 Research Outline

Machining is a part of the manufacturing process where the desired shape and size of the end product is obtained through metal removal. With advancement in manufacturing technology, it is necessary to understand the machining process, in particular the tool-workpiece interactions to achieve optimization through improvement in tool life, surface finish of finished product, and power consumption.

Ti-6Al-4V alloy is a versatile material for industrial applications because of its high strength-to-weight ratio, combined with high ductility and corrosion resistance but considered to be a difficult-to-machine material [1] owing to a number of reasons. Past studies [1 – 8] indicated that some reasons for difficulty in machining Ti and its alloys include:

- (i) High temperatures generated in a very narrow adiabatic shear band as a result of (a) intense shear concentration in this band and (b) poor heat dissipation from this band due to low thermal conductivity of Ti [2], [3],
- (ii) Segmentation in chips that occurs due to localization of heat during machining. It is reported that the chip segmentation is usually associated with a cyclic variation in cutting forces. This in turn causes vibrations affecting the work piece-tool machine system stability [4], [5],

- (iii) Continuous contact at or near the apex of the tool with the segment being formed due to no relative motion between the segment and the tool face for a considerable portion of the chip segmentation cycle [6],
- (iv) Titanium's chips are very thin resulting in small contact area with the cutting tool (about one-third of that of steel at same feed rate and depth of cut). This causes high stress accumulation at the tip of the cutting tool [7],
- (v) High reactivity of titanium with conventional tool materials such as cemented carbides, borides, or nitrides resulting in dissolution wear at high temperatures [8]. Thus to maintain a reasonable tool life (flank wear less than 200 μm), current machining practices in industry employ various coolants to reduce the cutting zone temperature. Often flooded machining and cryogenic cooling strategies have been employed in machining of titanium alloys to reduce temperature in the cutting zone and also to influence chip segmentation.

When machining titanium alloys, a segmented chip is normally produced. Segmented chip formation is believed to be either due to the growth of cracks from the outer surface of the chip [9] or adiabatic shear band formation which is caused by the localized shear deformation resulting from the predominance of thermal softening over strain hardening [2] and [10]. The onset of shear localization is determined by the cutting speed, which is very low for conventional machining of titanium alloys [11]. Shear localization results in variation of cutting and feed forces with large fluctuations in its magnitude. The consequent vibrations, coined as 'chatter' in the metal cutting process limits the material removal rate and accentuates the problem of tool wear [11]. Thus, chip formation and its morphology

are important features of metal machining and yield important information on the cutting process itself. It is evident from the literature that the cooling strategies and their correlations with cutting forces, tool wear have been extensively investigated during machining of several alloys [12 – 28]. However, the correlations between cooling strategies and their effect on the chip segmentation, coefficient of friction and cutting forces during machining have not been adequately established.

1.2 Research Objectives

In this work, the role of cryogenic machining and friction reduction in improving the machining efficiency of Ti-6Al-4V alloys have been studied. To examine the role of temperature, orthogonal machining of Ti-6Al-4V was conducted at a constant speed and feed rate of 43.3 m/min and 0.15 mm/rev respectively under ambient and cryogenic temperatures. Chips formed under these conditions were examined using metallographic methods to quantify various chip parameters such as chip thickness, shear displacement and shear angle. In addition, the sensitivity of Ti-6Al-4V to fracture was studied by conducting Charpy impact tests. The correlation between toughness and chip fracture was then established.

The role of friction in improving machining efficiency was studied by conducting pin-on-disk experiments. Ti-6Al-4V pins were subject to sliding against uncoated WC-Co disks under dry/unlubricated and lubricated sliding conditions. In addition, tungsten disulphide (WS_2) nanoparticles were added to the conventional metal removal fluid to study their effect on reducing COF. Finally a mechanism has been proposed to explain the effect of adding nanoparticles.

Chapter 2

LITERATURE SURVEY

2.1 Theory of Metal Cutting

During metal removal, forces act on the cutting tool and the work piece. In addition, the heat generated due to friction between the tool and the work piece leads to changes in the grain structures of the workpiece. This results in softening of the material including adiabatic softening which damages the work piece and the tool. To overcome this problem, a detailed study of metal cutting have been conducted considering the tool geometry and materials used.

The process of machining of metals is the most widely used and versatile mechanical manufacturing process employed in any industry. Machining is a process that removes unwanted material in a controlled manner from the work piece, as chips, to give the desired shape. Machinability of a cutting tool comprises of three main aspects – (i) Tool life, (ii) Surface finish, and (iii) Energy consumed for machining. Most research in this field focuses on optimization of the process by producing products with finer surface finish, consuming less power and increased tool life.

The commonly considered machining variables are: tool material, tool geometry, cutting fluid, cutting speed, cutting depth, and feed rate. It is well known that most of the work done in metal cutting is converted to heat, and that results in a temperature rise in the tool, work piece, and chip. All the machining variables mentioned before affect the temperature distribution.

Temperature is always of concern in machining. For example, higher cutting rates generate more heat; the cutting fluid cools work pieces and tools; and the tool selection is limited by temperature and burr formation. To lower the cutting zone temperature, cryogenic coolants such as liquid N₂ are usually applied to remove the heat. This technique is known as cryogenic machining. The coolant is applied locally at the cutting tool, at the work piece, or at the chip. For ductile materials, chips are produced by deforming the work piece in a certain way that most of the deformation takes place in a particular shear plane, which minimizes the plastic work.

Friction between the chip and the cutting tool also plays a dominant role in machining process. High friction values result in highly localised temperature at the tool-work piece interface. This reduces the tool life due to high wear rate. Friction during machining may be reduced by (i) Improving the tool finish and sharpness of the cutting edge, (ii) Using tool materials with low-friction coefficient, (iii) Increasing the cutting speed, (iv) Increasing the rake angle, (v) Using metal removal fluids (MRF). [9]

There are three regions of interest in a cutting process as shown in Figure 2.1 [10]. The plastic deformation characteristics of the material in the primary deformation zone, friction-wear characteristics in the secondary deformation zone, and surface finish in the tertiary deformation zone. Improvements in machining require combined knowledge of not only physics, chemistry and material behaviour but also heat transfer, solid mechanics and tribology. [9]

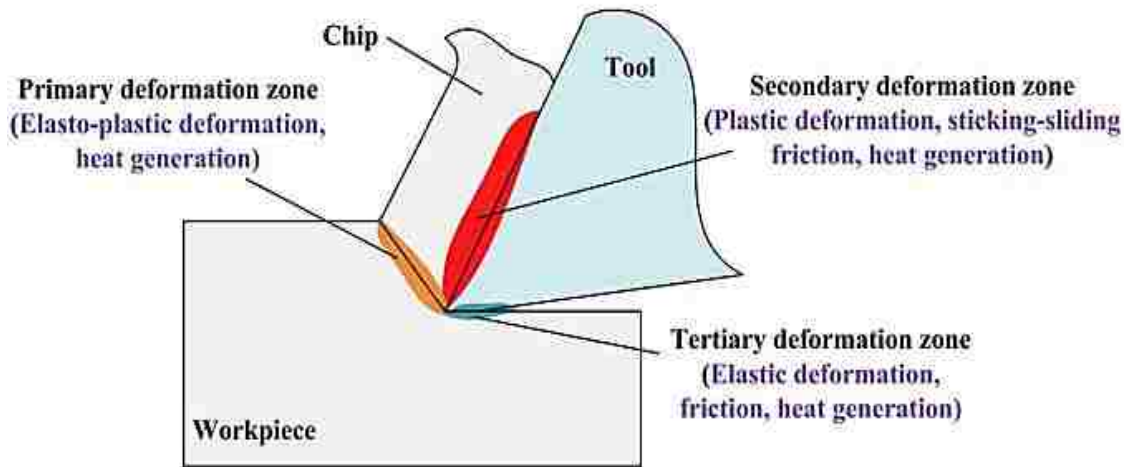


Figure 2.1: Deformation zones in a workpiece during orthogonal machining process [10]

2.1.1 Mechanisms and Mechanics of Metal Cutting

During machining, the plastic flow takes place in a localized region called shear plane as shown in Figure 2.2 [10]. This shear plane is assumed to extend from the cutting tool obliquely up to the uncut surface ahead of the tool. The sheared material begins to flow along the cutting tool face in the form of small pieces called chips. The compressive force applied to form the chip is called cutting force. When the chip flows over the tool, it wears off the tool. Due to friction, frictional heat is produced. The heat generated raises the temperature of the workpiece, cutting tool and the chip. The temperature rise in the cutting tool tends to soften the material and causes loss of keenness in the cutting edge often leading to its failure.

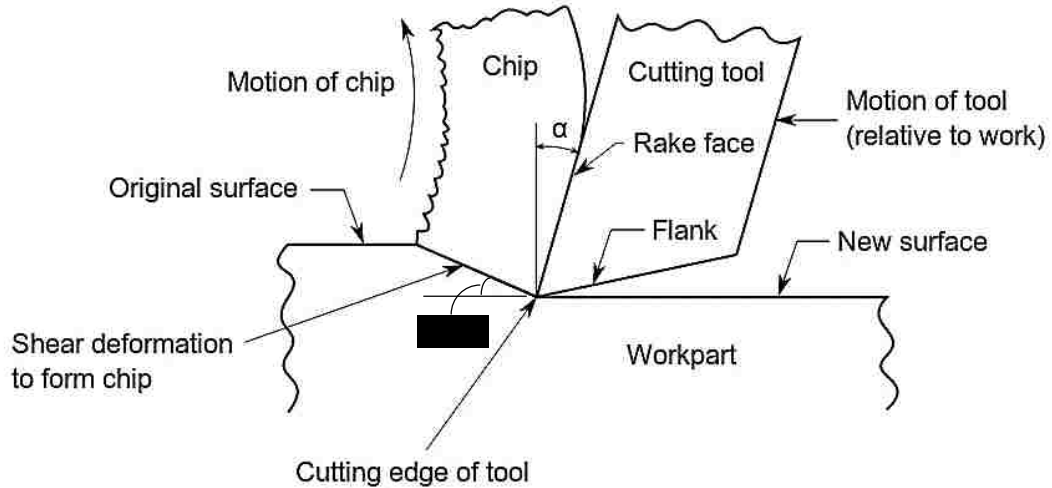


Figure 2.2: Mechanism of metal cutting in an orthogonal machining process showing a cutting tool with rake angle ' α ' forming a chip with a shear angle ' ϕ ' [10]

2.1.2 Types of Metal Cutting Process

Metal cutting processes are mainly classified into two types:

- i. Orthogonal cutting process
- ii. Oblique cutting process

2.1.2.1 Orthogonal Cutting Process

Orthogonal cutting is a type of turning operation in which the cutting tool generates a surface parallel to the original one [11]. In this process, the cutting tool is placed perpendicular to the relative motion of the tool and work piece as shown in Figure 2.3 (a).

2.1.2.2 Oblique Cutting Process

In oblique cutting process, the cutting edge is inclined at an acute angle with the normal to the cutting velocity vector as shown in Figure 2.3 (b).

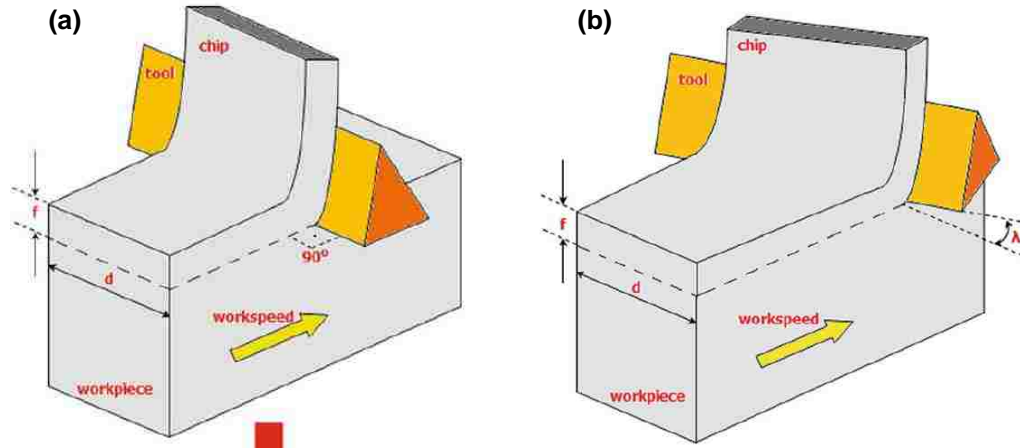


Figure 2.3: Schematic of metal cutting showing (a) orthogonal cutting process where the cutting tool is perpendicular to the direction of machining, and (b) oblique cutting process where the cutting tool is at an angle ' λ ' to the direction of machining [11]

2.1.3 Chip Formation

The type of chip being formed during machining is influenced by a number of factors such as mechanical properties of the workpiece material, tool signature and machining parameters (cutting speed, feed rate, depth of cut, and cooling strategies).

The nature of the chip formed during a machining process is highly variable. Not all metals and alloys withstand the high shear strain occurring in the region of the shear plane without fracturing. The chips then become discontinuous and possess the advantage that they are easily cleared from the cutting zone. However, most ductile materials do not fracture at the shear plane which leads to the formation of continuous chips and causes problems for the machinist.

Chips can summarily be classified into two broad categories (Figure 2.4): Steady state continuous chips and cyclic chips. Cyclic chips can in turn be classified into four different types (Figure 2.5):

- Wavy chips (Figure 2.5(a))
- Segmental chips (Figure 2.5 (b))

- Catastrophic shear chips or serrated chips (Figure 2.5 (c)) and
- Discontinuous chips (Figure 2.5 (d))

Wavy chip formation is usually associated with cyclic variations in un-deformed chip thickness, rake angle and clearance angle variation which mainly occurs due to chatter. The limited rigidity and low damping ability of the cutting tools results in oscillation. Thus a part of the machine tool system experiences resonance and consequently vibrates at large amplitudes [12, 13].

Segmental chips are similar to continuous chips but with a periodic variation in chip thickness. Such chips are formed due to the slow, forward movement of the plastic zone that forms a ramp on the free surface of the chip. This is followed by a rapid return of the plastic zone back towards the tool because of partial fracture, thus forming a step on the chip segment. The instability in the primary shear zone is associated with negative stress-strain material characteristics at large strains. The instability in the secondary shear zone arises from frictional relaxation oscillations leading to stick-slip friction on the tool. [12]

Catastrophic shear chips are usually observed in difficult-to-machine materials such as Ti alloys. Depending on the thermal properties of the material, such chips are formed even at very low cutting speeds. Two different theories concern the basic origin of this type of chip formation. One theory describes the chip formation process on the basis of thermal origin while the other is on the basis of periodic development of cracks in the original surface of the work piece [14]. A detailed review of the two theories will be described in Section 2.6.

Discontinuous chips are formed by upsetting the work material just ahead of the tool tip and the failure mechanism is brittle in nature. During this process, strain concentrates in a narrow band followed by crack formation ahead of the tool tip due to stress concentration leading to rupture along the shear surface. [12, 15]

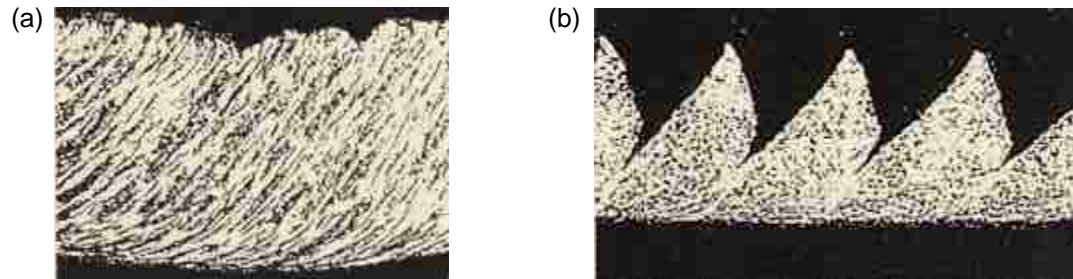


Figure 2.4: Two broad categories of chip segments formed during orthogonal machining of Ti 140A at different experimental conditions, namely, (a) continuous chips of Ti 140A formed at a cutting speed of 30 m/min, feed rate of 0.13 mm/rev, (b) cyclic chips of Ti 140A formed at a cutting speed of 45 m/min and feed rate of 0.26 mm/rev [12]

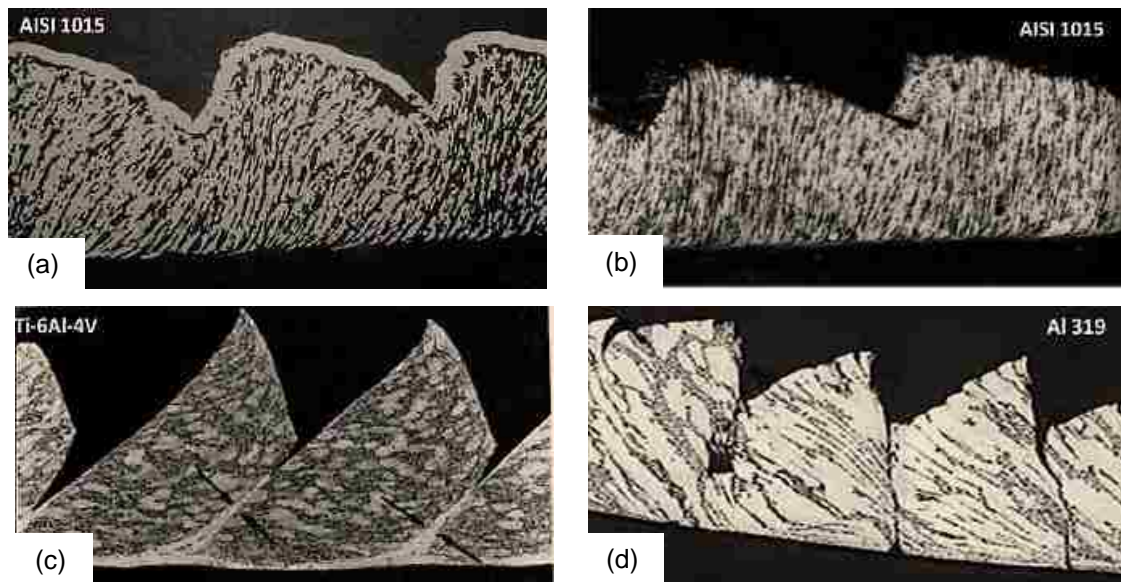


Figure 2.5: Types of cyclic chip segments (a) wavy chips formed during machining AISI 1015 at a cutting speed of 30 m/min and feed rate of 0.13 mm/rev, (b) segmented chips formed during machining of AISI 1015 at a cutting speed of 50 m/min and feed rate of 0.20 mm/rev, (c) catastrophic shear chips formed during machining of Ti-6Al-4V at a cutting speed of 5 m/s and feed rate of 0.12 mm/rev, (d) discontinuous chips formed during machining of 319Al at a cutting speed of 35 m/min and feed rate 0.25 mm/rev [14, 15]

2.1.4 Forces and Stresses Generated during Orthogonal Cutting

During the machining process, force is applied to the tool to cut the materials and according to Merchant [16], in equilibrium conditions, the forces between the tool face and chip and between the work piece and the chip along the shear plane are equal. A force diagram is shown in Figure 2.6.

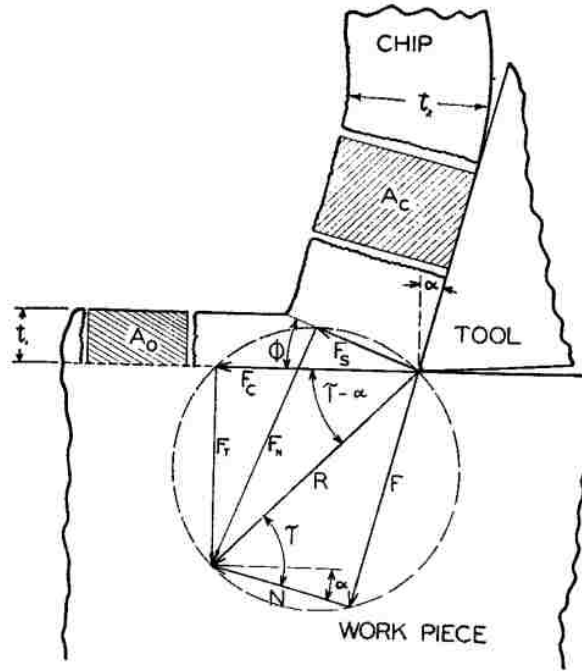


Figure 2.6: Merchant circle diagram showing the different forces generated during an orthogonal cutting process where F_c and F_T or F_f are the cutting and feed forces, F_s and F are the shear forces on the shear plane and rake face, F_N and N are the normal forces on the shear plane and rake face respectively, ϕ and α are the shear and rake angles respectively, A_c and A_o are the cut and uncut chip thickness respectively. [16]

The relationship between various forces is as follows [16]:

$$F_s = F_c \cos \phi - F_f \sin \phi \quad (2.1)$$

$$F_N = F_c \cos \phi + F_f \sin \phi \quad (2.2)$$

$$F = F_c \sin \alpha + F_f \cos \alpha \quad (2.3)$$

$$N = F_c \cos \alpha - F_f \sin \alpha \quad (2.4)$$

where F_c and F_f are the cutting and feed forces, F_s and F are the shear forces on the shear plane and rake face, F_N and N are the normal forces on the shear plane and rake face respectively, ϕ and α are the shear and rake angles respectively.

2.1.5 Microstructural Deformation due to Orthogonal Cutting

Machining is a high-strain rate deformation process that generates large strains and strain gradients in the work piece. Thus chip formation is accompanied by large plastic flow at large strain rates [17]. A comprehensive microstructural analyses helps in understanding the effect of machining on the work material and chip formation. Quantification of different factors, such as chip thickness, shear angle also helps in optimization of the machining process.

A cross-sectional optical micrograph showing the primary deformation zone in a copper work piece that was subjected to orthogonal cutting is shown in Figure 2.7. Ramalingam and Black [17] used SEM and TEM to analyze the plastic deformation zone at the root of the chip in steel. They concluded that a dynamic equilibrium exists between strain hardening and recovery during the chip formation, and that plastic flow in machining is a microscopically heterogeneous deformation process. Zhang and Alpas [19] observed the deformed microstructure of aluminum alloy (6061 Al) and measured the shear angle from the displacement of the extrusion lines, which act as inherent microstructural markers. They also established a method to determine the plastic strain gradients in the material ahead of the tool tip through the measured shear angle as shown in Figure 2.8 & Figure 2.9. Ni et al. performed TEM investigations on copper [18] and aluminum [20] and observed elongated dislocation structures in the primary deformation zone.

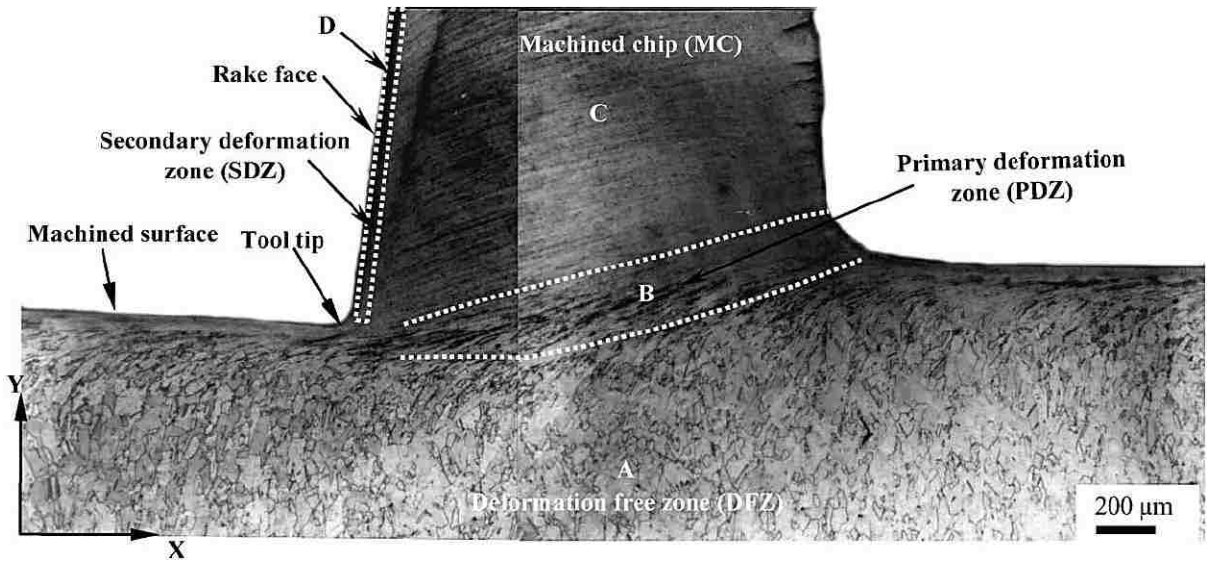


Figure 2.7: Cross sectional optical micrograph of Cu just ahead of the tool tip after orthogonal machining [18]

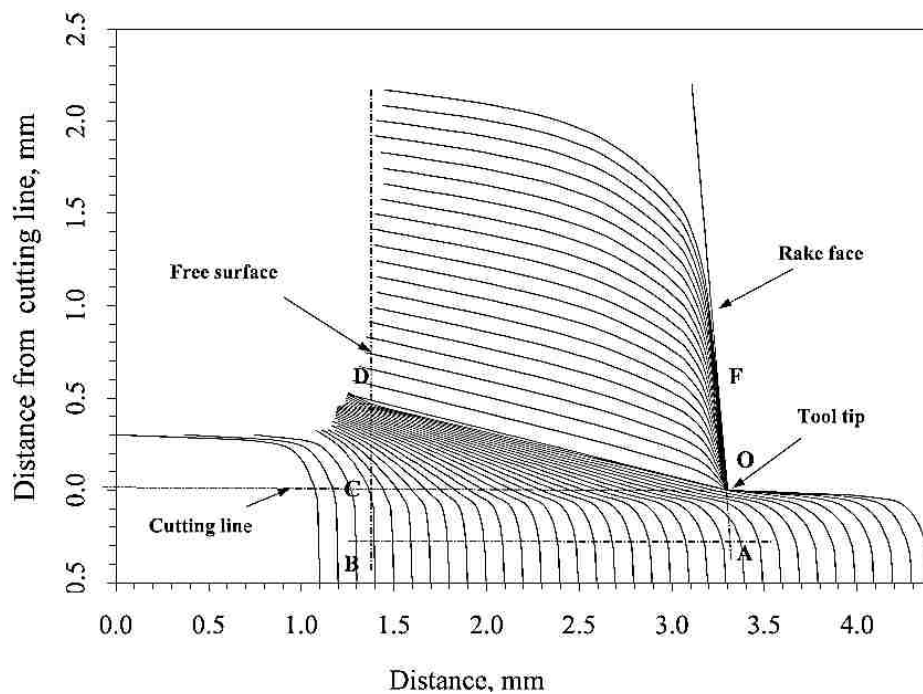


Figure 2.8: A computer generated image of the cross-section of the machined workpiece with the chip still attached. The image was obtained by determining the location of each point on the deformation lines and these were plotted to actual scale shown on the diagram [19]

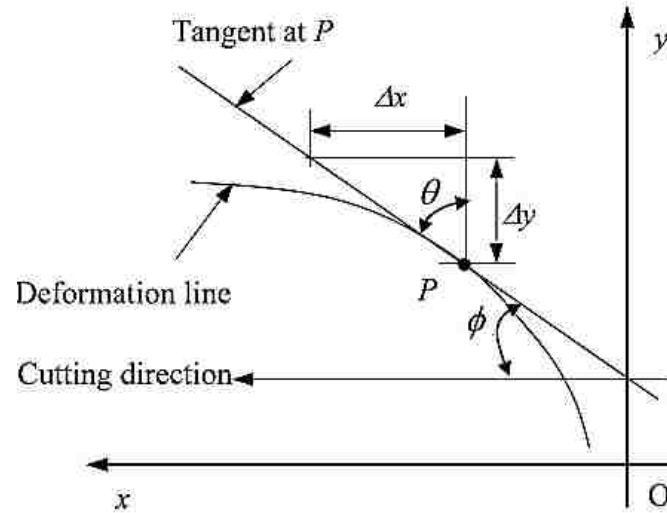


Figure 2.9: Schematic diagram showing the measurement of shear angles ' ϕ ' from the slopes of the deformation lines at an angle of ' θ ' [19]

2.1.6 Estimation of Shear Angle

Zhang and Alpas [19] used the extrusion lines of 6061 Al as a marker and from the change in orientation of these lines due to shearing, the shear angle was measured. A computer generated, accurate representation of the flow lines they presented is shown in Figure 2.9. The shear angle values were then computed from the slope of these lines (Figure 2.9) according to the following formula:

$$\phi = \tan^{-1} \left(\frac{\Delta y}{\Delta x} \right) \quad (2.5)$$

Elmadagli and Alpas [21] used the same procedure to measure the angle in cases involving orthogonally machined, commercially pure copper samples. However, instead of flow lines, they used the deformed grains as the marker and found that the shear angle varied from 9° to 21° from tool tip to chip root.

2.1.7 Estimation of Flow Stress

The microhardness of a material just ahead of the tool tip and below the machined surface vary from one point to another. Tabor [22] related the amount of deformation with the hardness, considering the fact that both these factors are related to elastic limit. The criteria for plastic flow in a solid body subjected to principal stresses σ_1 , σ_2 , and σ_3 is given by the von Mises relation [23]:

$$2\sigma_0^2 = (\sigma_1 - \sigma_2)^2 + (\sigma_2 - \sigma_3)^2 + (\sigma_3 - \sigma_1)^2 \quad (2.6)$$

where σ_0 is the yield stress in uniaxial tension.

The mean pressure σ_m can be defined as follows:

$$\sigma_m = \frac{\sigma_1 + \sigma_2 + \sigma_3}{3} \quad (2.7)$$

Based on assumptions made by Hill et al. [24], this equation can be solved. They concluded that plastic yielding would occur when the mean pressure, σ_m

$$\sigma_m = 3\sigma_0 \quad (2.8)$$

The assumptions made by Hill et al. [24] are (i) The deformed area is not too large compared with the size of the specimen, (ii) σ_m is independent of the applied load and size of the indentation, (iii) Frictionless compression is performed.

Marsh [25] proposed that the Vickers hardness of a material could be related to the corresponding flow stress, $\bar{\sigma}$ by the relation

$$\bar{\sigma} = \frac{H}{3} \quad (2.9)$$

This approximation is commonly used by researchers to predict the flow stress at different positions on work material subjected to cutting operations [20, 21].

2.1.8 Estimation of Flow Strain

Equivalent plastic strain is a function of plastic deformation and is given by the relation [23],

$$d\bar{\varepsilon} = \frac{\sqrt{2}}{3} [(d\varepsilon_1 - d\varepsilon_2)^2 + (d\varepsilon_2 - d\varepsilon_3)^2 + (d\varepsilon_3 - d\varepsilon_1)^2]^{\frac{1}{2}} \quad (2.10)$$

where $\varepsilon_1, \varepsilon_2, \varepsilon_3$ are the three principal strains.

The above equation can further be reduced as follows:

$$\bar{\varepsilon} = \left[\frac{2}{3} (\varepsilon_1^2 + \varepsilon_2^2 + \varepsilon_3^2) \right]^{\frac{1}{2}} \quad (2.11)$$

For a material that has been subject to sliding, the equivalent strain generated in the subsurface can be estimated by measuring the shear angle. The shear angle is measured from subsurface microstructural features like flow lines or grain boundaries which bend in the direction of sliding. The shear angle θ is equal to the angle between the tangent drawn to the deformed marker at a point of interest and its original orientation at the point (before deformation). The relation between equivalent plastic strain ε and shear angle θ is:

$$\bar{\varepsilon} = \frac{\sqrt{3}}{3} \tan \theta \quad (2.12)$$

Since the displacement of the feature, acting as a microstructural marker, is the result of shear deformation parallel to the surface, any contribution of compression or rotation of the features is ignored. This theory has been widely used for estimation of equivalent strain in wear experiments [19, 26] and has been confirmed by Zaat et al [27]. This method is

also useful for estimation of equivalent strain in other processes where substantial deformation occurs.

2.2 Titanium Alloys – An Overview

Titanium is a chemical element with symbol Ti and atomic number 22. It is a lustrous transition metal with a silver color, low density and high strength. It is highly resistant to corrosion in sea water and chlorine environment. The element occurs within a number of mineral deposits, principally rutile and ilmenite, which are widely distributed in the Earth's crust and lithosphere, and it is found in almost all living things, rocks, water bodies, and soils.

Titanium can be alloyed with iron, aluminum, vanadium, and molybdenum, among other elements, to produce strong, lightweight alloys for aerospace (jet engines, missiles, and spacecraft), military, industrial process (chemicals and petro-chemicals, desalination plants, automotive, medical prostheses, orthopedic and dental implants, and other applications.

2.2.1 Crystal Structure

Pure titanium exhibits an allotropic phase transformation at approximately 995 °C (Figure 2.10 (a)), changing from a body-centered cubic crystal structure (β phase) at higher temperatures to a hexagonal close-packed crystal structure (α phase) at lower temperatures. The exact transformation temperature is strongly influenced by interstitial and substitutional elements and therefore depends on the purity of the metal. The hexagonal unit cell of the α phase is shown in Figure 2.10 (b) indicating also the room temperature values of the lattice parameters a (0.295 nm) and c (0.468 nm). The resulting c/a ratio for

pure α titanium is 1.587, smaller than the ideal ratio of 1.633 for the hexagonal close-packed crystal structure. The unit cell of the body centered cubic (bcc) β phase is illustrated in Figure 2.10 indicating also one variant of the six most densely packed $\{110\}$ lattice planes and the lattice parameter value of pure β titanium at 995 °C ($a = 0.332$ nm). The close-packed directions are the four $\langle 111 \rangle$ directions.

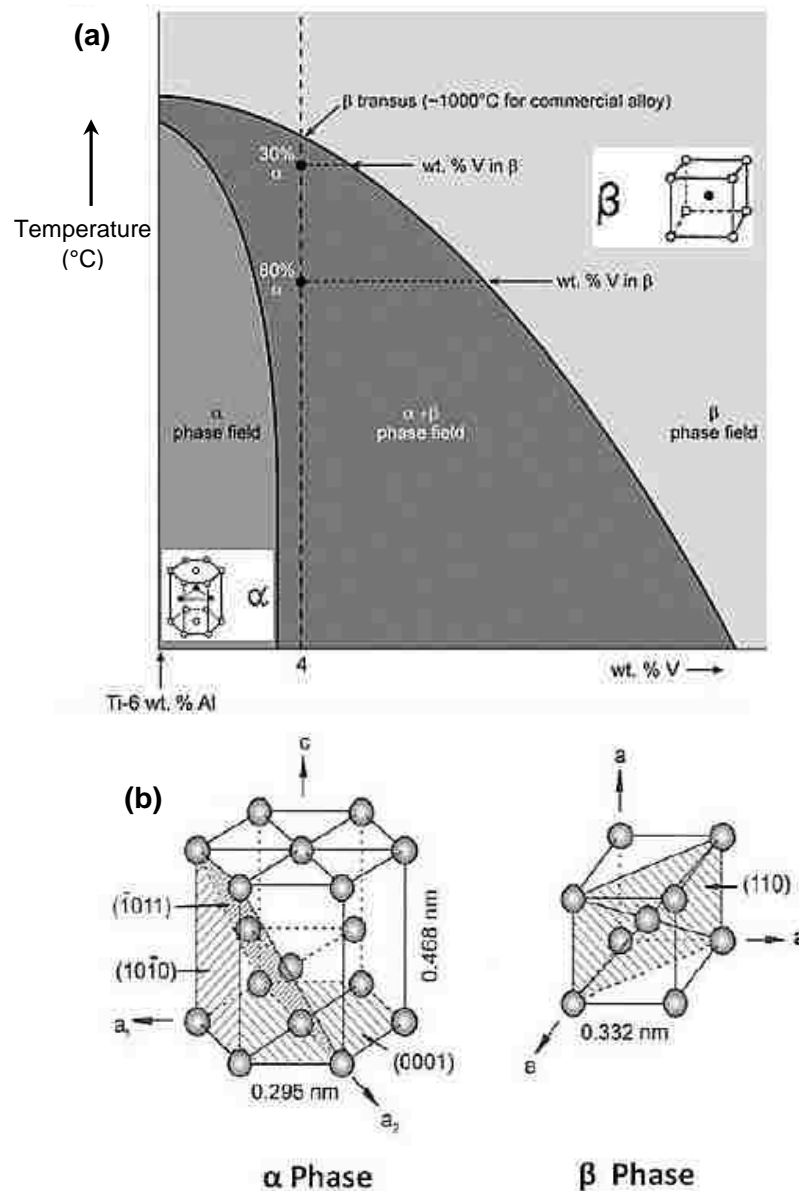


Figure 2.10: (a) Phase diagram of Ti-6Al-4V showing the different types of titanium alloys based on the alloying composition, (b) Unit cell of hexagonal close packed structure and body centered cubic structure of the α and β phase in a Ti-6Al-4V alloy [28]

2.3 Introduction to Ti-6Al-4V

Ti-6Al-4V or Ti64, is the most commonly used titanium alloy and is designated as a Grade 5 alloy. It has a chemical composition of 6% aluminum, 4% vanadium, 0.25% (maximum) iron, 0.2% (maximum) oxygen, and the remainder titanium [1]. It is stronger than commercially pure titanium while having the same stiffness and thermal properties (excluding thermal conductivity, which is about 60% lower in Grade 5 Ti than in CP Ti) [28]. Among its many advantages, it is heat treatable and has an excellent combination of strength, corrosion resistance and weldability.

This alpha-beta alloy is the workhorse alloy of the titanium industry. It is fully heat treatable in section sizes up to 15mm and is used up to approximately 400°C (750°F). Since it is the most commonly used alloy – over 70% of all alloy grades melted are a sub-grade of Ti-6Al-4V, its uses span many aerospace airframe and engine component uses and also major non-aerospace applications in the marine, offshore and power generation industries in particular. Generally, Ti-6Al-4V is used in applications up to 400°C. It has a density of roughly 4420 kg/m³, Young's modulus of 115 GPa, and tensile strength of 1000 MPa [28]. By comparison, annealed type 316 stainless steel has a density of 8000 kg/m³, modulus of 193 GPa, and tensile strength of only 570 MPa [28] and tempered 6061 aluminum alloy has 2700 kg/m³, 69 GPa, and 310 MPa, respectively.

2.3.1 Mechanical Properties of Ti-6Al-4V

Both the α and β phases deform [29, 30] in the Ti-6Al-4V alloy although the amount of deformation is different for both the phases. The deformation of the phases in Ti-6Al-4V alloy is dependent on the size of the grains. The deformation of fine grains in the Ti-6Al-4V alloy is of the iso-stress type because most of the dislocations are found in the β

phase (Figure 2.11), which means the amount of deformation in the α and β phases are not same. For the same alloy with a higher grain size, the system is a mixture of the iso-stress and iso-strain types because both phases experience strain. Because of the larger size of the β phase, a higher amount of stress is concentrated due to the larger slip distance that also deforms the adjacent α grain [30].

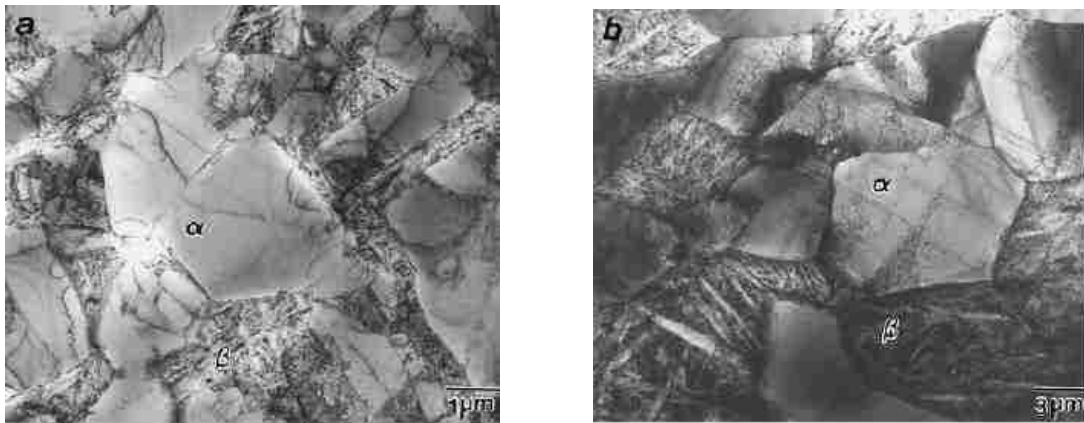


Figure 2.11: TEM bright-field images of: (a) fine ($3 \mu\text{m}$); and (b) coarse ($11 \mu\text{m}$) grained Ti-6Al-4V deformed at 600°C with a strain rate of 10^{-3}s^{-1} ($\epsilon=0.3$) [30]

The mechanical characteristics found in Ti-6Al-4V are sensitive to processing parameters such as strain rate and temperature. It is vital to understand their relationship to study its deformation modes as well as to properly interpret the relationship between its microstructure and processing variables along with its properties under different loading conditions. The typical true stress-strain curves of Ti-6Al-4V alloys deformed at different strain rates and temperatures are shown in Figure 2.12. It can be seen that true stress increases with true strain and reaches a maximum value before fracture. This depicts that plastic deformation of Ti-6Al-4V alloy is greatly dependent on strain rate and temperature, though the effect of the latter is more predominant [31]. The variation in yield strength and ultimate tensile strength with temperature seen in Figure 2.13. It is observed that the variation of yield strength and ultimate tensile strength decreases monotonously with

increase in temperature. At higher temperatures ($> 300\text{ }^{\circ}\text{C}$), the effect of thermal softening resulted in decrease in strength of Ti-6Al-4V.

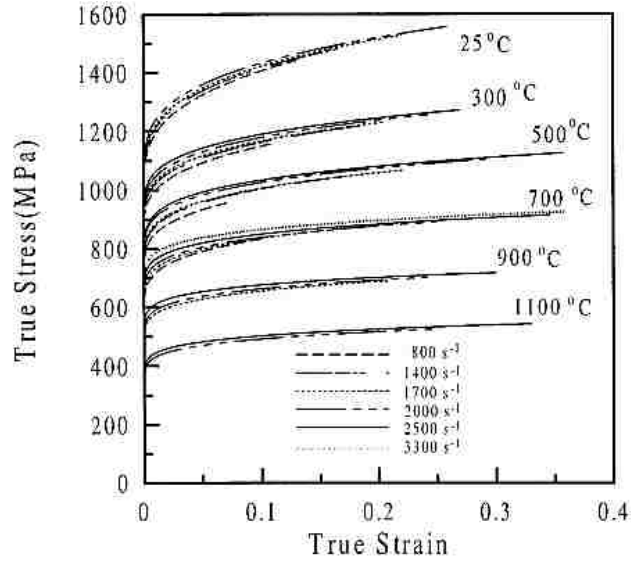


Figure 2.12: True stress-strain curves for Ti-6Al-4V at various temperatures and strain rates [31]

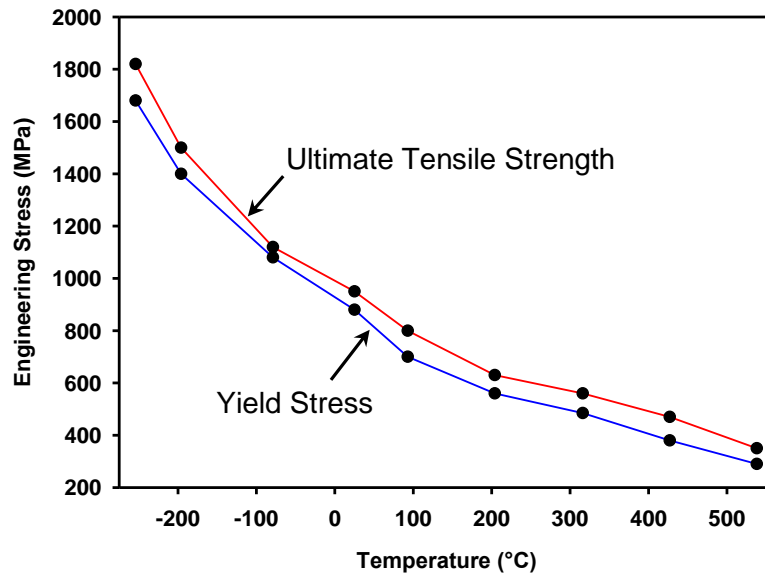


Figure 2.13: Variation of ultimate tensile strength and yield stress of Ti-6Al-4V with temperature [32, 33, 34]

Figure 2.14 shows the effect of temperature on strain rate sensitivity. Strain rate sensitivity (m) is calculated using the following equation for constant temperature and strain [23]:

$$m = \left(\frac{\partial \ln \sigma}{\partial \ln \dot{\epsilon}} \right) \Big|_{\epsilon, T} \quad (2.13)$$

where m is the strain rate sensitivity, σ is the flow stress, $\dot{\epsilon}$ is the strain rate, ϵ is the strain and T is the temperature.

For all four strain rate conditions, the sensitivity increases. Figure 2.12 and Figure 2.14 show that when the strain rate is higher, the strain hardening decreases at a critical temperature. However, in cases with low temperatures, the effect of strain rate is not as significant. The sensitivity increases at a very high rate when the temperature is sufficiently high (e.g. above 500°C) when deforming at a constant strain rate.

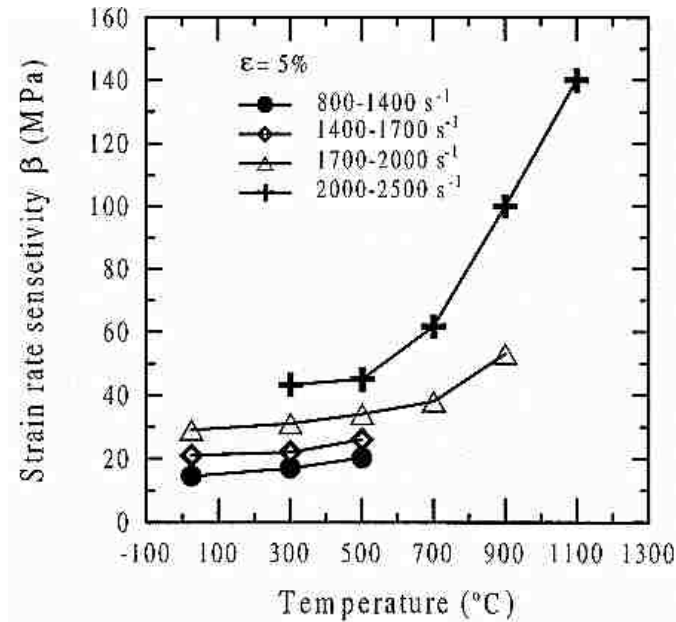


Figure 2.14: Variations of strain rate sensitivity as a function of temperature for deformation at a true strain of 0.05 under different strain rate ranges [31]

The hardness of the annealed Ti-6Al-4V alloy increases from 33.5 HRC at room temperature to about 42 HRC at low temperatures, as shown in Figure 2.15 [35]. Titanium alloys experience an increase in strength at low temperatures [36]. Compared to α -Ti, Ti-6Al-4V shows a sharp rise in flow stress below room temperature. At around 0 K, the flow stress of Ti-6Al-4V is 1600MPa, whereas for α -Ti, it is around 750MPa [36]. In the low-strain-rate deformation process, the flow stress of Ti-6Al-4V reaches a plateau at around 600K, and there is a well-defined discontinuity at temperatures between 400K and 800K. Within this temperature range, the flow stresses of α -Ti and Ti-6Al-4V are very close. This feature is not found in the high-strain-rate deformation process. Above this temperature range, strain hardening decreases drastically due to the dynamic recovery that results in a decrease in flow stress [36]. These characteristics are shown in Figure 2.16.

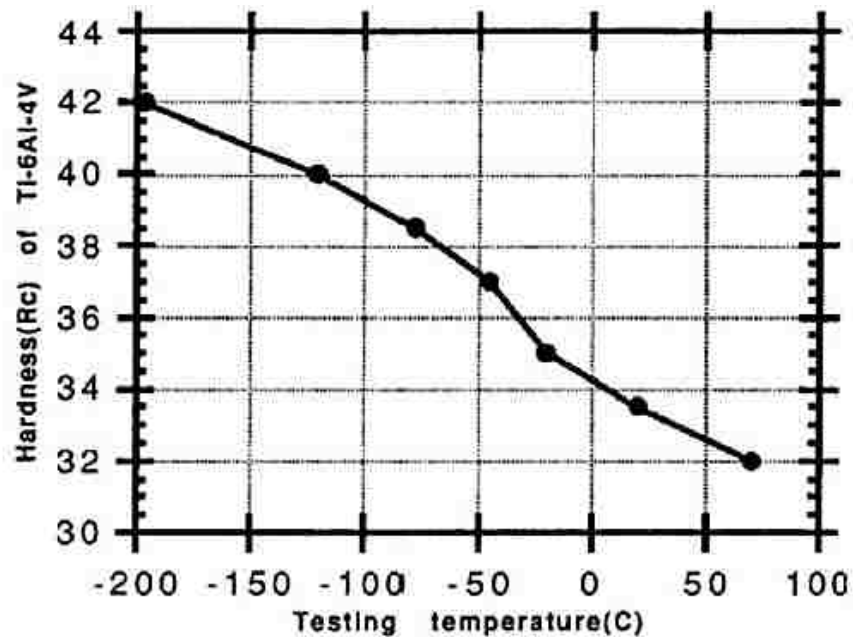


Figure 2.15: Variation of hardness of Ti-6Al-4V with temperature measured on a Rockwell C-scale [35]

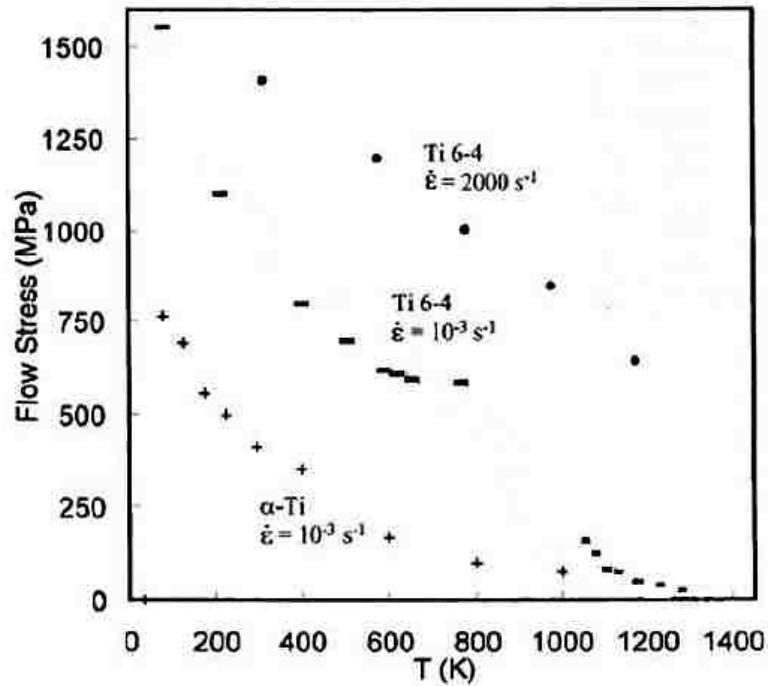


Figure 2.16: Temperature dependence of yield stress of Ti-6Al-4V at low and high strain rates compared to α -Ti [36]

2.4 Machining of Ti-6Al-4V

Titanium alloys are known as difficult-to-machine materials. There are a myriad of problems in machining titanium which depend on the type of alloy being machined. Based on the available literature, some basic challenges include variation of chip thickness, high thermal stress, high pressure loads, springback, and residual stress.

To address these problems, latest techniques such as application of high pressure coolant, cryogenic cooling, tap testing, thermally enhanced machining, hybrid machining, and use of high conductive cutting tool and tool holder have also been discussed and correlated.

Machinability is judged in terms of four different criteria: (i) chip formation, (ii) cutting force or power requirement, (iii) tool life, and (iv) surface condition of the finished

product [7]. Research in this field started in the early 1950s and has continued in order to optimize the machining operations.

2.4.1 Machinability of Ti-6Al-4V

Properties such as high strength-to-weight ratio, strength at high temperature, ductility and fracture resistance make Ti-6Al-4V a suitable option for various industrial applications, although these properties make it difficult to machine. Many researchers have noted different problems that arise during Ti-6Al-4V machining and their relation to material properties. [1 – 8]

1. Generation of high localized cutting zone temperatures at the tool-workpiece interface during machining of Ti-6Al-4V. Machining operation accumulates high amount of deformation within the material, and a large portion of this deformation converts into heat. The heat becomes localized which causes high temperature generation within a narrow zone leading to further deformation occurring in that particular region. This localization (or heterogeneous deformation) results in cyclic chip formation as discussed in Section 2.1.3. [1 – 5]
2. Formation of cyclic chip segments as mentioned above causes oscillations in cutting and thrust components of forces that eventually result in chatter. [6]
3. Approximately 80% of the generated heat is conducted into the tool during machining Ti-6Al-4V (due to low thermal conductivity), whereas in cases using steel, the absorbed heat is approximately 50%. This high amount of heat, along with the oscillation produced during machining titanium alloys, is thought to be the reason for wear on flank faces. [7]

4. Chips come into contact with the tool as they form and slide on the rake face of the tool during machining. When two different materials slide against each other, a solid solution may form. Wear on the dissolving material occurs from solution wear, diffusion wear or delamination wear. All these wear processes are related to the chemical stability of the materials [8]. Titanium alloys show high chemical reactivity with tool materials such as uncoated carbide and poly-crystalline diamond tools.

In summary, material properties are the primary reasons for difficulties in machining titanium alloys. Thus studying the characteristics of the chips is necessary to solve or minimize problems since they help to understand the material behaviour. This study would be useful in overcoming the problems in machining Ti alloys.

2.5 Chip Formation Mechanisms

The Ti-6Al-4V alloy produces serrated chips not only under conventional, high-speed machining but also at low cutting speeds [36]. Two mechanisms for serrated chip formation were proposed initially by researchers. These were the adiabatic shear mechanism and periodic crack development mechanism. However, the research work conducted later tends to support the adiabatic shear mechanism.

2.5.1 Adiabatic Shear Mechanism

Metallic materials strain harden when plastically deformed. Further deformation requires the application of extra amounts of stress. Due to heat entrapment in titanium alloys, two opposing effects, strain hardening and thermal softening, occur simultaneously to create an unstable condition. Researchers [2, 3, 4, 13] have proposed that thermoplastic

shear instability is the root cause of serrated or catastrophic shear chip formation in titanium alloys.

Based on high-speed imaging, a mechanism for serrated chip formation in the Ti-6Al-4V alloy was proposed [2] and described with the help of a schematic, which is shown in Figure 2.17. According to Komanduri [2], serrated chip formation is a two-stage procedure. In the first stage, thermal softening and strain hardening results in instability, which leads to strain localization along a shear surface (band). This shear surface originates from the tool tip and gradually curves upwards until it meets the free surface. Therefore, a concave surface is formed. In the second stage, the tool's gradual advancement applies an increased amount of force, at which point a crack initiates at the tool tip and gradual flattening increases the contact between the tool and the material ahead. Until this stage, there is almost no relative velocity between the bottom surface of the chip segment being formed and the tool. The chip being formed pushes the previously formed chip by bulging and gradually flattening, thus shifting its contact towards the tool face. As the upsetting progresses, more and more stress is generated, which causes intense shear between the segment being formed and the one before it. This leads to the formation of shear bands, which occurs at all cutting speeds. The intense shear at higher cutting speeds separates the individual segments due to the gradual decrease in contact between any two segments.

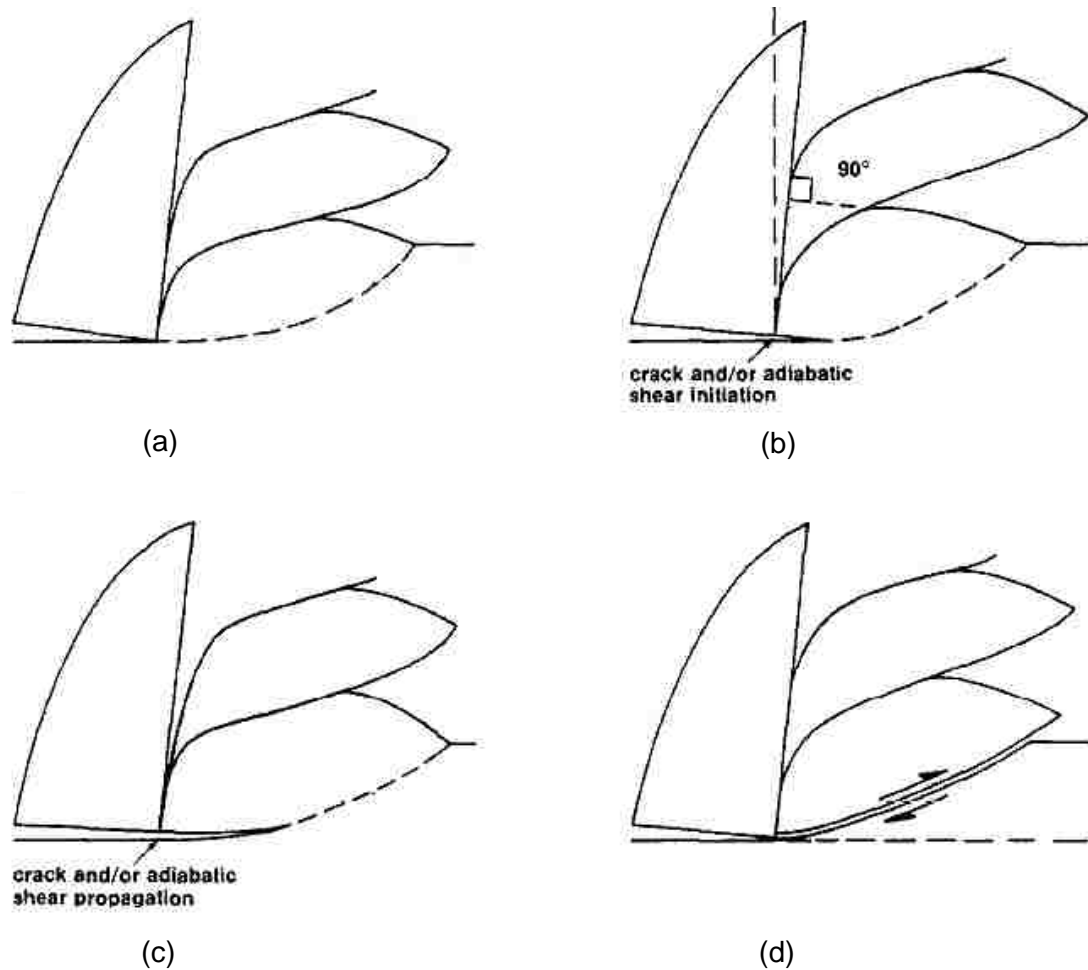


Figure 2.17: Sequential steps leading to serrated chip formation in Ti-6Al-4V. (a) Thermal softening and strain hardening results in instability, which leads to strain localization along a shear surface (band). This shear surface originates from the tool tip and gradually curves upwards until it meets the free surface, (b) Tool's gradual advancement applies an increased amount of force, at which point a crack initiates at the tool tip and gradual flattening increases the contact between the tool and the material ahead, (c) Propagation of the crack along the path of strain localization, (d) The chip being formed pushes the previously formed chip by bulging and gradually flattening, thus shifting its contact towards the tool face. As the upsetting progresses, more and more stress is generated, which causes intense shear between the segment being formed and the one before it. [2]

2.5.2 Periodic Crack Development Mechanism

In Ti-6Al-4V, serrated chips are found even at very low cutting speeds. At low cutting speeds, the generated heat will also be low. Thus it was proposed that the adiabatic shear theory of serrated chip formation may not prevail because the basis of this theory is of thermal origin. Nakayama et al. [37] developed a different theory for serrated chip

formation. They ran tests on extremely cold-worked (brittle) brass and suggested that periodic crack development is the basis of chip serration rather than adiabatic shear. They explained their theory with the help of a schematic, which is shown in Figure 2.18.

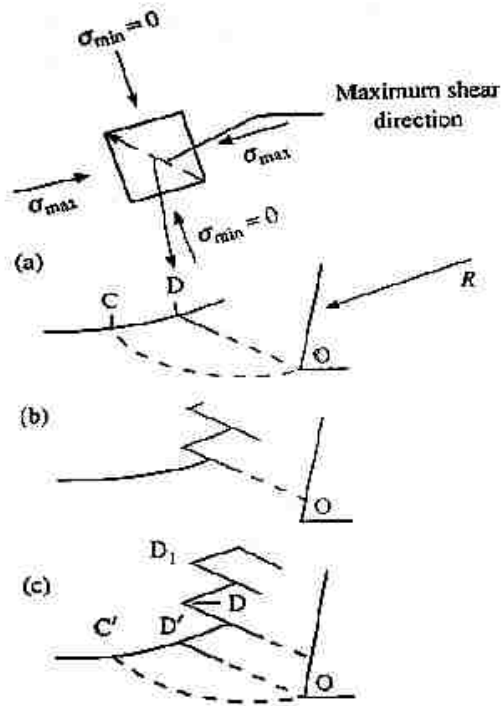


Figure 2.18: Formation of a serrated chip through periodic crack development process. (a) Material at point C moves upward along CD, which has the same applied load direction. (b) A shear crack initiates at point D, which runs from the surface in a downward direction toward the tool tip along the path DO, (c) As the tool advances, the chip glides outward along the cracked surface until the next crack forms at D' [37]

The figure shows that the material at point C moves upward along CD, which has the same applied load direction. A shear crack initiates at point D, which runs from the surface in a downward direction toward the tool tip along the path DO. As the tool advances, the chip glides outward along the cracked surface until the next crack forms at D'. The reason for the crack formation at point D is shown in the Figure 2.18 (a). As the tool advances, it provides compressive stress. Because D is on the surface, the compressive force along the σ_{min} direction is zero. For being the crack arresting force zero, the shear force at D is the

maximum that leads to crack initiation. As the crack propagates into the material, the value of the crack arresting force gradually rises. The crack is initially continuous, which is called gross crack, but it becomes discontinuous because of the arresting force, which creates micro cracks.

2.6 Cryogenic Machining

Cryogenic machining refers to machining of any material at very low temperatures, below $-150\text{ }^{\circ}\text{C}$. Normal boiling points of permanent gases such as helium, hydrogen, neon, nitrogen, oxygen, normal air as cryogenics lie below $-180\text{ }^{\circ}\text{C}$. Cryogenic gases have a wide variety of applications in industry such as health, electronics, manufacturing, automotive and aerospace industry particularly for cooling purposes. Liquid nitrogen is the most commonly used element in cryogenics. It is produced industrially by fractional distillation of liquid air and is often referred to by the abbreviation, LN_2 . LN_2 melts at $-210\text{ }^{\circ}\text{C}$ and boils at $-198.79\text{ }^{\circ}\text{C}$. Nitrogen is the most abundant gas, composes about four-fifths (78.03%) by volume of the atmosphere. It is a colorless, odorless, tasteless and non-toxic gas. These characteristics of LN_2 have made it a preferred coolant in machining processes. The main functions of cryogenic cooling in metal cutting were defined by Hong and Zhao [31] as removing heat effectively from the cutting zone, hence lowering cutting temperatures, modifying the frictional characteristics at the tool/chip interfaces, changing the properties of the work piece and the tool material. So, it will be useful to study the heat generation and temperature distribution in a machining process for better evaluation of the subject.

2.6.1 Heat Generation during Machining

In any machining process, heat is generated as a result of the plastic deformation of the layer being cut and overcoming friction on the tool–chip and tool–work interfaces. This heat is dissipated by the four systems in processing the material such as the cutting tool, the work piece, the chip formed and the cutting fluid. The greater part of the heat passes into the chip, while a proportion is conducted into the work material. This proportion may be higher for low rates of metal removal and small shear zone angles, but the proportion is small for high rates of metal removal [38]. O’Sullivan and Cotterell [39] measured machined surface temperature using thermocouples in turning of aluminum alloy 6082-T6 with carbide inserts and their test results indicated that an increase in cutting speed resulted in a decrease in machined surface temperatures. This reduction was attributed to the higher metal removal rate which resulted in more heat being carried away by the chip and thus less heat being conducted into the work piece [38]. The main regions where heat is generated during the orthogonal cutting process are shown in Figure 2.1 [1]. Majumdar et al. [40] developed a finite element-based computational model to determine the temperature distribution in a metal cutting process. They indicated the maximum temperature generation occurred at the primary deformation zone of the tool – chip interface. Aspinwall et al. [41] employed infrared pyrometer and FE model as direct and indirect techniques to measure cutting temperatures in turning of hardened hot work die steel and AISI H13 with PCBN (polycrystalline cubic boron nitride) tool. They obtained good correlation between two techniques and their model also predicted the highest temperatures at the tool-chip interface.

Heat generation and temperatures in the primary and secondary zones are dependent on a combination of the physical and chemical properties of the work piece material and cutting tool material, cutting conditions such as the cutting speed, the feed rate, the depth of cut, the cutting tool geometry, and the cutting fluid [42]. When low alloy engineering steel was machined with cemented carbide tool, it was seen that cutting temperature increased with increasing cutting speed and feed rate. In addition, the effect of air and water as a coolant decreased while the cutting speed increased [43]. The other factor affecting the cutting tool temperature is the contact length between the chip and the tool, and it was determined that the temperature was increased with the contact length for orthogonal cutting of aluminum [38].

2.7 Effects of Cryogenic Cooling in Machining Processes

2.7.1 Effect on Material Properties

The mechanical properties of several grades of carbide – cobalt alloys (K3109, K313, K420, K68 and SP274) at cryogenic temperatures were investigated and their indentation tests indicated an increase in the hardness of all the tested materials compared to the material's hardness at room temperature [44, 45]. These carbide grades generally retained their toughness, high transverse rupture and impact strength as the temperature decreased toward liquid nitrogen temperature. So, it was determined that these carbide tool materials were suitable for cryogenic cooling strategies. The effects of cryogenic temperature on some work piece materials such as AISI 304 stainless steel [46], AISI 1008 [46, 48] and 1010 low carbon steels, AISI 1070 high carbon steel, AISI E52100 bearing steel, Ti–6Al–4V titanium alloy [35] and A390 cast aluminum alloy were also investigated.

Authors [44, 47, 48, 49] observed the influence of cryogenic temperature on chip formation. For example, the embrittlement temperature of low carbon steels was determined to be between $-50\text{ }^{\circ}\text{C}$ and $-120\text{ }^{\circ}\text{C}$ from standard material tensile and impact tests. Thus, pre-cooling the work piece or chip cooling method was recommended for AISI 1008 and 1010 low carbon steels due to favorable chip breakability in cryogenic machining. AISI 1070 and E52100 have high strength levels even at room temperature. Their rapid increase in strength with decreasing temperatures lead to higher cutting forces. Thus an effective cryogenic approach involves applying the cryogenic coolant to the cutting zone adjacent to the chip/tool interface. Hong and Broomer [46] also recommended this approach for machining AISI 304 stainless steel. For cast aluminum alloy A390, the authors recommended cooling the cutting tool instead of the work piece. Since, keeping the cutting tool cool may decrease the tool's tendencies to adhere to the soft aluminum matrix phase and in turn reduce build-up edge formation. Cooling the cutting tool may also enhance its hardness and resistance to the abrasive wear of the Si phase in A390. Ti-6Al-4V alloys showed rapid increase in their strength and hardness as the temperature decreases. Therefore, simultaneously cooling the work piece to enhance the chemical stability of the work piece, and cooling the cutting tool to enhance the hardness and chemical stability of the tool were recommended as an effective cryogenic strategy for titanium alloy. [44]

2.7.2 Effect on Cutting Temperature

In all cryogenic cooling studies, cutting temperatures were experimentally measured using thermocouples and sometimes cutting temperatures were estimated theoretically with finite element analysis (FEA). For instance, the maximum cutting zone temperature under

dry cutting of AISI 1008 at a cutting speed of 4 m/s and a feed of 0.255 mm was predicted to be 460 °C. For the same cutting conditions, under cryogenic machining conditions, the cutting zone temperature was predicted to be 255 °C. Thus a 44% decrease in cutting zone temperature was achieved during cryogenic cutting when compared with dry cutting conditions [48]. In machining different kind of steels [50, 51, 52, 53], LN₂ jet application reduced average cutting temperature by about 10 – 35% depending on the work materials, tool geometry and cutting parameters. For instance, while machining C-40 steel at a cutting speed of 144 m/min and a feed rate of 0.24 mm/rev, the maximum cutting zone temperature was measured to be 680 °C. For the same conditions the cutting zone temperature was measured to be 575 °C under cryogenic conditions. These measured chip – tool interface temperatures were also predicted by a FE model. The authors achieved comparable temperature data with an average deviation of 5.4%. The predicted temperatures were 710 °C and 600 °C under dry and cryogenic cutting conditions, respectively. But it was seen that cryogenic cooling effect slightly decreased with the increase in cutting speed and feed rate due to difficulty in penetrating the cryogenic coolant at the tool – chip interface. Hong and Ding [54] compared various cryogenic cooling strategies in machining of Ti–6Al–4V as shown in Figure 2.19.

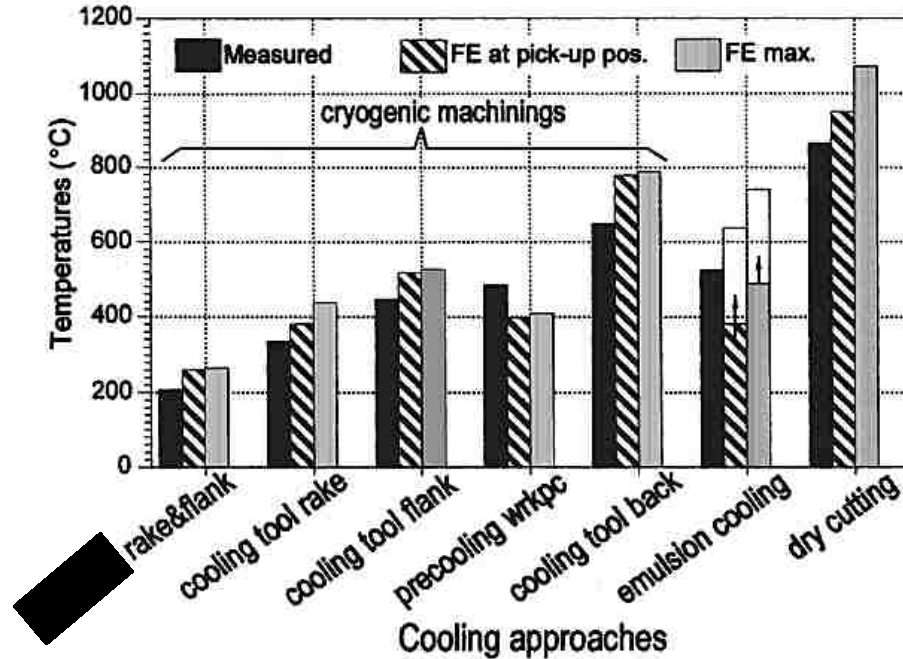


Figure 2.19: Measured and predicted cutting tool temperatures under different machining environments [54]

They found that simultaneous cryogenic rake and flank jet cooling of the tool were four times better than the dry cutting in that the cutting zone temperature was predicted to decrease from 1050 °C to 210 °C. They also made a sample alignment worst to best as regarding controlling of cutting temperature: dry cutting, cryogenic tool back cooling (conductive remote cooling), emulsion cooling, pre-cooling the work piece, cryogenic flank cooling, cryogenic rake cooling, and simultaneous rake and flank cooling. With the exception of tool back cooling, all tested cryogenic cooling approaches significantly reduced the tool – chip interface temperature. Tool back cooling may be an ineffective approach because the distance of the frozen area (i.e. the tool back face) from the cutting edge is considerably larger, compared to other cryogenic cooling approaches.

2.7.3 Effect on Tool Wear and Tool Life

Most of the studies examined the flank wear formation since in practice the amount of flank wear is used more frequently in determining the tool life [55]. In all the studies, the flank wear was estimated as per ISO 3685:1993 standard [56]. In machining of some materials reductions in tool flank wear was up to five folds as seen in Table 2.1 with cryogenic indirect cooling [57, 58]. Wang et al. [58] machined a stainless steel ceramic (RBSN – Reaction bonded silicon nitride) with cubic boron nitride diamond tool under dry and cryogenic conditions. The length of cut before which tool failure initiated (average flank wear < 200 μm) was found to be 10 mm under dry conditions and this increased to 55 mm under cryogenic conditions. Similarly, in machining of AISI 304 stainless steel by indirect cryogenic cooling, tool life was increased more than four times [59]. Wang et al. [60] distinctly employed a hybrid machining method in their indirect cryogenic system with plasma heating enhanced machining of Inconel 718 and their results indicated an improvement of 156% in tool life when compared with conventional machining.

Table 2.1: Tool wear under different machining conditions [58], [60]

Material	Cutting tool	Cutting condition	Cutting length (mm)	Tool wear, V_B (mm)
RBSN	CBN50	Dry	30	2
		Cryogenic	80	0.88
Ti-6Al-4V	H13A cemented carbide	Oil cooling	46	1.1
		Cryogenic	46	0.22
Inconel 718	WG-300	Dry	62	0.85
		Cryogenic	110	0.6
Tantalum	H13A cemented carbide	Dry	52	0.45
		Cryogenic	158	0.28

Dhananchezian et al. [61] reported a reduction in flank wear due to cryogenic machining by 31% over wet machining while turning Ti-6Al-4V. At a cutting velocity of 63 m/min and feed rate of 0.159 mm/rev, the flank wear was 536 μm and 370 μm for wet and cryogenic machining, respectively (Figure 2.20 (a)). It was mentioned that the reduction in cutting zone temperature was responsible for low tool wear rates. At the same

cutting conditions mentioned above, the temperature at the tool – workpiece interface was measured to be 400 °C under wet machining while the temperature was 150 °C under cryogenic machining conditions as measured using a non-contact, infrared thermometer (Figure 2.20 (b)).

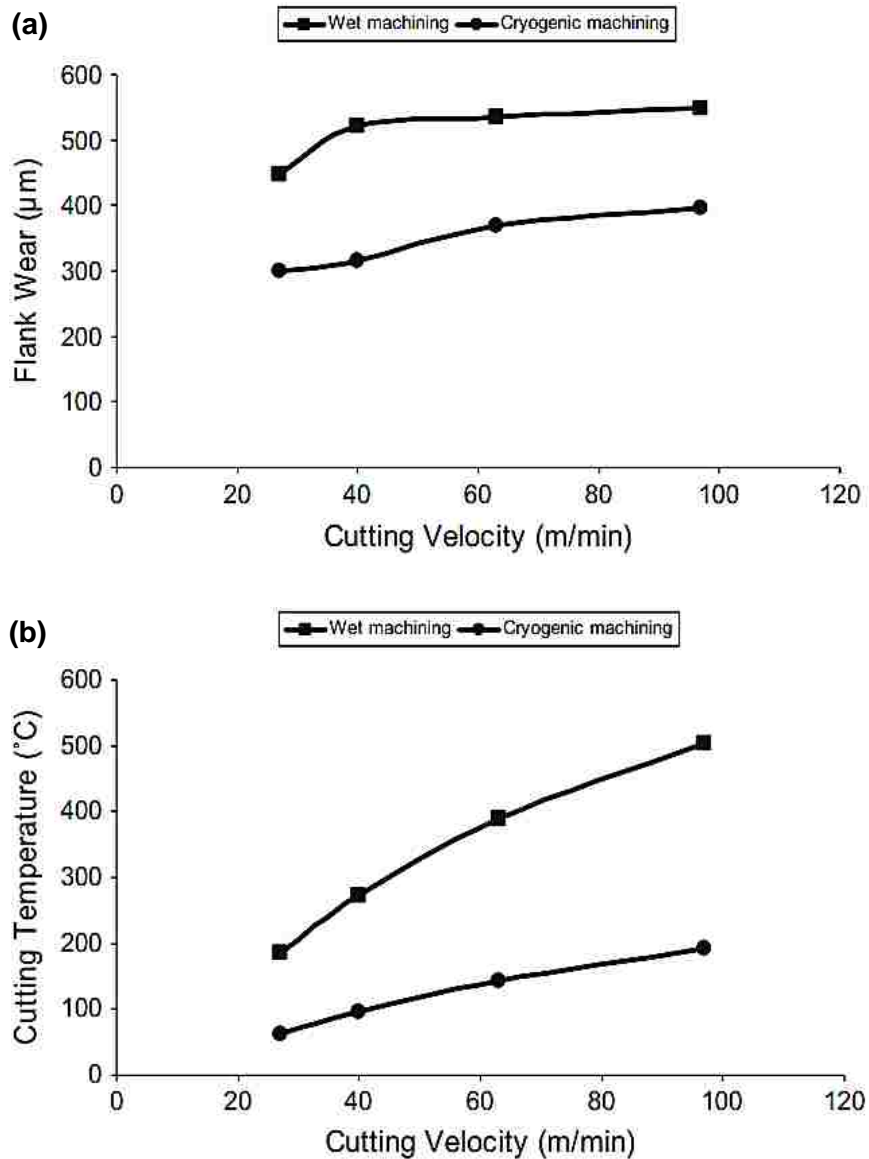
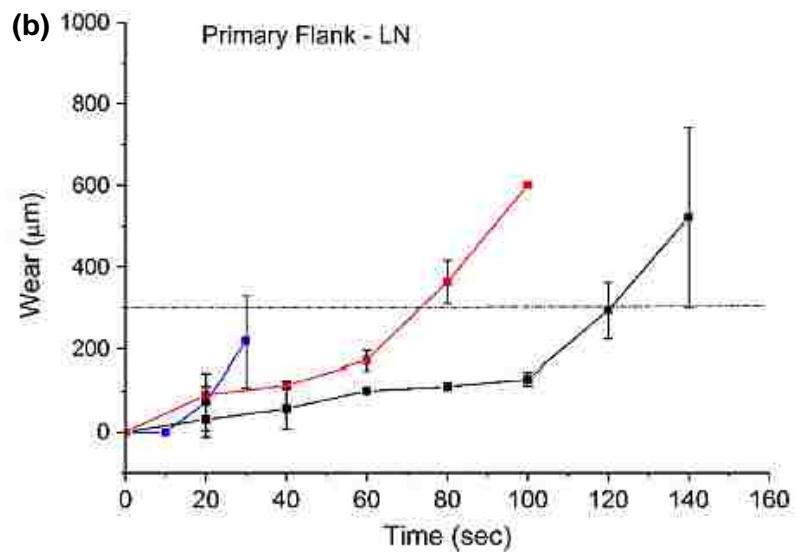
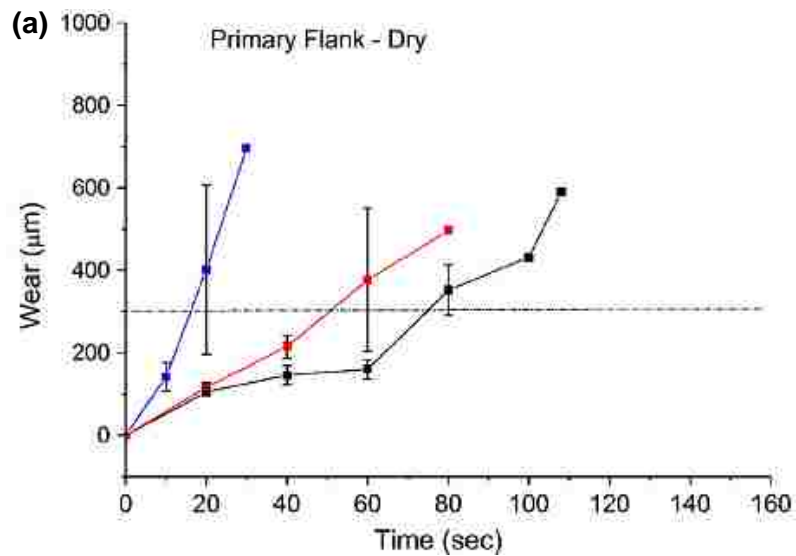


Figure 2.20: Comparison of (a) flank wear, (b) cutting zone temperature under wet and cryogenic machining of Ti-6Al-4V with increasing cutting velocity [61]

Tool life can be expressed in terms of time or volume of material removal before cutting tools wear out or fracture. The end of a tool's life occurs when the average flank wear exceeds 300 μm or the maximum flank wear reaches 600 μm , whichever occurs earlier [56]. Bermingham et al. [62] studied the flank wear in dry and cryogenic conditions by dividing the flank face into two different portions, primary flank and nose, at different feed rates. They found that with increased feed rates, the tool life decreased. But in all feed rates, the tool life at cryogenic conditions was higher (Figure 2.21).



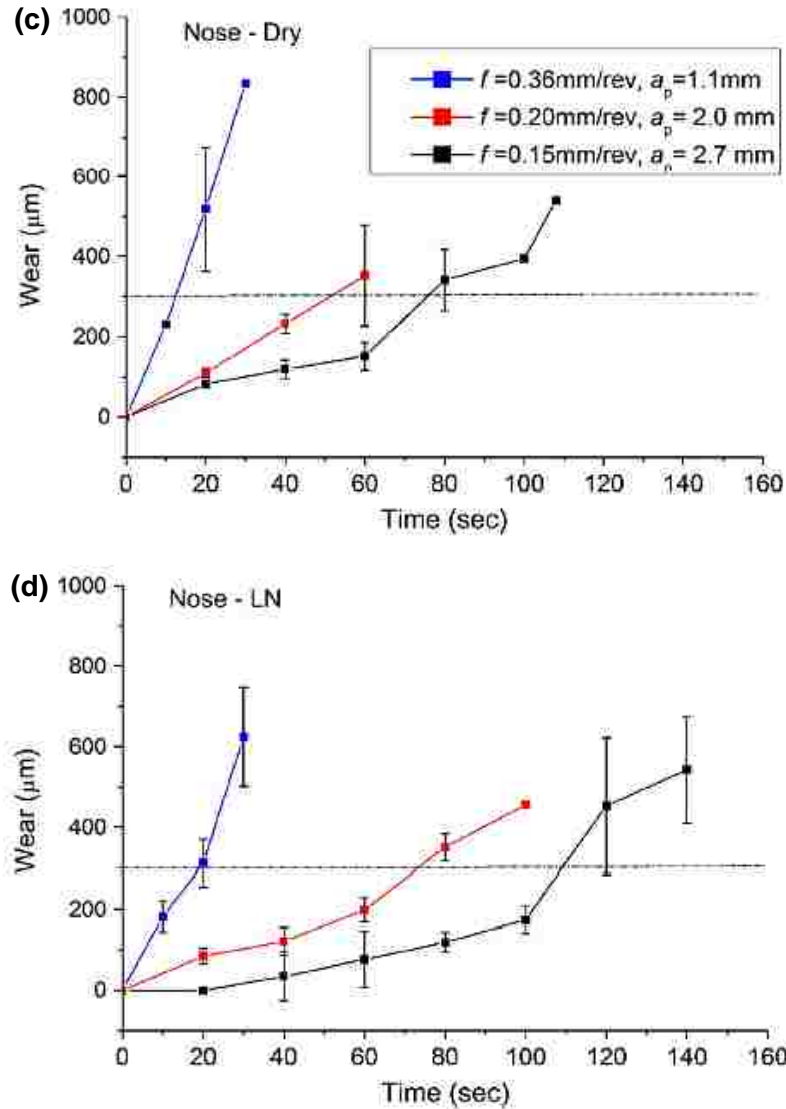


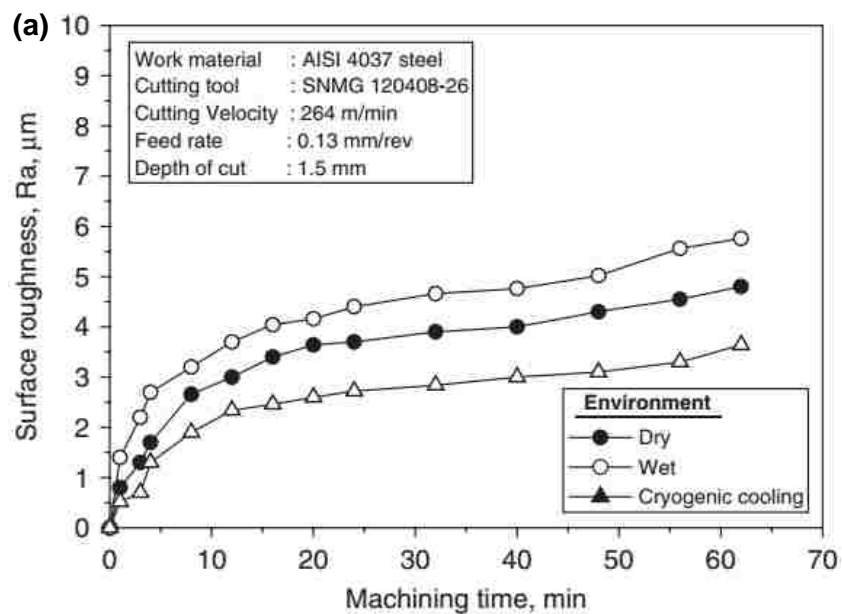
Figure 2.21: (a, b) Average wear of the primary flank during dry cutting and using cryogenic coolant, (c, d) Average wear of the nose during dry cutting and using cryogenic coolant [62]

2.7.4 Effect on Surface Roughness and Dimensional Deviation

Surface roughness is generated from two components, the ideal or geometric finish and natural finish. While the ideal or geometric finish results from the geometry and kinematic motions of the tool, the natural finish can result from vibrations, tool wear or built-up edge formation, etc. The dimensional deviation or inaccuracy is determined as the difference between applied depth of cut and obtained depth of cut [63], and whether the

dimensions of the final workpiece deviates from its desired value. Accuracy is highly affected by the cutting forces and the stiffness of the cutting tool, the tool holder and part fixtures [64]. Surface finish and dimensional deviation could be also affected even with very stiff and accurate machine tools. In such a condition, negativity was correlated with high cutting temperature and insufficient cooling [65].

One example of cryogenic jet cooling on dimensional deviation and surface roughness was shown in Figure 2.22. Values of dimensional deviation and surface roughness obtained under cryogenic cooling were less than dry and wet machining.



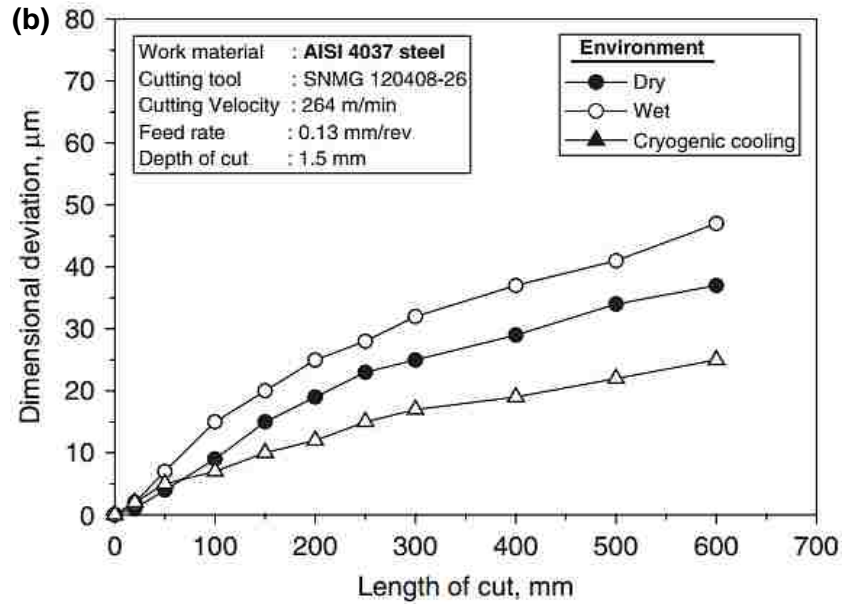


Figure 2.22: Variation of (a) surface roughness, and (b) dimensional accuracy with machining time under different cutting environments [52]

Dhananchezian et al. [61] measured the surface roughness in wet (emulsion of cutting fluid) and cryogenic machining of Ti-6Al-4V at different cutting speed using TiAlN coated tungsten carbide tool insert. The value of the surface roughness at a cutting speed of 97 m/min and a feed rate of 0.16 mm/rev was 3.4 μm and 2.2 μm for wet machining and cryogenic cooling respectively. They found that the cryogenic condition reduced surface roughness to a maximum of 35% over wet machining (Figure 2.23) due to the low tool wear rate (Figure 2.20 (a)).

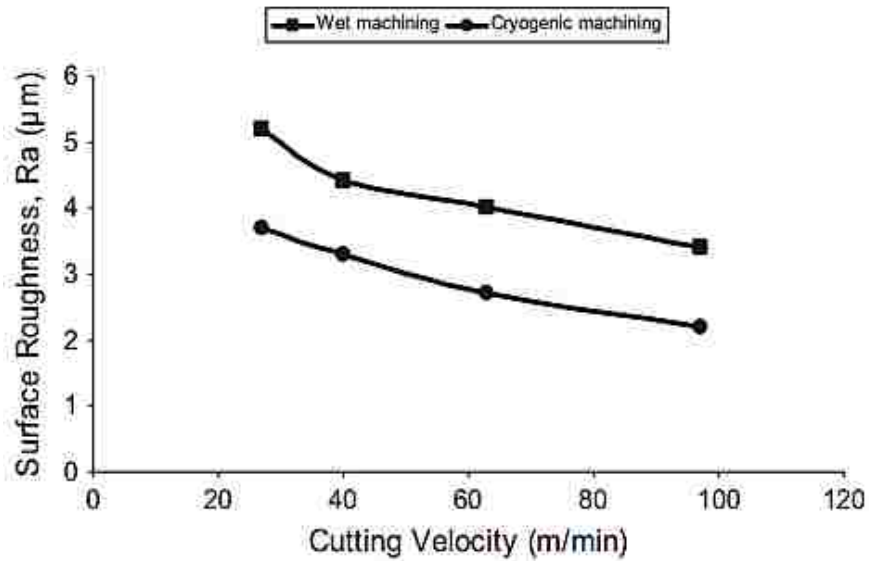


Figure 2.23: Variation of surface roughness with cutting velocity under wet and cryogenic machining of Ti-6Al-4V [61]

2.7.5 Effect on Cutting Forces

Researchers measured the components of the forces in different types of cryogenic cooling approaches. Bermingham et al. [62] cooled the flank face of the tool and observed that no change occurred in the feed component of force but the cutting force was lower than the dry machining. Dhananchezian et al. [61] cooled the flank and the rake face along with the tool surface and observed that cryogenic machining required less force than wet machining when an emulsion of cutting fluid was used as a coolant. They noted that lower temperatures during cryogenic machining (Figure 2.20 (b)) were responsible for lower values of both components of forces. They also found that the cutting and feed forces decreased with increased cutting velocity (Figure 2.24). On the other hand, Sun et al. [66] used compressed air cryogenic cooling and found that the cutting and feed forces were higher at the beginning of the machining process but lower when it ended than in dry machining.

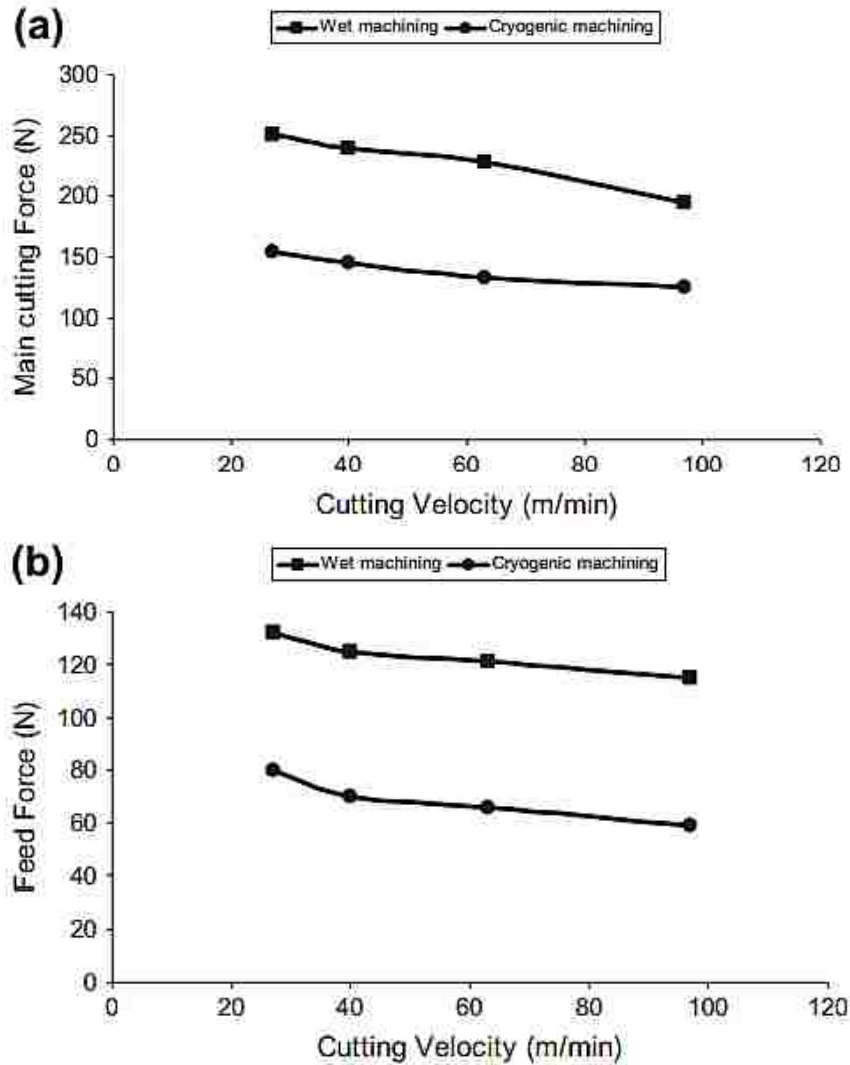


Figure 2.24 Comparison of (a) cutting, and (b) feed forces under wet and cryogenic machining of Ti-6Al-4V with increasing cutting velocity [61]

2.8 Introduction to Nano-fluids

In any metal cutting operation, the cutting fluid functions in three ways: cools the workpiece surface and the cutting tool, removes the chips from the cutting zone, and lubricates the tool–workpiece interface. Dhar et al. [67] observed that the application of cutting fluids during machining facilitates economy of tools, maintains tight tolerances, and protects surface properties from damages. However the use of cutting fluids during machining occupies 16 – 20% of the cost of production in the manufacturing industry.

Hence, excessive use of these fluids should be avoided. A new class of cutting fluids was thus synthesized by mixing metallic, non-metallic, ceramics, or carbon nanoparticles in a conventional cutting fluid because nanofluids show better stability, extremely good thermal conductivity, and no negative effect on pressure drop. There have been many investigations on the tribological properties of lubricants with different nanoparticles added. Many researchers [68 – 77] have reported that the addition of nanoparticles to lubricant is effective in reducing wear and friction.

Chinas-Castillo and Spikes [68] investigated the effect of particle size on friction and wear during rolling and lubricated sliding conditions of a M2 steel ball on a steel disk using gold particles of size 5 and 20 nm. The results showed that gold particles of 20 nm were more effective in reducing friction and wear than gold particles of 5 nm. This difference might be because the 5 nm particles allow more asperities interaction between the ball and the disk during rolling experiments than do the 20 nm particles. Liu et al. [69] employed the dialkyldithiophosphate (DDP) modified copper nanoparticles as additives in liquid paraffin. Results showed that the nanoparticles of smaller size were more likely to interact with the surfaces of the friction pairs to form a surface protective film, which increased anti-wear ability. Rapoport et al. [70] studied the inorganic fullerene-like (IF) particles as additives in lubricant. They found that smaller and more nearly spherical IF particles were likely to exhibit superior rolling, lower affinity to the metal surface, decreased contact temperatures, higher elasticity, and higher chemical resilience. A low concentration of nanoparticles is sufficient to improve tribological properties, such as 0.05% DDP–PbS [71], 0.1% EHA–TiO₂ [72], 0.1% DDP–ZnS [73], 0.15% DDP–Cu [74], 0.2% OA–PbS [75]. Qiu et al. [76] found that the concentration of Ni nanoparticles between 0.2 and 0.5%

provides the best anti-wear behaviour and friction reduction. Tao et al. [77] demonstrated that 1% is considered the optimum concentration for the diamond nanoparticles in paraffin oil.

The use of nanoparticle blended lubricating oils have been used in conventional machining processes such as turning, milling and grinding processes. Table 2.2 gives a summary of the various nanoparticles that have been used in the past along with their benefits.

Table 2.2: Summary of various nanoparticles used in different machining processes [78]

Types of nanoparticle(s)	Base fluid	Size (nm)	Process	Findings
xGnP	Vegetable oil	10	Milling	0.1 wt% xGnP with 1 µm dia. and 10 nm thickness showed lowest friction coefficient.
SiO ₂	ECOCUT SSN 322 mineral oil	5–15	Milling	Reduction in power, cutting force, and specific energy.
Carbon onions	Alumicut oil	5–20	Milling	Highest carbon onion concentration (1.5 wt%) yielded minimum cutting force and surface roughness.
MoS ₂	ECOCUT HSG 905S oil	20–60	Milling	0.5 wt% MoS ₂ produced best surface and surface quality deteriorated as MoS ₂ concentration increased to 1 wt%.
SiO ₂	ECOCUT SSN 322 oil	5–15	Milling	0.2% SiO ₂ generated thin protective film and % increase of SiO ₂ conc. showed reduction in surface roughness.
SiO ₂	ECOCUT SSN 322 oil	5–15	Milling	0.2 wt% SiO ₂ with high air pressure and 60° nozzle orientation recorded minimum cutting force. 1 wt% SiO ₂ with 2 bar air pressure and 30° nozzle angle yielded best surface.
MoS ₂	ECOCUT HSG 905S oil	20–60	Milling	1 wt% MoS ₂ with 4 bar air pressure and 30° nozzle orientation recorded minimum cutting force. 0.5 wt% MoS ₂ with 4 bar air pressure and 60° nozzle angle yielded best surface.
MoS ₂	Paraffin oil, CANMIST oil and Soybean oil	<100	Grinding	High MoS ₂ concentration yielded high G-ratio with MQL and low G-ratio with flood lubrication.
Al ₂ O ₃	Deionized water	40, 100, and 200	Grinding	4% Al ₂ O ₃ conc. yielded best G-ratio while best surface was produced under flood cooling.
xGnP TM	IPA, TRIM SC200	5–10	Grinding	Large size platelets were found to be more effective than small ones. 1 wt% graphite platelets produced best surface finish.
ND	Paraffin oil	30 and 150	Grinding	30 nm size particles yielded smoother surface than 150 nm particles. Size did not affect grinding force while nanoparticle conc. did not have effect on surface roughness, 4% ND (30 nm) produced best surface.

Based on available literatures, the following section delineates on the application of different nano-cutting fluids and their effect on different machining performance parameters in various machining processes.

2.9 Effect of Nanofluids on machining

The addition of nanoparticles into base fluid can enhance the overall convective heat transfer coefficient and lubricating properties of the coolant. It also reduces tool wear,

surface roughness, cutting force, and chip thickness compared with dry machining and conventional fluid machining. [70 – 81]

2.9.1 Effect on Cutting Forces and Surface Roughness

Sarhan et al. [79] used the mixture of nano SiO₂ with an average size of 10 nm and ordinary mineral oil as a lubricant to reduce the consumption of lubricant and power during machining of AA6061-T6 on a vertical milling machine. Two types of lubrication were used: (i) the ordinary mineral oil and, (ii) the same mineral oil with SiO₂ nanoparticles at a concentration of 0.2 wt.%. The nanoparticles were mechanically mixed with the mineral oil and were subjected to sonication for 15 minutes to ensure that the nanoparticles were uniformly suspended and did not agglomerate. Results from the experiment show a noticeable reduction in the cutting force by using nanoparticle lubrication as compared to the ordinary mineral oil as illustrated in Figure 2.25.

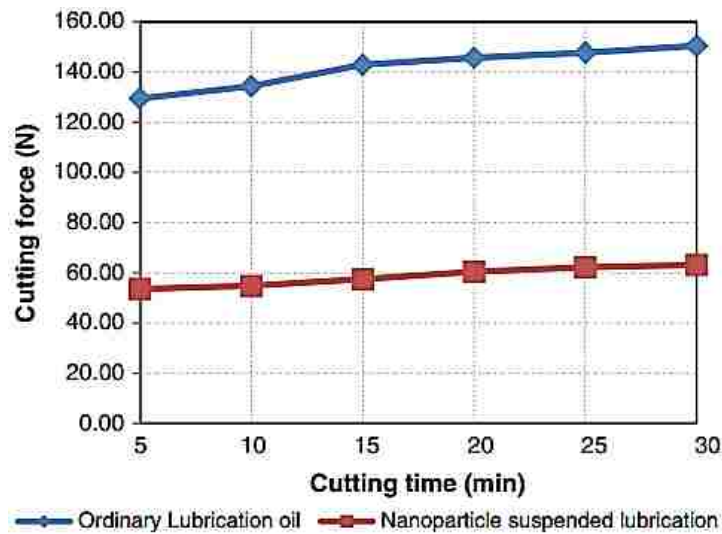


Figure 2.25: Variation in cutting forces while machining with base oil and nanoparticle suspended base oil [79]

Sayuti et al. [80] performed milling operation on a vertical milling machine with carbon onion-enriched nano- fluid on aerospace duralumin workpiece and noticed an

improvement in surface quality and reduction in cutting forces. Carbon onion consists of concentric graphitic shells and it is one of the fullerene related materials with C60 and carbon nanotubes. It has been proven that it can provide similar lubrication as graphite when tribologically tested in ambient air [80]. In this study, four different concentrations, that is, 0.0, 0.5, 1.0, and 1.5 wt.% of carbon onion were mixed with Alumaticut® oil during the milling process. The highest carbon onion concentration (1.5 wt.%) yielded the minimum cutting force and surface roughness. They achieved 21.99% and 46.32% reduction in cutting forces (Figure 2.26) and surface roughness (Figure 2.27), respectively, as compared with those obtained when using normal lubrication oil.

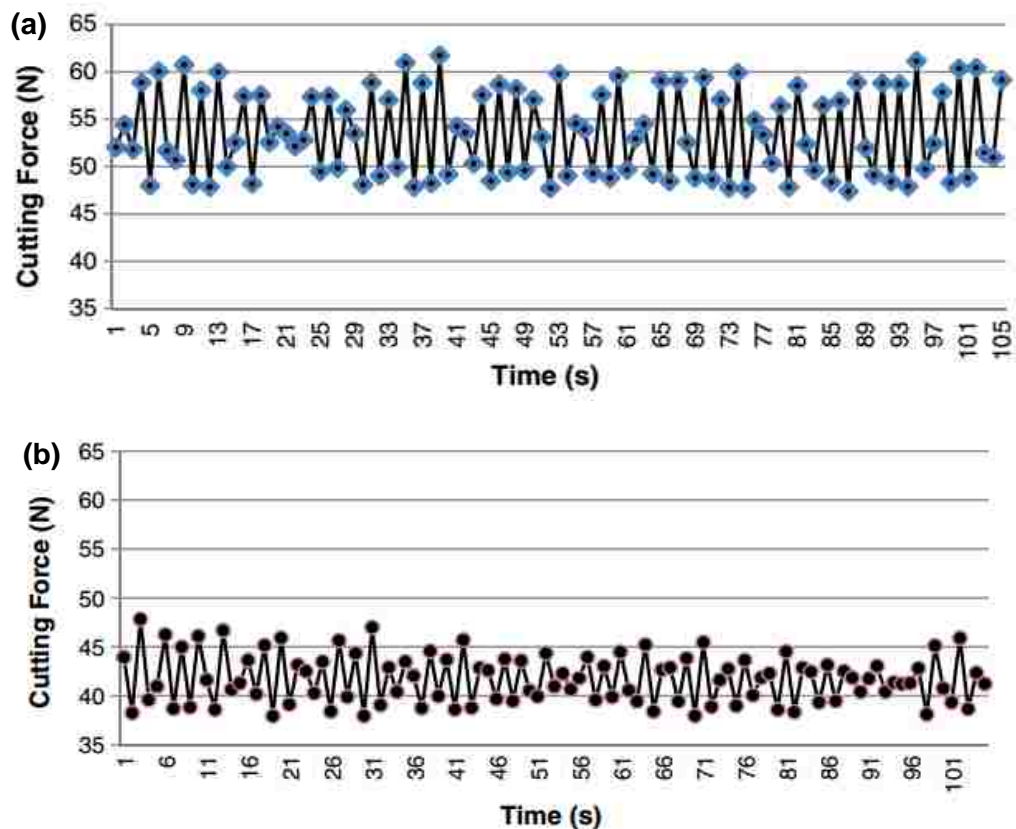


Figure 2.26: Cutting force generated during milling of Al-2017 with (a) normal lubricating oil, and (b) 1.5 wt.% nanoparticle blended lubricating oil. A 22% decrease in cutting force was achieved using the 1.5 wt.% nanoparticle blended lubricant compared to the base lubricant [80]

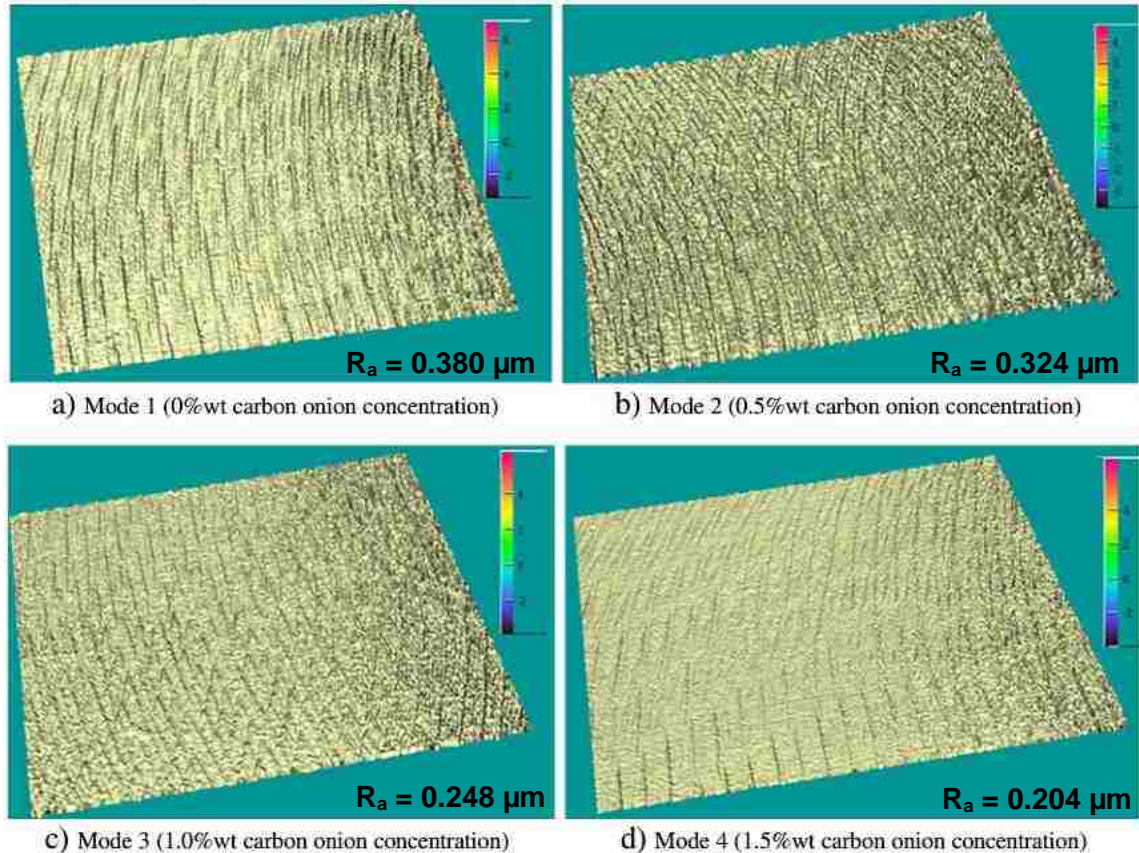


Figure 2.27: Surface profile of machined surface under (a) normal lubricating conditions, (b) 0.5 wt.% carbon-onion enriched lubricating conditions, (c) 1 wt.% carbon onion enriched lubricating conditions, (d) 1.5 wt.% carbon onion enriched lubricating conditions. The average surface roughness of the machined surface decreased from $0.380 \mu\text{m}$ under normal lubricating oil conditions to $0.204 \mu\text{m}$ under 1.5 wt.% carbon-onion blended lubricating oil conditions [80]

Rahmati et al. [81] investigated the morphology of surface produced by end milling of Al6061-T6 alloy on a vertical machining center using MoS_2 nano-lubrication. The experiments were conducted using ordinary lubricant as the first mode of lubrication and nano-enhanced lubricant having MoS_2 nanoparticles in an ordinary lubricant as the second mode. The concentrations of MoS_2 nanoparticles in base oil were 0.0, 0.2, 0.5, and 1.0 wt%. The presence of MoS_2 nanoparticles in lubricant improved the machined surface quality due to the rolling action at the machining zone. This mechanism is explained later in Section 2.9.4. The average surface roughness was measured after each machining test with a surface profilometer (Mitutoyo SJ-201). From the results, it was noticed that 0.5

wt% MoS₂ nanoparticle concentration produced the lowest surface roughness. However, when the concentration was increased to 1 wt%, a decrement in the surface quality was observed as shown in Figure 2.28.

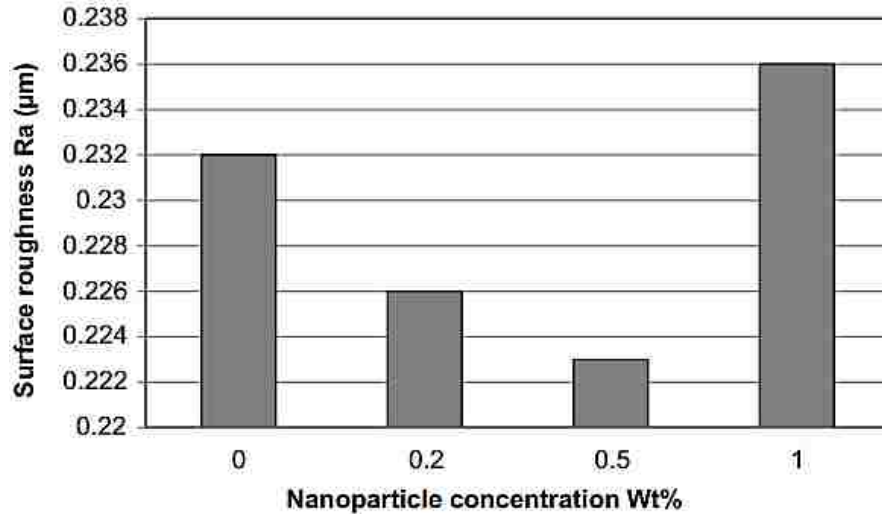


Figure 2.28: Variation in surface roughness of the machined Al6061 sample with increasing nanoparticle concentration. The least average surface roughness was recorded using the 0.5 wt.% nanoparticle concentration in lubricating oil [81]

Erh et al. [82] carried out an investigation on the morphology of the machined surface during milling of Al6061-T6 using SiO₂ nano-lubrication system. The increase of SiO₂ concentration at 0.2 wt.% increased the growth of thin protective film on the tool–chip interfaces as shown in Figure 2.29. These formations of the thin film on the machined surface enhanced the machining performance by improving the surface quality and cutting forces as shown in Figure 2.30.

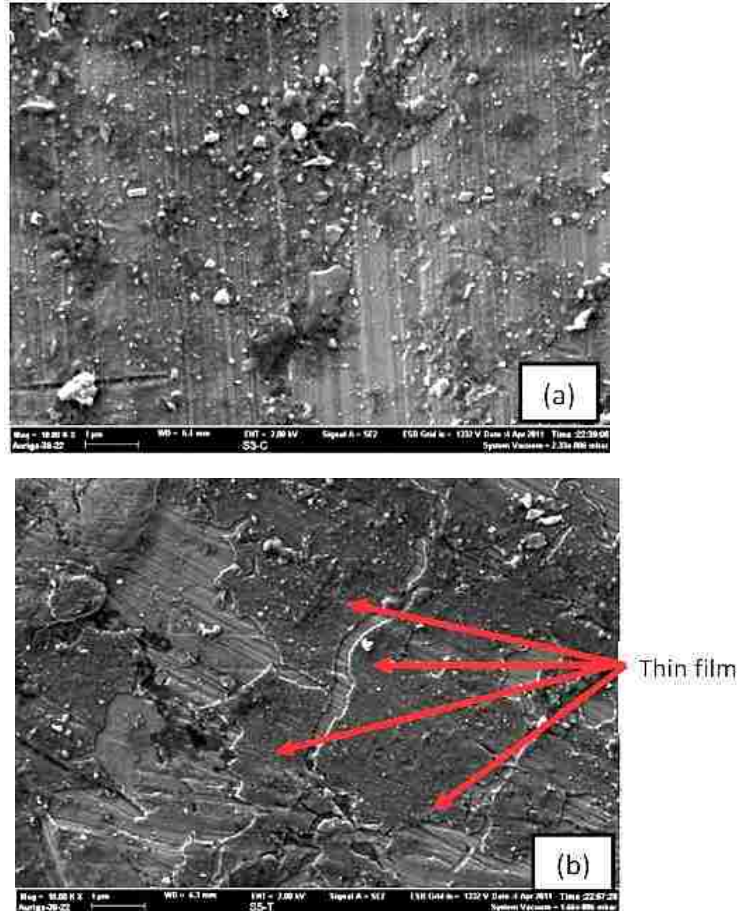


Figure 2.29: SEI micrographs of the surface of Al6061 subjected to milling with (a) normal lubricating oil, (b) 0.2 wt.% SiO₂ blended lubricating oil [82]

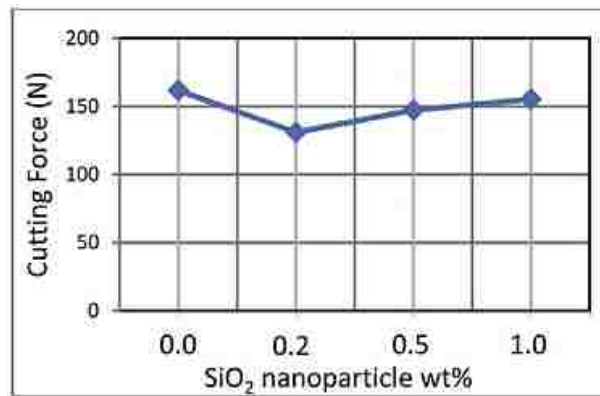


Figure 2.30: Cutting forces during milling of Al6061 with increasing nanoparticle concentration. The least cutting force was recorded with 0.2 wt.% SiO₂ concentration in lubricant oil [82]

Lee et al [83] studied the micro-drilling process using nano-fluid MQL. They observed that both pure and nano-fluid MQLs could decrease the drilling torques, but the

nano-fluid MQL was much more effective than pure MQL. However the addition of nano-diamond particles improved lubrication and cooling effects with their enhanced penetration and entrapment at the drilling interface. As a result, the magnitudes of torques were significantly reduced as shown in Figure 2.31. Lubrication and cooling effects of the nanofluids were evaluated based on their ability to prevent burr formation during the drilling process. From Figure 2.32, it can be observed that the use of nano-fluid MQLs reduced the burr formation during the micro-drilling process.

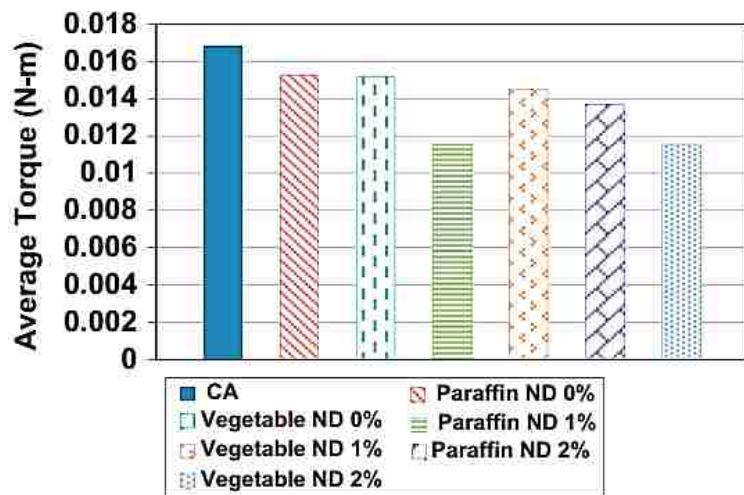


Figure 2.31: Average torque generated during micro-drilling of Al6061 with different coolants [83]

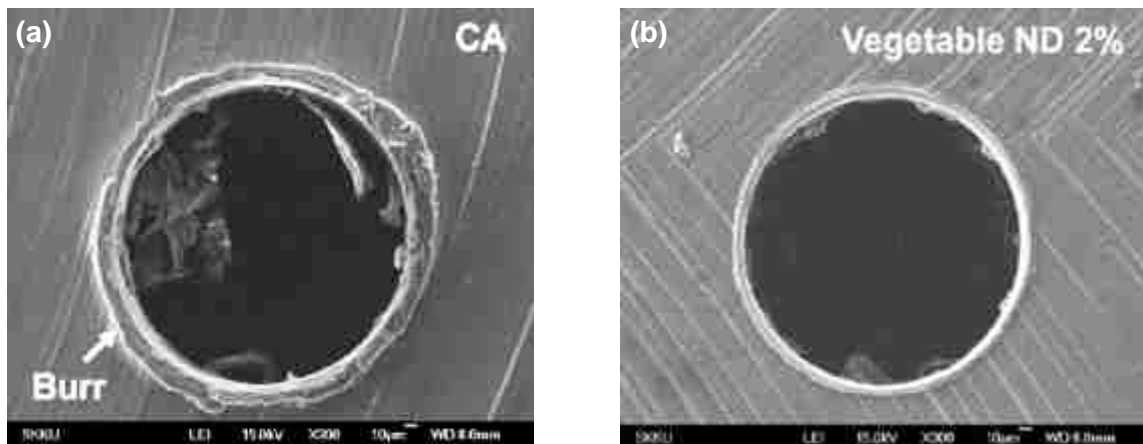


Figure 2.32: SEM Micrographs of the drilled holes under (a) compressed air (CA) lubrication, (b) vegetable oil with 2 wt.% nanodiamond (ND) particles [83]

2.9.2 Effect on COF and Wear Rate

Several researchers studied the friction reduction and anti-wear properties of nanoparticles by conducting pin-on-disk, block-on-ring or reciprocating sliding tests. Wu et al. [84] studied the tribological performance of CuO, TiO₂ nanoparticles blended in API-SF engine oil (SAE30 LB51153). It was observed that the COF of SF oil containing nanoparticles, especially for CuO and TiO₂, are lower than those of SF oil without nanoparticles (Figure 2.33).

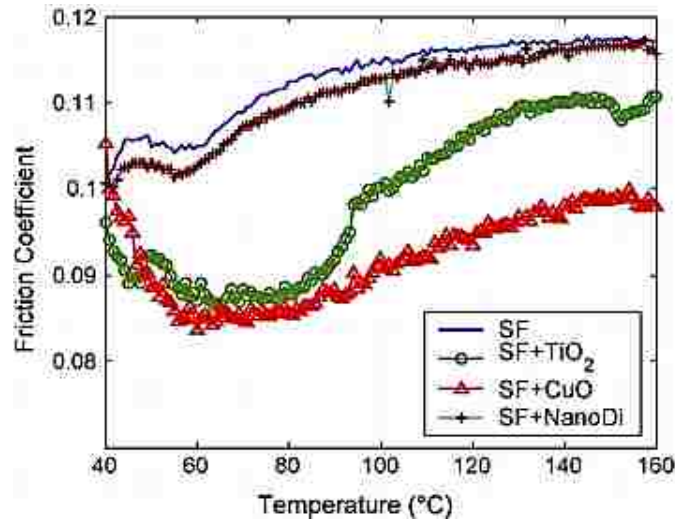


Figure 2.33: Friction coefficient of the SF oil with and without nanoparticles [84]

One of the reasons suggested by the authors was the effect of viscosity. In general, low temperature results in low viscosity. The viscosity of SF oil containing nanoparticles is higher than that of the SF oil without nanoparticles. The SF oil with TiO₂ has the highest viscosity among the tested oils and hence, shows the lowest friction coefficient at the temperature around 40 °C. The higher viscosity increases the Sommerfeld number [77], such that the lubrication regime may change from boundary lubrication into mixed or hydrodynamic lubrication, so a lower friction coefficient can be observed at lower temperature. The other reason stated is that of the rolling mechanism exhibited by TiO₂

nanoparticles. The rolling effect of nanoparticles was also reported by Rapoport et al. [70] and Tao et al. [77]. A detailed explanation of the rolling behaviour is given in section 2.9.4.

Rapoport et al [85] studied the tribological properties of inorganic fullerene (IF) type WS_2 particles under mixed lubrication conditions by conducting pin-on-disk experiments. The time-dependence of the friction force for oil and oil+ IF blend at load of 260 N is shown in Figure 2.34. It was observed that the frictional force generated under nanoparticle blended condition was much lower than under base oil alone.

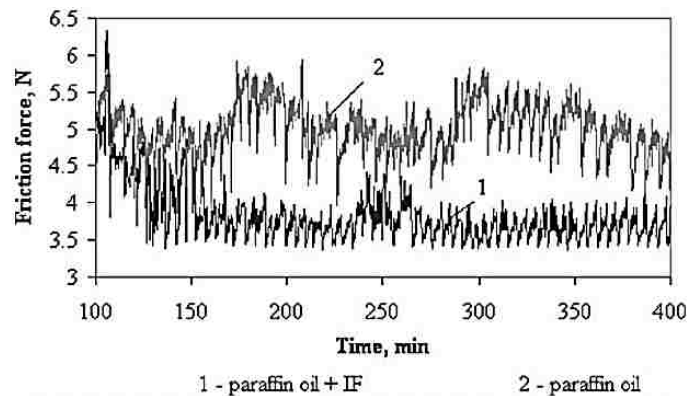


Figure 2.34: The time-dependence of friction force for oil and oil + IF blend at load of 260 N. The friction force under IF nanoparticle blended oil was found to be lower than the plain lubricating oil throughout the sliding experiment [85]

The wear of the pin rubbed with oil + IF lubricant was lower in comparison to the pin lubricated with oil only at all studied loads as shown in Figure 2.35. This effect becomes more predominant with increasing load, suggesting that the favourable role of IF increases with load. At a load of 475 N the wear rate of a pin lubricated by oil was more than six times higher in comparison to oil + IF blend. The reason for such a behaviour can be explained by the third body mechanism (Figure 2.36).

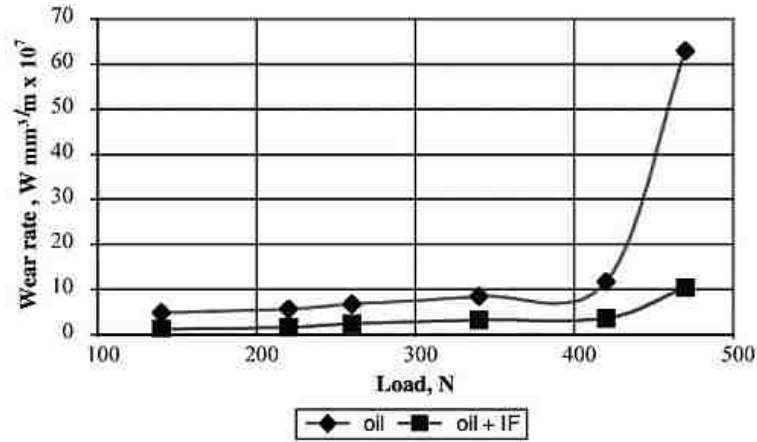


Figure 2.35: The effect of load on the wear rate of pin lubricated with oil and oil + IF lubricants [85]

It is expected that under severe contact conditions, when the thickness of the lubricant film is less than that of the size of the IF nanoparticles, the third body consists not only of the oil and wear debris, but also of the delaminated nanosheets of IF nanoparticles. The straight asperity contact is limited by the presence of IF nanoparticles, which are partially confined in the valleys of the contacting surfaces and by the transferred films of IF at the asperity crests. It is expected that the first bodies covered with the IF nanoparticles (in valleys or as transferred films) facilitate the shearing of the third body. IF nanoparticles can be furnished from the valleys to the contact surface, improving thereby the friction behaviour.

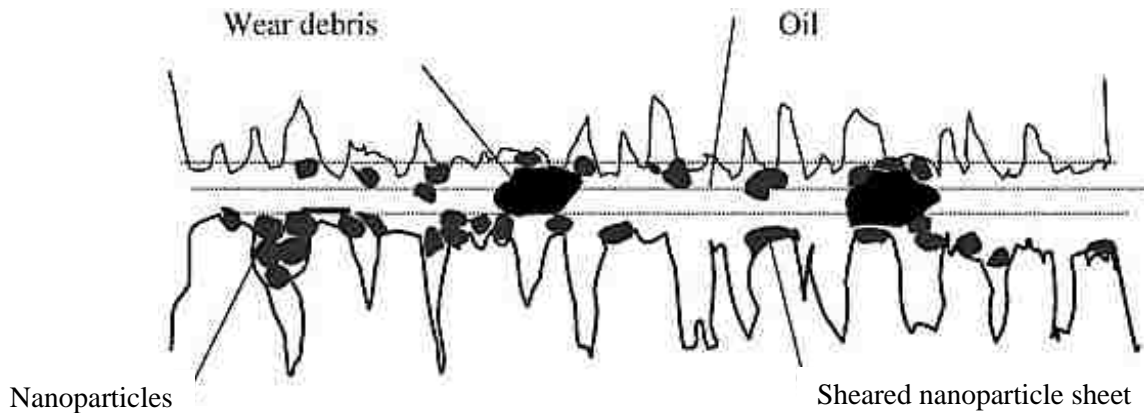


Figure 2.36: Schematic of third body model under friction with nanoparticles [85]

A.H. Battez et al. [86] studied the friction reduction properties of CuO nanoparticle as a lubricant for NiCrBSi coating (a Nickel-based alloy coating usually employed for high temperature applications). The wear tests were conducted under block-on-ring configuration. The tribological behaviour of the base oil and nanofluids showed an increase in the COF when the load increased from 165 to 214 N (Figure 2.37). This behaviour and the COF values affirm that tests were carried out in the mixed lubrication regime. The authors observed that under the mixed lubrication regime, there were more frequent solid contacts and the increase in the normal load results in an increase in the number of contacts at the tips of asperities and the load was supported by the deformation of contacting asperities. The proximity of asperities results in adhesive contacts caused by either physical or chemical interactions and friction arises due to adhesion and deformation. For both loads there was a friction coefficient drop off with the increase in the concentration of CuO nanoparticles.

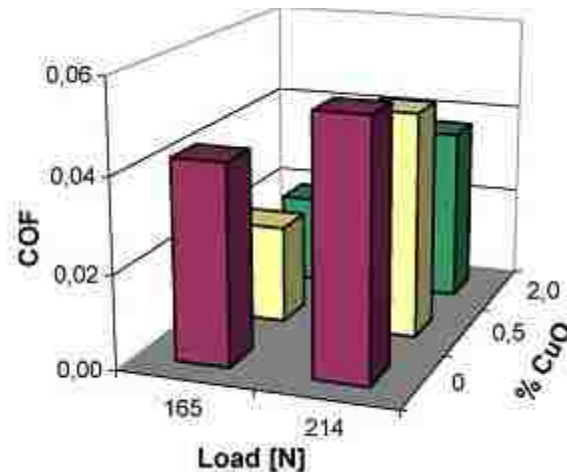
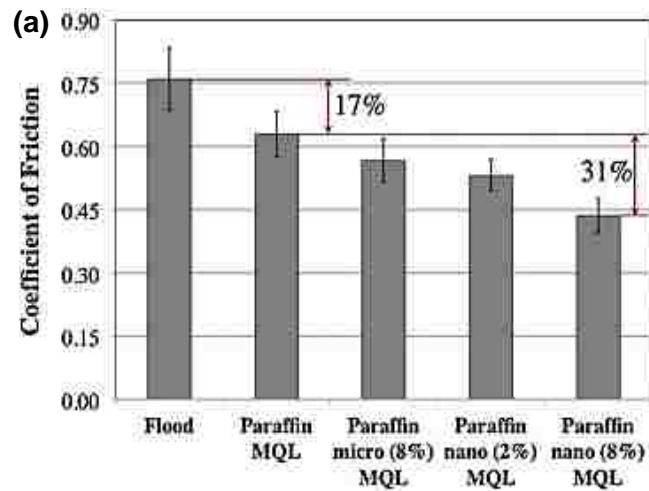


Figure 2.37: Mean friction coefficients for base oil and nanofluids [86]

Kalita et al. [87] explored the effect of oil-based nano-fluid on friction coefficient and specific energy in grinding EN24 steel under the MQL technique. An external fluid

delivery system (precision dispenser-AMCOL Corporation) was used for MQL grinding. The compressed air was supplied at a pressure of 60 psi and the MQL flow rate was 2.5 mL/min. The surface grinding was conducted on a surface grinder loaded with a vitreous-bonded Al_2O_3 grinding wheel. It was found that both soybean-based and paraffin-based nanofluids performed better with an enhancement of nanoparticles concentration. The lowest COF of 0.22 and a maximum reduction of 53% in energy consumption (power required for unit volume removal of the material) were recorded with nanolubricants and also 50% increment in G-ratio of grinding wheel (volume of workpiece material removed per unit volume wear of grinding wheel) was achieved by the use of nanolubricants as shown in Figure 2.38.



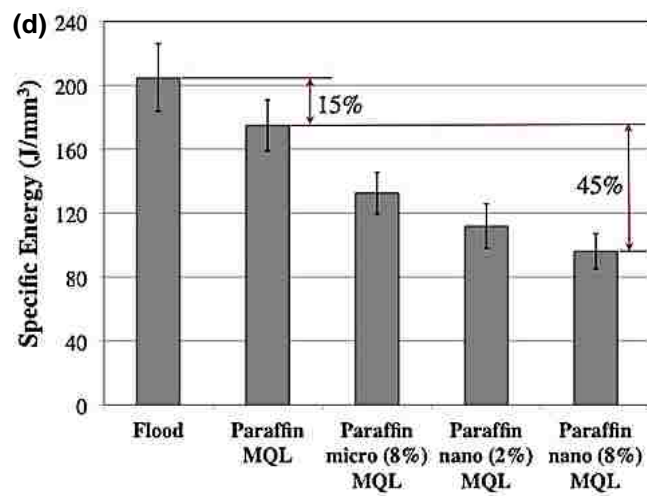
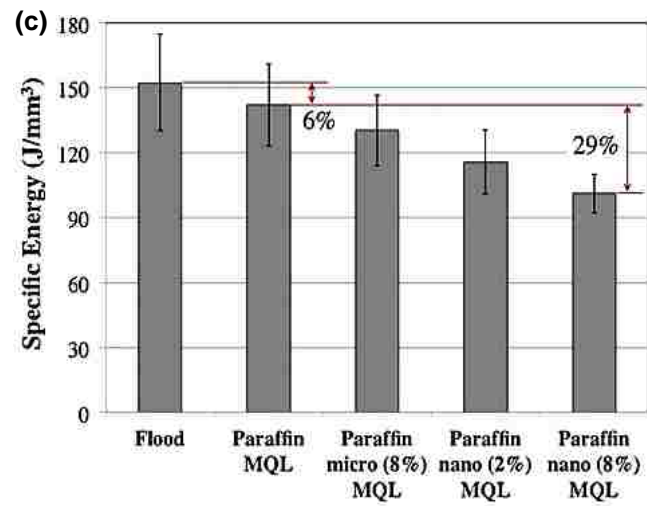
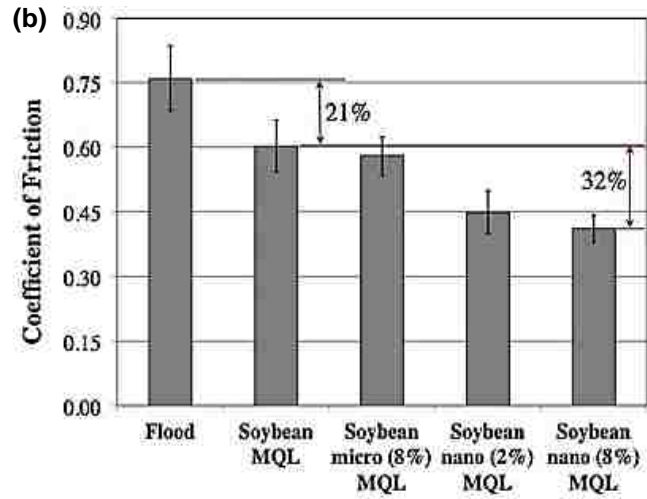


Figure 2.38: Magnitude of (a,b) COF, (c,d) specific energy obtained during grinding of EN24 steel using different lubricants [87]

2.9.3 Effect on Cutting Zone Temperature

The reduction in cutting zone temperatures is essential for maintaining a low COF during machining process. Researchers have reported a significant decrease in the cutting zone temperatures while machining with coolants as against dry conditions. Lee et al. [88] measured the grinding zone temperature during sliding of grey cast-iron disks (GC200, KS) using disk-on-disk configuration while varying the normal load. The authors employed two types of coolants: (i) normal lubricating oil, and (ii) lubricating oil blended with graphite nanoparticles with 0.1 vol.% and 0.5 vol.% concentration. To prevent agglomeration, alkyl aryl sulfonate (a dispersant) was mixed with the lubricating oil. This mixture of lubricating oil + dispersant + nanoparticles was subjected to sonication for 30 minutes and then used for sliding experiments. When using normal lubricant, the temperature typically rose to 120 °C, but when using nano-lubricants the final temperature peaked at 60 °C (Figure 2.39).

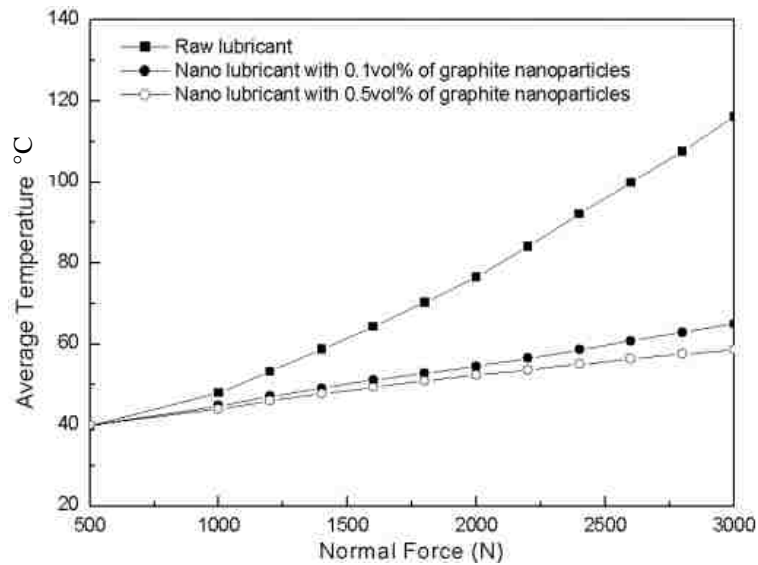


Figure 2.39: Variation of grinding zone temperatures during sliding of grey cast iron disks under different cooling environments [88]

2.9.4 Mechanism of Friction behaviour of Nanoparticles

Three main mechanisms which lead to reduced friction and wear are discussed in the literature.

1. **Rolling:** The IF nanoparticle acts as a ball bearing between the mating surfaces [89]. When the rolling mechanism is effective, the nanoparticles act as nanoscopic ball bearings between the contact surfaces and provide extremely low friction coefficients (0.01 and below). It was postulated that the quasi-spherical IF NP are ideally suited to provide this kind of friction mechanism [89]. The demonstration of rolling behaviour of a nanoparticle for one rotation is shown in Figure 2.40 (a) through (f).
2. **Sliding:** Given the low surface energy of its basal (001) plane and its robustness, the IF nanoparticle acts as a separator providing low friction and facile shearing between the mating surfaces as shown in Figure 2.41. During the sliding motion the IF nanoparticle preserves its shape under normal and shear stress without rolling or exfoliation. Sliding is regarded as a very low friction mechanism when it occurs between weakly interacting, smooth surfaces [90]. Nonetheless if the sliding particles are made of a hard material, degradation of the mating surfaces by abrasion, plowing, or indentation is inevitable. In such a case, a rough surface patch is observed on the workpiece [85].

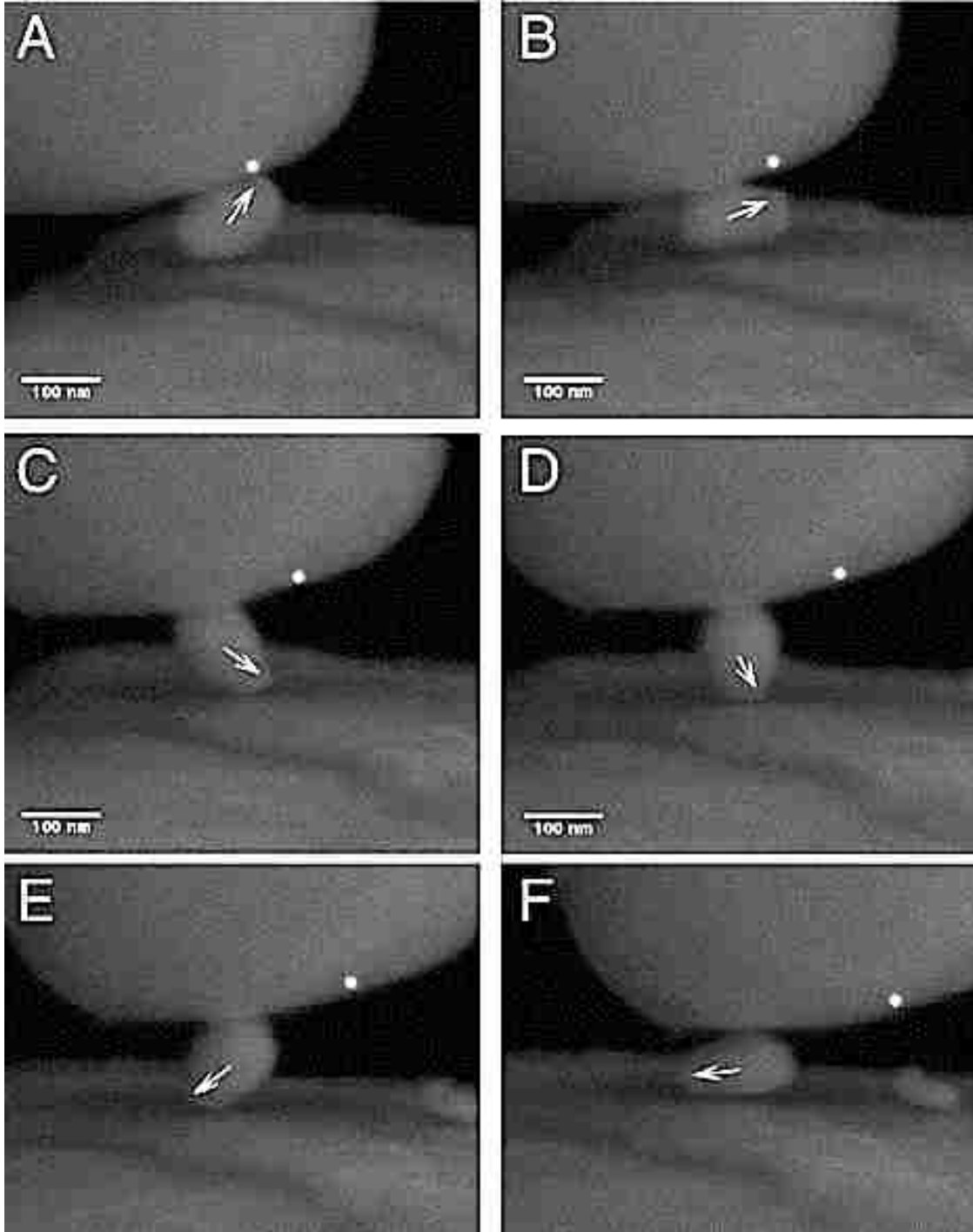


Figure 2.40: Demonstration of rolling friction mechanism where an IF nanoparticle completes one complete rotation is shown from images (a) through (f). The rotation can be tracked with the help of arrow marks shown in the nanoparticle [93]



Figure 2.41: Demonstration of sliding behaviour of an IF nanoparticle. The white dot represents the initial point of sliding [93]

3. **Exfoliation and transfer of films (third body):** Exfoliated layers from the IF nanoparticles are deposited on the asperities of the mating surfaces providing easy shearing [91]. Exfoliation and transfer of WS₂ nanosheets (designated third body) [85] were considered to be the predominant mechanism for reducing both friction and wear in the case of IF nanoparticles. It was shown that under large mechanical loads and shear forces, the nanoparticles are deformed and compressed. This structural deformation gives rise to dislocation and dislodging of WS₂ nanosheets from the nanoparticle surface. The external nanosheets of the IF nanoparticles, a few monolayers thick each are gradually transferred onto the substrate, thus reducing the friction between the two mating surfaces as shown in Figure 2.42. Furthermore, this process reduces the local heating, and hence the plastic deformation of the underlying metal surface and its oxidation. This slowing down the wear [92]. However extensive exfoliation eventually damages the IF nanoparticles and causes degradation of the tribological behaviour.

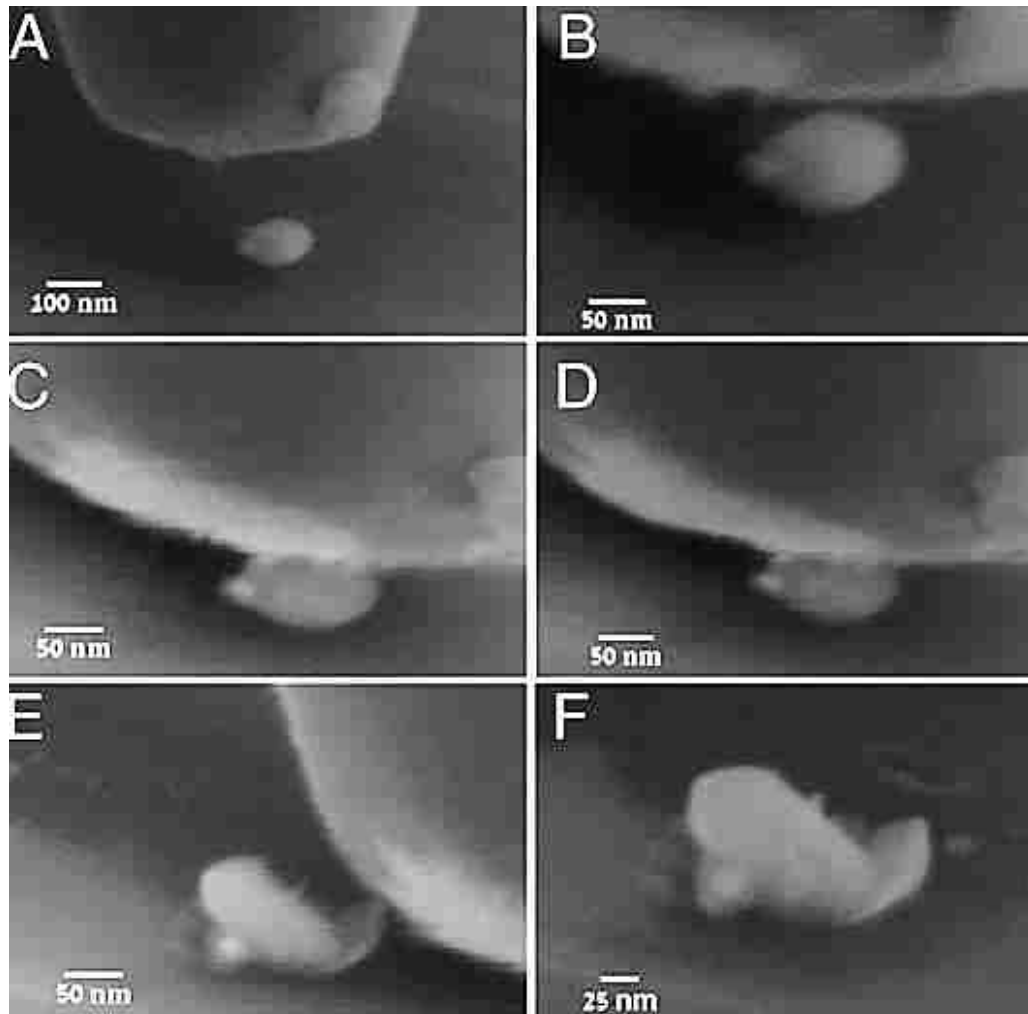


Figure 2.42: Demonstration of exfoliation mechanism for an IF nanoparticle. (a,b) The microscope probe is positioned closer to the nanoparticle, (c,d) Uniaxial compression of the nanoparticle by the microscopic probe, (e,f) When the microscopic probe begins to slide after making contact, the nanoparticle begins to exfoliate and this forms a film over the surface of the workpiece [93]

A simple schematic representation of the three mechanisms of friction reduction in nanoparticles is shown in Figure 2.43 [93].

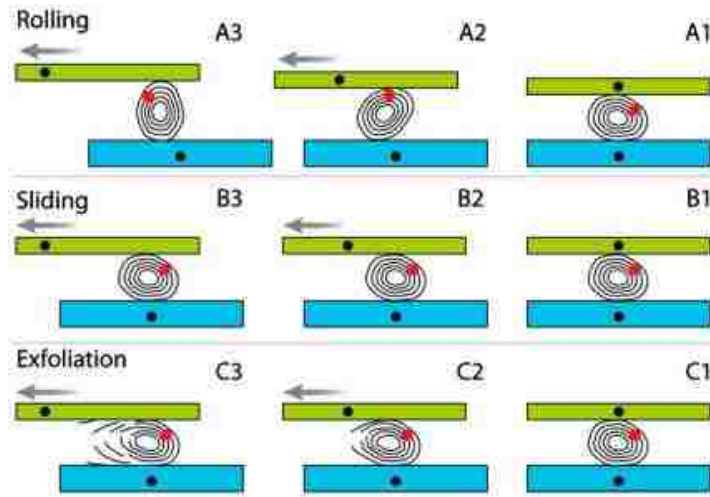


Figure 2.43: Schematic representation of the three dominant friction reduction mechanisms for a nanoparticle [93]

2.10 Summary of Literature Survey

In this chapter, the previous research work on serrated chip formation and their subsequent difficulties during machining of Ti alloys have been discussed. To overcome the difficulties, the concept of cryogenic and nanolubricant machining was introduced. The majority of the literature work is limited to analysing the tool wear, cutting zone temperature, surface roughness of the machined part. Though essential, the factors that have been considered thus far do not provide an holistic approach in preventing the problems of machining Ti alloys. Improvement in machinability can be effected by approaching the problem in two ways. (i) To examine the role of cryogenic machining in chip segmentation process, (ii) To examine the role of nanoparticles in influencing the COF at the tool – workpiece interface. The present study is directed towards this area of research.

Chapter 3

EXPERIMENTAL PROCEDURE

3.1 Workpiece and Tool Materials

A hot-extruded Ti-6Al-4V rod was machined into a tubular shape with an outer diameter of 25.41 mm and a 2.50 mm wall thickness before performing the orthogonal cutting tests. The optical microstructure of Ti-6Al-4V, taken using a Keyence digital microscope, consisted of α (HCP structure) and β (BCC structure) phases at room temperature as shown in Figure 3.1. The length of the β phase was $4.86 \pm 2.86 \mu\text{m}$ and the width was $1.03 \pm 0.46 \mu\text{m}$, and were elongated along the direction of extrusion of the workpiece rod. The microhardness of the material was measured to be $380 \pm 3.01 \text{ HV}$ using a 50 g load for 12 s. The composition of the alloy is presented in Table 3.1 [1].

Uncoated tungsten carbide cutting tools (Figure 3.2 (a)) were used during in-situ machining while polycrystalline diamond (PCD) tools (Figure 3.2 (b)) with a rake angle of 0° were used during high speed machining of Ti-6Al-4V.

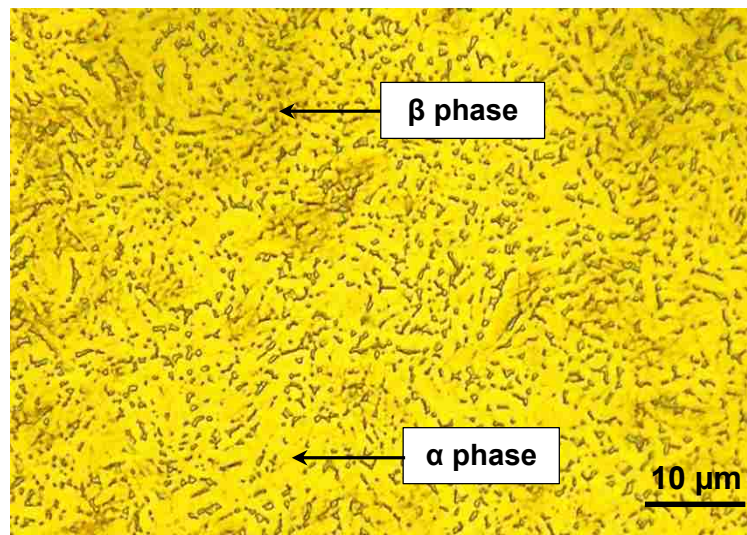


Figure 3.1: Optical microstructure of Ti-6Al-4V after etching with Kroll's reagent for 10 s showing the presence of α and β phases

Table 3.1: Chemical composition of Ti-6Al-4V [1]

Al	V	C	Fe	N	O	H	Ti
5.50 - 6.75	3.50 - 4.50	≤ 0.08	≤ 0.40	≤ 0.03	≤ 0.20	≤ 0.02	Balance

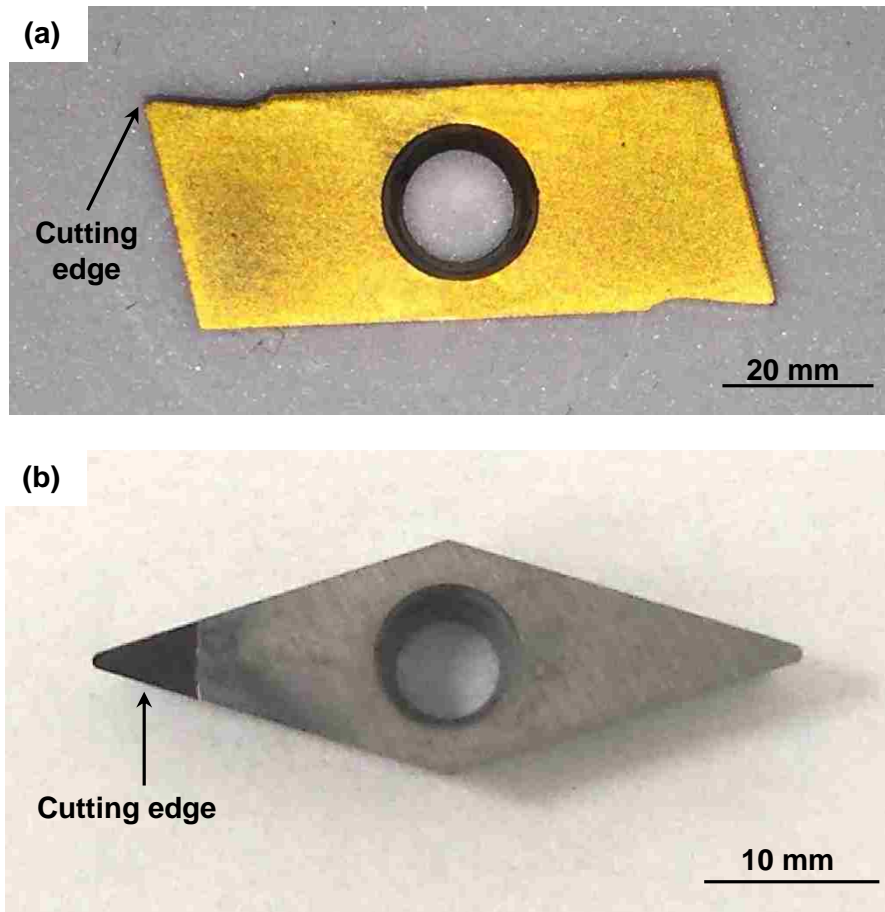


Figure 3.2: Cutting tools used for (a) in-situ experiments – uncoated tungsten carbide tool, (b) conventional machining – PCD tool

3.2 Conventional Orthogonal Machining

All orthogonal tests were performed on a Harrison M300 lathe, which is a compact and reliable center lathe. The lathe is equipped with a rapid-action foot controlled spindle brake with electrical disengagement to perform interrupted orthogonal cutting. The spindle speed may be selected from 12 different speeds ranging from 40 to 2500 rpm and feed rates

ranging from 0.03 to 1 mm/revolution. In preliminary testing, variation of cutting and thrust forces at different cutting speeds of 7, 15, 30 and 45 m/min were studied at a constant feed rate. As the cutting and thrust forces did not change significantly with the speed, the highest speed of 45 m/min was selected for further tests while maintaining a constant feed rate of 0.15 mm/rev. A PCD tool with a rake angle of 0° was used to machine the workpiece. A PCD insert was chosen as it has excellent wear resistance, high fracture strength and high dimensional stability properties. It was also reported that the PCD tool performed better in terms of wear resistance during machining of titanium alloy. [15]

3.2.1 Measurement of Force Components

During orthogonal cutting, cutting and thrust forces are two important forces exerted by tool on the workpiece. A two axis force sensor developed by Shilpi [15] was used in this study. The idea was to develop a practical measurement system that could be installed easily in the lathe machine without changing the configuration of the lathe or the workpiece. The force sensor was attached with a tool holder mounting and equipped with a slot such that the mounting can be placed easily in the tool holder post of the lathe machine. An actual image of this tool holder mounting with the force sensor attached is shown in Figure 3.3.

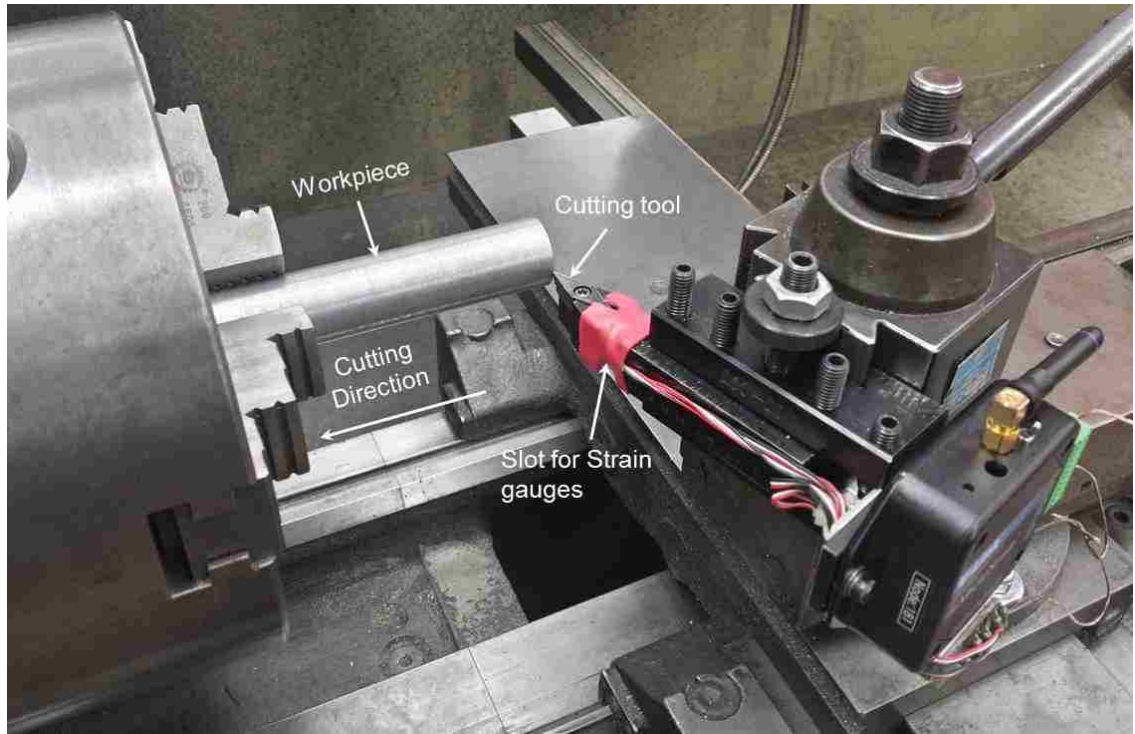


Figure 3.3: Experimental setup for orthogonal machining showing the position of cutting tool and the strain sensor assembly for obtaining cutting force data

3.2.2 Components of Force Measurement System

The data acquisition system comprised of a strain sensor, a wireless transmitter system (V-Link 2.4 GHz Wireless Voltage Node), an analog base station (MicroStrain 99 Micro TxRx wireless base station w/ analog outputs) and a computer loaded with data acquisition software 'Agile Link'. The strain sensor attached to the narrow groove in the modified tool holder picked up the strains produced in the tool holder as it bent under the loads exerted on it during the turning operation. It transmitted the signals via electrical wires to the strain sensor which then wirelessly transmitted them to the base station. The base station transmitted the data to the PC via a USB cable and 'Agile Link' was used to convert the streamed data to a readable format, which was also displayed in form of curves for the two measured forces. Figure 3.4 illustrates a schematic describing the entire data acquisition process during orthogonal cutting process.

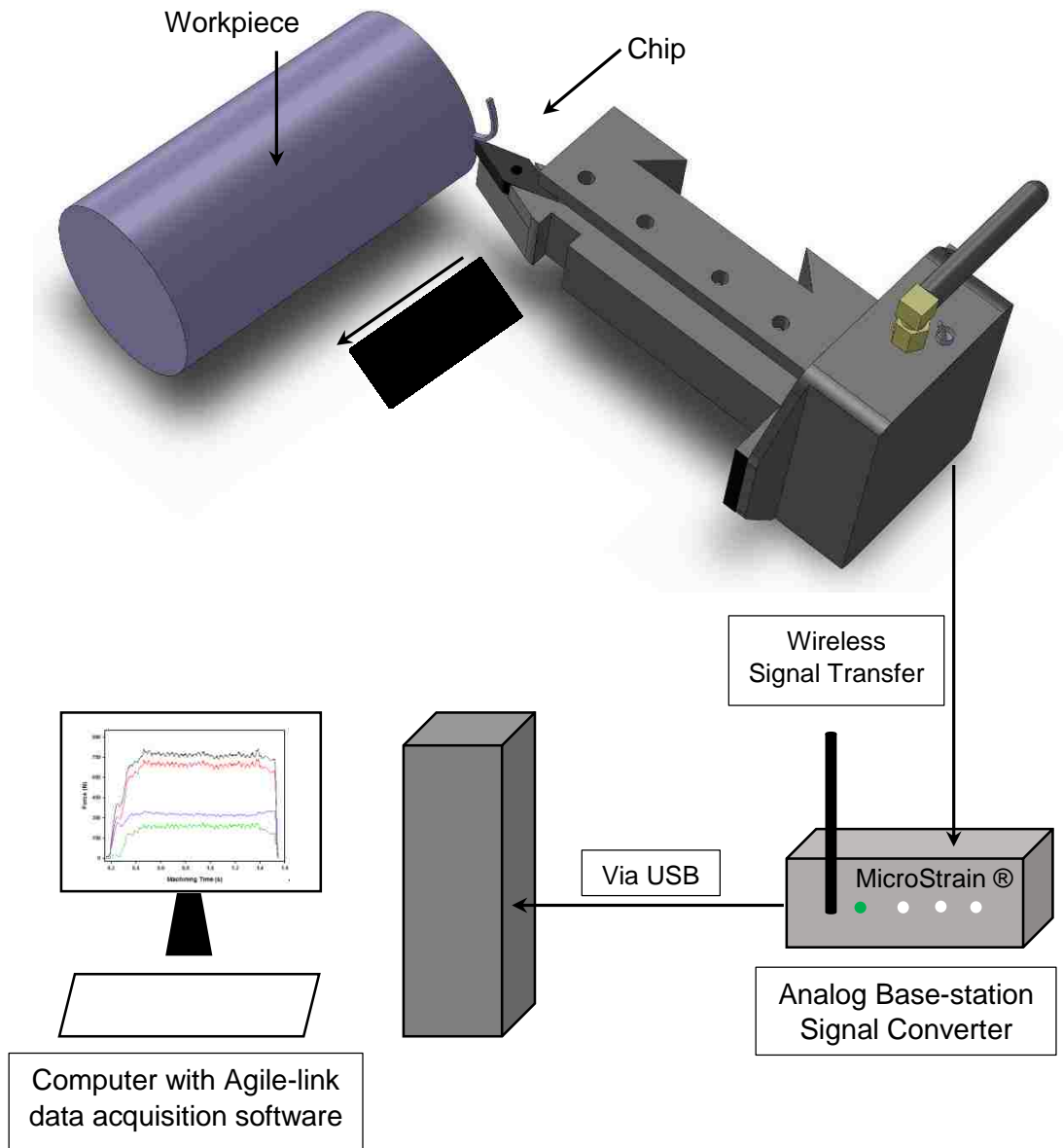


Figure 3.4: Data acquisition system of the force sensor where the electrical signal obtained during machining is transferred wirelessly to the base station and then via USB to the PC

3.2.3 Calibration of Force Sensor

The strain gauge produces an electrical signal depending on the strain applied on it. So to convert that signal to force, the sensor needed to be calibrated in both cutting and feed directions. To calibrate the force sensor in the cutting direction, the system was mounted on a vice in such a way that the gravity force acted in the cutting direction. Cutting tool was replaced with an attachment for calibration. The attachment consisted of a screw to hold a hanger plate where the loads were hanged. The weights were attached gradually on the hanger plate and the corresponding voltage was measured via a data acquisition system (see Section 3.2.4). The total force applied on the screw was calculated using the following equation:

$$F_{System} = M \times g + m \times g \quad (3.1)$$

where F_{system} is the total force acting on the system, M is the mass of the applied load, m is the mass of the hanger plate, g is the acceleration due to gravity.

The voltage readings from the sensor against an applied load were recorded. The relationship between the applied load and voltage were found to be linear for both the cutting and feed forces. The corresponding calibration graphs and their equations are shown in Figure 3.5 (a-b).

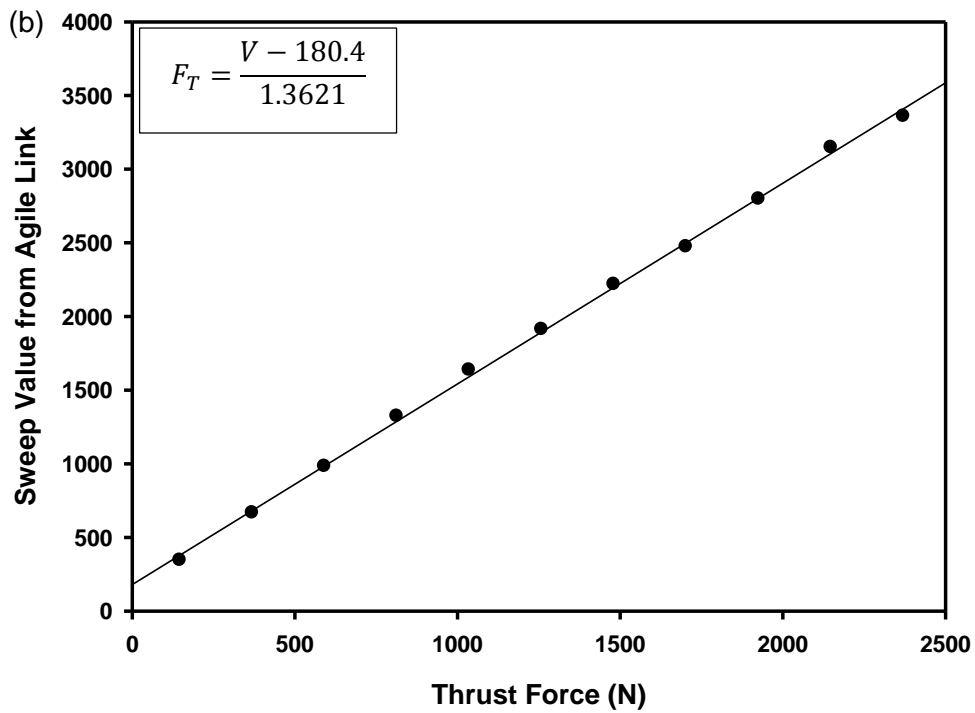
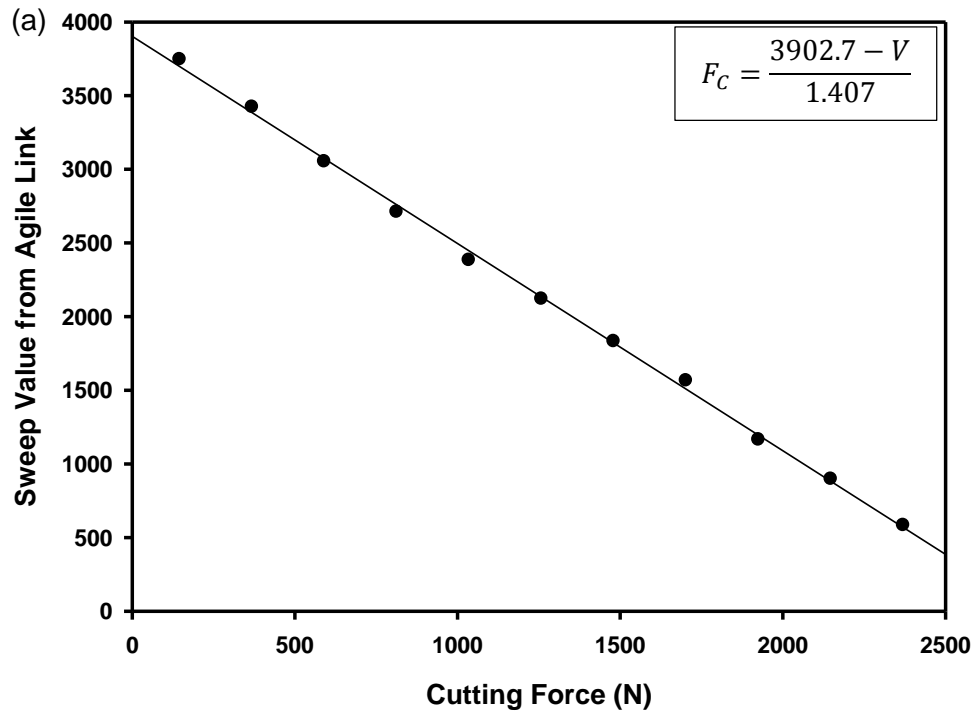


Figure 3.5: Calibration curves of the force sensor in (a) cutting force direction, (b) thrust force direction

3.3 Cryogenic Machining Approach

For cryogenic machining tests, the Ti-6Al-4V workpiece was precooled in a bath of liquid N₂ for at least 15 minutes before the start of the machining process. This was done to ensure that there was a homogenous temperature distribution throughout the sample. The workpiece was then removed from the coolant bath and immediately placed in the 3 jaw chuck for the orthogonal cutting. The tool post and the cutting tool were set in their appropriate positions such that the machining could be performed as quickly as possible to avoid heating-up of the sample.

3.4 Nanolubricant Machining Approach

An alternate approach in this study to improve the machining efficiency of Ti-6Al-4V was by the use of nano-lubricants. Nano-particles act as potential friction modifiers due to their excellent tribological properties by forming a boundary layer between the tool and the workpiece. The study under nanolubricant approach is two fold, (i) Study of tribological behaviour of Ti-6Al-4V material against uncoated WC-Co under different sliding conditions, (ii) Applying this tribological behaviour during orthogonal machining tests. Details of the individual tests are given in the following subsections.

3.4.1 Measurement of Coefficient of Friction

The magnitude of cutting forces generated during orthogonal machining of Ti-6Al-4V with uncoated WC-Co is affected by the friction at the tool-workpiece interface. Sliding friction tests were conducted using a pin-on-disk tribometer to measure the coefficient of friction (COF) values of Ti-6Al-4V pins. Pins with a 4 mm radius made of the same alloy as the workpiece (Ti-6Al-4V) used in orthogonal machining tests, were placed in sliding contact against an uncoated WC-Co disk (same material as the cutting tool used in

orthogonal tests) for 1×10^3 cycles, at a linear speed of 0.12 m/s and a normal load of 5.0 N. The friction sensitivity of the sensor was 1×10^{-3} .

Tests were conducted under dry/unlubricated, MRF and MRF + WS₂ lubricated sliding conditions. The optimum concentration of WS₂ was determined by performing iterative tests with variable concentrations of WS₂ in the MRF. The concentration that resulted in the smallest running-in COF was chosen to be the optimum concentration and this was used for the orthogonal machining tests.

To prevent the problem of agglomeration of nanoparticles, the nanolubricants were freshly prepared just before conducting the experiments. The desired quantity of nanoparticles were added to the MRF and were mechanically stirred and subjected to sonication for 30 minutes to obtain a homogenous distribution of the particles in MRF. This nanolubricant was then used immediately for the sliding experiments.

3.4.2 Orthogonal Machining Tests

To evaluate the role of WS₂ blended MRF in improving the machinability of Ti-6Al-4V, continuous turning tests were conducted with uncoated WC-Co cutting tool under different machining environments, namely dry, normal lubricant (MRF only) and WS₂ blended MRF at various cutting speeds and feed rates. The cutting speeds and feed rates for the tests were chosen such that the chip load factor (product of cutting speed and feed rate) is kept nearly constant for all the tests. Based on the compatibility of the M300 Harrison lathe, the cutting speeds and feed rates that were chosen for the orthogonal tests are shown in Table 3.2.

Table 3.2: Machining parameters for orthogonal tests

Cutting Speed		Feed Rate	Chip Load = Cutting Speed x Feed Rate
RPM	m/min	mm/rev	
370	29.524	0.4	11.810
540	43.089	0.25	10.772
1200	95.754	0.12	11.491

For all the turning experiments, the depth of cut was kept constant at 1 mm. During the lubricated test conditions, the coolant was supplied through two nozzles such that both the rake face and flank face of the cutting tool are cooled simultaneously. The flow rate of the coolant from both the nozzles combined was 30 mL/s and was supplied by a motor with a rated output power of 1/8 hp.

3.4.2.1 Measurement of Cutting Zone Temperature:

In metal cutting, the heat generated on the cutting tool is critical for determining the tool life. The temperature in the cutting zone depends on the mechanical and thermal properties of the workpiece material, coefficient of friction at the tool-workpiece interface and machining parameters such as cutting speed, feed rate and depth of cut [94]. In this experimental work, a K-type thermocouple with a temperature range of $-200\text{ }^{\circ}\text{C}$ to $1100\text{ }^{\circ}\text{C}$ was used for measuring the cutting zone temperature. The standard error in temperature measurement for a K-type thermocouple is $\pm 5\%$. The thermocouple was connected to the same data acquisition system as that of the force sensor to obtain a continuous stream of data. A 0.8 mm diameter hole was drilled on the cutting tool to an arbitrary depth such that the thermocouple could be housed reasonably close to the cutting edge as shown in Figure 3.6 (a-b). A thermally conductive paste was applied on the thermocouple to minimize the error in temperature measurement. Before using the thermocouple for the orthogonal tests,

it was first calibrated within the temperature range that would be observed in this study. The thermocouple connected to the data acquisition system produces electrical signal proportional to the temperature of the environment it is kept in. To calibrate the thermocouple, a furnace was heated to different temperatures ranging from 200 to 1000 °C. Once the desired temperature was obtained in the furnace, the thermocouple was placed in this furnace and the corresponding voltages were obtained from the Agile Link software. The relationship between voltage and temperature were plotted and they were found to be linear. The calibration curve and their relationship is shown in Figure 3.7.

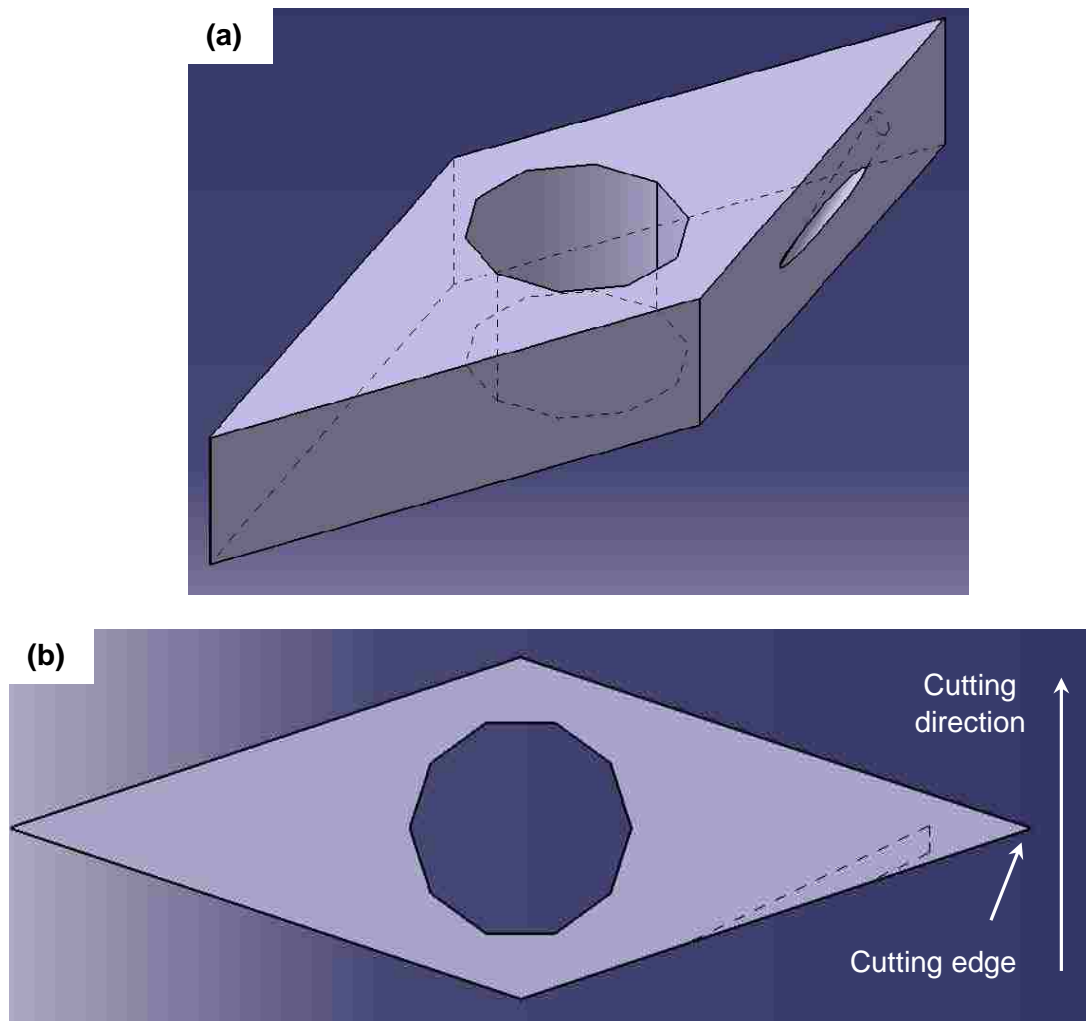


Figure 3.6: (a) An isometric view of the modifications made in the cutting tool for housing the thermocouple during continuous cutting of Ti-6Al-4V, (b) A top view of the cutting tool showing the depth of the hole for the thermocouple, and its proximity to the cutting edge

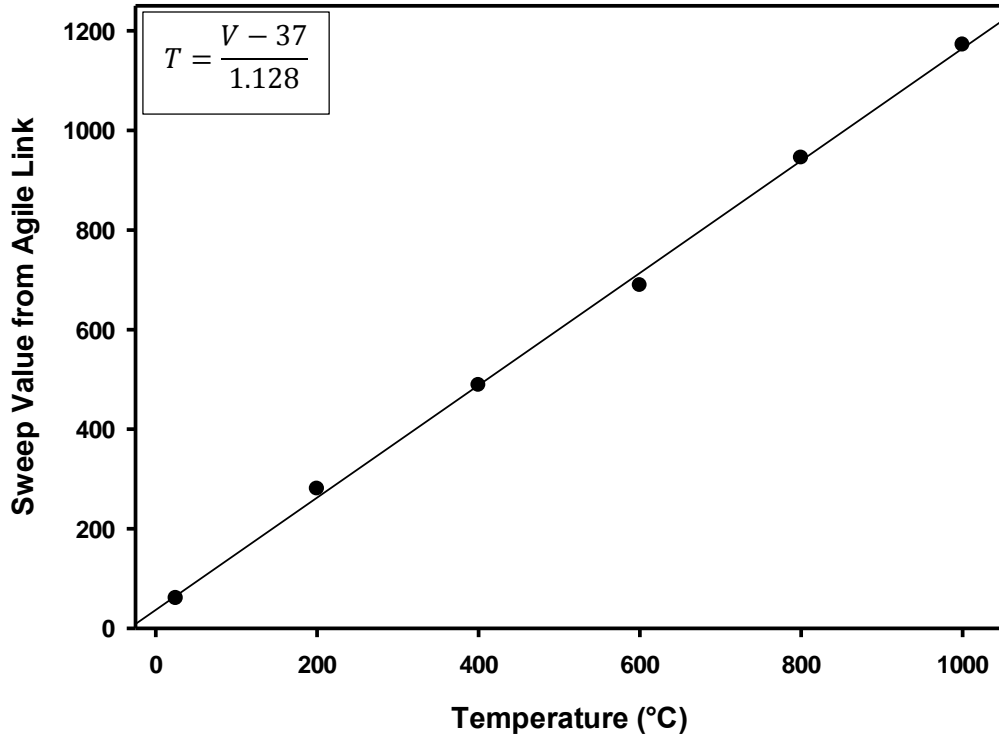


Figure 3.7: Calibration curve for the thermocouple used during continuous turning of Ti-6Al-4V

3.5 Surface Roughness Measurements

The surface morphologies of the machined surface were observed using a non-contact, optical surface profilometer (WYKO NT 1100), which was used in the vertical scanning interferometry (VSI) mode to determine the three-dimensional elevation of surface profiles and hence, the average (R_a) and root mean square (R_q) surface roughness values.

The WYKO NT1100 provides high resolution, 3D surface measurement capability, from sub-nanometer roughness to millimeter-high. Advanced optics ensures sub-nanometer vertical resolution at all magnifications. The Vertical Scanning Interferometry (VSI) mode was used in this study instead of the Phase Shifting Interferometry (PSI) mode due to the higher roughness of the machined surface. The basic interferometric principles

are similar in both the techniques. However, in VSI mode, the white-light source is filtered with a neutral density filter, which preserves the short coherence length of the white light, and the system measures the degree of fringe modulation, or coherence, instead of the phase of the interference fringes.

3.6 Metallography

Chips obtained after machining were mounted with epoxy so that they stood on their edge in order to make the cross-section after polishing straight across its length. The samples were prepared using the standard metallographic preparation techniques. Final polishing was performed using a 0.10 μm diamond suspension. They were then ultrasonically cleaned in ethanol and etched using Kroll's reagent (6 parts of HNO_3 + 2 parts of HF + 92 parts of water) for 20 seconds. A scanning electron microscope was used to observe the deformation in the chips.

3.7 In-situ Machining Experiments

The mechanisms of chip formation under cryogenic conditions were observed using an in-situ setup that is comprised of a 3-jaw chuck lathe where the work piece was placed, and an optical microscope to observe the cutting process. The cutting tool was made to contact with the outer surface of the cylindrical workpiece so that the cutting zone ahead of the tool tip was observed on the flat surface of the workpiece as shown in Figure 3.8. A Proscope HR2 digital microscope was used for acquiring images of chip formation during real time orthogonal machining. The HR2 microscope had an 8.5 mm long high resolution 2 MP color sensor with a 200x magnification lens.

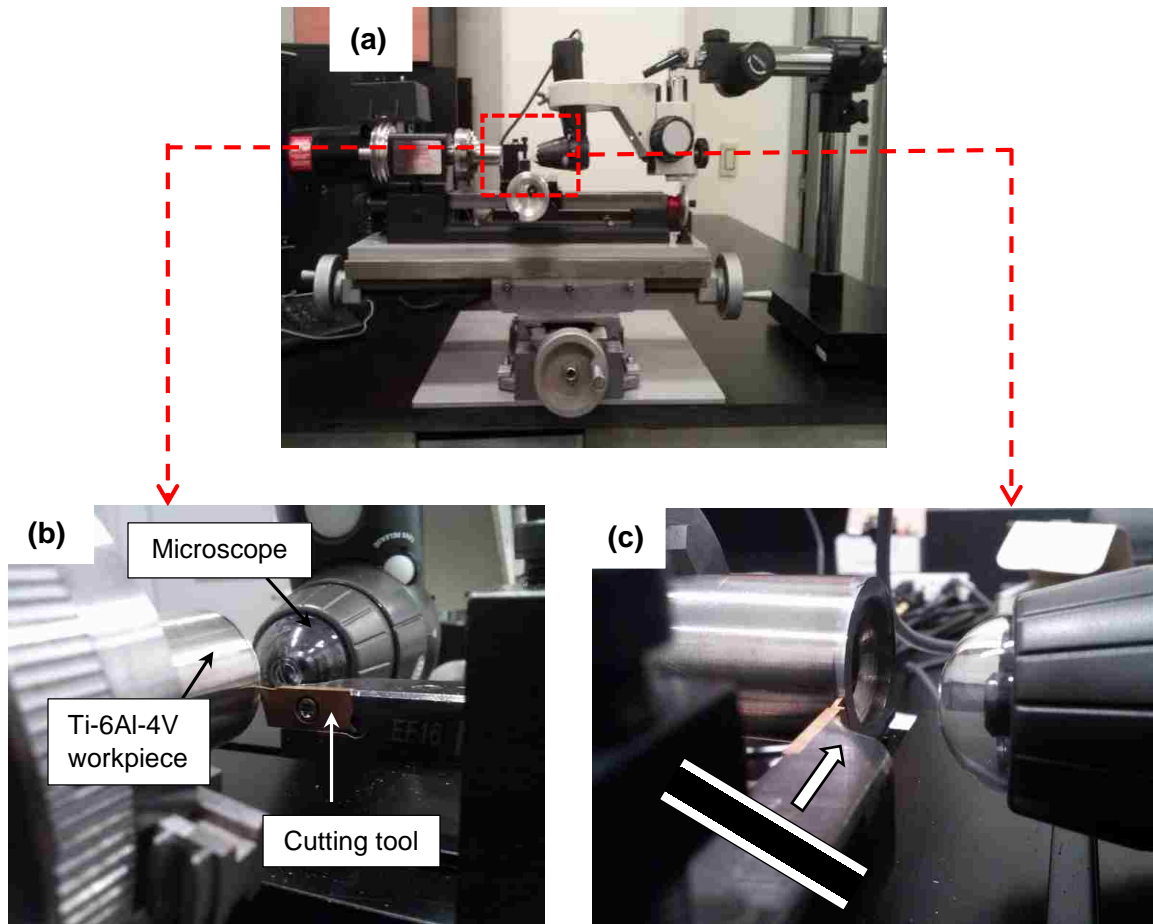


Figure 3.8: (a) Overview of the experimental setup for in-situ machining of Ti-6Al-4V, (b, c) Close up view of the setup showing the cutting tool, feed direction, and the microscope in the sample plane of view as the workpiece

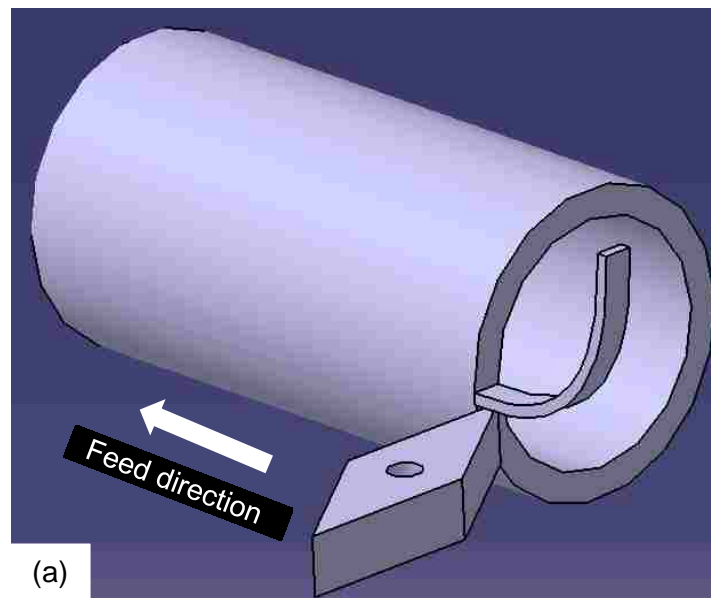
The machining operation was carried out at a cutting speed of 0.05 m/min as Ti-6Al-4V alloys exhibit serrated chip formation over a range of speeds [13]. The cutting process produced serrated chips under ambient machining conditions, and thus the experiment is deemed suitable for observation under cryogenic machining condition as well.

Ti-6Al-4V samples were machined at a constant speed of 0.05 m/min and a feed of 0.06 mm both under ambient and cryogenic temperatures. For cryogenic testing, the sample was precooled in a bath of liquid N₂ for 20 minutes before machining, and then immediately tested for a duration of 20 seconds. The sequence of events leading to serrated chip

formation were observed during this time period. The machined samples from ambient and cryogenic tests were then examined under a SEM to observe the differences in chip characteristics.

3.8 Differences in Cutting Geometries between In-situ and Conventional Machining

The differences in experimental setup for the in-situ and high speed machining setup is shown in Figure 3.9. The primary difference is in the direction of cutting, or feed direction. In the in-situ experiments, the feed is towards the diameter of the extruded rod or along the circumference of the workpiece, while in conventional machining, the feed is along the face/ periphery of the workpiece. The in-situ experiment is setup such that the cutting tool and the workpiece could be brought in the same plane while focusing with the Proscope microscope as shown in Figure 3.8.



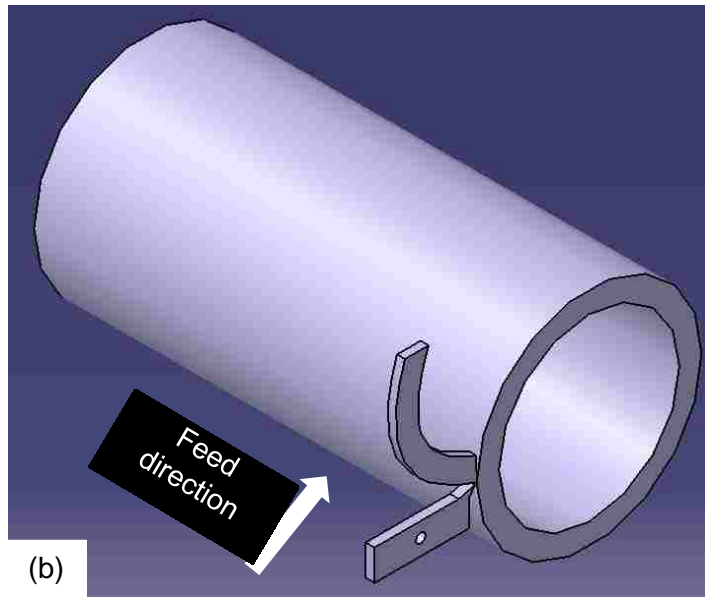


Figure 3.9: 3D models to illustrate the difference between (a) conventional machining, and (b) in-situ machining

Chapter 4

EXPERIMENTAL RESULTS

The role of cryogenics in influencing chip segmentation and the effect of nanoparticles in influencing COF at the tool – workpiece interface were investigated. Of particular interest was the study of toughness and fracture surfaces of Ti-6Al-4V tested at cryogenic temperatures which could explain the correlation between temperature and chip segmentation behaviour. In addition, a comparative study was undertaken by performing quantitative analyses on the chips obtained during ambient and cryogenic machining conditions. Pin-on-disk experiments were conducted under different sliding environments to examine the role of nanoparticles in influencing COF. All these results are presented in this chapter.

4.1 Conventional Orthogonal Machining of Ti-6Al-4V – Ambient and Cryogenic Conditions

Conventional or high speed machining of Ti-6Al-4V was carried out on a Harrison M300 lathe at a constant speed and feed rate of 43 m/min and 0.15 mm/rev under ambient and cryogenic conditions to simulate a real time machining process as described in section 3.2. The role of cryogenic machining in influencing chip segmentation can be studied by a quantitative driven microstructural study. Thus the chips obtained from the orthogonal machining were subject to metallographic analyses as described in section 3.6. In addition, the cutting and feed forces generated under ambient and cryogenic conditions were plotted. All these results are presented in this section.

4.1.1 Measurement of Forces during Orthogonal Machining

Cutting and feed forces were measured using the force sensor assembly as described in section 3.2.3. These forces were then used to analytically calculate the resultant and shear forces.

The average cutting and feed forces were calculated from the time range when the workpiece was in direct contact with the cutting tool. The duration of each test is approximately 1.4 to 1.6 seconds. Under dry machining conditions, the magnitude of average cutting force was 750 ± 56 N, while under cryogenic conditions, the average cutting force slightly reduced to 700 ± 34 N. The resultant ' F_R ' and shear force ' F_S ' under each condition was calculated using the relations,

$$F_R = (F_c^2 + F_f^2)^{1/2} \quad (4.1)$$

$$F_S = F_c \cos \phi - F_f \sin \phi \quad (4.2)$$

where ' F_c ' and ' F_f ' are the cutting and feed forces respectively, ϕ is the shear angle as defined in Figure 2.6.

The resultant force was found to be higher than all the other forces for both machining conditions. However, the resultant force was lower for the cryogenic condition compared to dry condition. A similar trend was observed for the shear force as well.

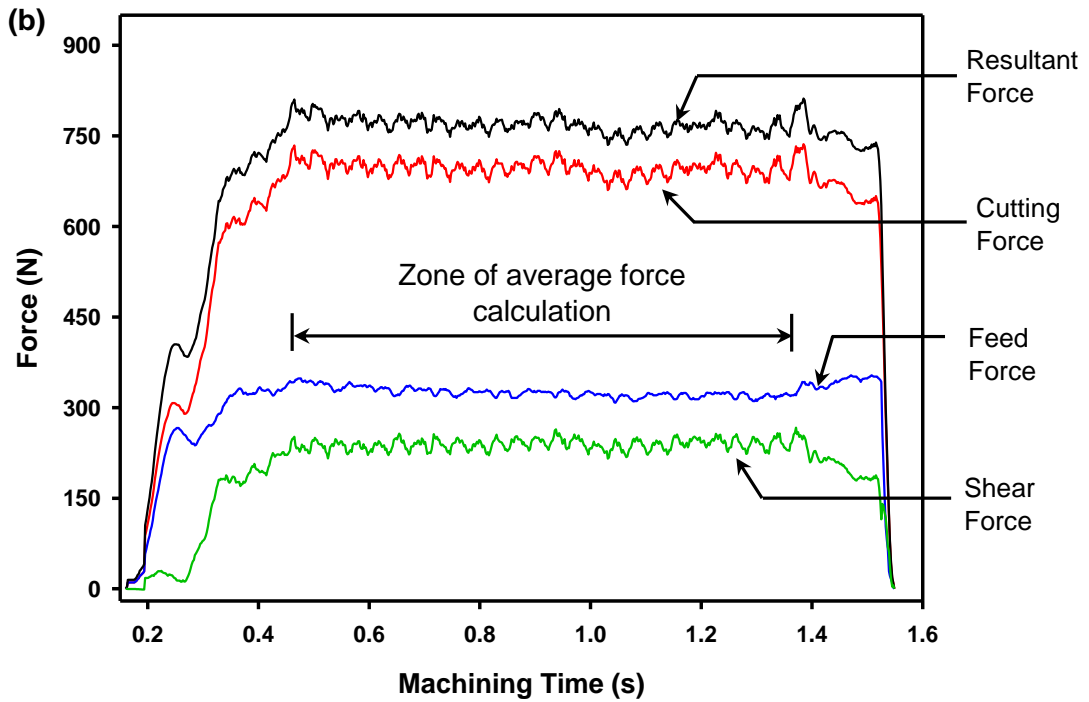
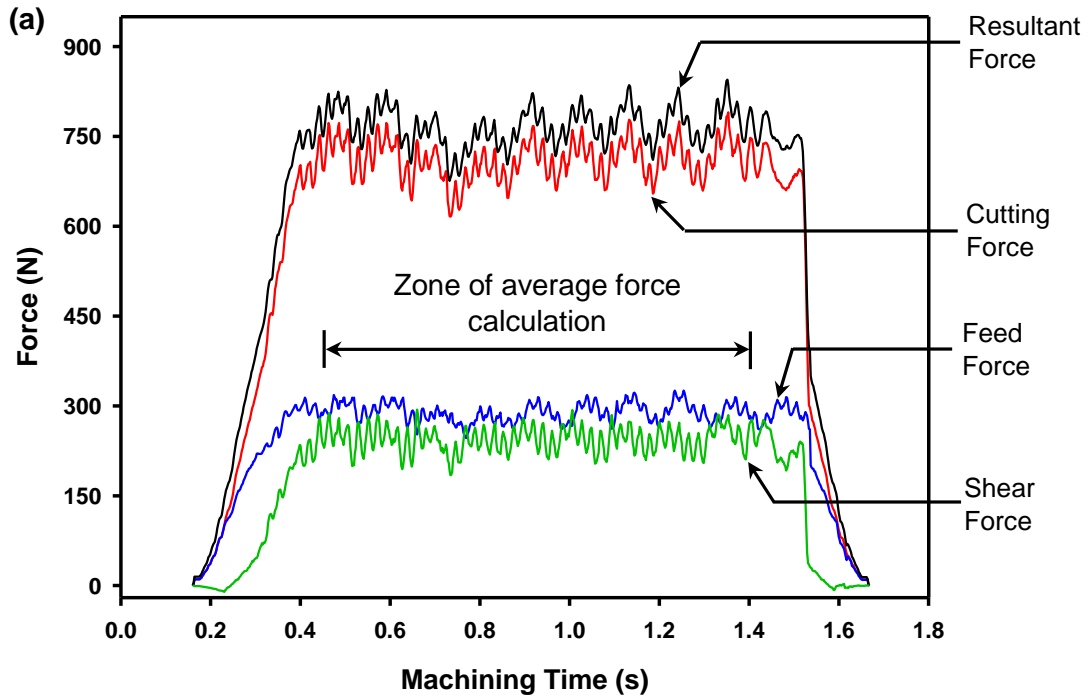


Figure 4.1: Variation of cutting, feed, resultant and shear forces during orthogonal machining of Ti-6Al-4V under (a) ambient, and (b) cryogenic machining environments

4.1.2 Quantitative Analyses of Chip Morphology

Chips obtained after machining were mounted with epoxy so that they stood on their edge in order to make the cross-section after polishing straight across its length. The polished chips were then examined under an inverted optical microscope (Zeiss Axio vert A1) to obtain their microstructures. Figure 4.2 (a-b) show the microstructure of the chips obtained under ambient and cryogenic machining conditions, respectively. A systematic quantitative analysis is useful for characterizing and distinguishing the differences between the chips obtained from both the machining conditions.

4.1.2.1 Chip Thickness

Serrated chips exhibit a maximum and minimum chip thickness. The measurements are recorded by measuring the perpendicular distance between the rake face and the highest point in the case of maximum chip thickness, and lowest point in the case of minimum chip thickness. In each case, measurements were taken by analysing approximately 55 to 60 chips. From Table 4.1, it can be observed that the maximum chip thickness obtained under dry machining conditions was higher than under cryogenic condition. A similar trend was observed for the minimum chip thickness as well.

The average chip thickness was taken to be half the sum of the maximum and minimum chip thickness. The average chip thickness was found to be lower under cryogenic condition than under ambient machining condition. The magnitude of the average chip thickness was measured to be $107.8 \pm 5 \mu\text{m}$ under cryogenic environment, while under dry condition it was $158.3 \pm 13.8 \mu\text{m}$.

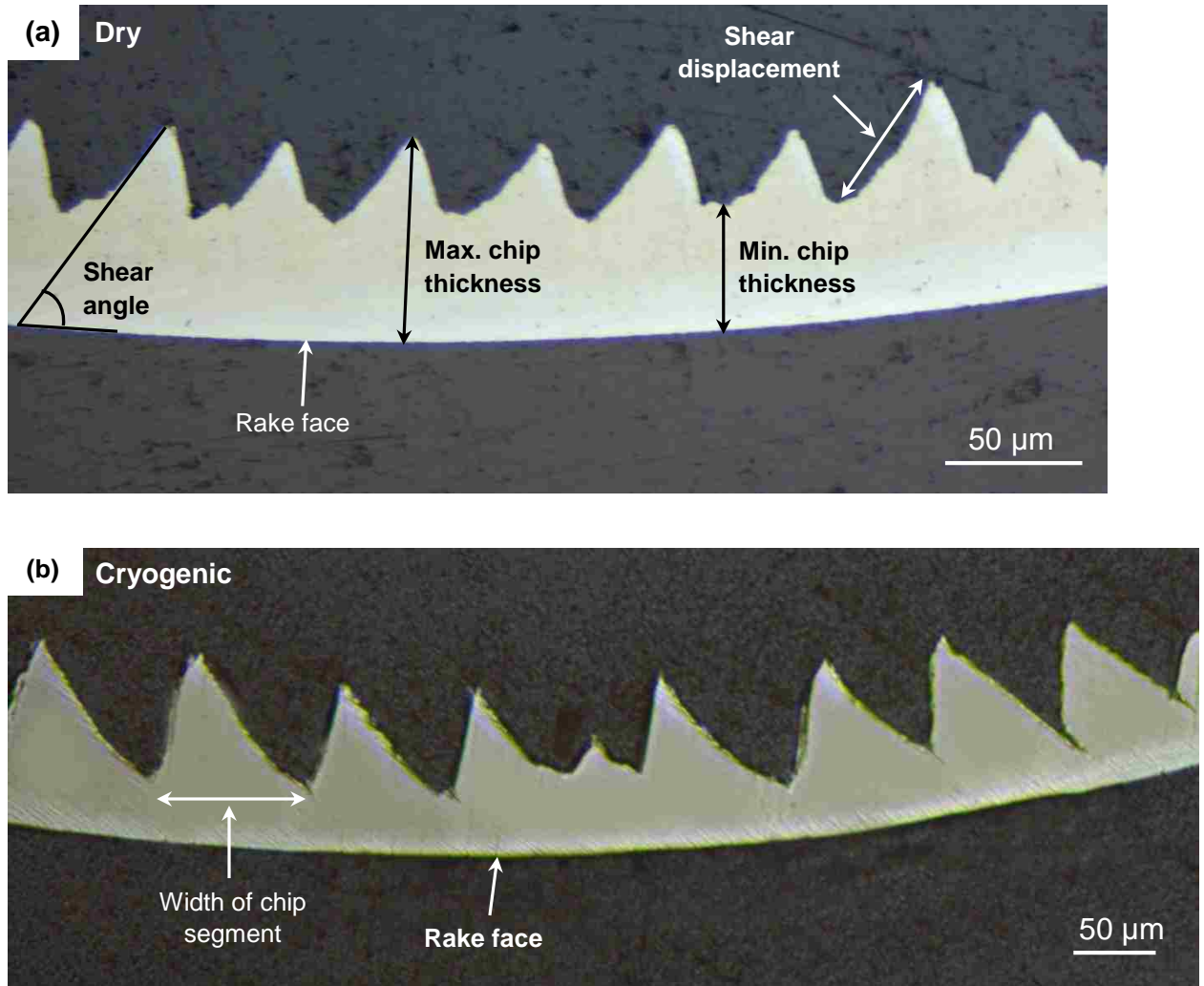


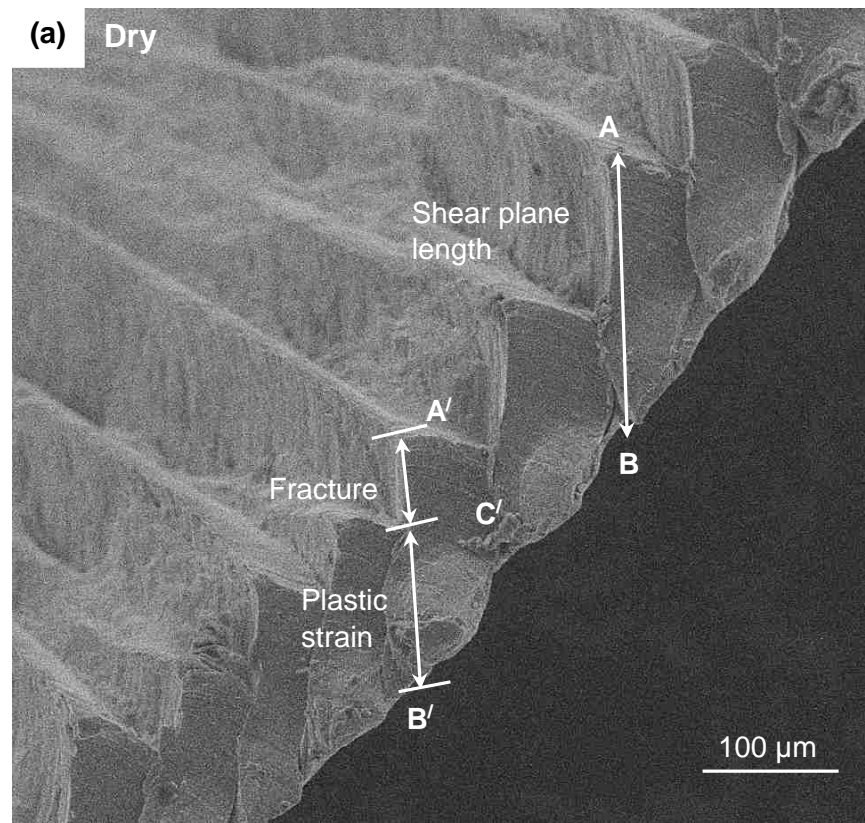
Figure 4.2: (a) Optical microstructure of chips obtained during dry machining of Ti-6Al-4V showing the closely spaced chip segments, (b) Optical microstructure of chips obtained during cryogenic machining of Ti-6Al-4V showing broader chip segments with cracks between successive chip segments. The method adopted to measure the various chip parameters are also indicated

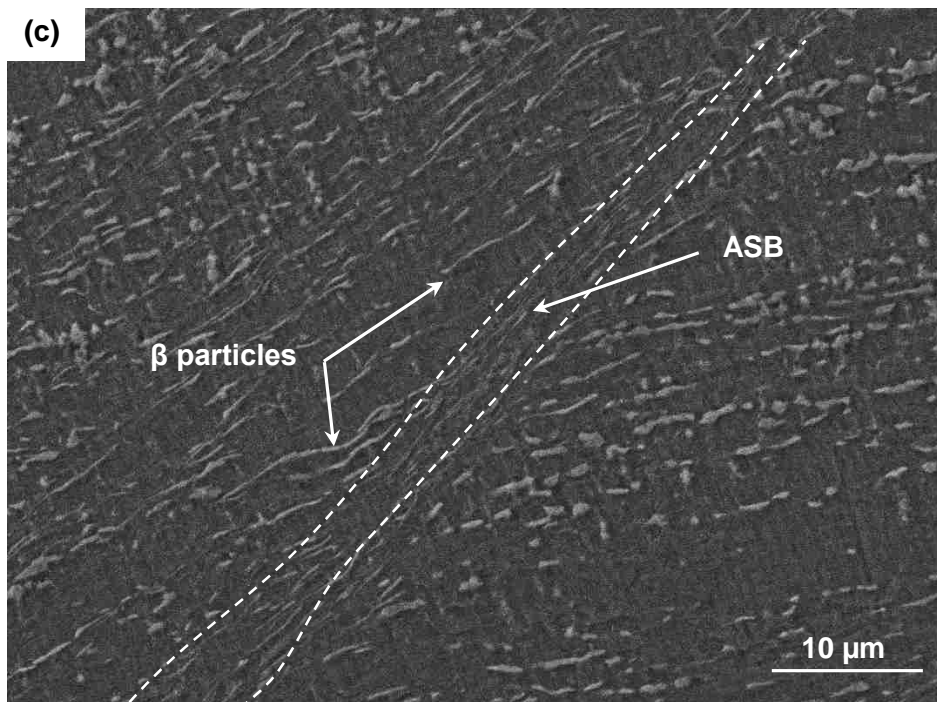
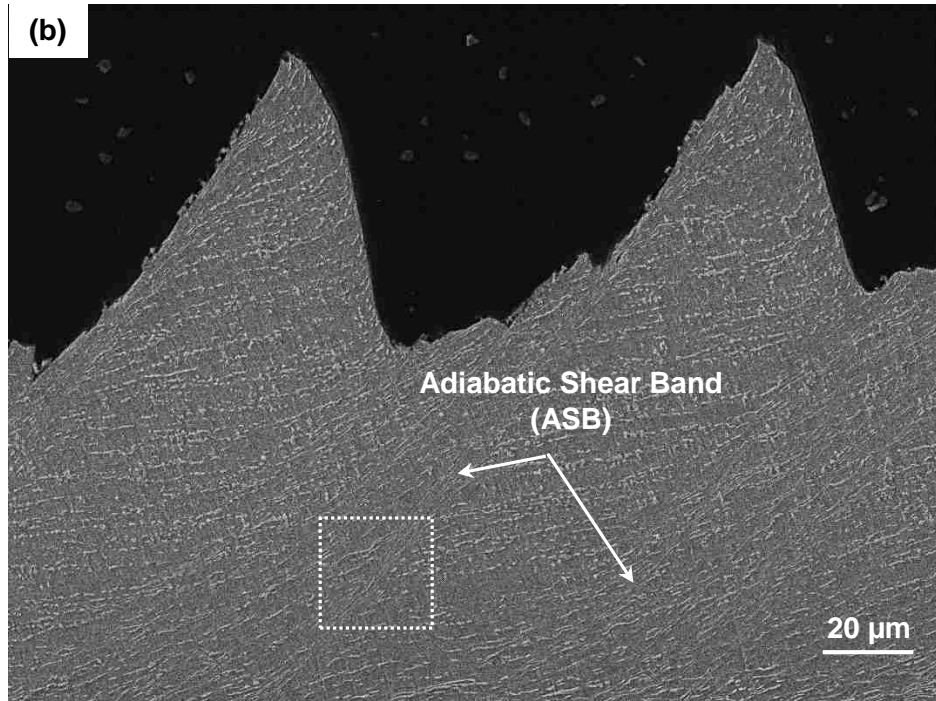
4.1.2.2 Shear Displacement

Shear displacement is the distance by which a chip segment has displaced itself from the immediate successive chip segment during serrated chip mechanism. The method adopted in this work to measure the shear displacement is shown in Figure 4.1 (a). The shear displacement during dry condition was measured to be $127.9 \pm 11.4 \mu\text{m}$ while that under cryogenic condition was measured to be $147.9 \pm 15.1 \mu\text{m}$. The shear plane length is

shown as length AB in Figure 4.2 (a). It represents the maximum length of deformation a material undergoes while forming a segment. The chip segments remain attached to each other over a portion of length shown as B/C'. Over this length, plastic strain is localized into adiabatic shear bands (ASB). Highly deformed grains in a region between the segments, and the ASB, are shown in Figures 4.3 (b - c).

The formation of shear localized chips observed during metal cutting [9], [12 – 14], [97] is governed by an instability criterion developed by Recht [97]. The shear instability caused by the material flow in the ASB as shown in Figure 4.2 (c) eventually causes separation of the chip segments [13]. A schematic of the typical chip produced during dry cutting of Ti-6Al-4V illustrating the shearing of successive chip segments resulting in formation of ASB is shown in Figure 4.2 (d).





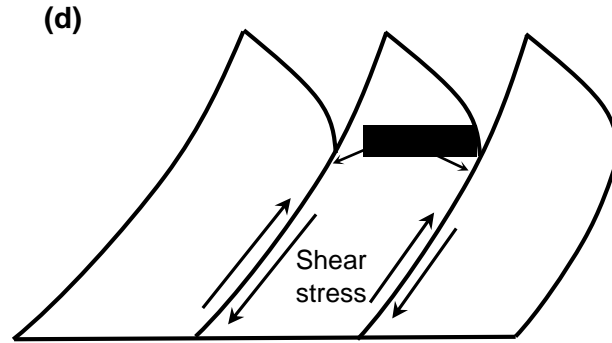


Figure 4.3: (a) SEM of chip segments obtained during dry machining of Ti-6Al-4V indicating the steps involved in a chip formation in SEI mode, (b) Microstructure of the chip after etching with Kroll's reagent showing the shear localization in SEI mode, (c) Higher magnification of the zone marked by a white box in (b) showing the adiabatic shear band and β particles in SEI mode, (d) Schematic representation of a chip obtained from dry machining condition illustrating the formation of adiabatic shear bands (ASB) due to intersegment shearing

Flow localization resulting in formation of shear bands were also observed during cryogenic machining of Ti-6Al-4V [35], [62], [95], [96]. Micrograph of a typical chip obtained during cryogenic machining of Ti-6Al-4V is presented in Figure 4.3 (a). It is observed that the segments are attached over a very small part of the shear plane length but are separated over a large part of the shear plane length as schematically illustrated in Figure 4.3 (b). This implies that the contribution of fracture is very high in the chip segment formation under cryogenic temperatures. The mechanical property that influences fracture of a material – toughness, is later discussed in Section 4.1.5 to explain the reasons for prominent chip fracture at cryogenic temperatures.

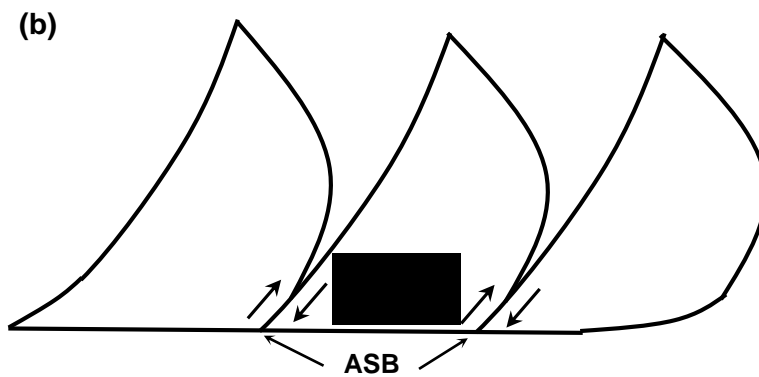
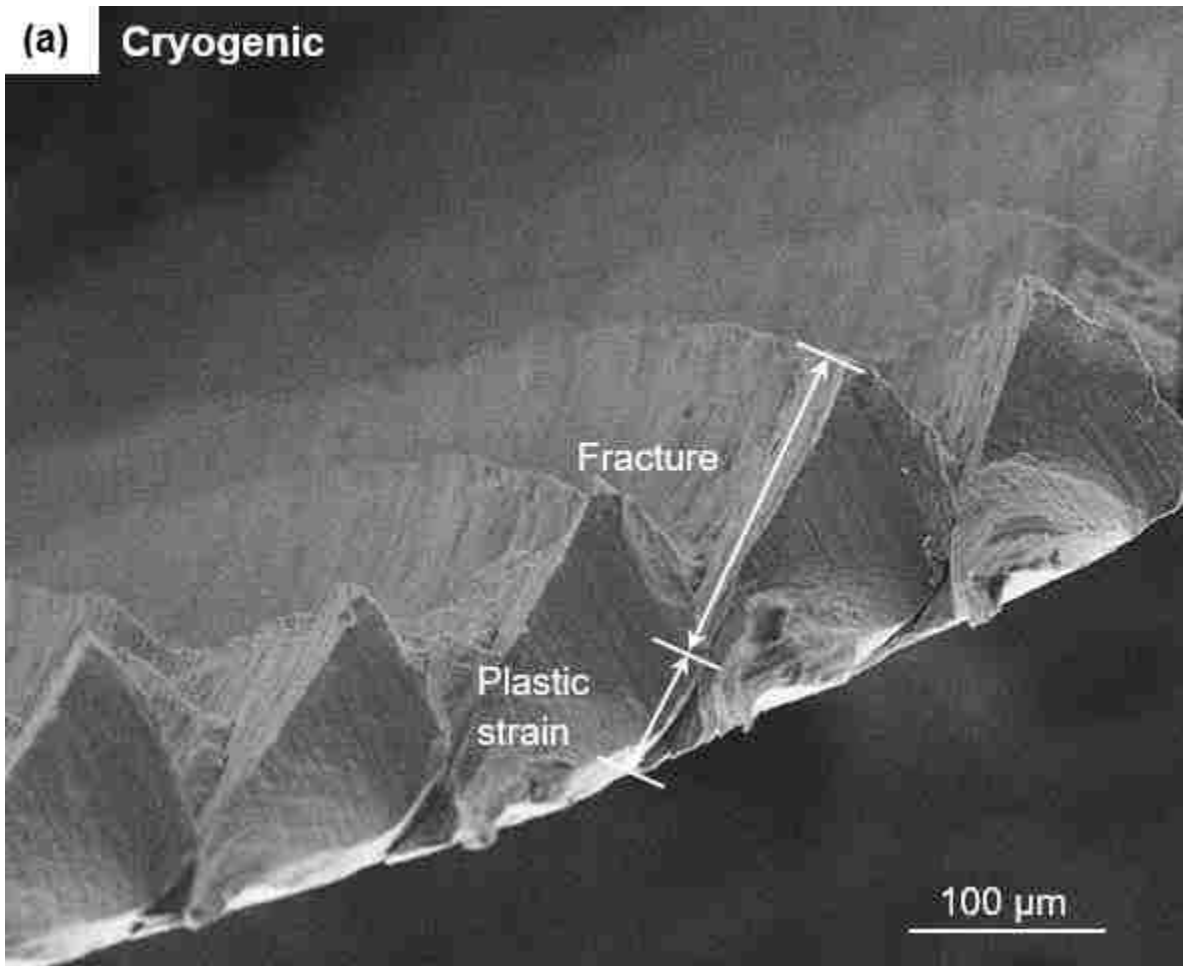


Figure 4.4: SEM of chips obtained from cryogenic machining of Ti-6Al-4V showing a typical chip formed under low temperatures in SEI mode, (b) Schematic representation of a chip obtained from cryogenic machining condition showing easier fracture between chip segments compared to the chips obtained from dry machining condition

4.1.2.3 Shear Angle

The calculation of shear force and other parameters such as chip velocity, velocity in the shear direction etc., require the magnitude of the shear angle. Thus it was measured accurately from the microstructure as shown in Figure 4.2 (a). Though an appreciable difference in the value of shear angle was not achieved, the average magnitude of shear angle under cryogenic condition was found to be lower than in dry machining condition. The value of the shear angle was measured to be $49.3^\circ \pm 1.2^\circ$ under dry environment while that under cryogenic was measured to be $46.9^\circ \pm 1.0^\circ$.

4.1.2.4 Width of chip segment

The width of chips is a measure of the frequency of chip segmentation [4]. Chips formed under cryogenic conditions are known to exhibit lower plastic deformation within the chip segment compared to chips from ambient conditions [96]. The average width of a chip segment under dry condition was $127.5 \pm 14.3 \mu\text{m}$ while that under cryogenic condition was $143.3 \pm 7.6 \mu\text{m}$. Thus it is conceivable that chip segmentation was more prominent under cryogenic condition compared to dry machining condition.

4.1.2.5 Lateral Displacement of Chip Segments

The lateral displacement between chip segments was measured for both the cryogenic and dry machining conditions. Under dry conditions, it was observed that there was no separation between the chip segments. However, the chips obtained under cryogenic machining conditions showed an average lateral displacement of $19.9 \pm 3.4 \mu\text{m}$. SEM of the chips (SEI mode) obtained under both the machining conditions are shown in Figures 4.5 (a - b).

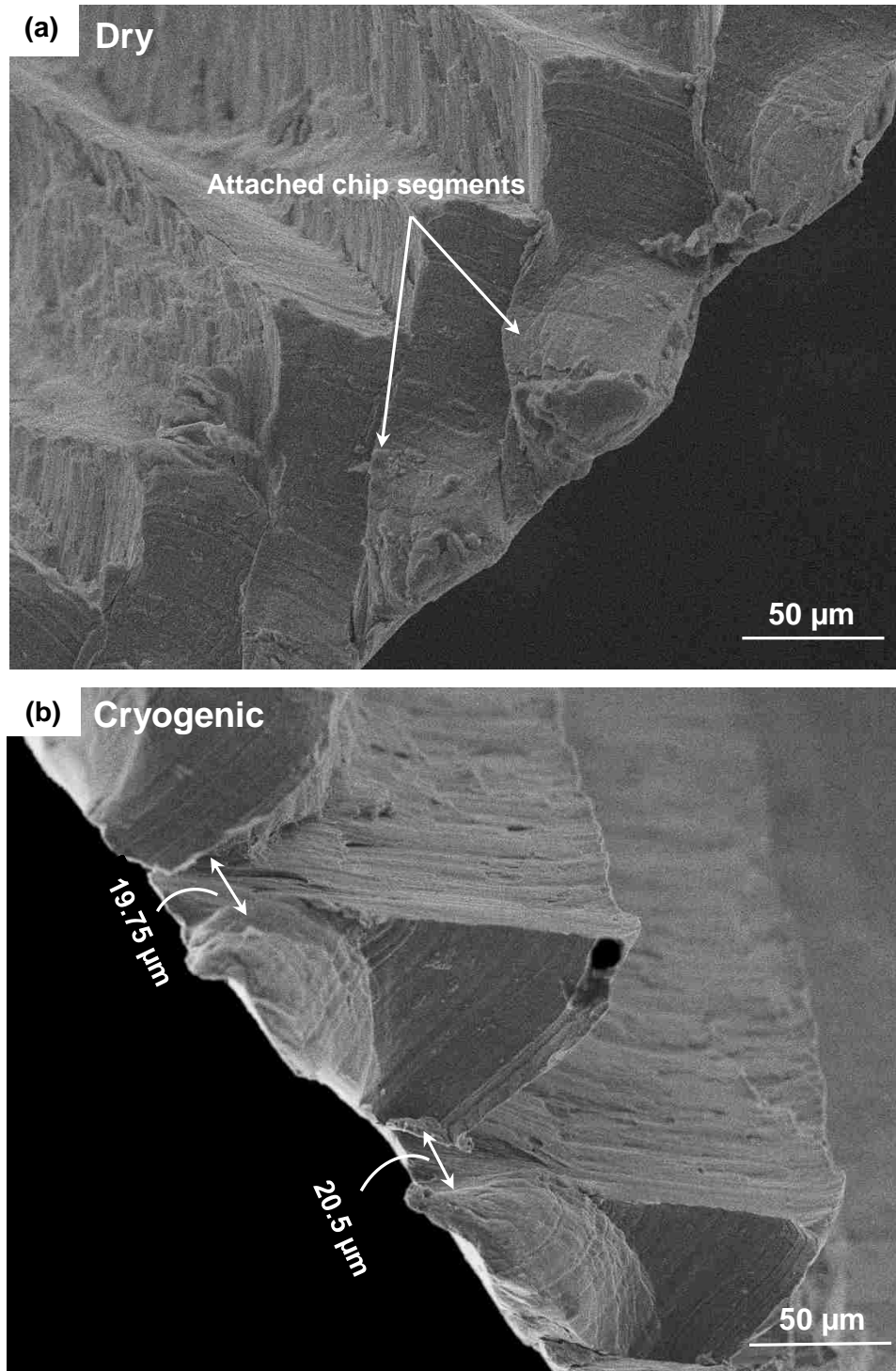


Figure 4.5: SEM of chip segments obtained during (a) dry, (b) cryogenic machining of Ti-6Al-4V alloy. The chips obtained under cryogenic machining conditions show a lateral displacement as against the chips from dry conditions that are seized together

Table 4.1: Chip parameters under ambient and cryogenic machining conditions

Chip parameter/ machining condition	Ambient machining	Cryogenic machining
Maximum chip thickness	204.40 ± 9.91 μm	155.11 ± 11.33 μm
Minimum chip thickness	112.20 ± 17.08 μm	60.48 ± 3.71 μm
Average chip thickness	158.30 ± 13.79 μm	107.80 ± 5.03 μm
Shear displacement	127.91 ± 11.35 μm	147.85 ± 15.05 μm
Normalized shear displacement (Shear displacement/ Maximum chip thickness)	0.63 ± 0.08	0.89 ± 0.14
Shear Angle	49.29° ± 1.23°	46.89° ± 1.02°
Width of chip segment	127.47 ± 14.30 μm	143.25 ± 7.58 μm
Lateral displacement of chip segments	–	20.2 ± 3.4 μm
Percentage of completely separated chip segments in the complete population	1.62%	14.52%

4.1.3 Fracture Surface Morphology

In addition to examining the lateral section of the chip for quantitative analyses, the fracture surfaces of the serrated chips from cryogenic machining were also observed. For better visualization, a low magnification SEM of the fracture surface is presented in Figure 4.6 (a) which indicates all the regions of interest. To study the behaviour of the fracture surface, a higher magnification SEM was performed in the region indicated in Figure 4.6 (a). Figure 4.6 (b) shows that the fracture was due to the presence of shear failure rather than the traditional ductile-brittle failure. A more detailed analyses of the fracture mechanisms and fracture toughness variations with temperature is presented in section 4.1.5.

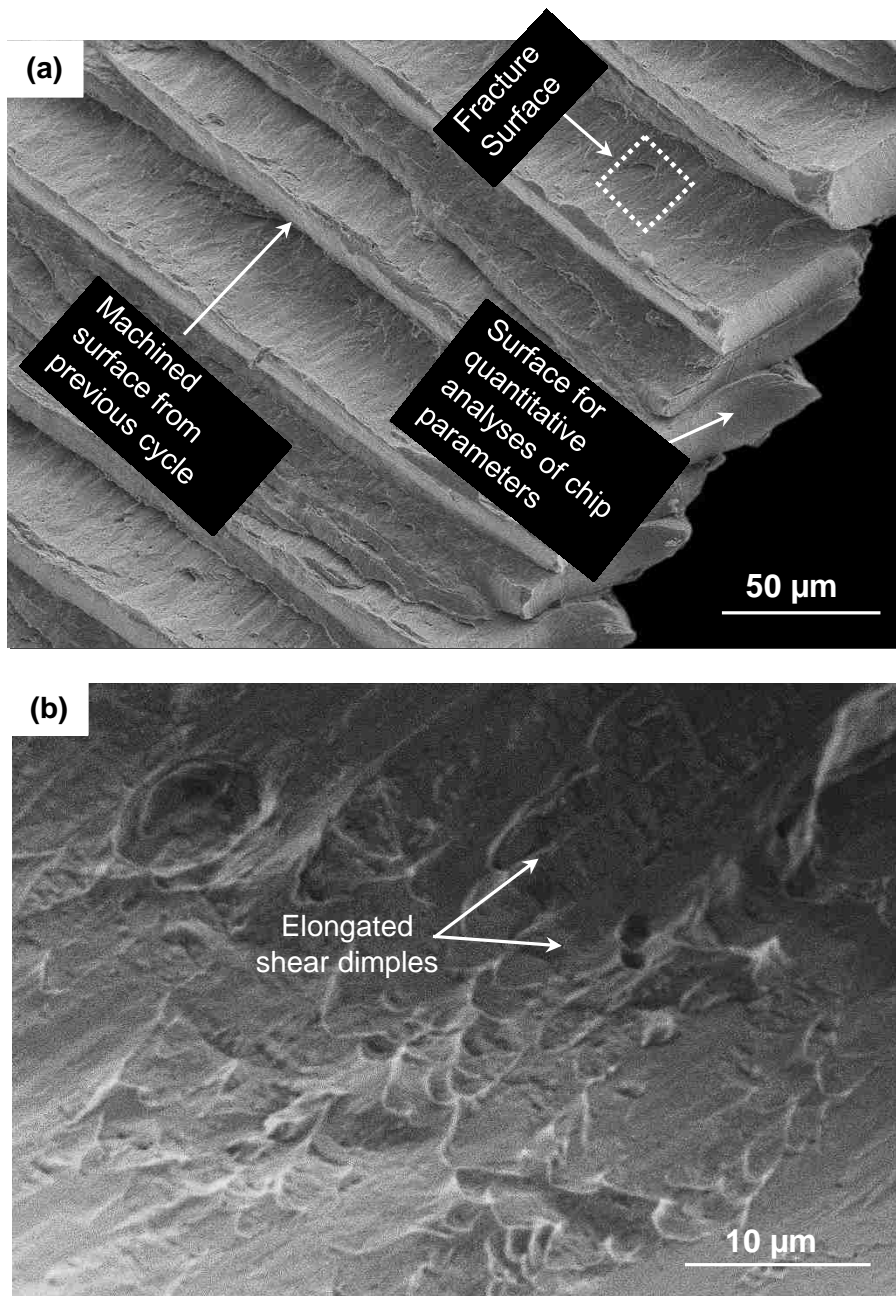


Figure 4.6: Low magnification SEM of fracture surface of chip segments obtained from cryogenic machining of Ti-6Al-4V indicating all the regions of interest, (b) High magnification SEM of fracture surface showing elongated shear dimples. The white box indicates the location where the high magnification SEM image was taken

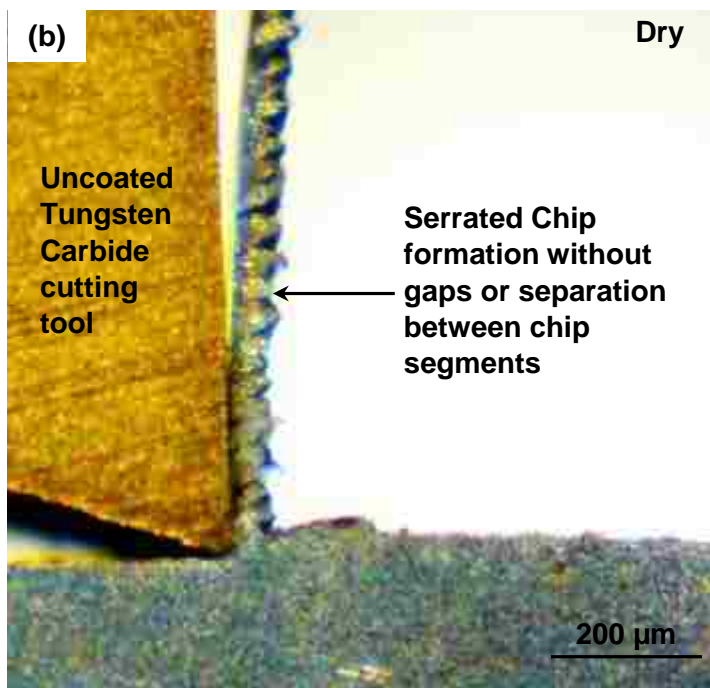
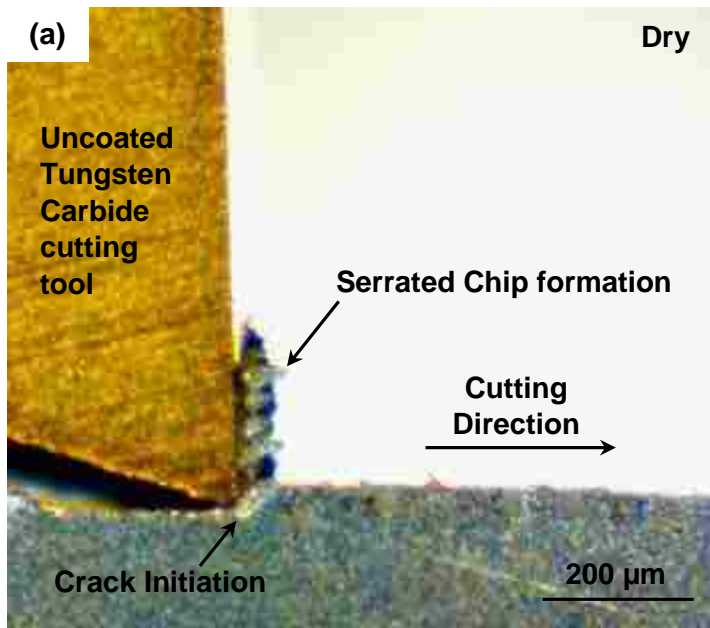
4.1.4 Microstructural Interpretation of Serrated Chip Formation

As discussed in section 3.7, in-situ machining of Ti-6Al-4V was carried out under very low speeds to capture the serrated chip formation in real time. Microstructural observation of the chip formation during in-situ machining of Ti-6Al-4V under ambient

and cryogenic environments is presented in Figures 4.7 (a-c). Strain localization and fracture events leading to serrated chip formation were observed. The first stage of chip formation under the ambient condition involved plastic instability, as a result of the opposing effects of thermal softening and strain hardening, leading to strain localization along a shear surface as indicated in Figure 4.7 (a). Recht [97] developed a criteria for materials that are affected by temperature and strain rate. The instability as proposed by Recht is governed by the equation,

$$\frac{d\tau}{d\varepsilon} = \frac{\partial\tau}{\partial\varepsilon} + \frac{\partial\tau}{\partial T} \cdot \frac{dT}{d\varepsilon} \quad (4.3)$$

This shear surface originated from the tool tip almost parallel to the cutting velocity vector (cutting direction) and gradually curved with the concave surface upwards until it met the free surface. This process repeated itself as strain becomes localized in the next chip segment as shown in Figure 4.7 (b). These observations are in good agreement as reported in [2], [13]. A high magnification SEM image (SEI mode) of the typical chips obtained from dry machining of Ti-6Al-4V is shown in Figure 4.7 (c).



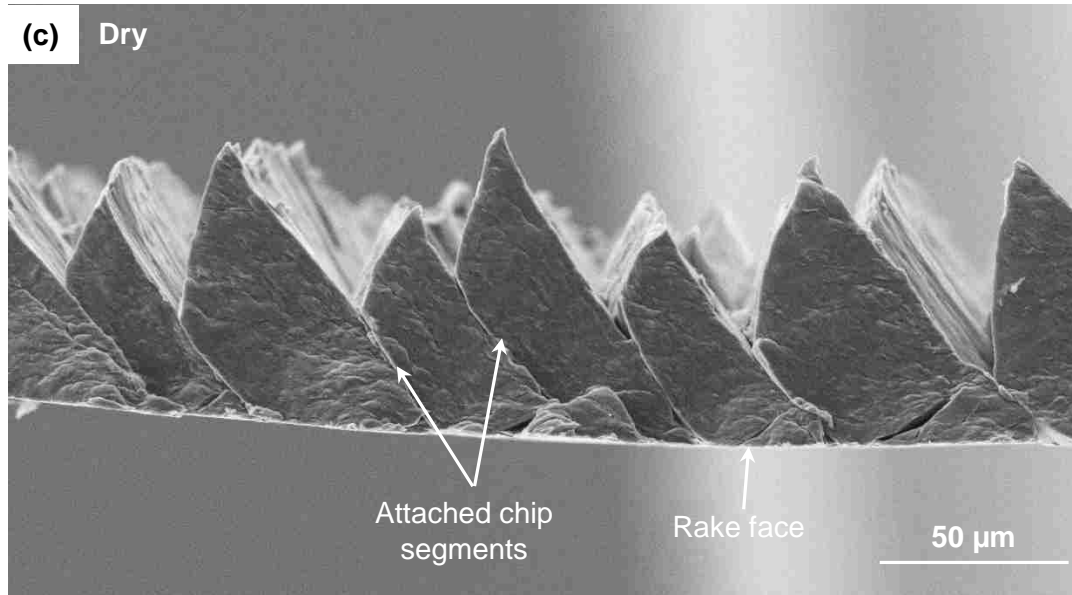


Figure 4.7: Microstructural observation during orthogonal cutting of Ti-6Al-4V under ambient conditions (a) showing crack initiation during chip formation, (b) showing serrated chip formation without gaps between chip segments, (c) High magnification SEM (SEI mode) of typical chips obtained from dry machining showing the attached chip segments

The mechanism of strain localization distinguishes serrated chip segments from continuous chip segments. To understand the concept of formation of a continuous chip segment, in-situ machining of AA6061 material was carried out under the same conditions as explained in section 3.7. The sequence of events leading to a continuous chip formation is shown in Figure 4.8 (a-d).

From Figure 4.8 (a), a small plastic zone is formed just ahead of the tool tip. With further tool advancement, it can be observed from Figures 4.8 (b-c) that the plastic zone increases in size. Finally the chip separated from the deformed zone and a continuous chip segment was obtained. The large size of the plastically deformed zone shows that there was no localization of strain, rather deformation was homogenous throughout the chip. This is in agreement with previously reported work. [14]

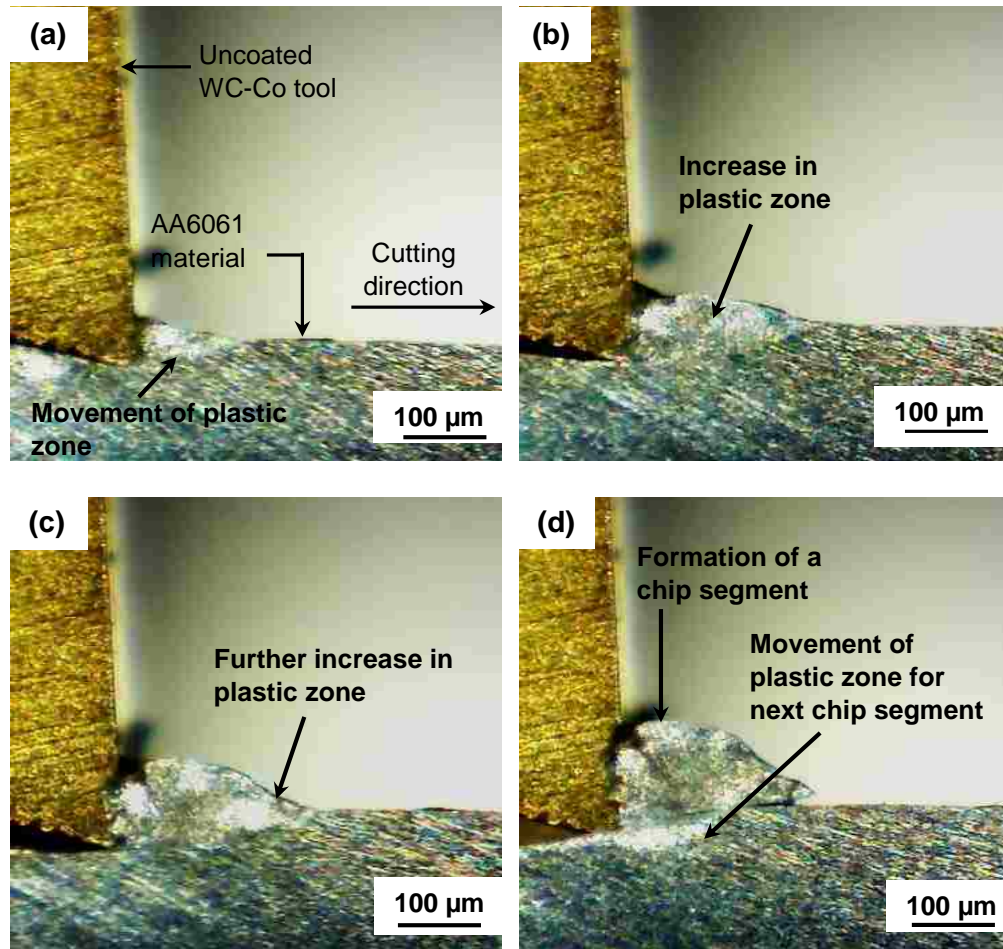


Figure 4.8: Sequential microstructural observation of continuous chip formation during in-situ machining of AA6061 where (a) Shows the initiation of a plastic zone just ahead of the tool tip, (b, c) shows increase in plastic zone size due to advancement in tool, (d) Formation of a chip segment separating from the deformed zone and the formation of a new plastic zone for the next chip segment

Serrated chip formation observed under pre-cooled cryogenic conditions shown in Figure 4.9 (c) closely resembled that under ambient machining conditions but with a principal difference. Under cryogenic conditions, chip fracture or cracks between successive chip segments was more prevalent resulting in higher chip segmentation. Chip morphology and segmentation play a predominant role in determining machinability and tool wear during the machining of titanium alloys. The fracture criterion during machining process thus plays a critical role in the chip formation process [98]. Improved chip

segmentation observed for tests performed at low temperatures with liquid N₂ suggests that the contribution of fracture is more pronounced under cryogenic conditions. The probable reasons for such phenomenon is discussed later in sections 4.1.5 and 5.4.

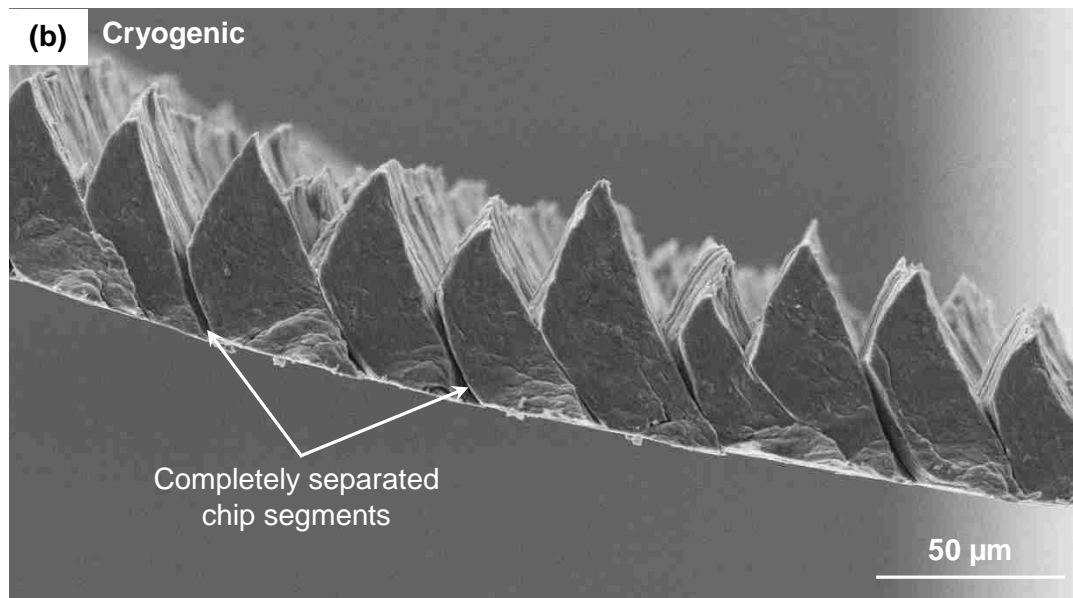
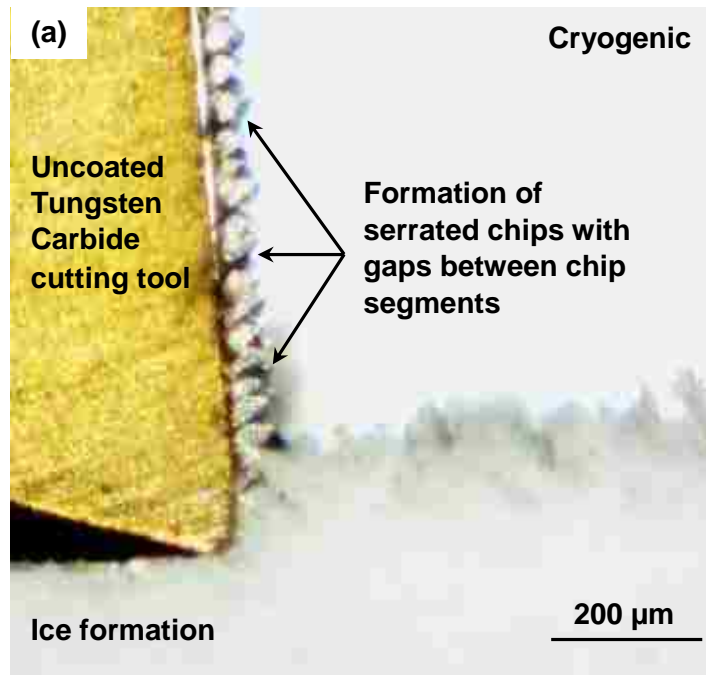


Figure 4.9: (a) Microstructural observation during orthogonal machining of Ti-6Al-4V under cryogenic conditions, (b) High magnification SEM image (SEI mode) showing typical chips obtained from cryogenic machining showing separations between chip segments

4.1.5 Effect of temperature on fracture behaviour of Ti-6Al-4V

The temperature sensitivity of Ti-6Al-4V to fracture was studied by conducting Charpy V-notch impact tests. The test was necessitated to explore the possible reasons for easier chip segmentation under cryogenic machining conditions. The size and specifications of the Charpy samples were in accordance with ASTM E23 – 12c standard [99]. The tests were conducted over a range of temperatures from 25 °C to –196 °C. Standard cooling baths were prepared by mixing liquid N₂ with solvents such as water, ethanol and methanol to obtain the intermediate temperatures and is outlined in Table 4.2. Initially the cooling bath were prepared by mixing the solvents in equal proportion and mechanically stirred vigorously so that the temperature throughout the cooling bath was homogenous. The temperature of the cooling bath was measured by a K-type thermocouple connected to a data acquisition system that provided the instantaneous temperature of the bath. The drop in temperature of this cooling bath over time was compensated by adding Liq. N₂ in arbitrary quantities such that the desired temperature was maintained.

Table 4.2: Cooling bath combinations to obtain different temperatures

Temperature	Coolant combination
–196 °C	Liq. N ₂
–116 °C	Liq. N ₂ + Ethanol
–95 °C	Liq. N ₂ + Methanol
0 °C	Ice + Water + Common salt
25 °C	No coolant – Ambient room temperature

The Ti-6Al-4V Charpy samples were immersed in the cooling bath for at least 30 minutes to ensure homogenous temperature distribution before being subject to impact

testing. The absorbed energy values during fracture were then plotted as a function of temperature and are shown in Figure 4.10. Ti-6Al-4V, a HCP metal with limited slip systems, is expected to exhibit lower impact toughness compared to a BCC metal (steel) with several slip systems for any given temperature. At room temperature, the impact toughness energy was measured to be 18.19 J. This decreased to a magnitude of 16 J at $-95\text{ }^{\circ}\text{C}$ and further reduced to $13.11 \pm 0.18\text{ J}$ at $-196\text{ }^{\circ}\text{C}$. In summary, it was observed that the fracture toughness of Ti-6Al-4V decreased linearly with decrease in temperature. In this experimental work, the fracture behaviour of Ti-6Al-4V at cryogenic temperatures was more important than the other temperatures. Thus iterative Charpy impact tests were conducted on the Ti-6Al-4V samples only for the cryogenic temperature condition.

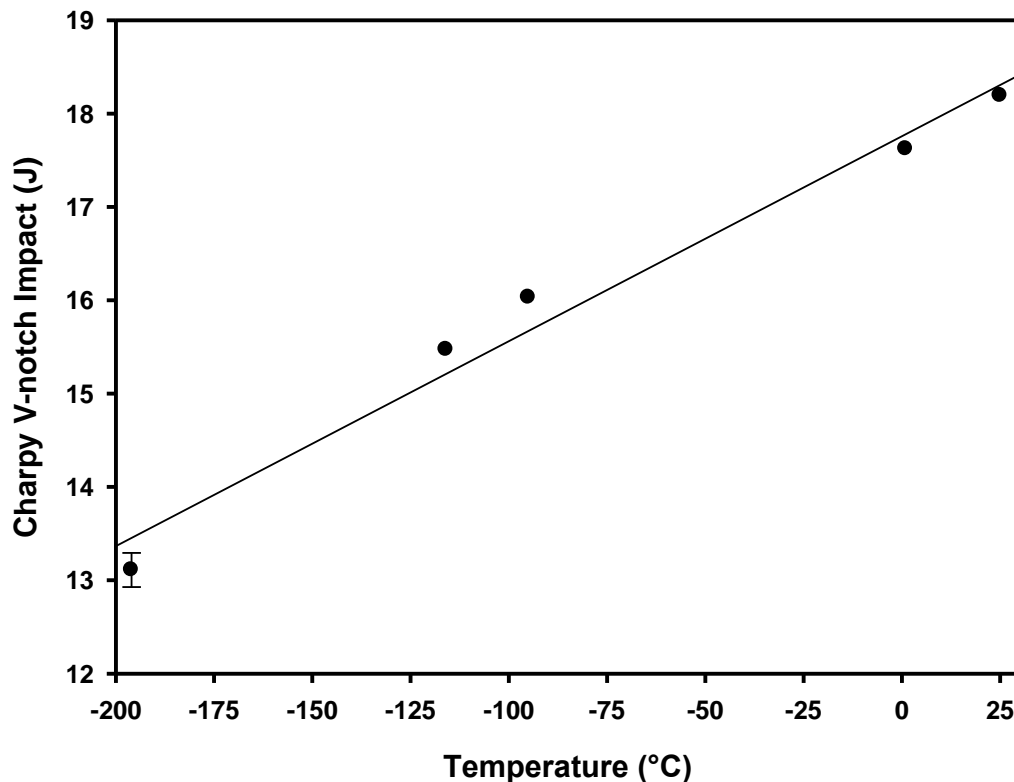


Figure 4.10: Variation of impact toughness of Ti-6Al-4V with temperature. A linear relationship was observed between toughness and temperature for Ti-6Al-4V

The crystal structure of a material is a reliable guide for qualitative prediction of temperature sensitivity to fracture. Thus to affirm the veracity of the toughness results for titanium alloys, charpy impact tests were also performed on 4140 steel, a body-centered cubic material, known to exhibit ductile to brittle transition with decrease in temperature (Figure 4.11). Steel exhibits ductile fracture at room temperatures and above which compliments the high absorbed energy of 82 J at 200 °C. Ductile fracture is characterised by the formation of well-developed shear dimples due to extensive microvoid coalescence. In stark contrast, the absorbed energy value plummets to 4.5 J at –196 °C, a characteristic of brittle fracture behaviour. 4140 steel exhibits cleavage fracture at cryogenic conditions. The absorbed energy values obtained from this test are in agreement with the values reported elsewhere [23]. Thus it can be safely said that the energy values obtained for Ti-6Al-4V are reliable.

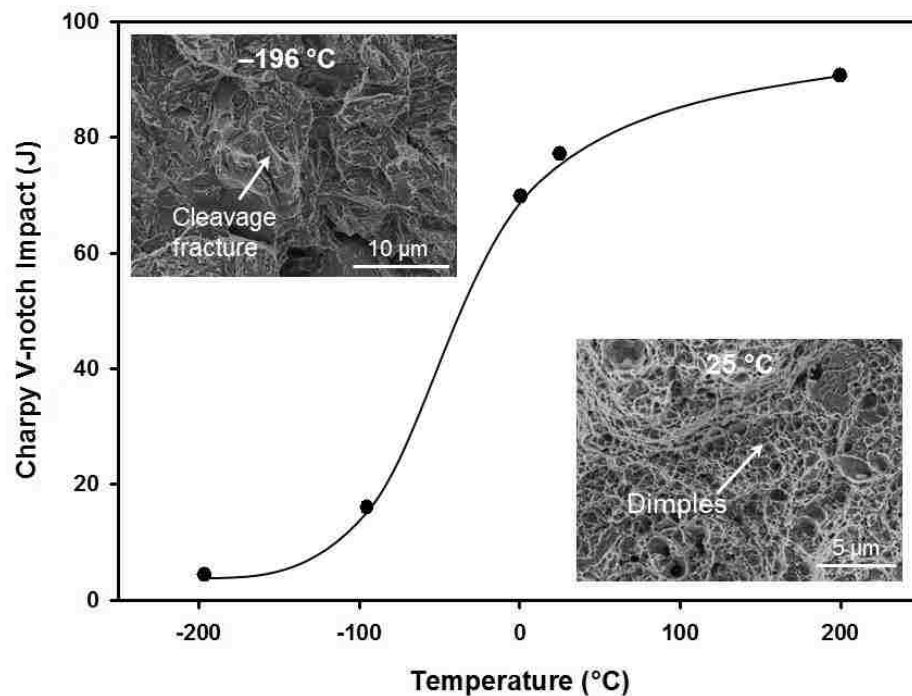
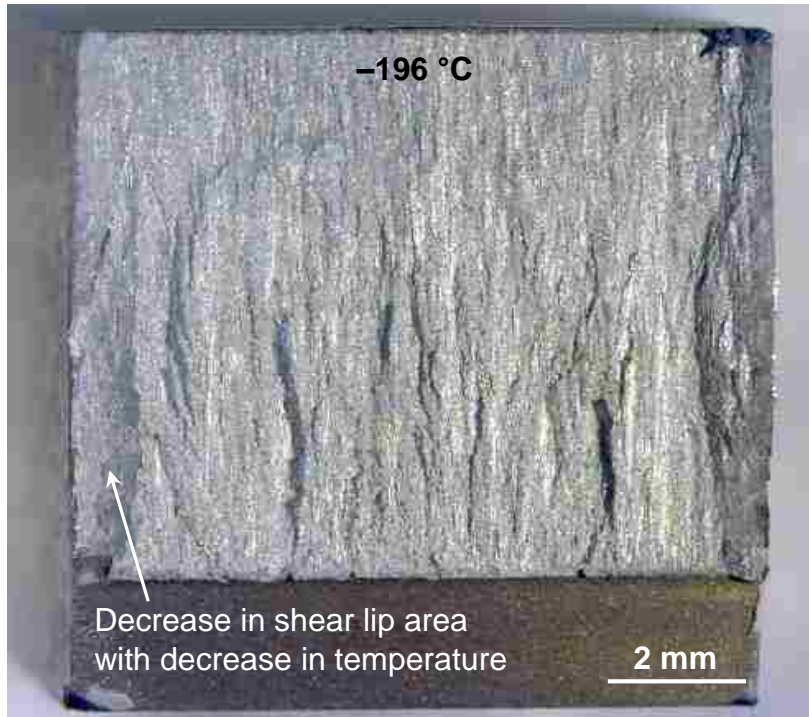


Figure 4.11: Variation of impact toughness of 4140 steel with temperature. The inset images show the fracture surfaces of the impact test samples tested at cryogenic and ambient temperatures

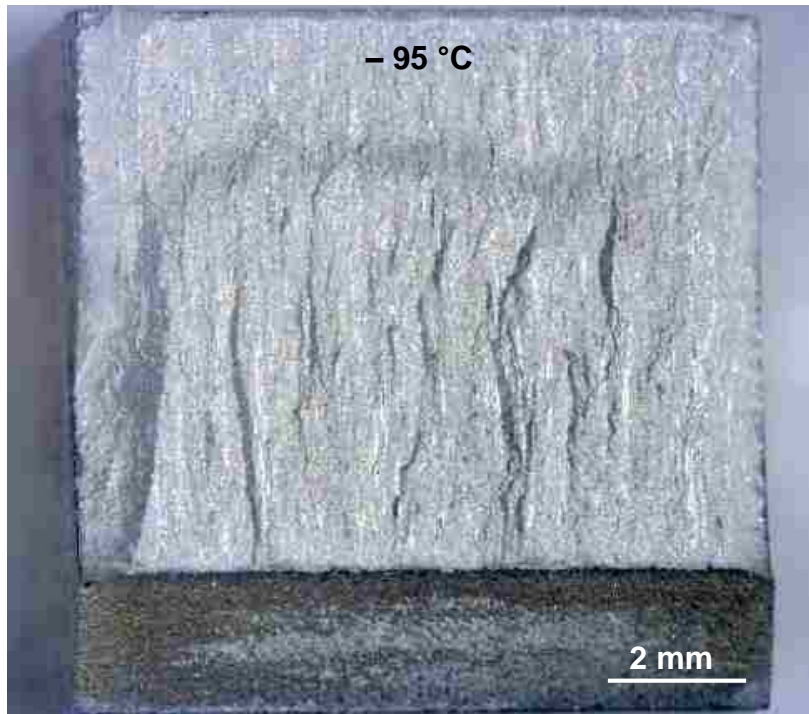
The fracture behaviour of several titanium alloys have been investigated in the past [100 – 102]. The fracture behaviour of a near α -titanium alloy (Ti-5Al-2.5Sn) with variation in temperature was studied [100]. The energy absorbed decreased from 40 kJ/m² at 300 K to 20 kJ/m² when the temperature was reduced from 100 °C to –196 °C. That is, a 50% decrease in fracture toughness was recorded. Similar behaviour was exhibited by other titanium alloys such as Ti-5Mo-4.5Al and Ti-11Mo-2.5Al [101], [102]. For Ti-5Mo-4.5Al, the fracture toughness decreased from 99 MPa \sqrt{m} to 67 MPa \sqrt{m} , and for Ti-11Mo-2.5Al, the fracture toughness decreased from 67 MPa \sqrt{m} to 40 MPa \sqrt{m} when the temperature was decreased from 300 K to 77 K. Beryllium exhibits a room temperature K_{Ic} value of about 23 MPa \sqrt{m} , and a 30% decrease occurred as temperature was reduced to 77 K.

The fractographs of the Ti-6Al-4V impact specimens presented in Figure 4.12 show that specimens with higher toughness exhibited well-developed shear lips compared to specimens with lower toughness. The percentage of shear lip area under cryogenic condition is approximately 27% while that under room temperature is 43%. Thus a 15% reduction in shear lip area is observed with decrease in temperature from 25 °C to –196 °C. The observed feature of decreasing shear lip area is in agreement with the decreasing energy values presented in Figure 4.10. Thus it could be hypothesized that the easier chip fracture under cryogenic condition was primarily due to the inducement of brittleness in the material which is characterized by (i) lower impact energy, and (ii) lower shear lip area. Further analysis on fracture surfaces of the specimens is discussed section 5.4.

(a)



(b)



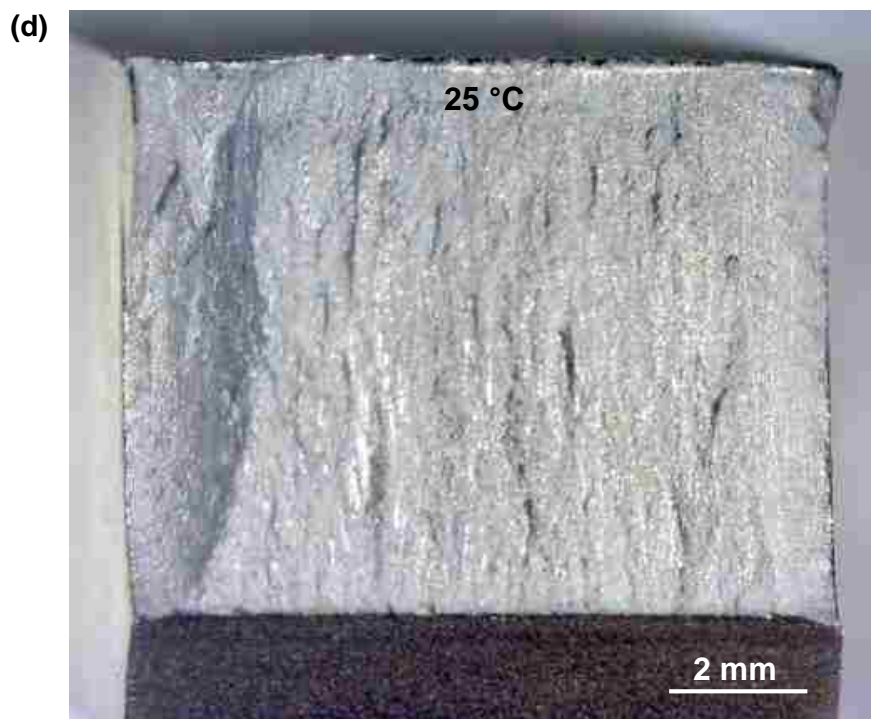
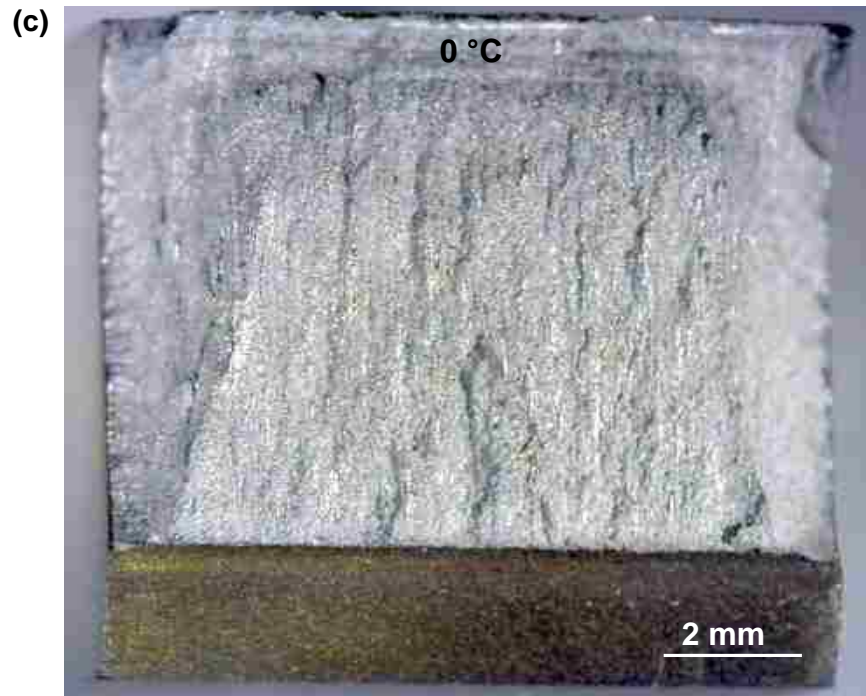


Figure 4.12: Low magnification optical macrographs of Ti-6Al-4V impact samples tested at (a) $-196\text{ }^{\circ}\text{C}$, (b) $-95\text{ }^{\circ}\text{C}$, (c) $0\text{ }^{\circ}\text{C}$, (d) $25\text{ }^{\circ}\text{C}$, showing the decrease in shear lip area with decrease in temperature

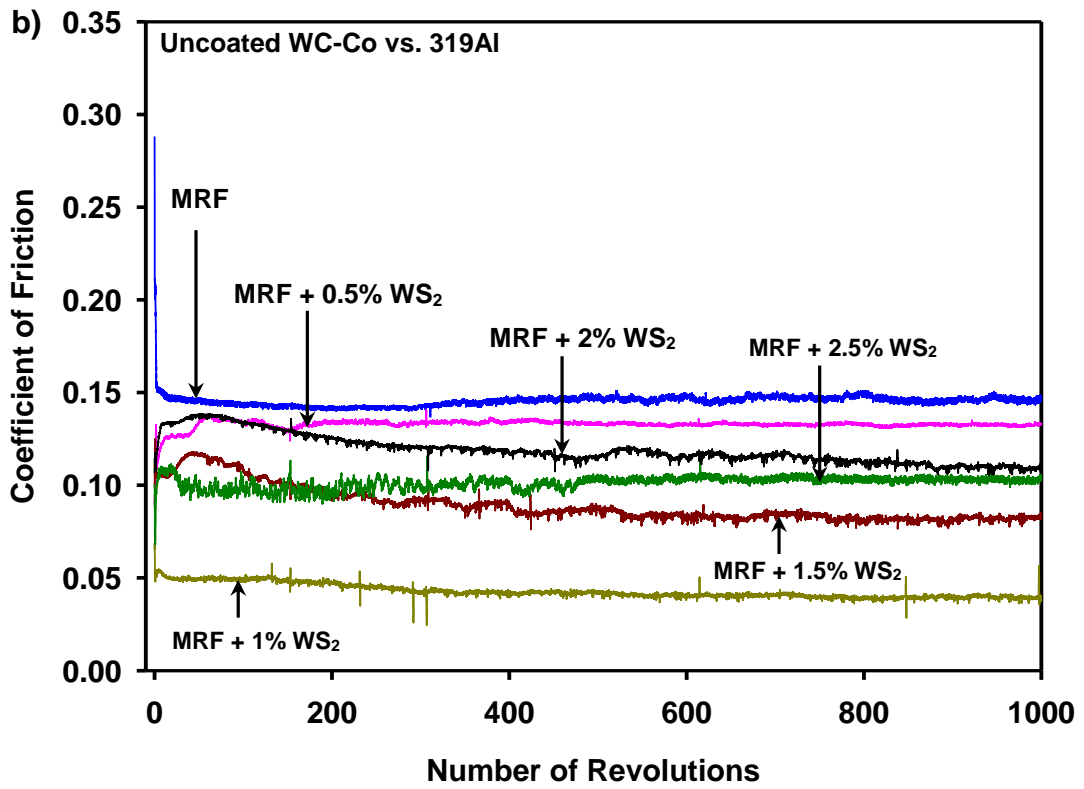
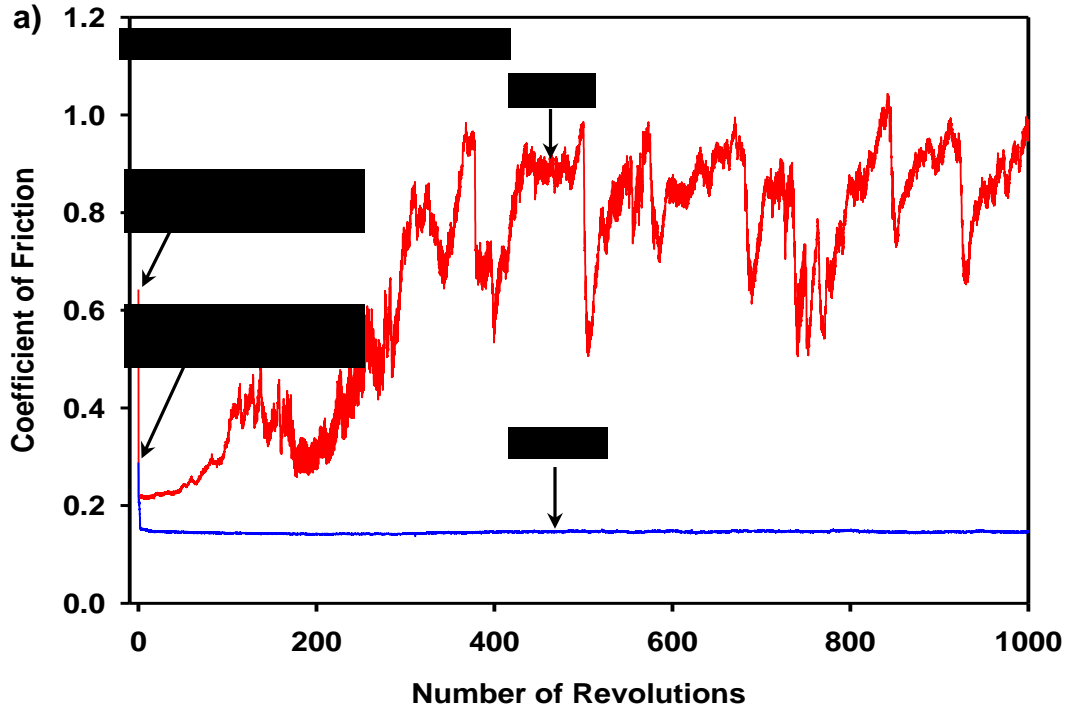
4.2 Nanolubricant Machining

As discussed in section 3.4, the nanolubricant machining approach consists of studying the tribological behaviour of the sliding materials (Ti-6Al-4V and uncoated WC-Co) and applying this knowledge in orthogonal machining. One of the primary objectives for the nanolubricant approach is to reduce adhesion on the cutting tool such that the tool life could be enhanced. Hypo-eutectic Al-Si alloys such as 319Al are known to cause tool failure due to extensive adhesion [103] similar to Ti-6Al-4V machining. Thus testing of 319Al would act as a reference in judging whether nanoparticles are truly capable of reducing adhesion. Consequently in this experimental work, the effect of WS₂ blended MRF in improving the machinability of 319Al and Ti-6Al-4V was investigated by considering their respective tribological performance against uncoated WC-Co under different sliding conditions. The sliding conditions that generated the least COF were then chosen for the orthogonal turning tests. Overall improvement in machinability was studied by observing the cutting forces, adhesion on the cutting tool, and surface roughness of the machined part. All these results will be discussed in the following sections.

4.2.1 Effect of WS₂ Nanoparticles on the COF of WC-Co vs. 319Al

Representative curves of variation of COF with sliding cycles for uncoated WC-Co versus 319Al under dry and MRF lubricated conditions are shown in Figure 4.13 (a). Under dry or unlubricated sliding tests, a high running in COF (μ_R) of 0.62 was generated followed by a decrease to 0.22 for a brief sliding period of 60 cycles. Thereafter the COF values were marked by sharp fluctuations until the end of the test and no steady state friction was recorded. The variation of COF under lubricated condition was tested using MRF as discussed in section 3.4.1. Using MRF, the running-in COF was reduced to 0.28,

which was 55% lower compared to dry sliding conditions. With further increase in sliding cycles, the COF slightly reduced to 0.18 and this value was maintained for the remainder of the test duration. The possibility of further decrease in COF was explored by adding WS₂ nanoparticles in the MRF as discussed in section 3.4.1. Figure 4.13 (b) shows the typical variation of COF for MRF and MRF + WS₂ lubricated conditions with sliding cycles. It was observed that the running-in COF values under MRF + WS₂ sliding conditions, irrespective of the concentration of WS₂, were always lower than under MRF test. The lowest running-in COF of 0.06 was recorded under MRF + 1% WS₂ sliding conditions and this concentration was used for the orthogonal tests. The average running-in and steady state COF values with their standard deviations were plotted against WS₂ concentrations as shown in Figures 4.13 (c-d). In succinct terms, the above tests indicate that the addition of nanoparticles contributed in reducing the friction at the pin-disk interface. This knowledge was applied to orthogonal machining of 319Al rod with uncoated WC-Co tool to ascertain an improvement in machinability using WS₂ nanolubricants which is discussed in the following section.



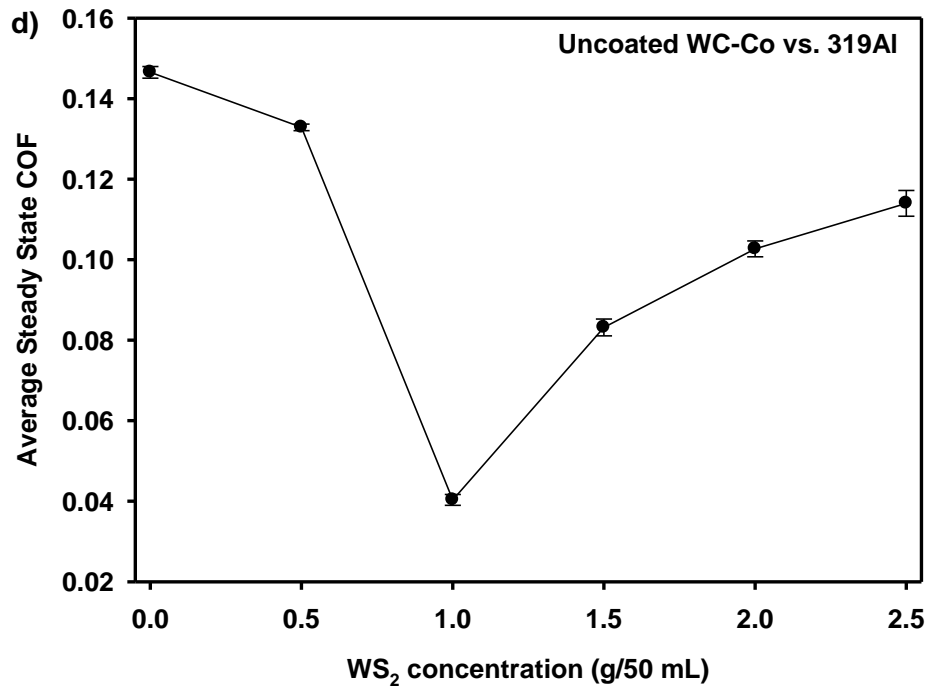
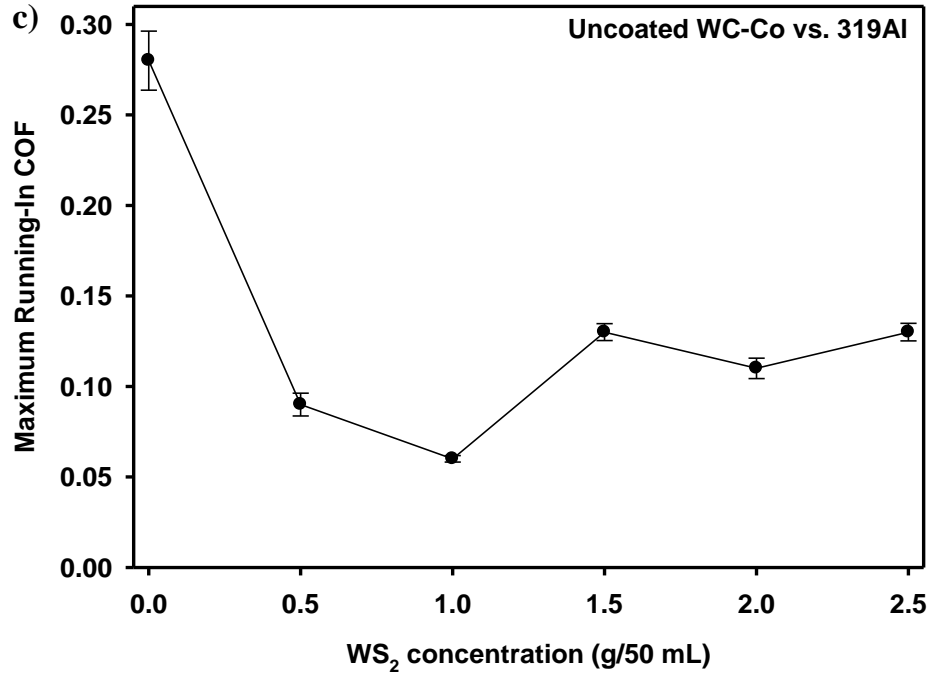
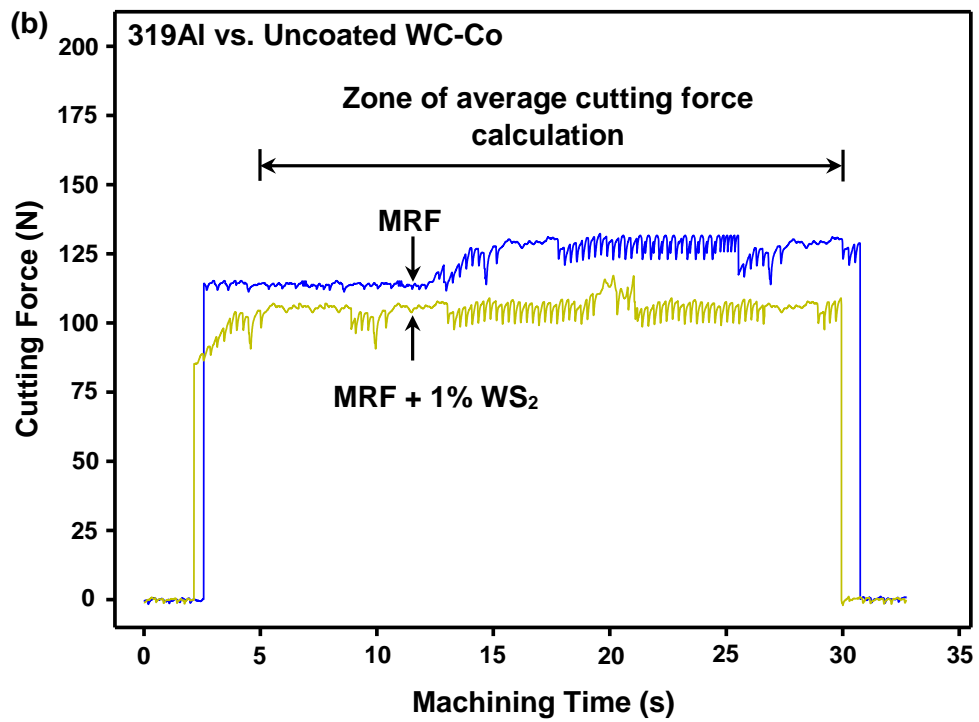
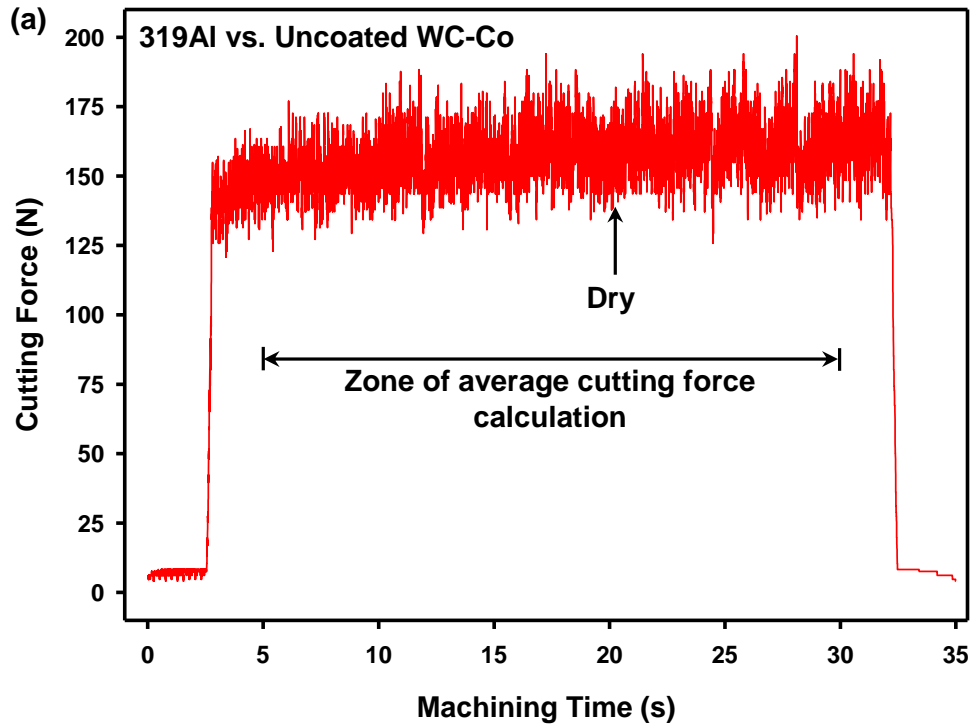


Figure 4.13: Variation of COF with the number of revolutions when uncoated WC-Co was tested against 319Al counterface in (a) dry (unlubricated) and with MRF lubricated conditions, (b) MRF, MRF + WS₂ lubricated conditions with varying concentrations. (c) Variation of running-in and steady state COF for MRF, MRF + WS₂ lubricated sliding conditions. Each point represents the average value of the three iterative tests performed in all test conditions. The error bars denote the standard deviation about the mean COF value from the three iterative tests

4.2.2 Effect of WS₂ Nanoparticles on Cutting Forces Generated with Uncoated WC-Co vs. 319Al

The typical trends of cutting forces of 319Al machined with uncoated WC-Co at a speed of 29.5 m/min, feed rate of 0.4 mm/rev and a 1 mm depth of cut, under different experimental conditions, namely dry, MRF and MRF + 1% WS₂ lubricated conditions are shown in Figures 4.14 (a-b) as a function of machining time. Accordingly, machining 319Al under dry or unlubricated test conditions were characterized by the occurrence of sharp spikes with a maximum cutting force of about 183 ± 11.51 N. The use of conventional MRF as a coolant during the machining process reduced the cutting force to 125 ± 10.34 N which was further reduced to 110 ± 6.83 N with the use of MRF + 1% WS₂. The low cutting forces are in agreement with the low friction values that were obtained during the pin-on-disk experiments. The amplitude of variations were also greatly reduced as shown in Figure 4.14 (b).

The average cutting force generated during the orthogonal machining tests are represented in the form of a bar chart and is shown in Figure 4.14 (c). The error bars indicate the standard deviation about the mean of the two iterative tests that were performed under the same conditions.



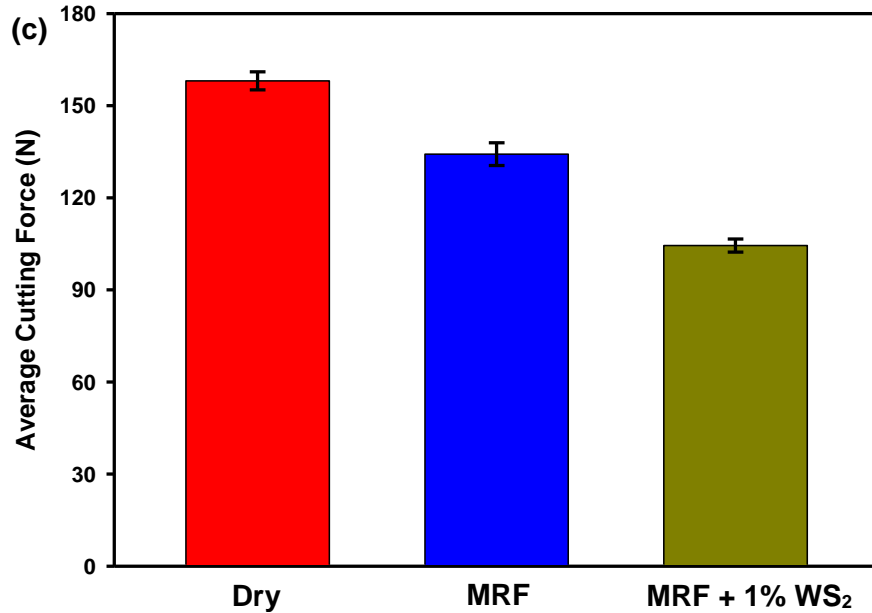
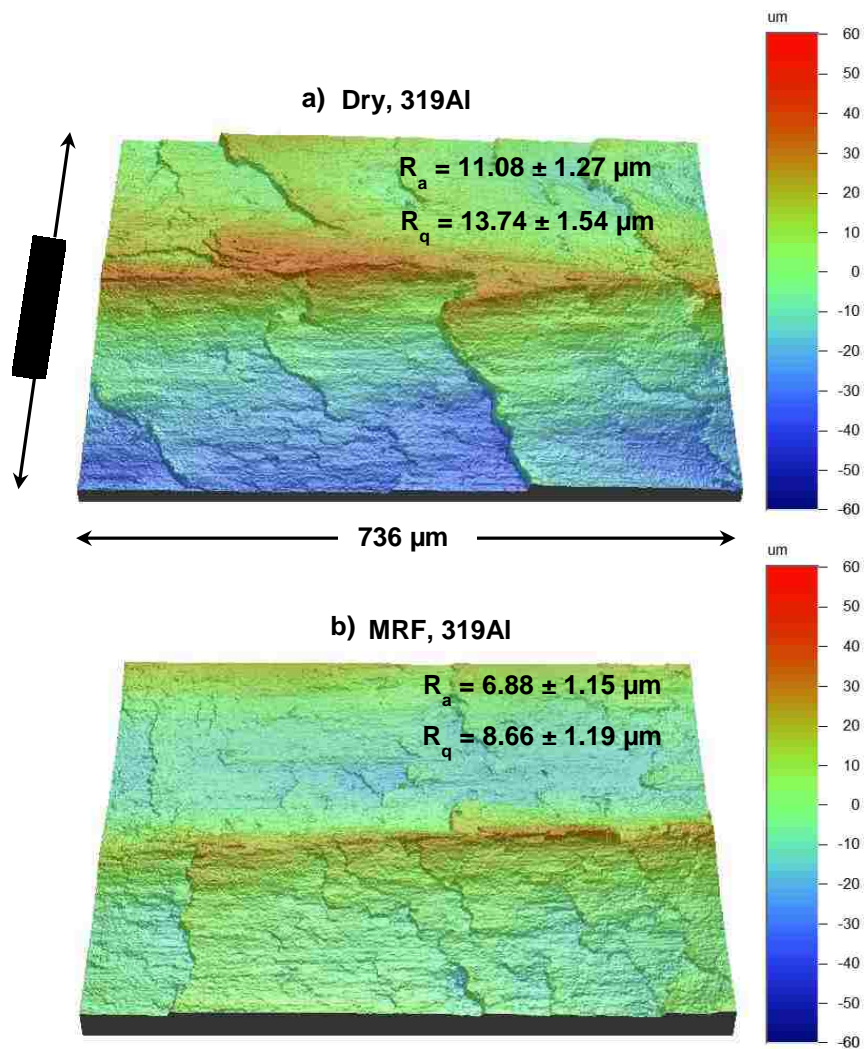


Figure 4.14: Variation of cutting forces generated during orthogonal cutting of 319Al at a cutting speed of 29.7 m/min, feed rate of 0.4 mm/rev and a 1 mm depth of cut under (a) dry machining condition, (b) MRF, MRF + WS₂ lubricated conditions. The average cutting force was calculated from the more stable response as shown in (a) and (b), (c) Bar chart showing a comparison of the average cutting forces during the orthogonal machining tests under different machining conditions. The error bar denotes the standard deviation about the mean cutting force from the two iterative tests

4.2.3 Effect of WS₂ Nanoparticles on the Surface Roughness of Machined Part

To assess the surface quality of the machined part, the surfaces were investigated for each machining condition using a non-contact, white light optical interferometer. Typical three dimensional profiles of the machined surfaces are shown in Figures 4.15 (a-c). The locations where the measurements were made is shown in Figure 4.15 (d). Compared to the machined surface produced under lubricated test conditions, the surface morphology produced under dry machining generated a rougher topography. The machined surface under MRF + 1% WS₂ lubricated test conditions had the smoothest topography while that under MRF lubricated test condition generated a low surface roughness. The highest surface roughness was recorded under dry machining condition with an average value

$R_a = 11.08 \pm 1.27 \mu\text{m}$ and root mean square value $R_q = 13.74 \pm 1.54 \mu\text{m}$. The use of coolants drastically reduced the surface roughness. The R_a and R_q under MRF lubricated conditions were $6.88 \pm 1.15 \mu\text{m}$ and $8.66 \pm 1.19 \mu\text{m}$ respectively. The addition of WS_2 nanoparticles in MRF further reduced the surface roughness to a R_a of $6.18 \pm 0.78 \mu\text{m}$ and R_q of $7.82 \pm 0.76 \mu\text{m}$. The results of the surface roughness (R_a and R_q) for all machining conditions are summarized in the form of bar charts and presented in Figure 4.15 (d). The bar chart emphasizes that the smoothest surface was obtained during WS_2 blended MRF machining conditions.



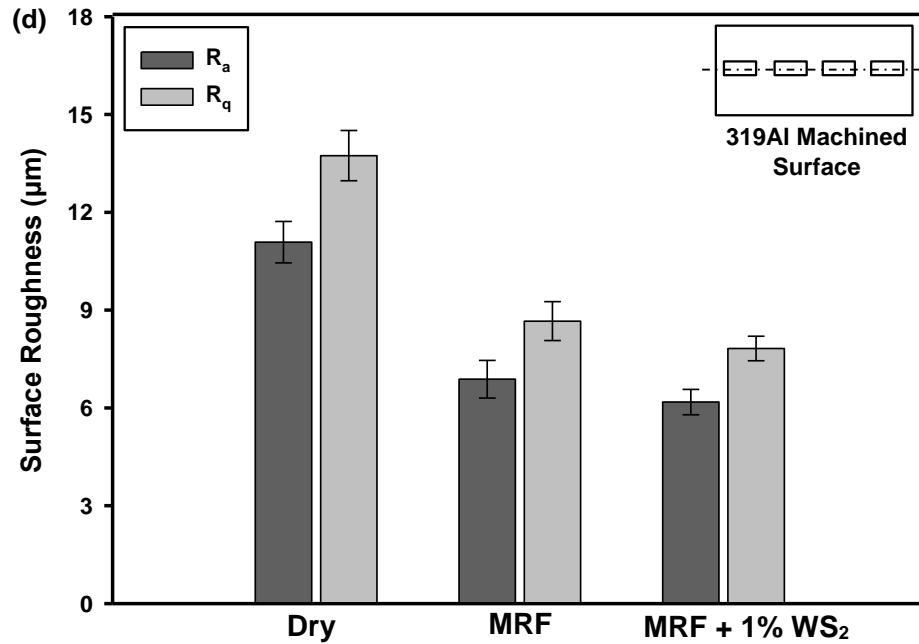
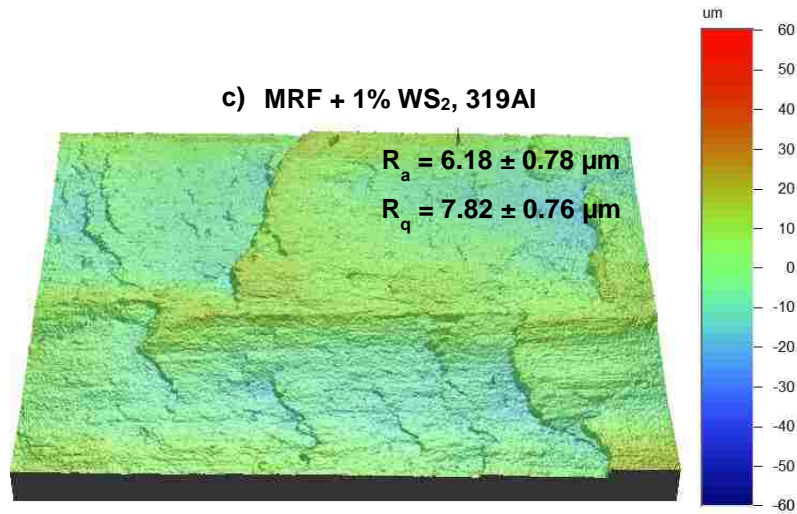


Figure 4.15: Surface profiles of machined surface in (a) dry, (b) MRF, (c) MRF + 1% WS₂ machining conditions. (d) Comparison of average and root mean square roughness for all machining conditions. The error bars represent the standard deviation about the mean surface roughness value from the two iterative tests. The inset image shows the spots on the machined surface where the roughness data were taken from

4.2.4 Effect of WS₂ Nanoparticles on Tool Wear and Adhesion

Scanning electron microscopy (SEM) was performed on the rake and flank faces of the uncoated WC-Co tool used in machining of 319Al under all test conditions. As Figure 4.16 (a,b) demonstrates, transfer of workpiece material to the cutting tool during dry

machining, and the transferred Al covered almost the entire area of the cutting edge resulting in formation of a thick built-up edge (BUE). Patches of aluminum adhesion could be observed during machining with the use of MRF (Figure 4.16 (c,d)) and MRF + 1% WS₂ (Figure 4.16 (e,f)) but to a smaller extent when compared to dry machining. The use of WS₂ blended MRF resulted in the least amount of adhesion among all machining conditions with a BUE of thickness 275 μm, a 30% decrease to that under dry conditions.

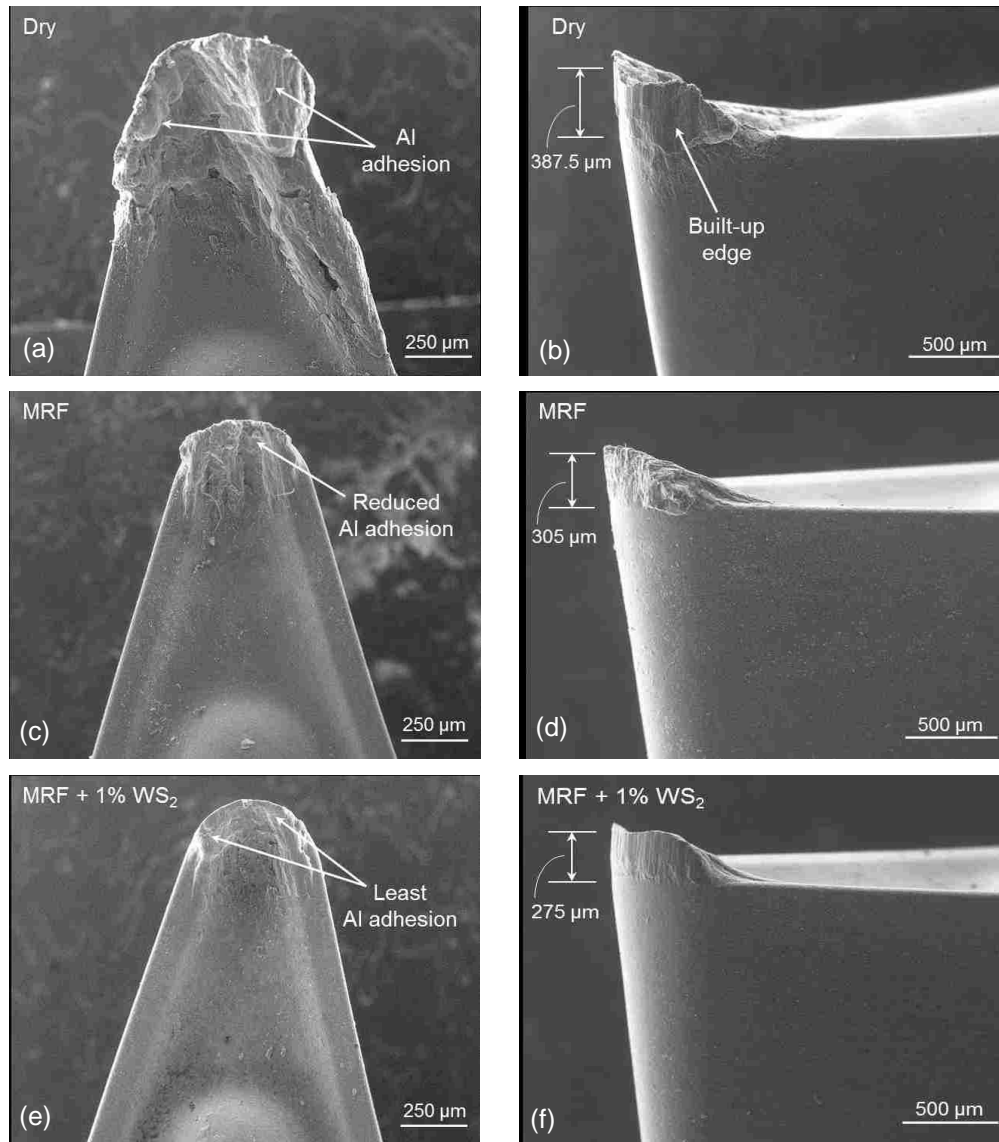
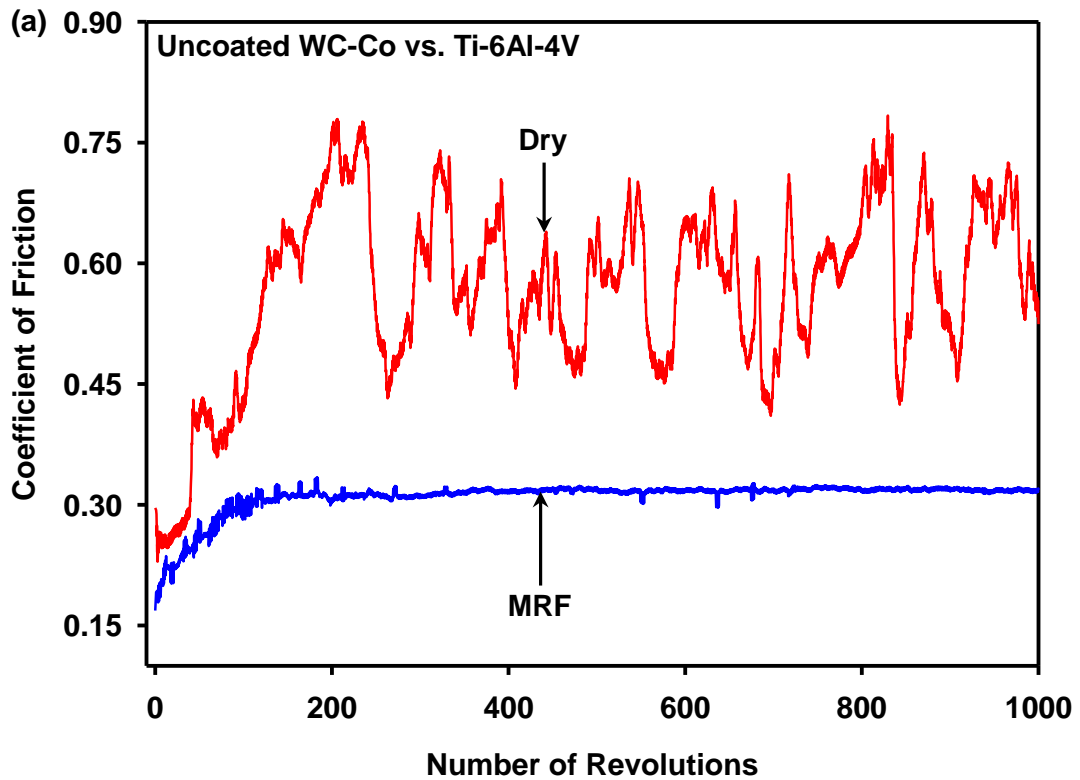


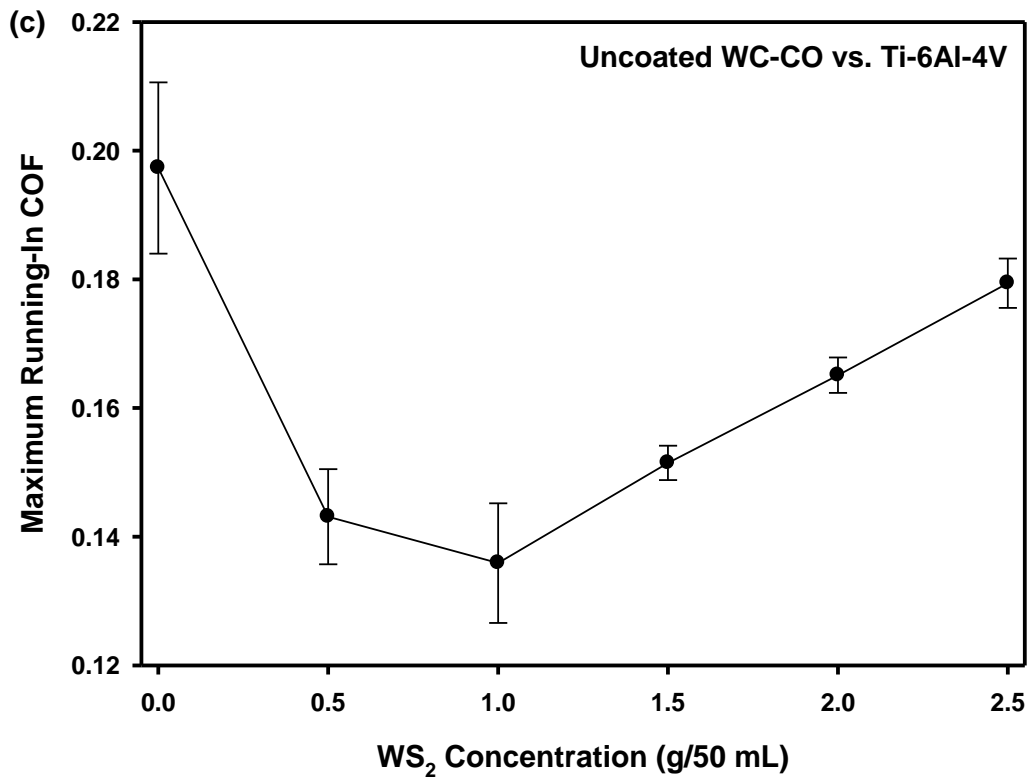
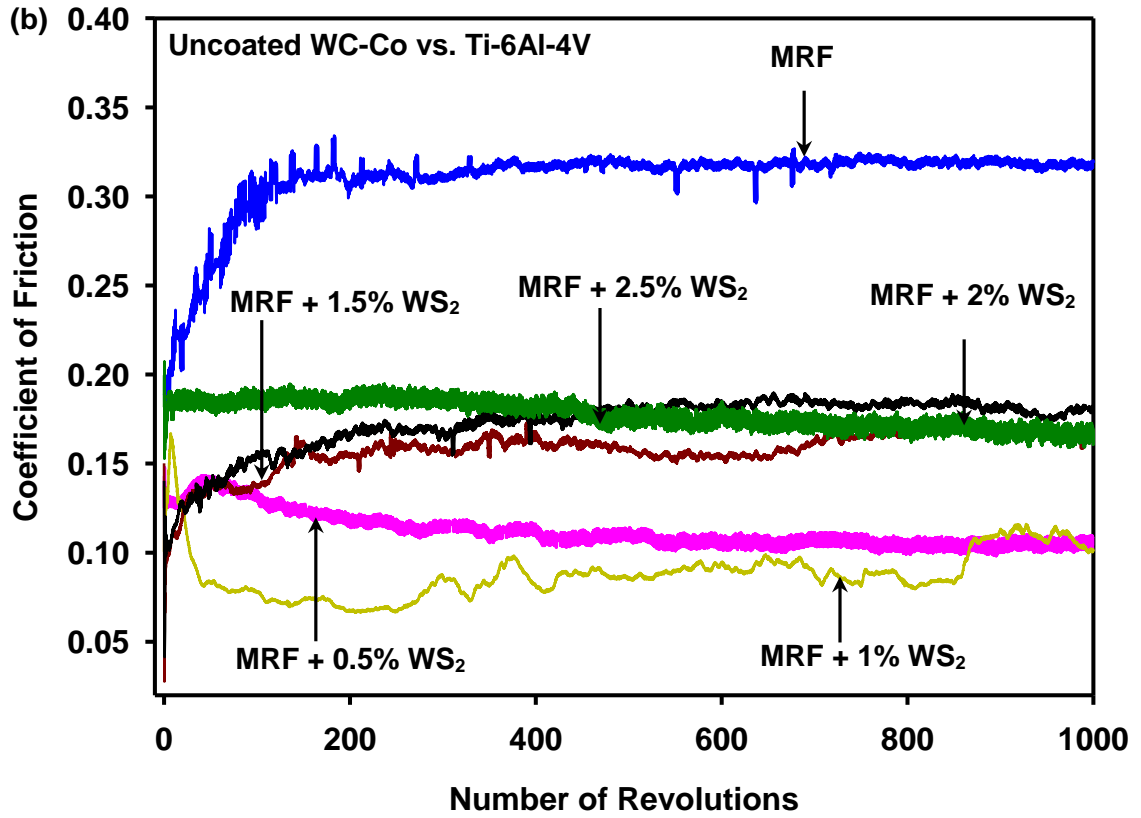
Figure 4.16: SEM (SEI mode) of the rake and flank faces of the uncoated WC-CO cutting tool after subjecting to orthogonal cutting of 319Al under (a), (b) dry; (c), (d) MRF; (e), (f) MRF + 1% WS₂ machining conditions

4.2.5 Effect of WS₂ Nanoparticles on the COF of WC-Co vs. Ti-6Al-4V

The typical trends of the COF (μ) values of Ti-6Al-4V sliding against uncoated WC-Co tested at different test conditions are shown in Figure 4.17 (a,b) as a function of number of revolutions. Accordingly, testing the COF under dry or unlubricated test conditions generated a high running-in COF (μ_R) of 0.40 (Figure 4.17 (a)). Following the running-in period, the COF decreased to 0.35 for a short sliding period of about 60 cycles, and then increased to 0.38. Beyond 200 cycles, large fluctuations in the COF were witnessed till the end of the test, and thus no steady state friction (μ_S) was recorded. The large fluctuations in COF were indicative of adhesion of counterface material to the sample. Under MRF lubricated sliding conditions, the running-in period occurred with a μ_R of 0.23. The COF slightly increased to 0.32 and it was maintained till the end of the test. The running-in period lasted for about 30 cycles and the rest of the cycle was marked by a low and stable COF indicating attainment of steady state friction with a value of 0.32. Further decrease in COF (μ_R and μ_S) could be achieved by addition of WS₂ nanoparticles in the MRF as shown in Figure 4.17 (b). Sliding tests carried out with WS₂ blended MRF suggests that irrespective of the concentration, the addition of nanoparticles in MRF decreased the COF (μ_R and μ_S) when compared to dry and MRF sliding conditions. The μ_R and μ_S for WC-Co decreased to 0.15 and 0.13 when tested with MRF + 0.5% WS₂ which was much lower than that under MRF sliding conditions. The lowest μ_R of 0.12 and μ_S of 0.08 was obtained for sliding tests with MRF + 1% WS₂. Additional increase in nanoparticle concentration led to increase in COF although they were still lower than the COF under MRF sliding conditions. A plot of μ_R and average μ_S values obtained from all iterative tests under MRF and MRF + WS₂ sliding conditions is shown in Figure 4.17 (c,d) which emphasizes that (i)

the COF (μ_R and μ_S) with the addition of nanoparticles in MRF was always lower than that under plain MRF sliding conditions, (ii) the 1% WS_2 blended in MRF was the optimum concentration of nanoparticle which resulted in the least μ_R and average μ_S . This optimum concentration of nanoparticles in MRF was later used during the orthogonal cutting process.





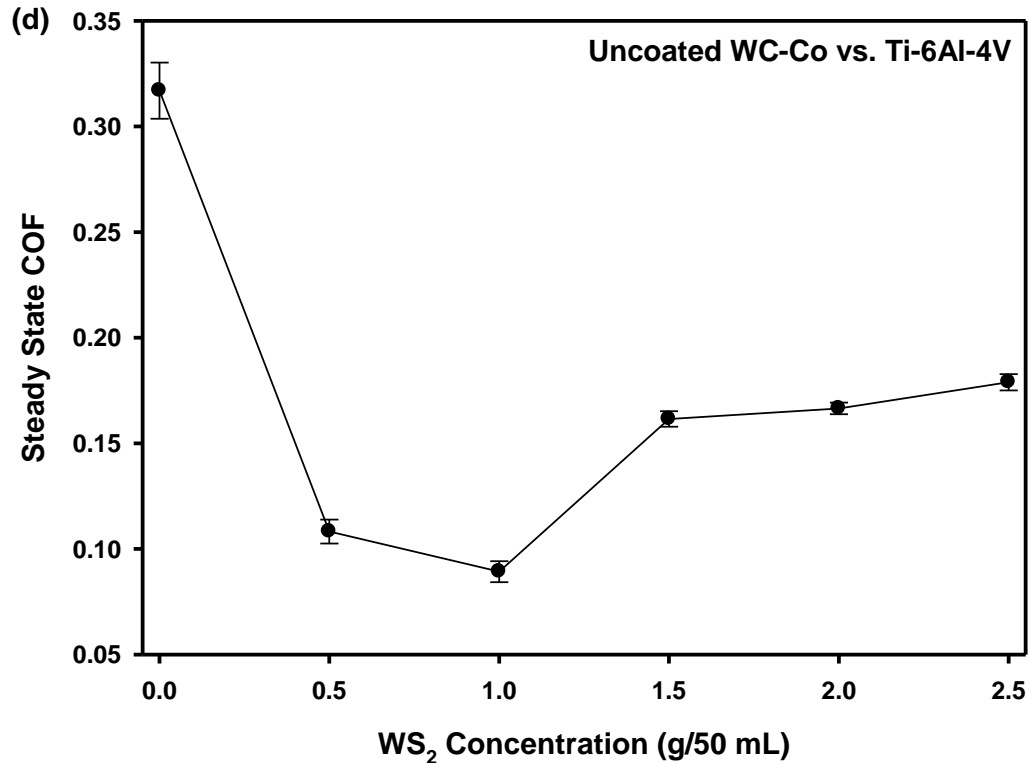
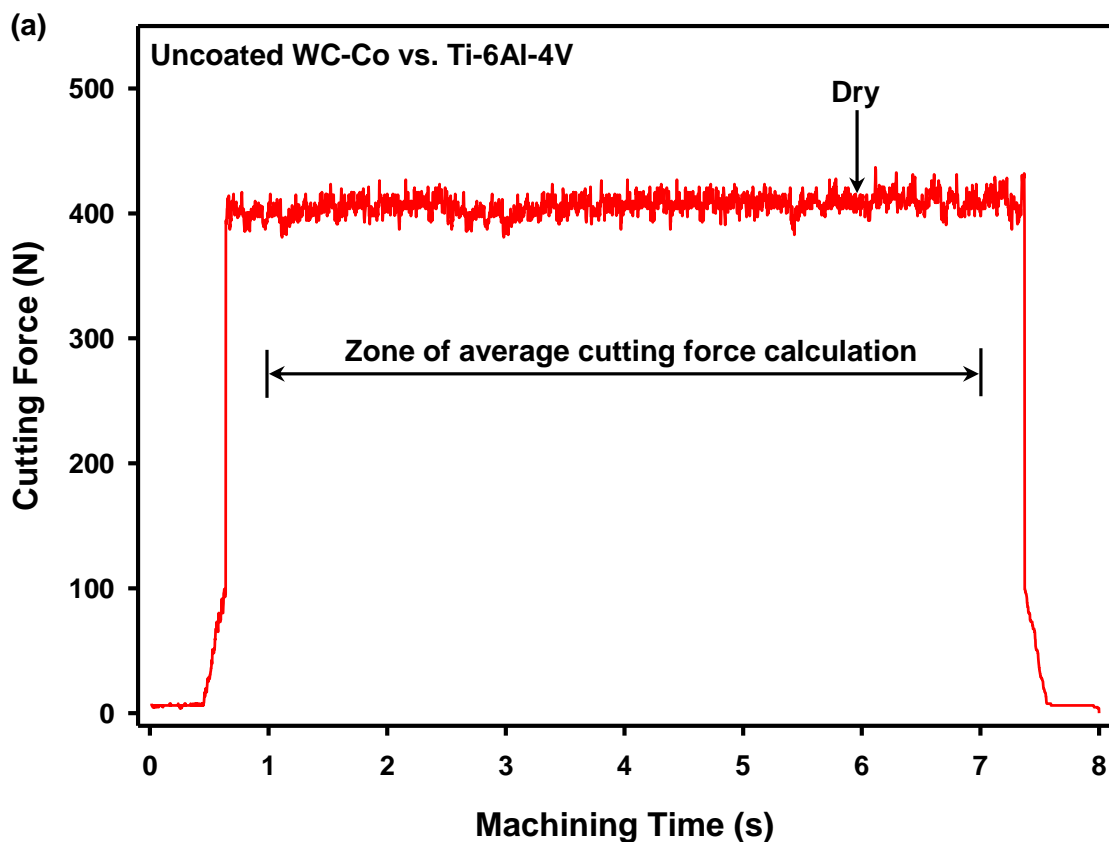


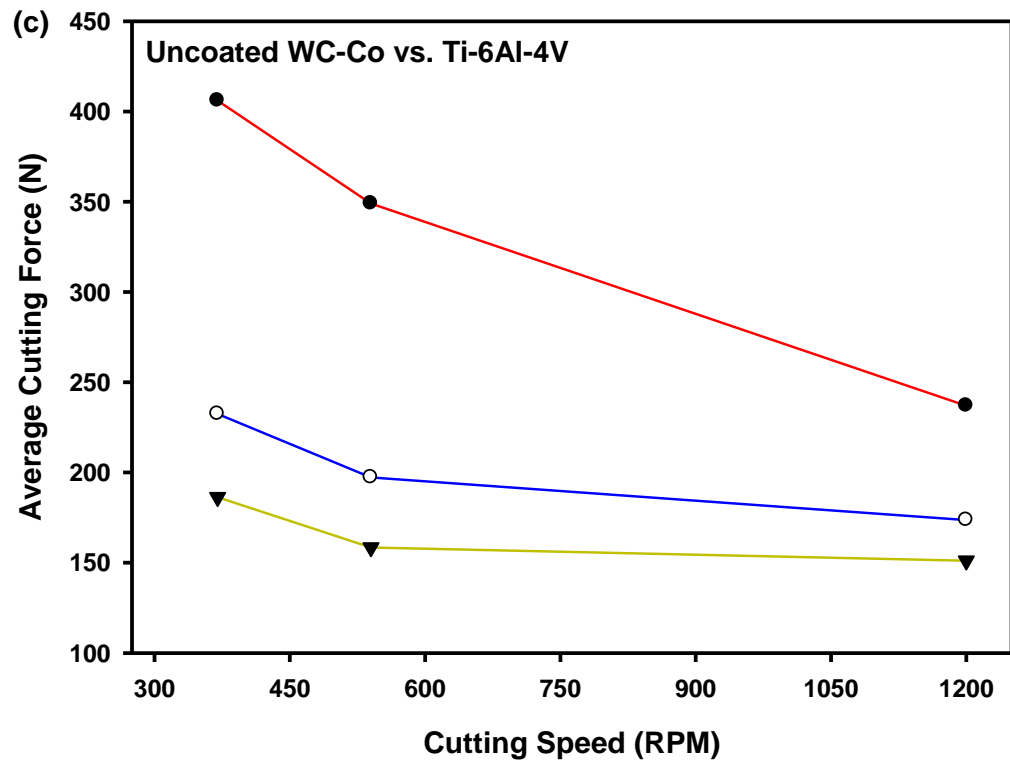
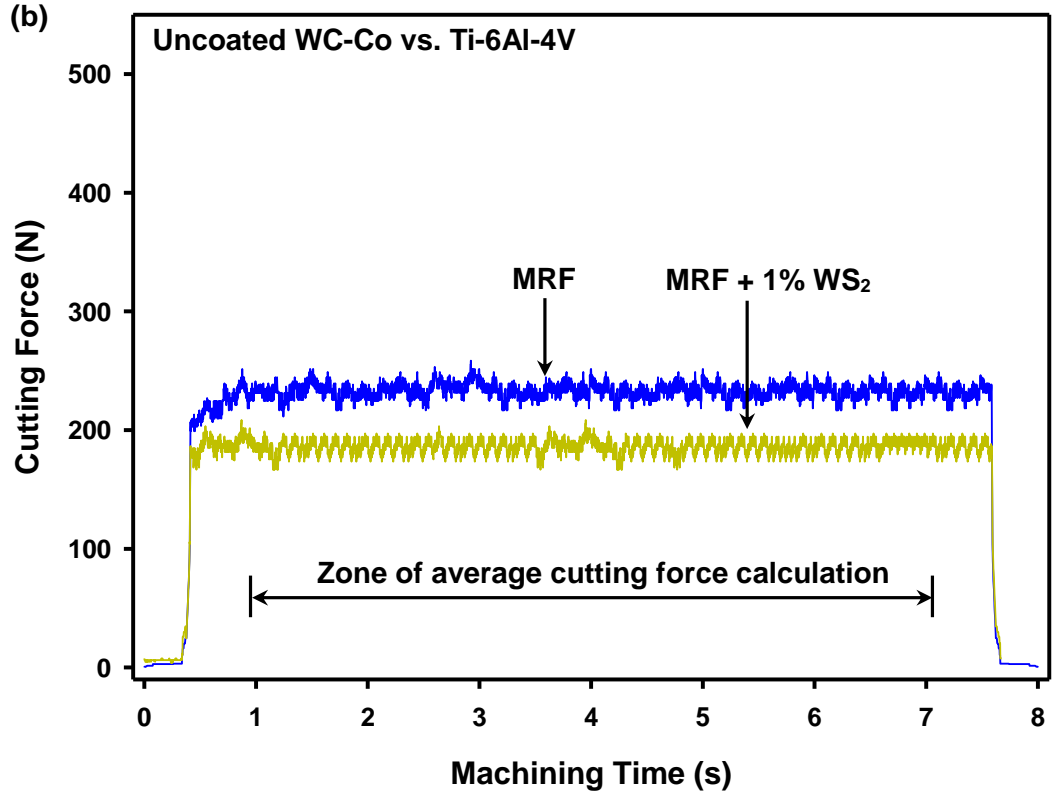
Figure 4.17: Variation of COF with the number of revolutions when uncoated WC-Co was tested against Ti-6Al-4V counterface in (a) dry (unlubricated) and with MRF lubricated conditions, (b) MRF, MRF + WS₂ lubricated conditions with varying concentrations. (c) Variation of running-in and steady state COF for MRF, MRF + WS₂ lubricated sliding conditions. Each point represents the average value of the three iterative tests performed in all test conditions. The error bars denote the standard deviation about the mean COF value from the three iterative tests

4.2.6 Effect of WS₂ Nanoparticles on Cutting Force Generated with Uncoated WC-Co vs. Ti-6Al-4V

The representative trends of cutting forces generated during orthogonal machining of Ti-6Al-4V with uncoated WC-Co under a cutting speed of 29.5 m/min, feed rate of 0.4 mm/rev, and a 1 mm depth of cut for dry, MRF and MRF + 1% WS₂ lubricated conditions are shown in Figures 4.18 (a-b). The cutting force generated during dry machining condition was 400 N. The use of conventional MRF as a coolant for the same machining process reduced the cutting force to 230 N, which was 42% lower than that under dry conditions. The use of 1% WS₂ blended MRF during the machining process further reduced

the cutting force to 190 N. Figure 4.18 (c) shows the plot of average cutting force with increasing cutting force. Under dry machining conditions, it could be observed that the cutting force decreased with increasing cutting speed due to the effect of thermal softening [94]. The generation of high cutting zone temperatures (Figure 4.18 (d)) softened the workpiece material resulting in its easier removal. Consequently the cutting force decreased with increasing cutting speed. For the tests under the application of coolants, the effect of thermal softening was not profound. However the coolant acts as a lubricant and reduces the friction at the tool-workpiece interface which results in decrease in cutting force.





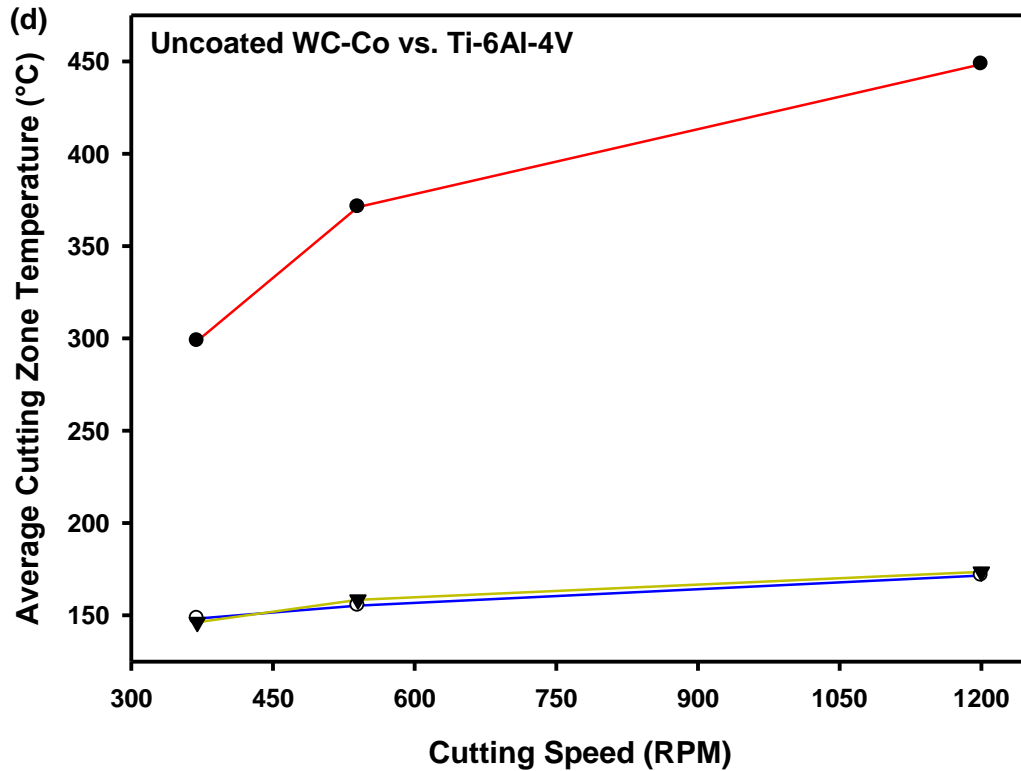


Figure 4.18: Variation of cutting forces generated during orthogonal cutting of Ti-6Al-4V at a cutting speed of 29.5 m/min, feed rate of 0.4 mm/rev and a 1 mm depth of cut under (a) dry machining condition, (b) MRF, MRF + WS₂ lubricated conditions, (c) Plot of comparison of the average cutting forces during the orthogonal machining tests under different machining conditions, (d) Plot of comparison of average cutting zone temperature generated during each machining condition

4.2.7 Effect of WS₂ Nanoparticles on Surface Roughness of Machined Part

The surface quality of the machined part was investigated using a non-contact, white light optical interferometer – WYKO NT1100. Typical three dimensional surface profiles generated during orthogonal machining at 95 m/min, feed rate of 0.12 mm/rev and a 1 mm depth of cut are presented in Figure 4.19 (a - c). The feed rate maintained in this test is relatively low compared to the other feed rates used in the machining experiments. From the experimental data, the surface profile produced during dry cutting of Ti-6Al-4V resulted in a profile that had an average surface roughness of 3.06 μm and root mean square roughness of 3.89 μm . With the application of MRF during the machining process, the R_a

and R_q values reduced to $1.29\ \mu\text{m}$ and $1.61\ \mu\text{m}$ respectively. The smoothest surface amongst all the experimental conditions was obtained from the MRF + 1% WS_2 tests. The low COF generated under the MRF + 1% WS_2 sliding conditions (Figure 4.19 (c)) resulted in a smooth surface finish. The R_a and R_q was measured to be $0.95\ \mu\text{m}$ and $1.08\ \mu\text{m}$ respectively.

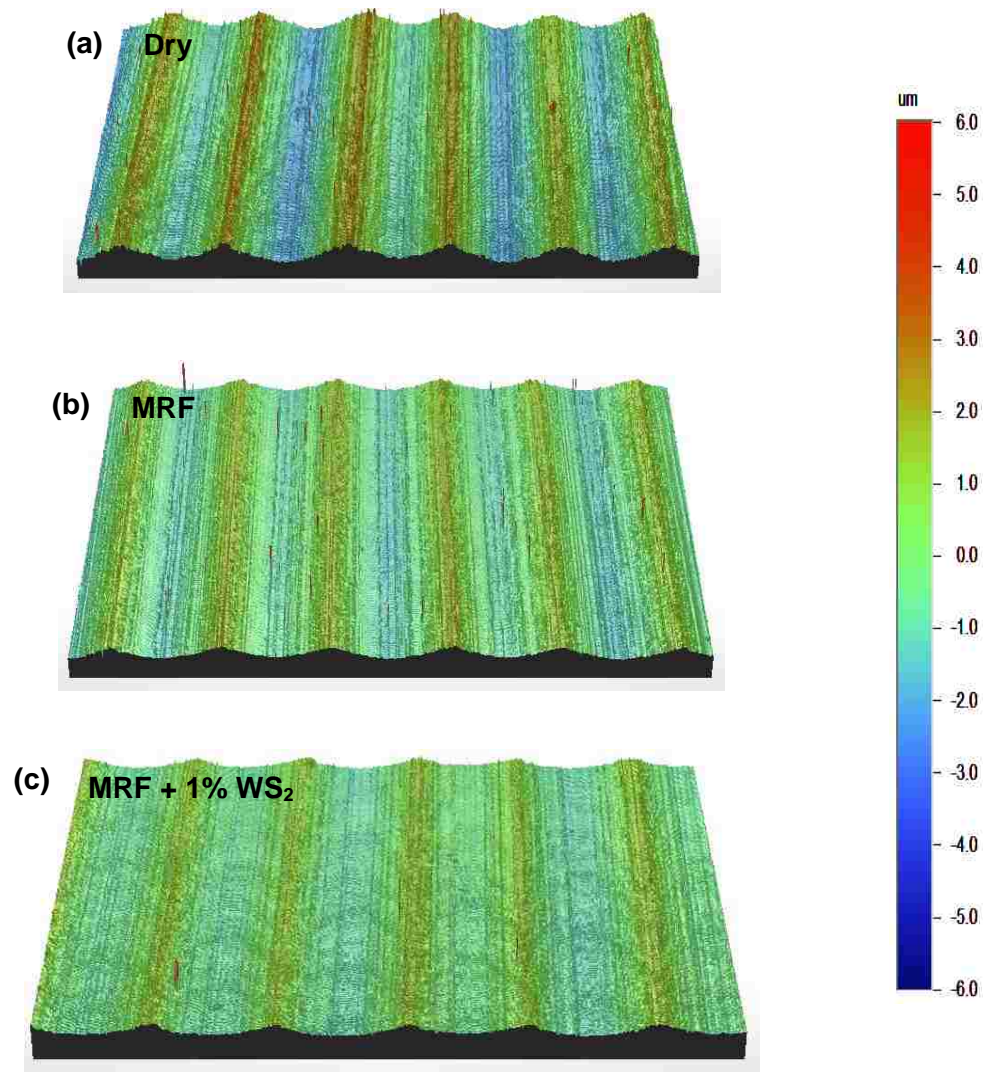


Figure 4.19: Surface profiles generated during orthogonal machining of Ti-6Al-4V at a cutting speed of 95 m/min, feed rate of 0.12 mm/rev and a 1 mm depth of cut under (a) dry, (b) MRF, (c) MRF + 1% WS_2 machining environments

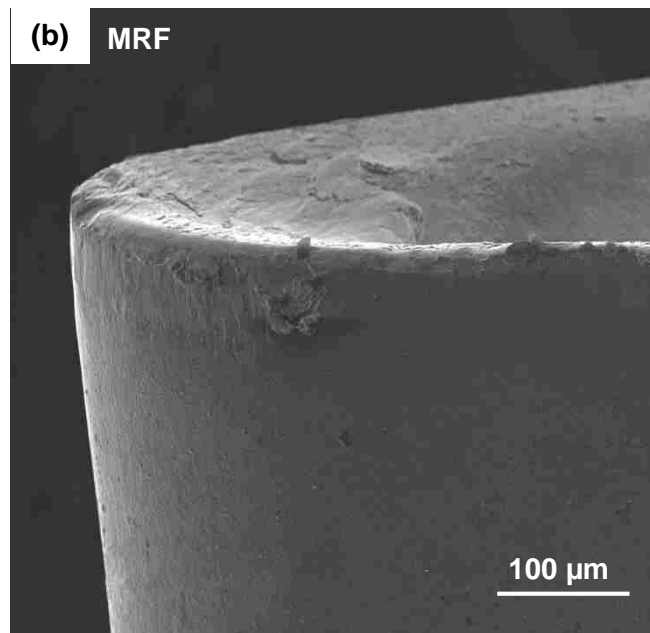
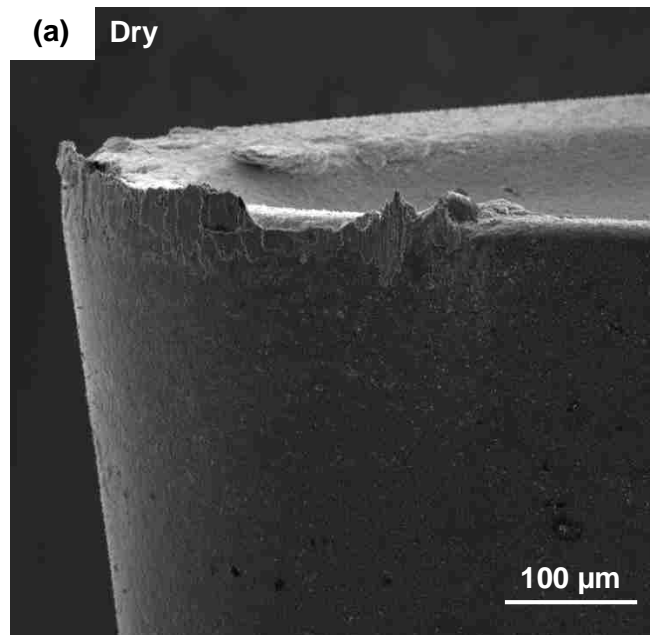
4.2.8 Effect of WS₂ Nanoparticles on Tool Wear and Adhesion

SEM (SEI mode) was performed on the rake and flank faces of the uncoated WC-Co tool subjected to orthogonal machining of Ti-6Al-4V at a cutting speed of 43 m/min, feed rate of 0.25 mm/rev and a 1 mm depth of cut. Before microscopic examination, the cutting tools were ultrasonically cleaned while being immersed in hexane for at least 10 minutes. This removed all the WS₂ nanoparticles that were present at the cutting edge. However to detect the presence of WS₂, Raman spectroscopy was conducted on the cutting edge (prior to observing the cutting tool under SEM) which will be discussed later in section 4.2.9.

Transfer of Ti to the cutting tool was observed under all three machining conditions – Dry, MRF and MRF + 1% WS₂. The highest amount of adhesion was observed during dry machining condition that led to the formation of BUE as shown in Figures 4.20 (a - b). Application of MRF slightly reduced the Ti build up, although the observed adhesion (Figures 4.20 (c-d)) could possibly be due to the failure of the coolant to effectively impinge on to the tool – workpiece interface. The lowest adhesion was observed during the MRF + 1% WS₂ tests (Figures 4.20 (e-f)).

The difference in adhesion levels could be correlated to the temperature generated during the machining process under different cutting conditions. For a constant strain regime, the yield stress of Ti-6Al-4V is inversely proportional to the temperature. Thus during the high temperatures generated during dry machining condition, the effect of thermal softening is predominant. In addition, the chemical reactivity of Ti-6Al-4V is higher at higher temperatures. Consequently the adhesion on the cutting tool is the highest under dry machining conditions. Under flooded cooling conditions, the temperature of the tool-workpiece interface is restricted to under 200 °C, and thus the adhesion wear is

reduced. In all cases, the α to β transformation would not have occurred since the maximum temperature generated during the machining was 450 °C. This temperature is less than 990 °C which is the phase transformation temperature for the α phase in Ti-6Al-4V.



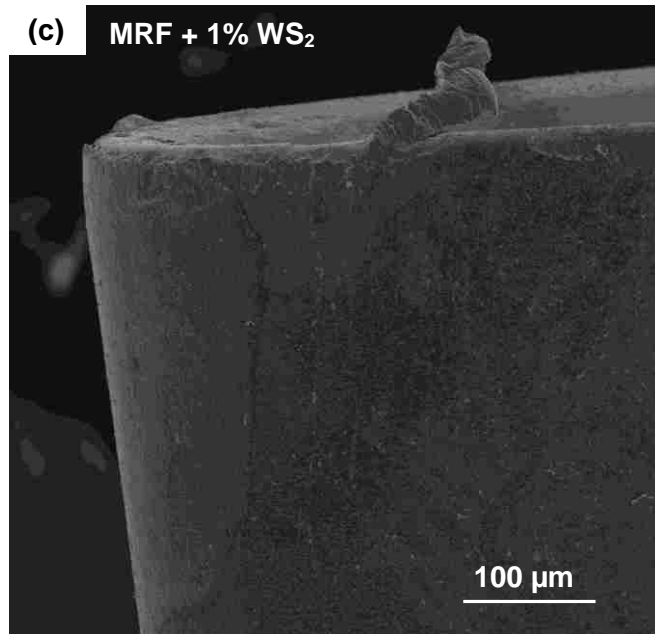
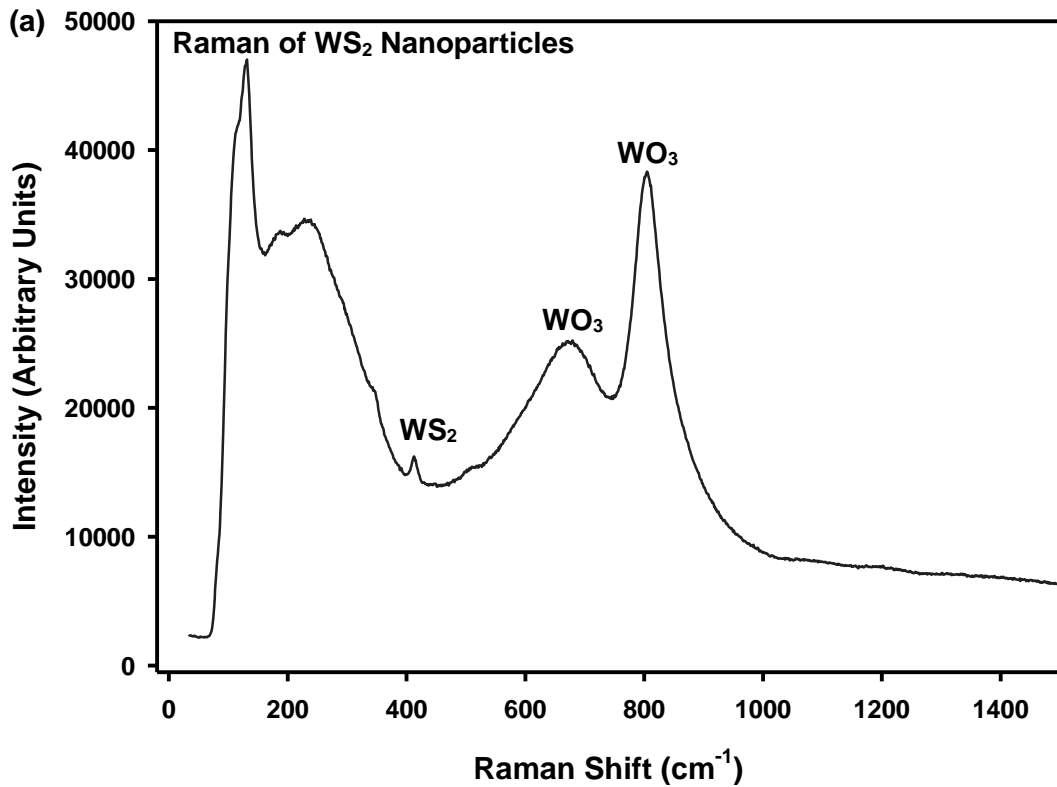


Figure 4.20: SEM (SEI mode) of the rake and flank faces of the uncoated WC-CO cutting tool after subjecting to orthogonal cutting of Ti-6Al-4V under (a), (b) dry; (c), (d) MRF; (e), (f) MRF + 1% WS₂ machining conditions.

4.2.9 Raman Spectroscopy on Cutting Edge:

The Raman spectra on the raw WS₂ nanoparticles and the cutting edge subjected to orthogonal machining under MRF + 1% WS₂ lubricated conditions against Ti-6Al-4V at a cutting speed of 29.5 m/min, feed rate of 0.4 mm/rev and a 1 mm depth of cut is shown in Figures 4.21 (a-b). The presence of WS₂ and the oxidized WO₃ is evidenced by the peaks generated at 406 cm⁻¹ and 672 cm⁻¹, 803 cm⁻¹ respectively for the raw WS₂ nanoparticles. In addition, the Raman spectra on the cutting edge showed similar peaks for WS₂ and WO₃ at 403 cm⁻¹ and 245 cm⁻¹, 315 cm⁻¹, 690 cm⁻¹ and 803 cm⁻¹, respectively. The Raman peak observed at 121 cm⁻¹ can be assigned to titanium dioxide (TiO₂) which is formed as a result of interaction between the workpiece material and atmospheric oxygen during the machining process.

The low frictional properties of WO_3 have been discussed in the literature [104, 105]. A crystalline WO_3 film deposited on a sapphire substrate tested against 440 C stainless steel sliders [104] was reported to be responsible for the low COF of 0.18. Banerji et al. [105] investigated the role of WO_3 during high temperature tribological behaviour of W-DLC coating against Ti-6Al-4V. They concluded that the formation of WO_3 at temperatures above 500 °C resulted in low COF and minimum adhesion of Ti-6Al-4V to the coating surface. Thus it can be conceived that the reduction in COF due to the presence of WO_3 and WS_2 at the cutting edge resulted in lowest amount of adhesion.



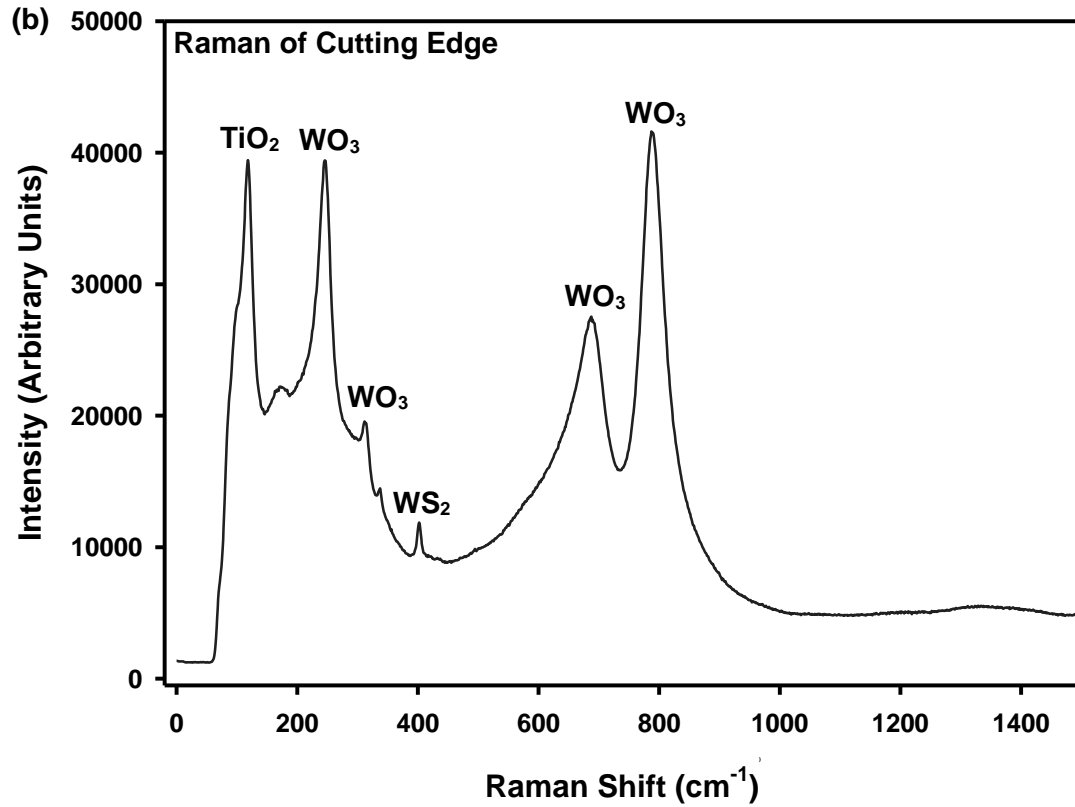


Figure 4.21: Micro-Raman spectra of (a) WS_2 nanoparticles, (b) the cutting edge that was subjected to machining of Ti-6Al-4V at a cutting speed of 29.7 m/min, 0.4 mm/rev, 1 mm depth of cut under MRF + 1% WS_2 conditions

Chapter 5

DISCUSSION

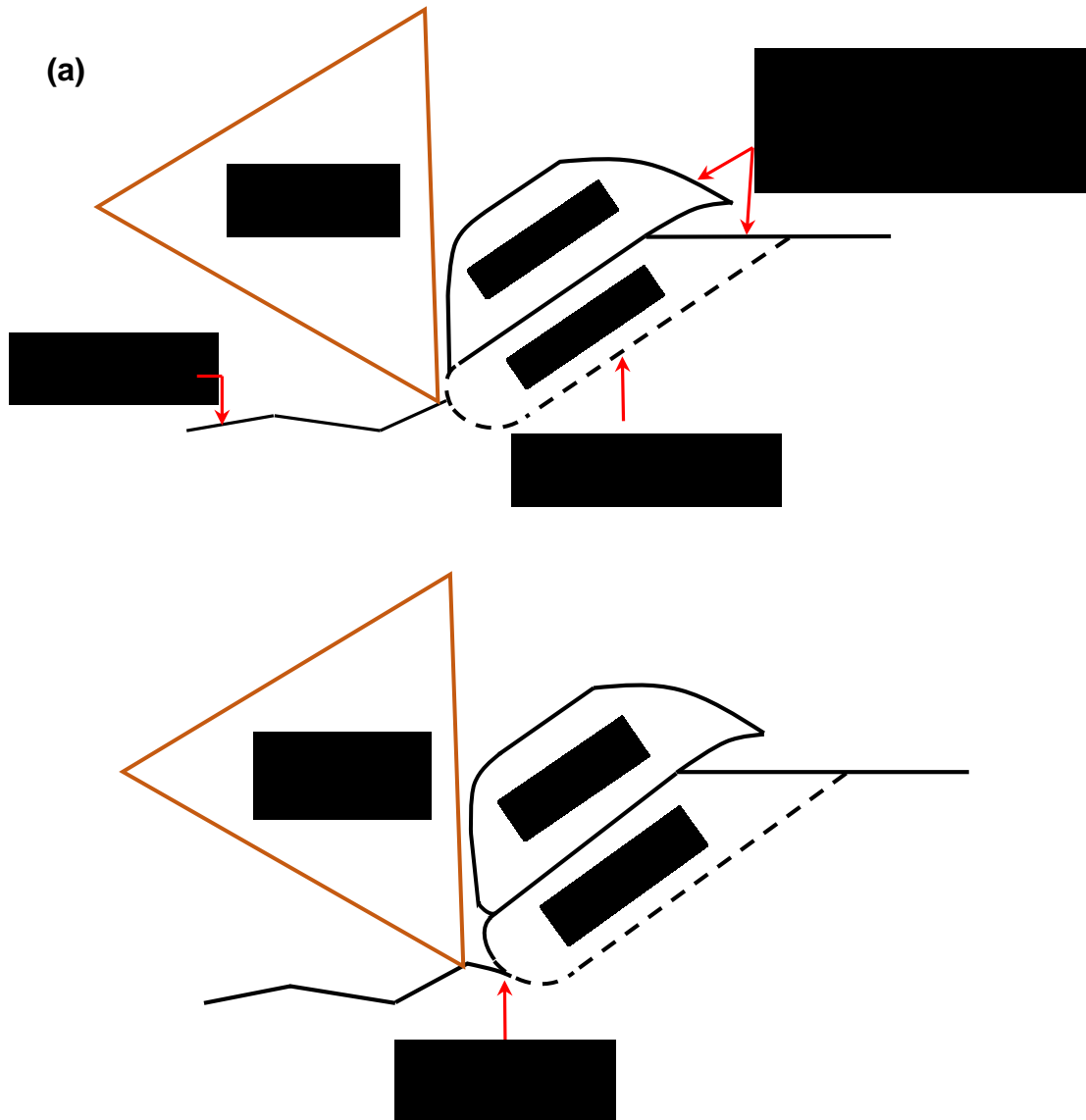
This section emphasizes two important aspects of the experimental work conducted in this study, namely, (i) correlating the fracture behaviour of Ti-6Al-4V at cryogenic temperatures with the chip segmentation process. A relationship between the in-situ microstructural observations and subsequent quantitative analyses of chip characteristics to define the significance of cryogenic machining is also established, (ii) proposing a third-body mechanism model to explain the role of WS₂ nanoparticles in reducing the COF of uncoated WC-Co when sliding against 319Al and Ti-6Al-4V.

5.1 Serrated Chip Formation Mechanism

A serrated chip formation mechanism is proposed on the basis of in-situ microstructural observations shown in Section 4.1.4. Accordingly there are four steps associated with the formation of serrated chips which are shown in Figures 5.1 (a-d).

The first step of serrated chip formation is the strain localization in the chip. The strain becomes localized along a straight path but close to the tool tip it forms a concave surface. The second step (Figure 5.1 (b)) is termed the crack initiation step and shows that a crack initiates at the tool tip and a fresh surface is generated. Also, a portion of the chip being formed is flattened by the rake face of the tool. After the crack initiation, it propagates in a stable manner, which constitutes the third step (Figure 5.1 (c)). This is the stable crack propagation step. Crack propagation follows the path of strain localization. During this step, continuous flattening of the chip being formed occurs. Also, the free surface of the chip starts to bulge due to the advancement of the tool. Gradual flattening and bulging

further closes the crack between the chip being formed and the one before it. When the stable crack advances sufficiently near to the free surface, it propagates in an unstable manner and forms a new chip. The entire process starts again as strain becomes localized for the next cycle.



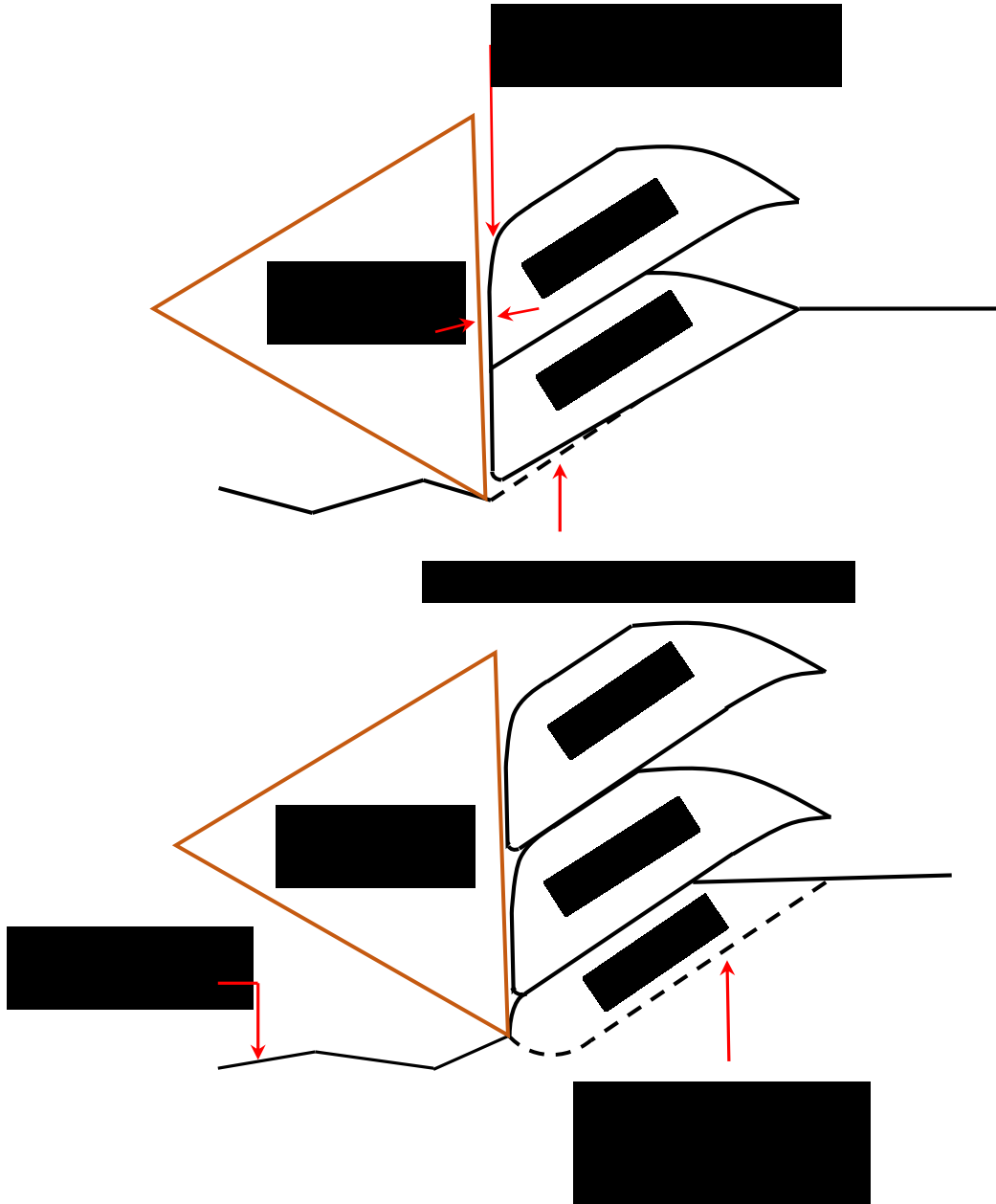


Figure 5.1: Sequential steps describing serrated chip formation under ambient machining conditions. (a) Thermal softening and strain hardening results in instability, which leads to strain localization along a shear surface (band). This shear surface originates from the tool tip and gradually curves upwards until it meets the free surface, (b) Tool's gradual advancement applies an increased amount of force, at which point a crack initiates at the tool tip and gradual flattening increases the contact between the tool and the material ahead, (c) Propagation of the crack along the path of strain localization, (d) The chip being formed pushes the previously formed chip by bulging and gradually flattening, thus shifting its contact towards the tool face. As the upsetting progresses, more and more stress is generated, which causes intense shear between the segment being formed and the one before it. The cycle repeats with the strain localization for the next chip segment

5.2 Correlation between Chips from In-situ and Conventional Machining

Microstructures obtained from dry in-situ and conventional machining show seizure between successive chip segments. That is, no gaps or cracks were formed between the chip segments. However under cryogenic machining conditions, such cracks were prominently formed and did not seize. The presence of cracks between chip segments formed under cryogenic machining is schematically represented in Figure 5.2. For comparison, a similar schematic for the chips formed under dry condition is also shown. From Figure 5.2, it can be hypothesized that the temperature of the shear band was not sufficiently high for the cracks to seize.

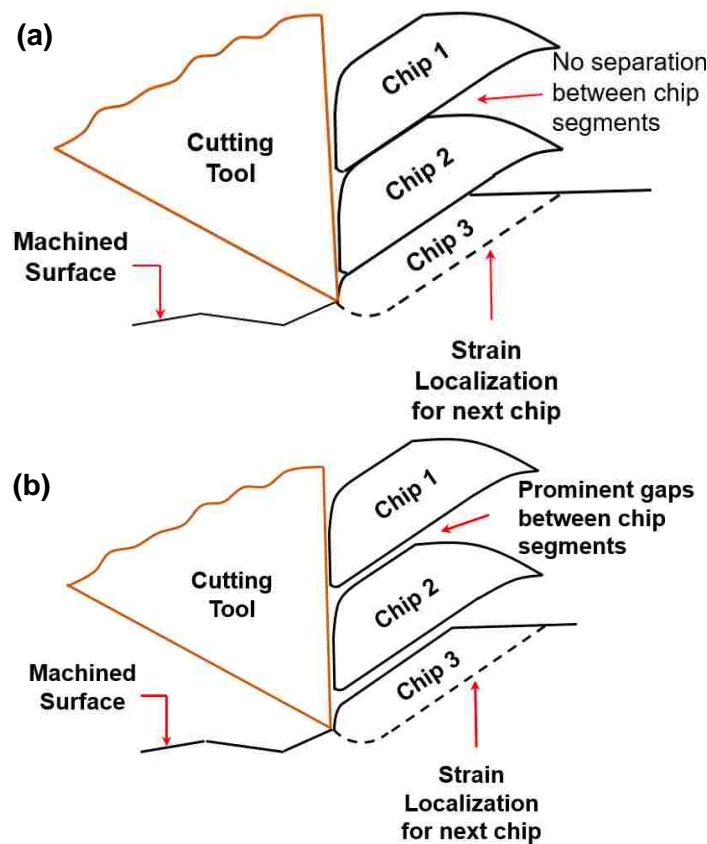


Figure 5.2: Serrated chip formation under (a) dry machining condition showing no separations between chip segments, and (b) cryogenic machining condition showing prominent gaps between successive chip segments

Microstructures of chips shown in Figure 4.7 (a) shows no separation between chip segments. Thus under dry conventional machining conditions, the temperature within the shear band was sufficiently high that the cracks near the rake face were able to seize together.

It was also observed that for the same cutting speed and feed rate, the chips produced under cryogenic conditions had higher shear displacement and higher shear angle compared to chips formed under dry machining conditions. Also the maximum and minimum chip thickness were lower in the cryogenic machining condition.

5.3 Tool Wear, Diffusion and Adhesion

Machining of Ti alloys involves generation of high cutting zone temperatures thus promoting the alloying tendency of Ti with the cutting tool material. The concept of dissolution wear and diffusion wear has been mentioned by N.P. Suh [8]. According to [8], when a pair of sliding materials ‘A’ and ‘B’ come in contact with each other, the materials will dissolve in each other if the free energy of the material pair decreases by the formation of a solution. This rate of dissolution increases with increase in temperature.

The rate of dissolution, \dot{c} , is expressed by the relation [8]:

$$\dot{c} = \frac{\partial c}{\partial t} = N_0 v \beta \exp\left(-\frac{\Delta G}{kT}\right) \quad (5.1)$$

where, N_0 is the number of available substitutional sites for A in B per unit volume, v is the frequency of atomic oscillation, β is the number of atoms joining the solution, ΔG is the activation energy necessary for dissolution, k is the Boltzmann constant, T is the absolute temperature at the interface of A and B.

From equation (5.1), it can be concluded that the rate of dissolution will be lower if the absolute interface temperature is low. Dissolution-controlled wear is normally observed in the case of uncoated WC-Co tools. However, in the case of PCD tools, the wear rate is controlled by diffusion rather than dissolution.

When Ti is machined with PCD tools, direct contact between the tool and the workpiece is prevented due to a barrier of TiC [97]. Once this layer is formed, the wear rate is controlled by diffusion rate of the tool material through this reaction layer.

The wear rate ‘ V ’ due to diffusion of carbon from the PCD to titanium can be computed using Fick’s law from the relation [8],

$$V = -\frac{v_t}{c_t} D \frac{\partial \left(\frac{c_i}{v_i} \right)}{\partial y} = -\frac{v_t D}{c_t \delta} \left(\frac{c_b}{v_b} - \frac{c_0}{v_0} \right) \quad (5.2)$$

where V is the wear rate of the tool, v_t is the molar volume of the tool material, c_t is the concentration of carbon in the tool material, c_i is the concentration of carbon at any point ‘ i ’ on the TiC layer, D is the diffusion coefficient of carbon in TiC reaction layer, δ is the thickness of TiC reaction layer. The subscripts ‘ b ’ and ‘ 0 ’ refer to the reaction layer-chip boundary and reaction layer-tool boundary interfaces, respectively.

In the sequence of serrated chip formation, the crack initiation and propagation step is the slowest step where intimate contact between the chip and the tool occurs [95, 97, 98, 105]. Thus to decrease the amount of adhesion, a low temperature coupled with smaller contact time is preferred. The velocity of the chip ‘ V_{chip} ’ under cryogenic conditions was calculated elsewhere [106] for the same cutting condition and it was reported that the V_{chip}

is higher under cryogenic conditions than under dry machining conditions. So it can be concluded that cryogenic machining helps in reducing material diffusion.

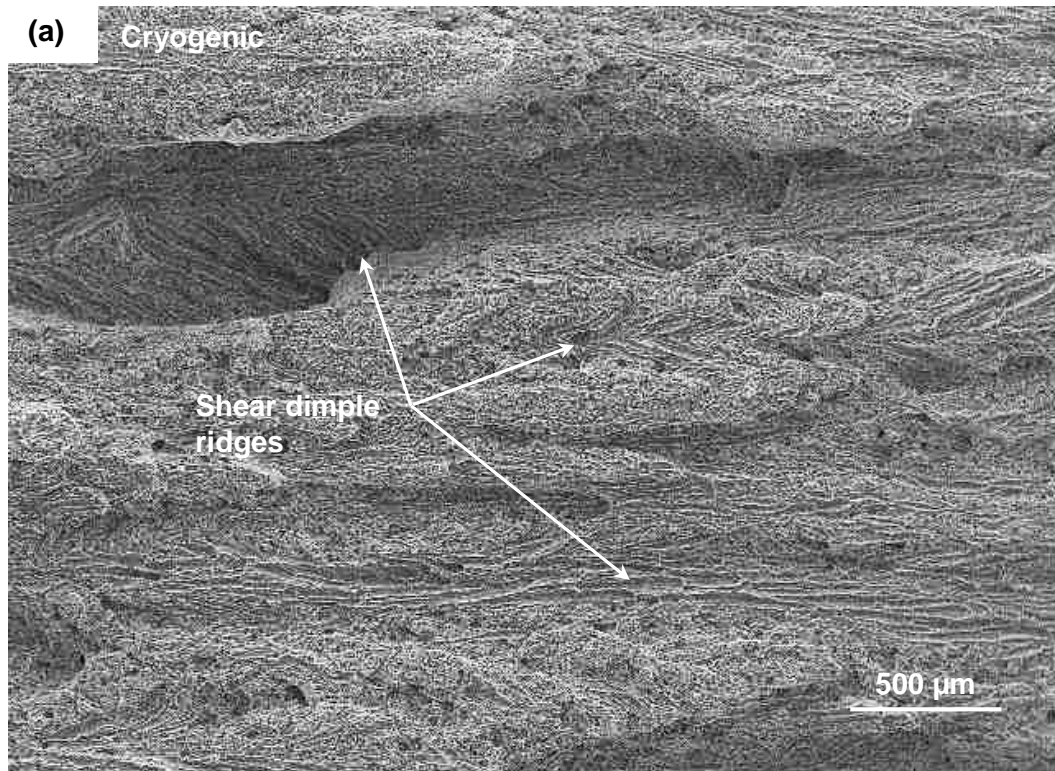
5.4 Analysis of Fracture Surfaces

Minimum toughness was associated with specimens that were subjected to very low temperatures indicating that the fracture behaviour of Ti-6Al-4V is temperature sensitive. Macroscopic observations (Figure 4.11) discussed in section 4.1.5 also indicated the observed decrease in toughness with decreasing test temperature in terms of reduced shear lip area. SEM micrographs of the fracture surfaces of Ti-6Al-4V alloys tested at cryogenic (Figure 5.3 (a) and 5.4 (a)) and room temperatures (Figure 5.3 (b) and 5.4 (b)) indicate that the observed decrease in toughness was due to the introduction of increasing amount of tearing topographical surfaces (TTS). The toughness behaviour of a fatigue pre-cracked unaged beta III Titanium alloy was investigated using charpy V-notch test [107], [108]. Shear dimple failure characterized by TTS was observed to be the predominant failure mechanism. Further investigations revealed that the TTS is formed due to repeated void initiation at a submicron level. Thompson and Chestnut [109] studied and concluded that the formation of TTS (aka shear ridges) involves micro-plastic tearing of the bulk material on a submicron level due to premature strain localization preventing the formation of well-developed voids during fracture. The critical instability for strain localization is given by the relation [110]

$$\gamma = \frac{n \times \rho \times C}{\beta \times \left(\frac{\delta\tau}{\delta\theta}\right) \varepsilon, \dot{\varepsilon}} \quad (5.3)$$

where γ represents the critical instability strain, n is the strain hardening exponent, ρ is the density of the material, C represents the specific heat capacity, β is the fraction of plastic

work that appears as heat (usually $0.9 \leq \beta \leq 1$), and $\left(\frac{\delta\tau}{\delta\theta}\right) \varepsilon, \dot{\varepsilon}$ represents the slope of the temperature dependence of flow stress at a constant strain and strain rate. Material properties such as density, specific heat and fraction of plastic work are not expected to vary with temperature. Thus it can be concluded that the shear instability under cryogenic conditions is promoted due to (i) decreasing strain hardening exponent, and/or (ii) increasing flow stress. Titanium alloys are also known to experience rapid increase in hardness with decreasing temperature [35]. Thus it is conceivable that the decrease in toughness characterized by presence of TTS, coupled with increase in hardness resulted in inducement of brittleness in Ti-6Al-4V resulting in easier chip fracture at cryogenic conditions.



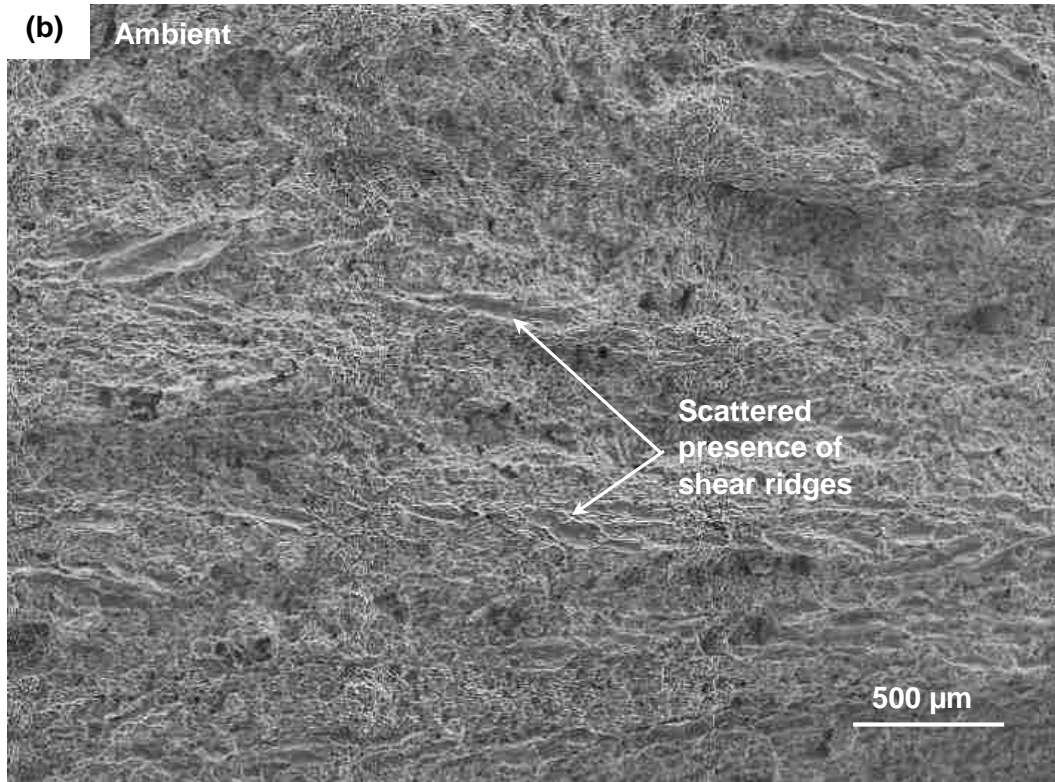


Figure 5.3: Low magnification SEM of fracture surfaces of Ti-6Al-4V at (a) cryogenic temperature, (b) room temperature

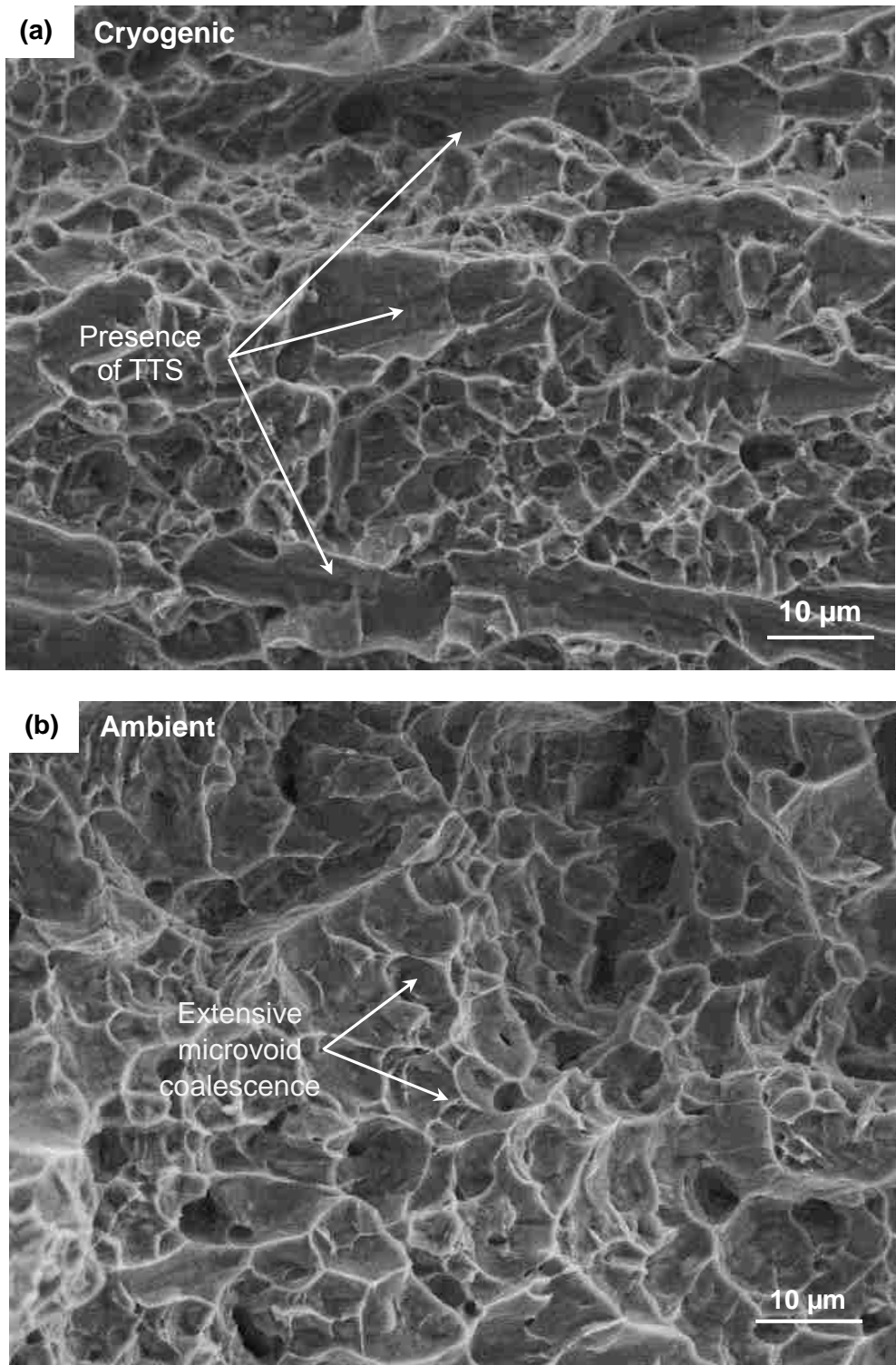


Figure 5.4: High magnification SEM of fracture surfaces of Ti-6Al-4V at (a) cryogenic temperature, (b) room temperature

5.5 Schematic Representation of Tearing Topographical Surface

SEM observations of the fracture surfaces of the samples tested at cryogenic and ambient temperatures indicate that the decrease in toughness with decrease in temperature was not due to the occurrence of conventional ductile-brittle or dimple-cleavage transition, but rather due to the introduction of increasing amounts of “shear” failure.

Spretnak [111] postulated that there are three basic requirements for the activation of such a shear instability: (i) a free surface, (ii) a stress gradient, (iii) a material that simulates a perfect plastic body. The above three requirements can be achieved at the notch root [112 - 115]. Figure 5.5 shows the slip-line field for a sharp crack tip in plane strain. Regions A and B are centered and have no strain concentration immediately ahead of the crack tip, but intense shear concentration will be formed just beneath it (Region C).

Once a crack or void is initiated at this site, continuous deformation will be concentrated along the slip-line directions which are in the same direction as that of the maximum shear stress. The fracture mechanism by formation of shear ridges is schematically represented in Figure 5.6. The process is initiated by intersection of a slip band or twin boundary as shown in Figure 5.6 a. With increasing strain, offsets are formed in the boundaries. The next step involves void nucleation by decohesion at the offset. The voids grow along these boundaries and finally fracture occurs due to extensive/ repetitive void coalescence.

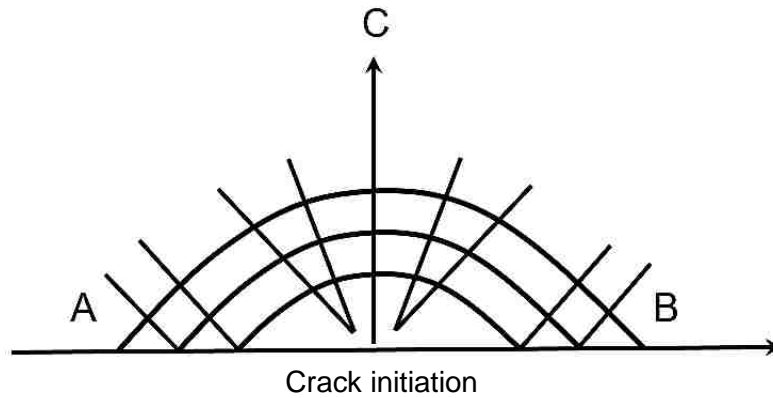


Figure 5.5: Slip line field for sharp crack in plane strain conditions [111]

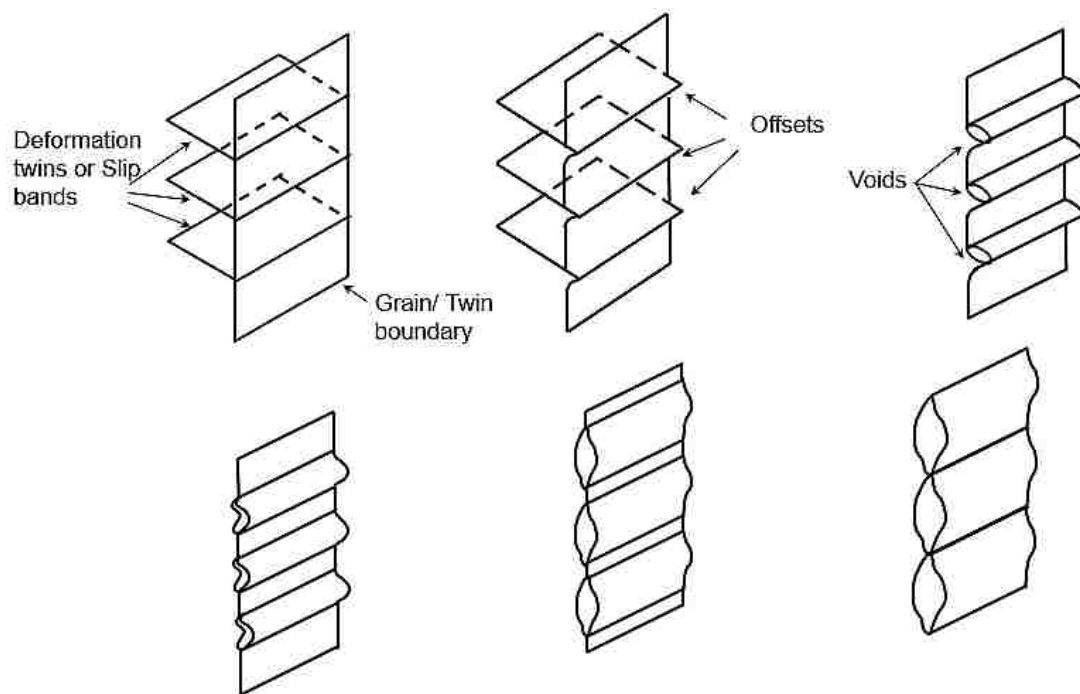


Figure 5.6: Schematic of the sequence of events during fracture by formation of shear ridges [108]

5.6 Influence of nanoparticles on COF

The experimental results presented in section 4.2 have demonstrated the enhancement of machining performance by the use of WS₂ nanoparticles blended in MRF. In addition to lowering the cutting forces, reductions in Al adhesion to the cutting tool and improvement in surface profile were also evident. An insight of the role of COF in

improving the machining efficiency of 319Al and Ti-6Al-4V can be gained from the COF curves obtained during the pin-on-disk experiments. Figure 4.12 shows the COF plot for dry, MRF and MRF + 1% WS₂ lubricated sliding conditions. The average μ_R and μ_S for dry conditions were 0.62 and 0.8, whereas that under 1% WS₂ condition were 0.06 and 0.04 respectively.

The frictional temperature increase due to relative motion between two surfaces in contact under a normal load of 'F', sliding at velocity 'v', depends on the COF ' μ ' [116]. The heat generated 'q' per unit contact area 'A_n', per second can be calculated using the relation

$$q = \frac{\mu F v}{A_n} \quad (5.4)$$

The temperature 'T_b' at the contacting surfaces as a result of heat 'q' across an area 'A_n' is related to the heat flux 'q' through the thermal conductivity of aluminum 'K' as

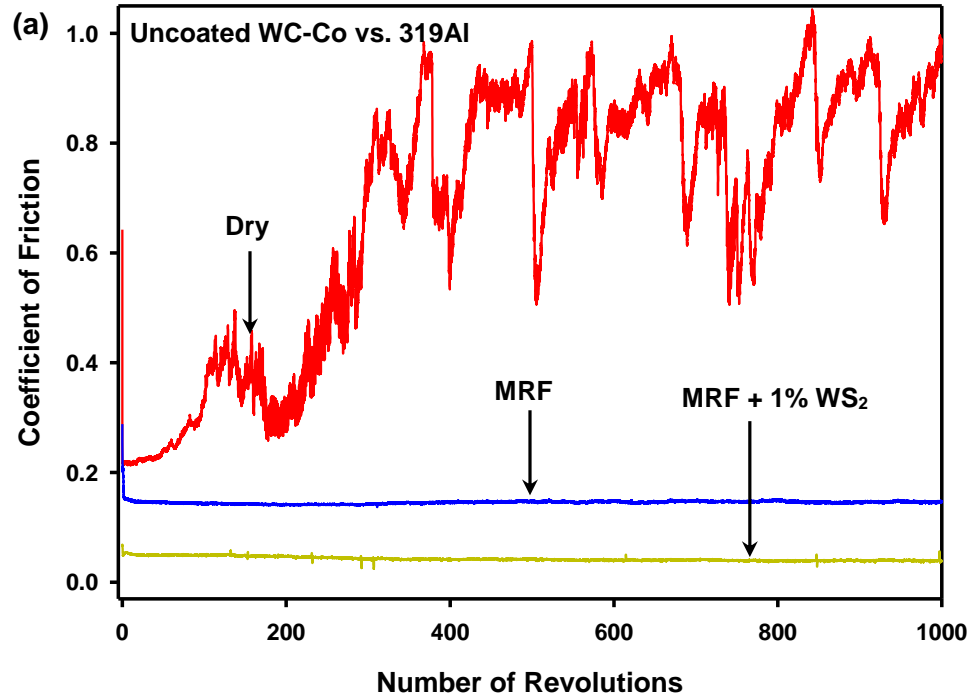
$$q = K \left(\frac{T_b - T_0}{L} \right) \quad (5.5)$$

where T₀ is the ambient temperature and L is the equivalent linear heat diffusion distance as defined in [108]. From (5.4) and (5.5), it can be inferred that the COF ' μ ' can be related to the contact temperature as

$$\mu = \frac{K A_n}{F v L} (T_b - T_0) \quad (5.6)$$

Equation (5.6) suggests that the COF can be correlated to the temperature generated during orthogonal machining of 319Al. A low COF generated during machining process would result in low contact temperatures thus limiting aluminum adhesion to the cutting

tool (Figure 4.16 (e-f)). In contrast, a high COF would result in high cutting zone temperatures which leads to softening of aluminum at the tool-workpiece interface thereby exacerbating the problem of adhesion (Figure 4.16 (a-b)). Figure 5.7 (b) shows the plot of variation of COF when uncoated WC-Co slides against Ti-6Al-4V under dry, MRF and MRF + 1% WS₂ lubricated environments. The trend is similar to that of 319Al. Thus machining with nanoparticle blended lubricant would lead to low adhesion wear and improve tool life.



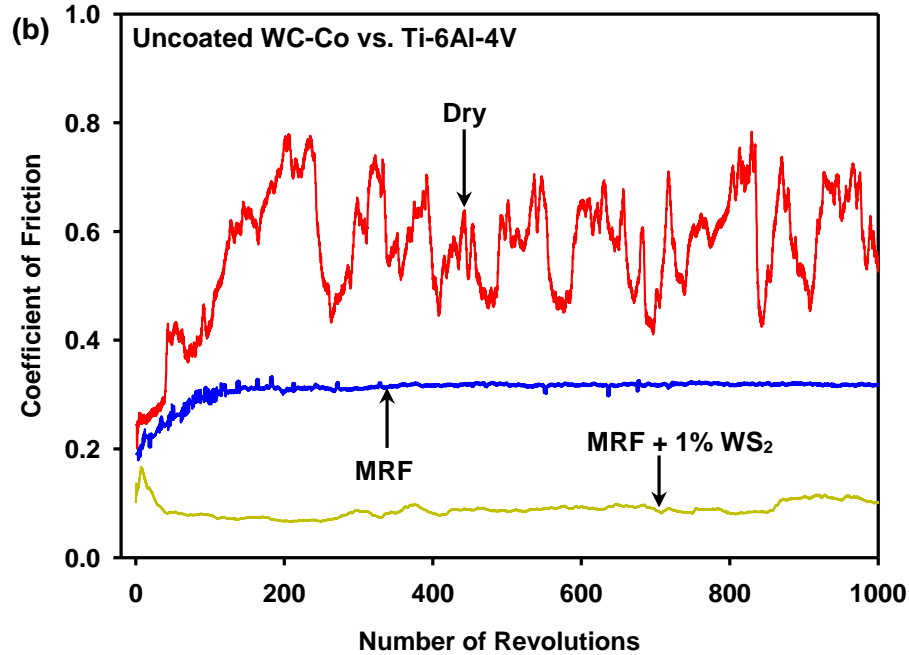


Figure 5.7: Variation of COF for uncoated WC-Co sliding against (a) 319Al, (b) Ti-6Al-4V pin, under different environments

5.7 Mechanism of Friction Reduction

The mixed lubrication regime may be defined by two types of friction generating regions: hydrodynamic full film regions and asperity regions [85]:

$$f = X_h f_h + X_A f_A \tag{5.7}$$

where f_h , f_A are the friction coefficients of the hydrodynamic and asperity contact and X_h , X_A are the fractions of the total contact load supported by fluid and by asperities, respectively.

The thickness of the lubricant film decreases with time leading to an increase in the asperity contact and thus an increase in the friction force is observed. It may be assumed that the applied load under the pin-on-disk test is shared between full film lubrication and straight asperity contact and thus a mixed lubrication is the dominant friction mechanism

under these conditions. When the thickness of the film becomes smaller than the characteristic size of the nanoparticles, the nanoparticles delaminate and/or they can be preserved in the valleys of the rough surfaces of the disk/ pin. The degree of deformation/delamination of the nanoparticles depends on the film thickness. The thinner the film, the larger is the fraction of delaminated nanoparticles. It may be assumed that under friction with a film thickness close to the size of nanoparticle (low loads) the shape of the nanoparticles is preserved and sliding/rolling of the nanoparticles at the interface seems to be the dominant friction mechanism [85]. The oil plays a considerable role in this case. When the film thickness is less than the size of nanoparticles (high loads, mixed lubrication), deformation and destruction of the nanoparticles lead to the formation of a transferred layer on the contact surface. It may be expected that with increasing load, the amount of delaminated WS_2 nanoparticles increases leading to formation of more stable solid transferred layer (Figure 5.8 (a)). In this case, the effect of oil is decreased. The WS_2 layer protects the contact surface and consequently enhances the wear resistance of contact surfaces. Thus low COF values are obtained during the pin-on-disk tests with MRF + nanoparticles sliding compared to regular MRF sliding conditions. Figure 5.8 (b - c) shows a schematic representation of the sliding tests illustrating the formation of a WS_2 layer on the Ti-6Al-4V pin.

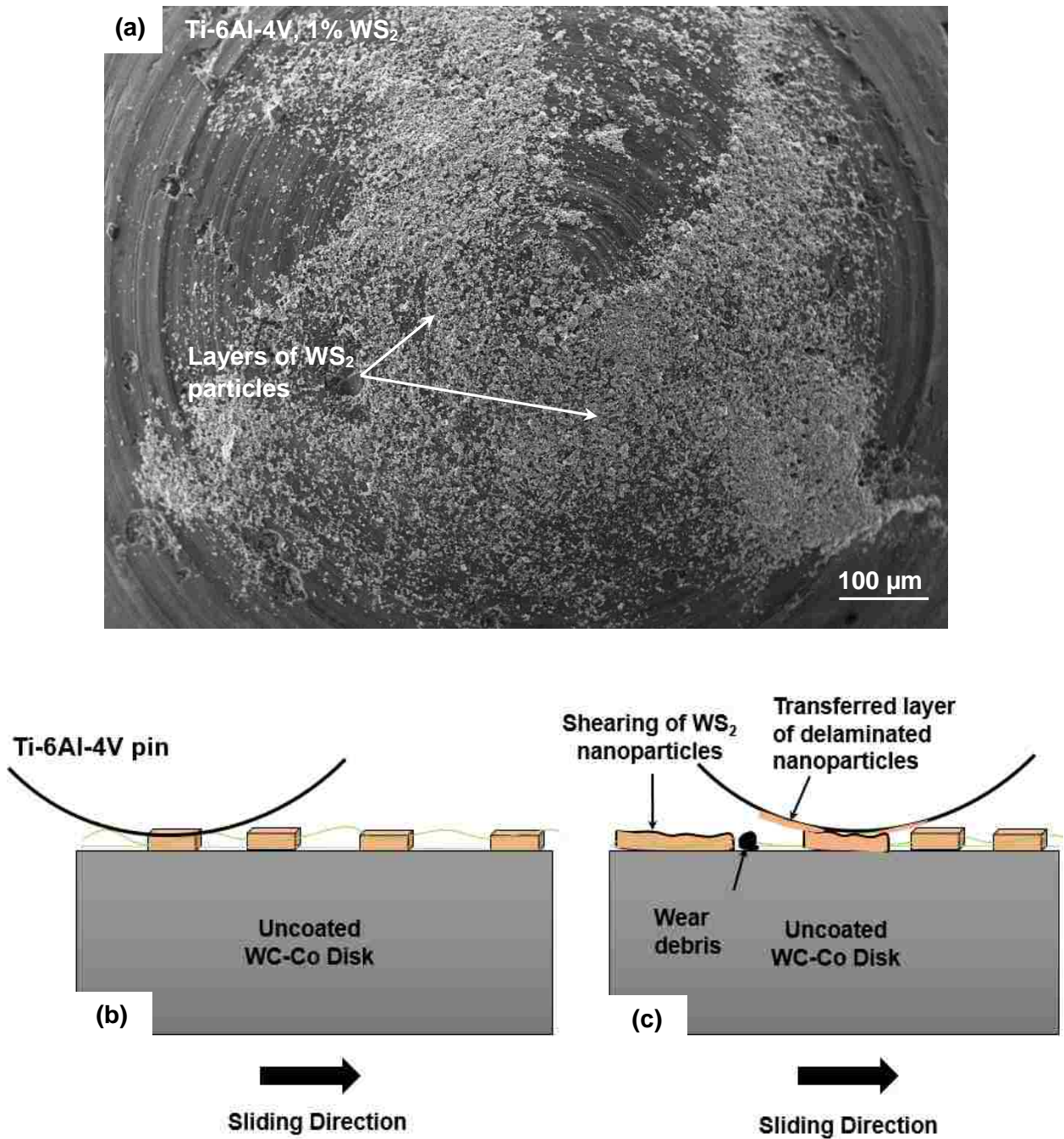


Figure 5.8: (a) SEM (SEI mode) of Ti-6Al-4V pin subject to pin-on-disk sliding tests under MRF + 1% WS₂ environment, Schematic illustration of (b) initial condition of the pin and nanoparticles in a lubricant medium, (c) shearing of WS₂ nanoparticles during pin-on-disk sliding tests and transfer of the sheared/ delaminated WS₂ nanoparticles

Chapter 6

CONCLUSIONS

6.1 Conclusions

Ti-6Al-4V alloy was subjected to orthogonal cutting at a constant speed and feed rate of 45 m/min and 0.15 mm/rev using a PCD tool under ambient and cryogenic conditions. The effect of temperature were studied based on characterization of fracture surface and microstructural interpretation of chip segments. The Ti-6Al-4V alloy was subjected to pin-on-disk tribological experiments to determine the COF under dry, MRF and MRF + WS₂ sliding conditions. The role of nanoparticles in influencing friction at the pin-disk interface was studied. The main conclusions are as follows:

1. Ti-6Al-4V alloy was subjected to conventional orthogonal machining at a constant speed and feed rate of 45 m/min and 0.15 mm/rev using a PCD tool under ambient and cryogenic conditions. The chips obtained from the machining process were examined microscopically. It was observed that the chips formed under cryogenic conditions were found to fracture more readily resulting in shorter chip segments.
2. The formation of a serrated chip consists of a severe plastic zone and a fracture zone. SEM on the chips formed under dry conditions revealed that the role of plastic strain is more prevalent compared to fracture and these chips exhibited mode II type of fracture. In contrast, the chips obtained from cryogenic conditions exhibited more fracture rather than plastic strain which is a characteristic of mode I type of fracture.

3. An in-situ experimental setup was developed to examine the chip formation mechanism during real time machining of Ti-6Al-4V under ambient and cryogenic machining conditions. A serrated chip formation mechanism consisting of four steps, namely, strain localization, crack initiation, crack propagation, and subsequent localization for next chip segment, was proposed.
4. Ti-6Al-4V samples were subjected to Charpy V-notch impact tests at different temperatures. This is was done to determine the temperature sensitivity of Ti-6Al-4V to fracture at cryogenic temperatures. It was observed that as the temperature decreased, the impact toughness of Ti-6Al-4V decreased. At very low temperatures, it was observed that the failure in the material occurred due to excessive presence of shear ridges.
5. The effect of nanoparticles blended in MRF in influencing COF was studied using pin-on-disk tests on Ti-6Al-4V and uncoated WC-Co. It was observed that irrespective of the concentration of nanoparticles in the MRF, the value of COF was found to be lower than when using MRF alone. In addition, 1% WS₂ in MRF resulted in the least COF value.
6. Orthogonal machining of Ti-6Al-4V with uncoated WC-Co was investigated under different machining environments – dry, MRF and MRF + 1% WS₂ at various cutting speeds and feed rates. Dry cutting at a speed and feed rate of 29 m/min and 0.4 mm/rev, generated a cutting force of 400 N. With the application of MRF, this was reduced to 230 N. The lowest cutting force of 190 N was obtained with MRF + 1% WS₂ lubricated conditions.

7. The surface roughness of the machined part obtained from a cutting speed of 95 m/min and feed rate of 0.12 mm/rev was examined using a non-contact profilometer – WYKO NT1100. The highest surface roughness was recorded under dry machining condition with an average roughness R_a of 3.06 μm and a root mean square roughness R_q of 3.89 μm . The lowest surface roughness was recorded under MRF + 1% WS_2 condition with a R_a of 0.95 μm and R_q of 1.08 μm .
8. A third body mechanism is proposed to explain the role of nanoparticles in reducing COF during sliding of Ti-6Al-4V pin against uncoated WC-Co disk. As a reference material, the same set of tests were also conducted on 319Al material. A schematic illustration of the delamination of the nanoparticles and subsequent transfer to the pin material is also presented.

6.2 Future Work

1. In this study, orthogonal machining of Ti-6Al-4V was done under a constant speed and feed rate. Further tests can be conducted under different speeds and feeds such that the chip load is constant. This will help to understand the effect of speed and feed rate in chip segmentation.
2. Rather than pre-cooling the workpiece for obtaining cryogenic temperatures, a cryogenic delivery system can be developed for continuous supply of liquid N_2 . Thus orthogonal tests can be done during continuous cooling. The difference in tool wear and material behaviour between precooling and continuous cooling can be understood.

3. Examine the role of β particles in causing crack propagation in the fracture surfaces of Ti-6Al-4V. This can be achieved by performing a cross-sectional microscopy study on the fracture surfaces.

REFERENCES

1. J.F. Kahles, M. Field, D. Eylon, F.H. Froes. Machining of titanium alloys, *Journal of Metals*, 37 (1985) 27 – 35.
2. R. Komanduri, B.F. Von Turkovich. New observations on the mechanism of chip formation when machining titanium alloys, *Wear*, 69 (1981) 179 – 188.
3. R. Komanduri. Some clarifications on the mechanics of chip formation when machining titanium alloys, *Wear*, 76 (1982) 15 – 34.
4. M. Brandt, M. Dargusch, S. Sun. Characteristics of cutting forces and chip formation in machining of titanium alloys, *International Journal of Machine Tools and Manufacture*, 49 (2009), 561 – 568.
5. A. Ginting, M. Nouari. Surface integrity of dry machined titanium alloys, *International Journal of Machine Tools and Manufacture*, 49 (2009) 325 – 332
6. N. Narutaki, A. Murakoshi, S. Motonishi, H. Takeyama. Study on Machining of Titanium Alloys, *CIRP Annals-Manufacturing Technology*, 32 (1983) 65 – 69.
7. A.R. Machado, J. Wallbank. Machining of Titanium and its Alloys – A Review, *Proceedings of the Institution of Mechanical Engineers, Part B: Journal of Engineering Manufacture*, 204 (1990) 53 – 60.
8. N.P. Suh. *Tribophysics*, Englewood Cliffs, Prentice-Hall, New Jersey, 1986.
9. M.C. Metal cutting principles, Oxford University Press, New York, 2005.
10. N.A. Abukhshim, P.T Mativenga, and M.A. Sheikh. Heat generation and temperature prediction in metal cutting: A Review and Implications for High Speed Machining, *International Journal of Machine Tools and Manufacture*, 46 (2006), 782 – 800.
11. A.P. Markopoulous. Finite element method in machining processes, *Spring briefs in Manufacturing and Surface Engineering*, 10 (2013) 11 – 27.
12. R Komanduri, R Brown. On the mechanics of chip segmentation in machining, *Journal of Engineering for Industry*, 103 (1981) 33 – 51.

13. R. Komanduri, Z.B. Hou. On thermoplastic shear instability in the machining of a titanium alloy (Ti-6Al-4V), *Metallurgical and Material Transactions A*, 33A (2002) 2995 – 3010.
14. A Vyas, M Shaw. Mechanics of saw-tooth chip formation in metal cutting, *Journal of Manufacturing Science and Engineering*, 121 (1999) 163 – 172.
15. S. Pratibha. Deformation state of aluminum-6% Silicon Alloy (319 Al) subjected to orthogonal cutting at different speeds and feed rates, 2010, *Electronic Theses and Dissertations*, University of Windsor, Paper 203.
16. M.E. Merchant. Mechanics of the metal cutting process II - Plasticity conditions in orthogonal cutting, *Journal of Applied Physics*, 16 (1945) 318 – 324.
17. S. Ramalingam, J Black. An electron microscopy study of chip formation, *Metallurgical Transactions A*, 4 (1973) 1103 – 1112.
18. H. Ni, A.T. Alpas. Sub-micrometer structures generated during dry machining of copper, *Materials Science and Engineering: A*. 361 (2003) 338 – 349.
19. H. Zhang, A.T. Alpas. Quantitative evaluation of plastic strain gradients generated during orthogonal cutting of an aluminum alloy, *Materials Science and Engineering: A*. 332 (2002) 249 – 254.
20. H. Ni, M Elmadagli, A.T. Alpas. Mechanical properties and microstructures of 1100 aluminum subjected to dry machining, *Materials Science and Engineering: A*. 385 (2004) 267 – 278.
21. M. Elmadagli, A.T. Alpas. Metallographic analysis of the deformation microstructure of copper subjected to orthogonal cutting, *Materials Science and Engineering: A*. 355 (2003) 249 – 259.
22. D. Tabor. A simple theory of static and dynamic hardness, *Proceedings of the Royal Society of London, Series A, Mathematical and Physical Sciences*, 192 (1948) 247 – 274.
23. G.E. Dieter, *Mechanical Metallurgy*, McGraw-Hill Publications, New York 1976.
24. R. Hill, E. Lee, S. Tupper. The theory of wedge indentation of ductile materials, *Proceedings of the Royal Society of London, Series A, Mathematical and Physical Sciences*, 188 (1947) 273 – 289.

25. D. Marsh. Plastic flow in glass, Proceedings of the Royal Society of London, Series A, Mathematical and Physical Sciences, 279 (1964) 420 – 435.
26. A.T. Alpas, H. Hu, J. Zhang, Plastic deformation and damage accumulation below the worn surfaces, Wear, 64 (1993) 188 – 195.
27. J.H. Dautzenberg, J.H. Zaat. Quantitative determination of deformation by sliding wear, Wear, 23 (1973) 9 – 19.
28. G. Lujering, J.C. Williams. Titanium, Springer-Verlag, 2007.
29. M. Thomas, S. Turner, M. Jackson. Microstructural damage during high-speed milling of titanium alloys, Scripta Materialia, 62 (2010) 250 – 253.
30. J. Kim, J. Kim, Y. Lee, C. Park, C. Lee. Microstructural analysis on boundary sliding and its accommodation mode during superplastic deformation of Ti–6Al–4V alloy, Materials Science and Engineering: A, 263 (1999), 272 – 280.
31. W.S. Lee, C.F. Lin. Plastic deformation and fracture behaviour of Ti–6Al–4V alloy loaded with high strain rate under various temperatures, Materials Science and Engineering: A, 241 (1998) 48 – 59.
32. J.K. Childs, M.M. Lencoe. Determination of materials design criteria for 6Al-4V Ti alloy at room and elevated temperature, Aerospace Structural Metals Handbook, 4 (1958) TR 58-246.
33. J.E. Campbell, R.L. Carlson. The mechanical properties of certain aircraft structural metals at very low temperatures, Aerospace Structural Metals Handbook, 4 (1958) TR 58-386.
34. C. Moosbrugger. Atlas of stress – strain curves, ASM International, The Materials Information Society, 2 (2002) 759.
35. Z. Zhao, S.Y. Hong. Cooling strategies for cryogenic machining from a materials view point, Journal of Materials engineering and performance, 1 (1992) 669 – 678.
36. A. Majorell, S. Srivatsa, R.C. Picu. Mechanical behaviour of Ti-6Al-4V at high and moderate temperatures-Part I: Experimental results, Materials Science and Engineering A. 326 (2002) 297 – 305.
37. K Nakayama. The formation of saw-toothed chip in metal cutting, 1 (1974) 572 – 577.

38. M.B. Silva, J. Wallbank. Cutting temperature: prediction and measurement methods— A Review, *Journal of Materials Processing Technology*, 88 (1999) 195 – 202.
39. D. O’Sullivan, M. Cotterell. Temperature measurement in single point turning, *Journal of Materials Processing Technology*, 118 (2001) 301 – 308.
40. P. Majumdar, R. Jayaramachandran, S. Ganesan, Finite element analysis of temperature rise in metal cutting processes, *Applied Thermal Engineering*, 25 (2005) 2152 – 2168.
41. D.K. Aspinwall, E.G. Ng, D. Brazil, J. Monaghan, Modelling of temperature and forces when orthogonally machining hardened steel, *International Journal of Machine Tools and Manufacture*, 39 (1999) 885 – 903.
42. N.A. Abukhshim, P.T. Mativenga, M.A. Sheikh. Heat generation and temperature prediction in metal cutting: A Review and implications for high speed machining, *International Journal of Machine Tools and Manufacture*, 46 (2006) 782 – 800.
43. M.P. Groover, G.E. Kane. A continuing study in the determination of temperatures in metals cutting using remote thermocouples, *Transactions of the ASME, Journal of Engineering Industry* (1971) 603 – 608.
44. S.Y. Hong, Z. Zhao. Thermal aspects, material considerations and cooling strategies in cryogenic machining, *Clean Products and Processes*, 1 (1999) 107 – 116.
45. S.Y. Hong, Z. Zhao. Cryogenic properties of some cutting tool materials, *Journal of Materials Engineering and Performance*, 1 (1992) 705 – 714.
46. S.Y. Hong, M. Broomer. Economical and ecological cryogenic machining of AISI 304 austenitic stainless steel, *Clean Products and Processes*, 2 (2000) 157 – 166.
47. S.Y. Hong, Y. Ding. Micro-temperature manipulation in cryogenic machining of low carbon steel, *Journal of Materials Processing Technology*, 116 (2001) 22 – 30.
48. S.Y. Hong, Y. Ding, R.G. Ekkens. Improving low carbon steel chip breakability by cryogenic chip cooling, *International Journal of Machine Tools and Manufacture*, 39 (1999) 1065 – 1085.
49. S.Y. Hong, Y. Ding. Improvement in chip breaking in machining a low carbon steel by cryogenically precooling the workpiece, *Transactions of the ASME, Journal of Manufacturing Science and Engineering*, 120 (1997) 76 – 83.

50. N.R. Dhar, S. Paul, A.B. Chattopadhyay, Role of cryogenic cooling on cutting temperature in turning steel, *Transactions of the ASME*, 124 (2002) 146 – 154.
51. N.R. Dhar, S. Paul, A.B. Chattopadhyay, The influence of cryogenic cooling on tool wear, dimensional accuracy and surface finish in turning AISI 1040 and E4340C steels, *Wear*, 249 (2002) 932 – 942.
52. N.R. Dhar, M. Kamruzzaman, Cutting temperature, tool wear, surface roughness and dimensional deviation in turning AISI-4037 steel under cryogenic condition, *International Journal of Machine Tools and Manufacture*, 47 (2007) 754 – 759.
53. N.R. Dhar, S. Paul, A.B. Chattopadhyay. Machining of AISI 4140 steel under cryogenic cooling-tool wear, surface roughness and dimensional deviation, *Journal of Materials Processing Technology*, 123 (2002) 483 – 489.
54. S.Y. Hong, Y. Ding. Cooling approaches and cutting temperatures in cryogenic machining of Ti–6Al–4V, *International Journal of Machine Tools and Manufacture*, 41 (2001) 1417 – 1437.
55. H. Zhao, G.C. Barber, Q. Zou. A study of flank wear in orthogonal cutting with internal cooling, *Wear*, 253 (2002) 957 – 962.
56. Tool-life testing with single-point turning tools, ISO 3685:1993
57. Z.Y. Wang, K.P. Rajurkar. Wear of CBN tool in turning of silicon nitride with cryogenic cooling, *International Journal of Machine Tools and Manufacture*, 37 (1997) 319 – 326.
58. Z.Y. Wang, K.P. Rajurkar. Cryogenic machining of hard-to-cut materials, *Wear*, 239 (2000) 168 – 175.
59. A.A. Khan, M.I. Ahmed. Improving tool life using cryogenic cooling, *Journal of Materials Processing Technology*, 196 (2008) 149 – 154.
60. Z.Y. Wang, K.P. Rajurkar, J. Fan, S. Lei, Y.C. Shin, G. Petrescu. Hybrid machining of Inconel 718, *International Journal of Machine Tools and Manufacture*, 43 (2003) 1391 – 1396.
61. M Dhananchezian, M Pradeep Kumar. Cryogenic turning of the Ti–6Al–4V alloy with modified cutting tool inserts, *Cryogenics*, 51 (2011) 34 – 40.

62. M Bermingham, J Kirsch, S Sun, S Palanisamy, M Dargusch. New observations on tool life, cutting forces and chip morphology in cryogenic machining Ti-6Al-4V, *International Journal of Machine Tools and Manufacture*, 51 (2011) 500 – 511.
63. K.A. Risbood, U.S. Dixit, A.D. Sahasrabudhe, Prediction of surface roughness and dimensional deviation by measuring cutting forces and vibrations in turning process, *Journal of Materials Processing Technology*, 132 (2003) 203 – 214.
64. R. Azouzi, M. Guillot, On-line prediction of surface finish and dimensional deviation in turning using neural network based sensor fusion, *International Journal of Machine Tools and Manufacture*, 37 (1997) 1201 – 1217.
65. N.R. Dhar, S. Paul, A.B. Chattopadhyay, On effect of cryogenic cooling on tool wear and job dimension and finish in turning Ni–Cr steel, in: *ICM 2000*, Dhaka, Bangladesh, 2000 301 – 310.
66. S. Sun, M Brandt, M. Dargusch. Machining Ti–6Al–4V alloy with cryogenic compressed air cooling, *International Journal of Machine Tools and Manufacture*, 50 (2010) 933 – 942.
67. N.R. Dhar et al. The influence of minimum quantity lubrication (MQL) on cutting temperature, chip and dimensional accuracy in turning AISI-1040 steel. *Journal of Materials Processing Technology*, 171 (2006), 93 – 99.
68. F. Chinas-Castillo, H.A. Spikes. Mechanism of action of colloidal solid dispersions, *Transactions of ASME*, 125 (2003), 552 – 557.
69. W. Liu et al. Study on the structure and tribological properties of surface modified Cu nanoparticles, *Materials Research Bulletin*, 34 (1999), 1361 – 1367.
70. L. Rapoport et al. Inorganic fullerene-like material as additives to lubricants: structure–function relationship, *Wear*, 225 (1999), 975 – 982.
71. S. Chen, W. Liu, L. Yu. Preparation of DDP-coated PbS nanoparticles and investigation of the antiwear ability of the prepared nanoparticles as additive in liquid paraffin, *Wear*, 218 (1998), 153 – 158.
72. Q. Xue, W. Liu, Z. Zhang. Friction and wear properties of a surface modified TiO₂ nanoparticle as an additive in liquid paraffin, *Wear*, 213 (1997), 29 – 32.

73. W. Liu, S. Chen. An investigation of the tribological behaviour of surface modified ZnS nanoparticles in liquid paraffin, *Wear*, 238 (2000), 120 – 124.
74. J. Zhou et al. Study on an antiwear and extreme pressure additive of surface coated LaF₃ nanoparticles in liquid paraffin, *Wear*, 249 (2001), 333 – 337.
75. S. Chen, W. Liu. Oleic acid capped PbS nanoparticles: synthesis, characterization and tribological properties, *Materials Chemistry and Physics*, 98 (2006) 183 – 189.
76. S. Qiu, Z. Zhou, J. Dong, G. Chen. Preparation of Ni nanoparticles and evaluation of their tribological performance as potential additives in oils, *Journal of Tribology*, 123 (2001), 441 – 443.
77. X. Tao et al. The ball-bearing effect of diamond nanoparticles as an oil additive, *Journal of Physics D*, 29 (1996) 2932 – 2937.
78. A.K. Sharma et al. Progress of nanofluid application in machining: A Review. *Materials and Manufacturing Processes*, 30 (2014) 813 – 828.
79. A.A.D. Sarhan et al. Reduction of power and lubricant oil consumption in milling process using a new SiO₂ nano-lubrication system, *International Journal of Advanced Manufacturing Technology*, 63 (2012), 505 – 512.
80. M. Sayuti et al. Cutting force reduction and surface quality improvement in machining of aerospace duralumin Al-2017-T4 using carbon onion nano-lubrication system. *International Journal of Advanced Manufacturing Technology*, 65 (2013), 1493 – 1500.
81. B. Rahmati et al. Morphology of surface generated by end milling Al6061-T6 using molybdenum disulfide (MoS₂) nano-lubrication, *Journal of Cleaner Production*, 66 (2013), 685 – 691.
82. O.M. Erh et al. Investigation on the morphology of the machined surface in end milling of aerospace Al6061-T6 for novel uses of SiO₂ nano-lubrication system, *Journal of Cleaner Production*, 66 (2013) , 655 – 663.
83. S.W. Lee et al. Experimental characterization of micro-drilling process using nanofluid minimum quantity lubrication, *International Journal of Machine Tools & Manufacture*, 51 (2011) 649 – 652.
84. Y.Y. Wu et al. Experimental analysis of tribological properties of lubricating oils with nanoparticle additives, *Wear*, 262 (2007) 819 – 825.

85. L. Rapoport et al. Tribological properties of WS₂ nanoparticles under mixed lubrication, *Wear*, 255 (2003) 785 – 793.
86. A.H. Battez et al. Friction reduction properties of a CuO nanolubricant used as lubricant for a NiCrBSi coating, *Wear*, 268 (2010) 325 – 328.
87. P. Kalita et al. Study of specific energy and friction coefficient in minimum quantity lubrication grinding using oil-based nanolubricants. *Journal of Manufacturing Processes*, 14 (2012), 160 – 166.
88. C. Lee et al. A study on the tribological characteristics of graphite nano-lubricants, *International Journal of Precision engineering and Manufacturing*, 10 (2009), pp. 85 – 90.
89. J.F. Wu, W.S. Zhai, G.F. Jie. Preparation and tribological properties of WS₂ nanoparticles modified by trioctylamine, *Proceedings of the Institution of Mechanical Engineers*, 223 (2009) 695 – 703.
90. L.J. Pottuz, J.M. Martin, M.I. Bouchet, M. Belin. Anomalous low friction under boundary lubrication of steel surfaces by polyols, *Tribology Letters*, 34 (2009) 21 – 29.
91. L. Rapoport et al. Friction and wear of fullerene-like WS₂ under severe contact conditions: friction of ceramic materials, *Tribology Letters*, 19 (2009) 143 – 149.
92. L. Rapoport et al. Modification of contact surfaces by fullerene-like solid lubricant nanoparticles, *Surface Coatings and Technology*, 163 (2003) 405 – 412.
93. O. Tevet et al. Friction mechanism of individual multilayered nanoparticles, *Proceedings of the National Academy of Sciences*, 108 (2011) 19901 – 19906.
94. K.H.W. Seah, X. Li. Influence of coolant on cutting tool performance, *Journal of Material Science and Technology*, 13 (1997) 199 – 205.
95. S.K. Joshi et al. Microstructural characterization of chip segmentation under different machining environments in orthogonal machining of Ti-6Al-4V, *Journal of Engineering Materials and Technology*, 137 (2015) 1 – 16.
96. S.Y Hong, Y. Ding, W. Jeong. Friction and cutting forces in cryogenic machining of Ti-6Al-4V, *International Journal of Machine Tools and Manufacture*, 41 (2001) 2271 – 2285.
97. R. Recht. Catastrophic thermoplastic shear, *Journal of Applied Mechanics*, 31 (1964) 186 – 193.

98. J. Hua, R. Shivpuri. Prediction of chip morphology and segmentation during the machining of titanium alloys, *Journal of Materials Processing Technology*, 150 (2004) 124 – 133.
99. Standard test methods for notched bar impact testing of metallic materials, ASTM E23 – 12c, 2015
100. M.P. Blinn, R.A. Williams. Design for Fracture Toughness, *Materials Selection and Design, ASM Handbook, ASM International*, 20 (1997) 533 – 544.
101. F.H. Froes, J.C. Chestnut, C.G. Rhodes, and J.C. Williams. Relationship of fracture toughness and ductility to microstructure and fractographic features in advanced deep hardenable titanium alloys, *ASTM*, 651 (1977) 115 – 150.
102. J.C. Williams, J.C. Chestnut, C.G. Rhodes, F.H. Froes, and R.G. Berryman. Development of high fracture toughness titanium alloys, *ASTM*, 651 (1977) 64 – 114.
103. S. Bhowmick et al. Tribological behaviour of Al-6.5%, -12%, -18% Si alloys during machining with CVD diamond and DLC coated tools, *Surface and Coatings Technology*, 284 (2015) 353 – 364.
104. A. Banerji et al. High temperature tribological behaviour of W containing diamond-like carbon (DLC) coating against titanium alloy, *Surface and Coatings Technology*, 241 (2014) 93 – 104.
105. P. Hartung, B.M. Kramer. Tool wear in titanium machining, *CIRP Annals, International Institution for Production Engineering Research*, 31 (1982), 78 – 80.
106. M.F. Rahman. Stress and strain concentrations during machining of Ti-6Al-4V during ambient and cryogenic temperatures, *Electronic Thesis and Dissertation (2014)*, Paper 5408.
107. H.J. Rack. Fracture toughness behaviour of unaged beta III Titanium, *ASTM International – Fracture Mechanics*, 1978.
108. R.G. Broadwell, C.F. Hickey Jr. Toughness and Fracture behaviour of Titanium, *ASTM International – Fracture Mechanics*, 1978.
109. A.W. Thompson, J.C. Chestnut. Identification of a fracture mode: The Tearing Topographical Surface, *Metallurgical Transactions A*, 10 (1979) 1193 – 1195.

110. S.P. Timothy, I.M. Hutchings. The structure of adiabatic shear bands in a titanium alloy. *Acta Metallurgica*, 33 (1985) 667 – 676.
111. J.W. Spretnak. A basis for design on allowable plastic strain, *EUR – 4820*, 6 (1971), Part L, 615 – 635.
112. C.A. Griffis and J.W. Spretnak. *Transactions, Iron and Steel Institute of Japan*, 9 (1969), 372 – 380.
113. C.A. Griffis and J.W. Spretnak. *Metallurgical Transactions*, 1 (1970), 550 – 551.
114. G. Green and J.F. Knott. *Journal of Engineering Materials and Technology*, 98 (1976) 37 – 46.
115. J.F. Knott. *The Mechanics and physics of fracture*, Metals Society/ Institute of Physics, 1975, 27 – 46.
116. S.C. Lim, M.F. Ashby. *Wear mechanism maps*, *Acta Metallurgica*, 35 (1987) 1 – 24.

LIST OF CONFERENCES

1. G. Krishnamurthy, S. Bhowmick, A.T. Alpas. Increasing Efficiency of Ti-alloy Machining by Cryogenic Cooling and using Ethanol in MRF, 4th International Conference on Virtual Machining Process Technology, University of British Columbia, Vancouver, BC, Canada, June 2nd – 5th 2015.

LIST OF PUBLICATIONS

1. G. Krishnamurthy, S. Bhowmick, W. Altenhof, A.T. Alpas. Increasing Efficiency of Ti-alloy Machining by Cryogenic Cooling and using Ethanol in MRF, CIRP Journal of Manufacturing Science and Technology, Under Review – August 2016.

VITA AUCTORIS

Name: Girish Krishnamurthy

Place of Birth: Ernakulam, Kerala, India

Date of Birth: 03rd December 1991

Education: Anna University, Chennai, India
B.E. Mechanical Engineering
September 2009 – April 2013

University of Windsor, ON, Canada

Department of Mechanical, Automotive and Materials
Engineering

September 2014 – August 2016